Numerical Studies of Strongly Correlated Quantum Systems

Simon Mathias Linsel

SIGILL. UNIVERSI TAT. LUDOVIC. MAXIM.

München 2025

Numerical Studies of Strongly Correlated Quantum Systems

Simon Mathias Linsel

Dissertation
an der Fakultät für Physik
der Ludwig–Maximilians–Universität
München

vorgelegt von
Simon Mathias Linsel
aus Herdecke

München, den 21. Oktober 2025

Erstgutachter: Prof. Dr. Fabian Bohrdt geb. Grusdt
Zweitgutachterin: Prof. Dr. Monika Aidelsburger
Tag der mündlichen Prüfung: 2. Dezember 2025

Zusammenfassung

Numerische Simulationen sind ein unverzichtbares Werkzeug der modernen Physik geworden, insbesondere im Kontext stark korrelierter Quantensysteme, die häufig nicht analytisch behandelt werden können. Viele Physiker betrachten die numerische Physik mittlerweile als eigene Fachrichtung neben der experimentellen und der theoretischen Physik. In den Veröffentlichungen, aus denen diese kumulative Dissertation besteht, werden stark korrelierte Quantensysteme studiert. Dafür werden eine Vielzahl moderner numerischer Methoden verwendet, unter anderem exakte Diagonalisierung, Matrix-Produktzustände, Quanten-Monte-Carlo und neuronale Quantenzustände. In dieser Dissertation werden drei Klassen von stark korrelierten Quantensystemen betrachtet: 1) Vom Hubbard-Modell abgeleitete frustrierte Quantenmagnete, 2) Toric Codes und 3) $\mathbb{Z}_2$ Gittereichtheorien.

Seit der Entdeckung der Hochtemperatursupraleitung in Cupraten in den 1980er-Jahren sind die Niedertemperaturphasen von Cupraten von zentralem Interesse für experimentelle und theoretische Studien. Modelle wie das Hubbard-Modell wurden eingeführt, um die effektive zweidimensionale Physik in CuO_2-Schichten zu modellieren. Das Verschwinden der antiferromagnetischen Ordnung als Konsequenz von Störstellen und deren Zusammenhang mit supraleitenden Phasen ist bedeutsam, um den Bindungsmechanismus von Elektronen in supraleitenden Phasen zu entschlüsseln. Dieser Bindungsmechanismus ist bis heute Gegenstand aktueller Forschung.

Mikroskopische Studien des $t-J$-Modells, eines Grenzfalls des Hubbard-Modells bei starken Interaktionen, legen Szenarien nahe, in denen Elektronen in zwei Partons fraktionalisieren: Ein Spinon (trägt den Spin) und ein Holon (trägt die Ladung). Mit Hilfe von Matrix-Produktzuständen wird in dieser Dissertation für einen paradigmatischen dotierten, frustrierten Quantenmagneten - das Majumdar-Ghosh-Modell - gezeigt, dass die Existenz eines gebundenen Parton-Zustands eng mit einer Feshbach-Resonanz verknüpft ist. Frustrierte Quantenmagnete werden zudem als Plattform vorgeschlagen, um Systeme weniger Teilchen zu untersuchen.

Der Toric Code ist ein Grundpfeiler der modernen Physik der kondensierten Materie und ein grundlegendes Modell für die Felder Topologie und Quantum Error Correction. Der Grundzustand des Toric Codes ist eine $\mathbb{Z}_2$ Quantenspinflüssigkeit und ist eines der einfachsten Beispiele für eine topologische Phase. Es wurde ein C++-Softwarepaket (ParaToric) entwickelt, in dem ein Continuous-Time-Quanten-Monte-Carlo-Verfahrem implementiert wird, um den Toric Code in einem parallel angelegten Feld zu simulieren. Der Algorithmus von Wu, Deng und Prokof'ev wurde um weitere Zustandsaktualisierungen erweitert, die Simulationen in bislang unzulänglichen Parameterbereichen ermöglichen. ParaToric erlaubt bislang unerreichte Systemgrößen und bildet die Grundlage für Publikationen mit den bisher größten Systemen auf dreieckigen, quadratischen, hexagonalen und kubischen Gittern. Es werden Schnittstellen für C, C++ und Python bereitgestellt, die eine nahtlose Integration von ParaToric in Projekte Dritter ermöglichen.

In dieser Dissertation werden neue geometrische Ordnungsparameter für $\mathbb{Z}_2$-Gittereichtheorien auf Basis von Perkolationstheorie eingeführt und getestet. Diese Ordnungsparameter können direkt aus experimentellen Messungen von Quantensimulatoren berechnet werden und sind konkurrierenden Ordnungsparametern in vielen Bereichen überlegen. Die Anwendung auf den Toric Code offenbart, dass selbst beim absoluten Nullpunkt Deconfined Phasen existieren, die nicht topologisch sind. Des Weiteren wird eine neue Netzwerkarchitektur für neuronale Quantenzustände eingeführt, die ungefähre Symmetrien in das Netzwerk kodiert. Diese Netzwerkarchitektur wird verwendet, um die Phasendiagramme nicht-stoquastischer Varianten des Toric Codes zu berechnen. Zu guter Letzt werden symmetriegeschützte topologische Phasen vorgeschlagen, die auch bei einer endlichen Temperatur existieren.

Abstract

Numerical simulations have become an indispensable tool in modern physics, particularly for strongly correlated quantum systems that are often inaccessible to analytical methods. Today, many physicists even regard computational physics as a new branch alongside experimental and theoretical physics. In the papers that constitute this cumulative dissertation, we investigate strongly correlated quantum systems using a wide range of modern numerical methods, including matrix product states, quantum Monte Carlo, and neural quantum states. We focus on three classes of strongly correlated quantum systems: 1) frustrated quantum magnets derived from the Hubbard model, 2) toric codes, and 3) $\mathbb{Z}_2$ lattice gauge theories.

The low-temperature phases of cuprates have been the focal point of experimental and theoretical studies since the discovery of high-temperature superconductivity in cuprates in the 1980s. Models such as the Hubbard model serve as a minimal effective theory for the quasi-two-dimensional electronic dynamics in the CuO_2 planes. The breakdown of antiferromagnetic order in the vicinity of dopants and its relation to the emergence of superconductivity are central to revealing the underlying electron pairing mechanism of the superconducting phase, a subject of active research to this day.

Microscopic studies of the $t - J$ model, a strong-coupling limit of the Hubbard model, suggest scenarios where electrons fractionalize into a spinon (carrying the spin) and a holon (carrying the charge). Using matrix product states, we show that the emergence of a bound parton-state in a paradigmatic doped frustrated quantum magnet, the Majumdar-Ghosh model, is associated with a Feshbach resonance. Additionally, we propose frustrated quantum magnets as a candidate platform for studying few-body physics.

The toric code is a cornerstone of modern condensed matter physics and a foundational model for the fields of topology and quantum error correction. Its ground state is one of the simplest examples of topology: a $\mathbb{Z}_2$ quantum spin liquid. We develop a continuous-time quantum Monte Carlo C++ package ParaToric for simulating the toric code in a parallel field. We extend the algorithm by Wu, Deng, and Prokof'ev with new updates, enabling the study of parameter regimes at intermediate to high temperature and/or low off-diagonal couplings, which were previously inaccessible. ParaToric enables unprecedented system sizes and was used for the largest published system size to date on the square, triangular, honeycomb, and cubic lattices. The source code is publicly available to the community and provides interfaces to C, C++, and Python, making ParaToric universally integrable into third-party projects.

In this dissertation, we propose and benchmark new geometric confinement order parameters for $\mathbb{Z}_2$ lattice gauge theories based on percolation theory. These order parameters can be calculated from snapshot measurements of state-of-the-art quantum simulators and outperform competing order parameters. Applying them to the toric code reveals that even at zero temperature, there are deconfined phases that are not topological. Further, we introduce a new architecture for neural quantum states, which incorporates approximate symmetries (in parameter regimes close to exact (gauge) symmetries) into the model and enables the study of quantum spin liquids in non-stoquastic variants of the toric code. Finally, we propose symmetry-protected topologically ordered phases that extend to finite temperatures.

Acknowledgments

First and foremost, I would like to thank Fabian Grusdt for his guidance over the past four years. I admire the passion for physics that he shares with everyone around him. He has built an outstanding group in which I have always felt – and will always feel – at home. I also commend his generosity. It is truly remarkable that we are given so many opportunities to travel abroad for conferences and research stays. Having spent both my Master's and my PhD in the Quantum Many-Body Group, Fabian has profoundly shaped me as a scientist, and I could not have wished for a better environment.

I am deeply grateful to Lode Pollet for his exceptional insights into numerical physics. Without him, the development of ParaToric would not have been possible. I continue to be amazed by his outstanding intuition in computational physics, especially his ability to identify bugs within minutes that take me weeks to find.

I would like to thank Annabelle Bohrdt for her continued guidance and for our many collaborations; she was, in many ways, a second supervisor to me. It is also a pleasure to thank Monika Aidelsburger for serving as my IMPRS co-supervisor and for her very helpful big-picture career advice. I thank Jan von Delft and Alexander Högele for serving on my doctoral committee.

Many thanks go to Norm Yao for hosting me as a guest in his wonderful group and for making my time at Harvard so special. I greatly admire his physical intuition, work ethic, and generosity. I have rarely encountered someone so dedicated to physics. I also thank all members of his group for the welcoming atmosphere.

I am grateful to all the PhD and Master's students for the wonderful time we shared, whether in the office or on road trips: Atiye Abedinnia, Giacomo Amadore, Annika Böhler, Pit Bermes, Tizian Blatz, Ola Carlsson, Gaia De Paciani, Gesa Dünnweber, Fabian Döschl, Tim Harris, Linus Hein, Lukas Homeier, Matjaž Kebrič, Hannah Lange, Helene Lösl, Nader Mostaan, Johannes Poersch, Felix Palm, Christian Reinmoser, Anka van der Walle, Reja Wilke, Henning Schlömer, Wenjun Zhang.

I thank Sam Mardazad, Martin Grundner, and Sebastian Paeckel for their SyTen-related support. I am grateful to Uli Schollwöck for his indispensable work in creating an excellent working environment for everyone in the chair. In addition, I thank Cordula Weber, Kathrin Higgen, and Sonya Gzyl for their administrative work. Without them, the chair and the grad school would not function.

It is also my pleasure to thank my collaborators: Eugene Demler, Gesa Dünnweber, Jad Halimeh, Lukas Homeier, Jack Kemp, Dom Kufel, Chris Laumann, Henning Schlömer, Uli Schollwöck, Reja Wilke, Duy Vu, and Norm Yao. Collaborations are among the most enjoyable parts of doing research, and I am grateful for the ideas, energy, and perspective each of them brought.

I thank Annika Böhler, Hannah Lange, Lukas Homeier, and Henning Schlömer for proofreading this dissertation, and Marc Ritter for providing his LaTeX-template.

Ein herzliches Dankeschön an die Evangelische Hochschulgemeinde der Technischen Universität München (EHG-TUM) für den geteilten Glauben, die Gemeinschaft, die entstandenen

Freundschaften und die tollen Aktivitäten. Ein besonderes Dankeschön an die Pfarrerinnen Ella Albers, Katharina Freisleder und Simone Oppel.

Mein größter Dank gilt meinen Freunden und meiner Familie für Eure Liebe und Eure Unterstützung. Ein besonderer Dank gilt meinen Eltern, Esther und Oliver, sowie meinen Brüdern, David und Aaron. Ihr unterstützt mich bei all meinen Plänen; mit Euch im Rücken kann ich alles schaffen. Nur mit Eurer Hilfe bin ich so weit gekommen.

List of publications

This dissertation is based on the following manuscripts (ordered in chronological order of appearance in this thesis):

P1 *ParaToric 1.0: Continuous-time quantum Monte Carlo for the toric code in a parallel field*,
Simon M. Linsel and Lode Pollet,
submitted to Scipost Physics Codebases,
doi: 10.48550/arXiv.2510.14781.
Reprinted on pages 16–54.

P2 *Percolation as a confinement order parameter in* $\mathbb{Z}_2$ *lattice gauge theories*,
Simon M. Linsel, Annabelle Bohrdt, Lukas Homeier, Lode Pollet, and Fabian Grusdt,
Physical Review B **110**, L241101 (2024),
doi: 10.1103/PhysRevB.110.L241101.
Reprinted on pages 56–71.

P3 *Percolation renormalization group analysis of confinement in* $\mathbb{Z}_2$ *lattice gauge theories*,
Gesa Dünnweber, Simon M. Linsel, Annabelle Bohrdt, and Fabian Grusdt,
Physical Review B **111**, 024314 (2025),
doi: 10.1103/PhysRevB.111.024314.
Reprinted on pages 73–86.

P4 *Independent e- and m-Anyon Confinement in the Parallel Field Toric Code on Non-Square Lattices*,
Simon M. Linsel, Lode Pollet, and Fabian Grusdt,
PRX Quantum **7**, 010332 (2026),
doi: 10.1103/gtth-cclr.
Reprinted on pages 88–99.

P5 *Approximately Symmetric Neural Networks for Quantum Spin Liquids*,
Dominik S. Kufel, Jack Kemp, DinhDuy Vu, Simon M. Linsel, Chris R. Laumann, Norman Y. Yao,
Physical Review Letters **135**, 056702 (2025),
doi: 10.1103/pgnx-11ph.
Reprinted on pages 101–124.

P6 *Topology meets symmetry breaking: Hidden order, intrinsically gapless topological states and finite-temperature topological transitions*,
Reja H. Wilke, Henning Schlömer, Simon M. Linsel, Annabelle Bohrdt, Fabian Grusdt,
submitted to Physical Review B,
doi: 10.48550/arXiv.2506.03146.
Reprinted on pages 126–141.

P7 *Emergent spinon-holon Feshbach resonance in a doped Majumdar-Ghosh model*,
Simon M. Linsel, Ulrich Schollwöck, Annabelle Bohrdt, and Fabian Grusdt,
Physical Review B **111**, 054430 (2025),
doi: 10.1103/PhysRevB.111.054430.
Reprinted on pages 153–160.

These publications are reprinted in their original form, resized to fit ISO A4 format. The following publication is not part of the thesis:

P8 *Realistic scheme for quantum simulation of $\mathbb{Z}_2$ lattice gauge theories with dynamical matter in (2+1)D*,
Lukas Homeier, Annabelle Bohrdt, Simon M. Linsel, Eugene Demler, Jad C. Halimeh, and Fabian Grusdt,
Communications Physics **6**, 127 (2023),
doi:10.1038/s42005-023-01237-6.

Contents

Chapter One

Introduction

Methodological reductionism analyzes complex systems by decomposing them into parts, interactions, and governing microscopic laws [1]. Holism, on the other hand, emphasizes properties that arise only at the level of the whole, and are neither apparent from, nor can be reduced to, components alone [2].[1] Physics needs both.

Collective effects in fluids such as waves and turbulence are *defined* only for a (large) ensemble of molecules. In a turbulent flow of water, tracking all interactions of a single H_2O molecule by definition does not provide any meaningful insight into turbulence. Instead, a mesoscopic (Boltzmann equation [4]) or macroscopic (Navier-Stokes equations [5]) *emergent* description is needed. From a reductionist viewpoint, these macroscopic theories are often controlled approximations of the microscopic descriptions within certain limits. Interestingly, very different microscopic interactions can lead to the same qualitative macroscopic physics. For example, emergent hydrodynamics can arise from electrons in graphene [6], ultra-cold atoms [7], active matter [8], light in non-linear systems [9], quark-gluon plasmas in heavy-ion collisions [10], and many other systems. From a holistic viewpoint, the physics of hydrodynamics depends only weakly on the underlying microscopic interactions and appears as an emergent macroscopic theory.

Analogous to emergent hydrodynamics, many physical phase transitions fall into so-called universality classes, where the qualitative behavior near the phase transition can be identical for very different microscopic interactions. Universality classes can be formally described using tools such as renormalization-group methods [11] and effective field theories [12]: as the scale changes (e.g., space or time), many microscopic details wash out and new variables, symmetries, and conservation laws emerge. However, near phase transitions, small changes in the microscopic details *qualitatively* change the physics, underlining the significance of the reductionist approach for macroscopic physics.

A famous example of emergent phenomena from condensed matter physics is the celebrated Hubbard model [13–17], which features unassuming microscopic interactions but exhibits a

---

[1] Anderson famously stated that “the whole becomes not merely more, but very different from the sum of its parts” [3].

complex emergent phase diagram that is subject to active research and scientific debate to this day. The Hubbard model provides an effective description of the $\mathrm{CuO_2}$-layers of cuprates, which were found to host *high-temperature* superconducting states in 1986 [18].[2] Ever since, the low-temperature phases of cuprates (and the Hubbard model) have been the focal point of experimental and theoretical studies. Superconductivity has had revolutionary technical applications across many fields, e.g., for strong magnets in particle colliders [19] and medical imaging (magnetic resonance imaging) [20], as well as for superconducting qubits [21]. This is one of the reasons why scientists care so much about designing materials with higher critical temperatures.

The *doped Mott insulator*, a phase regime of the Hubbard model at relatively low hole-doping, is believed to be central to understanding the emergence of superconductivity [22]. Fractionalized Fermi liquids (FL*) [23, 24] connect the physics of doped Mott insulators to two other fields: *quantum spin liquids* and *emergent gauge symmetries*. The fermionic annihilation operator $\hat{c}_{i\sigma} \sim \hat{f}_{i\sigma}\hat{b}_i^\dagger$ is composed of the spinon $\hat{f}_{i\sigma}$ with spin σ and zero charge, and the holon (or chargon) $\hat{b}_i$ has zero spin and charge $+e$. The spinons can form a long-range entangled quantum spin liquid with emergent gauge symmetries. These can be formally described by *lattice gauge theories*.

Doped Mott insulators, lattice gauge theories, and quantum spin liquids are all examples of strongly correlated quantum systems, and are generally very challenging to study, both analytically and numerically. For the standard repulsive single-band Hubbard model on a bipartite lattice, numerically exact fermionic QMC methods are sign-problem free at half-filling (due to particle-hole symmetry), but away from half-filling they generally suffer from a rapidly worsening sign-problem at low temperatures, strongly limiting access to the doped regime relevant for superconducting physics [25, 26]. Matrix product states are limited to cylinder geometries and cannot be used to simulate large, true two-dimensional systems. Other tensor network methods, such as projected entangled pair states, become numerically demanding at large doping (large required bond dimension) and simultaneously suffer from slow convergence [27, 28].

In this cumulative dissertation, we will apply state-of-the-art numerical methods, including matrix product states, quantum Monte Carlo, and neural quantum states, to tackle strongly correlated phases of matter. The dissertation comprises two Chapters: Chapter 2 includes all papers on toric codes and lattice gauge theory, and Chapter 3 includes a study on doped quantum magnets. At the beginning of both Chapter 2 and Chapter 3, we provide an overview of the theoretical foundations to connect the included papers and place them in a coherent context. In Chapter 4, we provide a conclusion and a perspective on open questions and possible follow-up studies.

Throughout this dissertation, we use natural units, thus setting the reduced Planck constant $\hbar$, the Boltzmann constant k_B, and the speed of light c to one.

---

[2] The Hubbard model was first written down decades before the experimental discovery of high-temperature superconductors.

Chapter Two

The toric code and related gauge theories

2.1 Topological phases

Historically, physical phase transitions were explained within the Ginzburg-Landau framework [29], which relies on a *local order parameter* signaling a phase transition between an ordered phase and a disordered phase. The ordered phase has a *spontaneously broken symmetry* compared to the disordered phase; the underlying Hamiltonian always has the full symmetry in both the ordered and disordered phases. A textbook example is the two-dimensional classical ferromagnetic Ising model on a square lattice, which describes interacting $\mathbb{Z}_2$ spins $s_i^z \in \{1, -1\}$ defined on lattice sites i:

$$H = -h \sum_{\langle i,j \rangle} s_i^z s_j^z, \tag{2.1}$$

where $\langle i, j \rangle$ denotes nearest neighbors. This Hamiltonian has a global $\mathbb{Z}_2$ symmetry ($s_i^z \rightarrow -s_i^z \ \forall i$). The local order parameter is the absolute value of the magnetization

$$m = \frac{1}{N} \sum_i s_i^z, \tag{2.2}$$

where N is the total number of spins. At high temperatures, the Ising model hosts a paramagnetic phase with $m = 0$. At low temperatures, the spins align, i.e. $m \neq 0$, in a random direction (either $m > 0$ or $m < 0$) and thereby spontaneously break the $\mathbb{Z}_2$ symmetry. The critical temperature $(T/h)_\mathrm{c} \approx 2.269$ was calculated exactly by Onsager [30] and correctly predicted using the Kramers-Wannier self-duality [31].[1] The classical Ising model is fundamental to statistical physics, and rich physics emerges when generalizing it. We will consider three of these generalizations in the following. This chapter could actually be called “The Ising model and its variants”.

---

[1] The three-dimensional classical Ising model still lacks an exact solution to this day [32]. However, it has been studied extensively with classical Monte Carlo methods [33–36] based on cluster updates [37, 38].

One of the most natural generalizations of the classical Ising model is the XY model, which features two-dimensional unit-length spins $\mathbf{s}_i \equiv (\cos\Theta_i, \sin\Theta_i)$, $\Theta_i \in [0, 2\pi)$:

$$H = -h \sum_{\langle i,j \rangle} \mathbf{s}_i \cdot \mathbf{s}_j = -h \sum_{\langle i,j \rangle} \cos(\Theta_i - \Theta_j). \tag{2.3}$$

The XY model has a global $O(2)$ symmetry ($SO(2)$ rotations + reflections of spins). The Mermin-Wagner theorem [39] states that for dimensions $d \leq 2$, continuous symmetries cannot spontaneously break at finite temperatures for sufficiently short-ranged interactions. Thus, the two-dimensional XY model does not have a phase transition that can be described by Ginzburg-Landau theory, i.e., no symmetry is ever broken. It was famously shown by Kosterlitz and Thouless [40] based on previous works by Berezinskii [41, 42], that the two-dimensional XY model has a phase transition that does not break any symmetry. At low temperature, vortices (topological defects) are bound in pairs, and the spin-spin correlation has quasi-long-range order (algebraic decay). At high temperature, vortices unbind and proliferate through the system; the correlations are short-ranged (exponential decay). These two phases are separated by a topological phase transition at the Berezinskii-Kosterlitz-Thouless (BKT) temperature. In 2016, Kosterlitz and Thouless (together with Haldane) were awarded the Nobel prize in physics *for theoretical discoveries of topological phase transitions and topological phases of matter*.[2]

In the next section, we will introduce a second class of topological phases, which were discovered by Haldane [43, 44].

2.2 Symmetry-protected topological order

The Ising model can be generalized to the antiferromagnetic quantum Heisenberg model

$$\hat{H} = h \sum_{\langle i,j \rangle} \hat{\mathbf{S}}_i \cdot \hat{\mathbf{S}}_j, \tag{2.4}$$

where the entries of the spin vector $\hat{\mathbf{S}}_j = (\hat{S}^x_j, \hat{S}^y_j, \hat{S}^z_j)$ can be represented as Pauli matrices and do not commute. The quantum Heisenberg model has a global $SU(2)$ symmetry and an additional time reversal symmetry. There are strong numerical indications that the ground state on the square and honeycomb lattices are semi-classical antiferromagnetic Néel states (i.e., spins ordered as ... ↑↓↑↓↑↓ ...); however, it is still a topic of active research [45]. In his revolutionary works, Haldane studied the one-dimensional quantum Heisenberg model and found the so-called Haldane phase for integer spins, which features topological boundary modes protected by the symmetry of the Hamiltonian [43, 44]. A simpler symmetry-protected topologically (SPT) ordered phase can be constructed using a variant of the one-dimensional quantum Heisenberg model, the Affleck-Kennedy-Lieb-Tasaki (AKLT) model [46]:

$$\hat{H} = \sum_{\langle i,j \rangle} \Big[\hat{\mathbf{S}}_i \cdot \hat{\mathbf{S}}_j + \frac{1}{3} (\hat{\mathbf{S}}_i \cdot \hat{\mathbf{S}}_j)^2 \Big]. \tag{2.5}$$

---

[2] https://www.nobelprize.org/prizes/physics/2016/press-release/

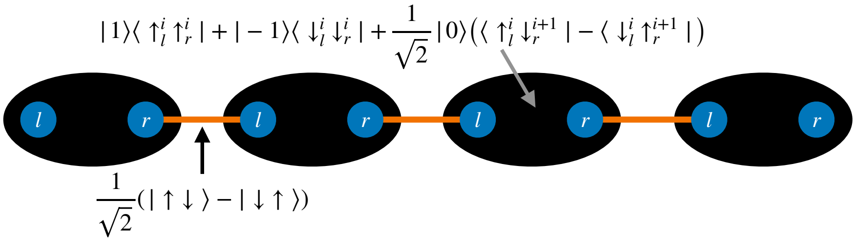

Figure 2.1: **Valence bond solid**. Each lattice site with spin-1 (black bubbles) is decomposed into a left (l) and right (r) spin-1/2 particle, which form singlets with the nearest neighbors, respectively. A projection operator projects the spin-1/2 particles back to spin-1 space with the S^z eigenstates $|-1\rangle$, $|0\rangle$, and $|1\rangle$. Figure adapted from [49].

This model is exactly solvable. To analytically express the ground state, we decompose each spin-1 into a left (l) and right (r) spin-1/2 particle, which are then projected back to spin-1 spins with the projector

$$P_i^{S=1} = |1\rangle\langle\uparrow_l^i\uparrow_r^i| + |-1\rangle\langle\downarrow_l^i\downarrow_r^i| + \frac{1}{\sqrt{2}}|0\rangle\left(\langle\uparrow_l^i\downarrow_r^{i+1}| - \langle\downarrow_l^i\uparrow_r^{i+1}|\right), \tag{2.6}$$

see Fig. 2.1. Here, $|-1\rangle$, $|0\rangle$, and $|1\rangle$ are spin-1 eigenstates; $|\uparrow\rangle$ and $|\downarrow\rangle$ are spin-1/2 eigenstates. The ground state is the *valence bond solid*[3]

$$|\psi_{\text{AKLT}}\rangle = \left(\prod_i P_i^{S=1}\right)\left(\prod_{\langle i,j\rangle} |\uparrow_r^i\downarrow_l^j\rangle - |\downarrow_r^i\uparrow_l^j\rangle\right). \tag{2.7}$$

To see that the ground state is gapped, we consider periodic boundaries, where every spin-1/2 is part of a singlet, and a triplet excitation costs a finite energy. The state does neither break spin-rotational nor time reversal, but has an ordered structure.

If we consider open boundaries, we have two dangling virtual spin-1/2 at the two boundaries, which are not part of any singlet. As long as we keep either time reversal or the spin-rotational symmetry intact and the gap remains finite, each edge spin can point in any direction and adds a degeneracy of 2 (two-dimensional irreducible representation) per edge, which is *protected by the symmetries*. This is one of the characteristic features of SPT. SPT phases can arise both in gapped and gapless ground states [50]. Compared to bulk topological phases, which feature long-range entanglement, SPT phases have short-range entanglement. In [P6], we propose finite-temperature SPT phases protected by 1-form symmetries [51] and connect them to the known Higgs-SPT phases of the toric code of the Ising gauge theory (see below).

In the next section, we will introduce a third topological phase, which was discovered around the same time as the BKT papers by Wegner [52] and also relies on a generalization of the classical Ising model.

---

[3] The AKLT model is closely related to the Majumdar-Ghosh model [47, 48] which has a valence bond solid ground state (dimerized singlets). We study it in the context of parton confinement in [P7] (included in Chapter 3).

2.3 Lattice gauge theories

The Ising model can be generalized to the transverse-field Ising model (TFIM):

$$\hat{H} = -h \sum_{\langle i,j \rangle} \hat{s}_i^z \hat{s}_j^z - J \sum_i \hat{s}_i^x. \tag{2.8}$$

Here, s^z and s^x are the usual Pauli operators. Like the classical Ising model, the TFIM has a global $\mathbb{Z}_2$ symmetry ($s_i^z \rightarrow -s_i^z$; $s_i^x \rightarrow s_i^x\ \forall i$).

The two-dimensional TFIM is dual to the classical three-dimensional Ising model, which has no known exact solution. However, the critical fields/temperatures can be calculated numerically, e.g., with quantum Monte Carlo (QMC) [53–55], tensor networks [56, 57], or linked-cluster approaches [58]. At zero temperature, the two-dimensional TFIM has an ordered ferromagnetic phase for $h \gg J$ and a disordered paramagnetic phase at $J \gg h$ with a quantum critical point at $(J/h)_\mathrm{c} \approx 3.04$ [59].

Wegner's duality mapping of the two-dimensional TFIM is given by [52]:

$$\begin{aligned} \hat{s}_i^z \hat{s}_j^z &\equiv \hat{\sigma}^x_{\langle i,j \rangle}, \\ \hat{s}_i^x &\equiv \prod_{\langle i,j \rangle \in \square_i} \hat{\sigma}^z_{\langle i,j \rangle}, \end{aligned} \tag{2.9}$$

where we define dual link variables $\hat{\sigma}$: $\hat{\sigma}_{\langle i,j \rangle}$ is defined on the link between lattice sites i and j and $\square_i$ is the elementary plaquette on the dual lattice which surrounds the real lattice site i (or, from the viewpoint of the real lattice, all links that are connected to i). Plugging Eq. (2.9) into Eq. (2.8) yields the (2+1)D *Ising gauge theory*:

$$\hat{H} = -h \sum_{\langle i,j \rangle} \hat{\sigma}^x_{\langle i,j \rangle} - J \sum_{\square} \prod_{\langle i,j \rangle \in \square} \hat{\sigma}^z_{\langle i,j \rangle}, \tag{2.10}$$

The Ising gauge theory is an example in the larger group of *lattice gauge theories* (LGTs), i.e., gauge theories discretized into a lattice. It has a *local* $\mathbb{Z}_2$ gauge symmetry with the generator

$$\hat{G}_j = \prod_{\langle i,j \rangle \in +_j} \hat{\sigma}^x_{\langle i,j \rangle}. \tag{2.11}$$

It is a product of all links connected to lattice site j ("star term"). Per definition, $\hat{G}_j$ is a symmetry of the Hamiltonian $[\hat{H}, \hat{G}_j] = 0\ \forall j$, resulting in a set of locally conserved quantities

$$\hat{G}_j \left|\psi\right\rangle \equiv g_j \left|\psi\right\rangle. \tag{2.12}$$

The set of $\{g_j \in \{-1, 1\}\}$ defines a *gauge sector*. The physics in different gauge sectors is generally *different*; it is not to be confused with the gauge symmetry, which, when applied, leaves the physics invariant. Here we choose $g_j = +1\ \forall j$, which is called a pure gauge theory [60], i.e., a gauge theory without static background charges.

By duality, the Ising gauge theory must have two phases connected by a continuous phase transition. However, since it has a local gauge symmetry, according to Elitzur's theorem [61] every operator $\hat{O}$ which is not gauge-invariant, i.e. $[\hat{O}, \hat{G}_j] \neq 0$, necessarily has zero expectation value $\langle \hat{O} \rangle = 0$ everywhere, thus the local gauge symmetry cannot be broken and no local order parameter can probe the phase transition. Wegner constructed *non-local* gauge-invariant Wegner-Wilson loops:

$$\mathcal{W}(C) = \prod_{\langle i,j \rangle \in C} \hat{\sigma}^z_{\langle i,j \rangle} \tag{2.13}$$

where C is a closed contour of links on the real lattice (from the point of view of the Ising gauge theory) with perimeter $\mathcal{P}(C) \sim L$ and enclosed area $\mathcal{A}(C) \sim L^2$ (a similar construction for a product of $\hat{\sigma}^x$-operators on the dual lattice is called 't Hooft loop [62]). For $h \gg J$, the pure gauge theory has a confined phase (dual to ferromagnetic phase) that obeys an area law $\langle \mathcal{W}(C) \rangle \sim \exp(-\alpha A(C))$ as a consequence of large fluctuations in the $\mathbb{Z}_2$ flux, $\prod_{\langle i,j \rangle \in \square} \hat{\sigma}^z_{\langle i,j \rangle}$. For $J \gg h$, the pure gauge theory has a deconfined, *topological* phase (dual to paramagnetic phase) that obeys a perimeter law $\langle \mathcal{W}(C) \rangle \sim \exp(-\alpha P(C))$ as a consequence of less fluctuations in the flux (most plaquettes have $\prod_{\langle i,j \rangle \in \square} \hat{\sigma}^z_{\langle i,j \rangle} = 1$) [60]. On a torus, the ground state splits into 4 topological sectors characterized by the eigenvalues of non-contractible Wegner-Wilson and 't Hooft loops.

The Ising gauge theory can be extended by *dynamical matter*, i.e., terms that couple the gauge field to matter:

$$\begin{aligned} \hat{H} = &- h \sum_{\langle i,j \rangle} \hat{\sigma}^x_{\langle i,j \rangle} - J \sum_{\square} \prod_{\langle i,j \rangle \in \square} \hat{\sigma}^z_{\langle i,j \rangle} \\ &- \lambda \sum_{\langle i,j \rangle} (\hat{a}^\dagger_i + \hat{a}_i) \hat{\sigma}^z_{\langle i,j \rangle} (\hat{a}^\dagger_j + \hat{a}_j) + \mu \sum_i \hat{a}^\dagger_i \hat{a}_i, \end{aligned} \tag{2.14}$$

where a_i is a hard-core bosonic annihilation operator defined on lattice site i. μ acts as a chemical potential for the bosons. The generator of the local $\mathbb{Z}_2$ symmetry is now given by

$$\hat{G}_j = (-1)^{\hat{a}^\dagger_j \hat{a}_j} \prod_{\langle i,j \rangle \in +_j} \hat{\sigma}^x_{\langle i,j \rangle}, \tag{2.15}$$

which can be rewritten into the so-called *Gauss law*

$$\hat{a}^\dagger_j \hat{a}_j = \frac{1}{2}\Big(1 - g_j \prod_{\langle i,j \rangle \in +_j} \hat{\sigma}^x_{\langle i,j \rangle}\Big), \tag{2.16}$$

relating electric field lines and the charge density. It is a discrete version of the Gauss law in classical electrodynamics, where the electric charge density ρ acts as a source of field lines of the continuous electric field $\boldsymbol{E}$:

$$\nabla \boldsymbol{E} = \frac{\rho}{\varepsilon_0}. \tag{2.17}$$

Here, ε_0 is the vacuum permittivity. In the *even* gauge sector ($g_j = +1 \, \forall j$), $\mathbb{Z}_2$ charges, i.e., sites j with $\hat{a}^\dagger_j \hat{a}_j = 1$, *must* be connected to an uneven number of electric fields $\hat{\sigma}^x_{\langle i,j \rangle} = -1$ where $\langle i, j \rangle \in +_j$, and every connected cluster C of neighboring spins with $\hat{\sigma}^x_{\langle i,j \rangle} = -1, \langle i, j \rangle \in C$ (called string) contains an even number of charges. For $J = \lambda = 0$, the energy cost E_{pot} for two charges connected by a string grows linearly with the length ℓ of the string: $E_{\text{pot}} \sim h \times \ell$. Thus, the electric field lines mediate a confining force between $\mathbb{Z}_2$ charges. The confinement of these charges is fundamental for understanding the phases of $\mathbb{Z}_2$ LGTs.

Fradkin and Shenker analytically proved that Eq. (2.14) only features two phases: a deconfined, topological phase for $h/J \ll 1, \lambda/\mu \ll 1$ [63], and a confined phase for $h/J \gg 1, \lambda/\mu \gg 1$. Surprisingly, the confined regime ($h/J \gg 1$, no free $\mathbb{Z}_2$ charges) and the Higgs regime ($\lambda/\mu \gg 1$, $\mathbb{Z}_2$ charges condense)[4] belong to the same phase [63] (compare to Fig. 1 in [P2]). Even though Eq. (2.14) only has a local $\mathbb{Z}_2$ symmetry, it can still capture some features of Wilson's famous $SU(3)$ lattice quantum chromodynamics [66], which famously demonstrated the color-confinement of quarks in the strong-coupling limit.

In LGTs with matter, the Wilson loops ('t Hooft loops) will always follow a perimeter-law (area-law) [60, 67], although the theories may still host confinement-deconfinement transitions. Thus, new order parameters are required. In the age of quantum simulators [P8, 68–72], it is vital to find order parameters that can be extracted from snapshot measurements. In [P2] we introduce a novel confinement order parameter for $\mathbb{Z}_2$ LGTs based on percolation theory [73]: If the $\mathbb{Z}_2$ strings (connecting $\mathbb{Z}_2$ electric charges) form a percolating net that extends across opposite ends of the system (winds around the system for periodic boundaries), the system is deconfined; otherwise it is confined. In [P3], we give the confinement order parameter from [P2] an analytical foundation: We apply a real-space renormalization group [74] approach for a classical limit of a $\mathbb{Z}_2$ LGT and show that the analytical phase boundaries qualitatively agree with classical Monte Carlo results. In [P4], we present a natural extension of the percolation order parameter to capture both electric and magnetic deconfinement in the context of the toric code. The order parameter is naturally accessible to experimental snapshot measurements.

2.4 Extended toric code

In the even gauge sector $g_j = +1 \, \forall j$, we can integrate out the matter by plugging Eq. (2.16) into Eq. (2.14):

$$\begin{aligned} \hat{H} &= -\mu \sum_{+} \prod_{\langle i,j \rangle \in +} \hat{\sigma}^x_{\langle i,j \rangle} - J \sum_{\square} \prod_{\langle i,j \rangle \in \square} \hat{\sigma}^z_{\langle i,j \rangle} - h \sum_{\langle i,j \rangle} \hat{\sigma}^x_{\langle i,j \rangle} - \lambda \sum_{\langle i,j \rangle} \hat{\sigma}^z_{\langle i,j \rangle}, \\ &\equiv -\mu \sum_{+} \hat{A}_+ - J \sum_{\square} \hat{B}_\square - h \sum_{l} \hat{\sigma}^x_l - \lambda \sum_{l} \hat{\sigma}^z_l, \end{aligned} \tag{2.18}$$

which is the toric code in a parallel field (also called the extended toric code or perturbed toric code). The term $\propto \mu$ ($\propto J$) is often referred to as the star-term (plaquette-term). The bare

---

[4] The Higgs phase is an SPT phase with edge modes and long-range order on the edge [64, 65].

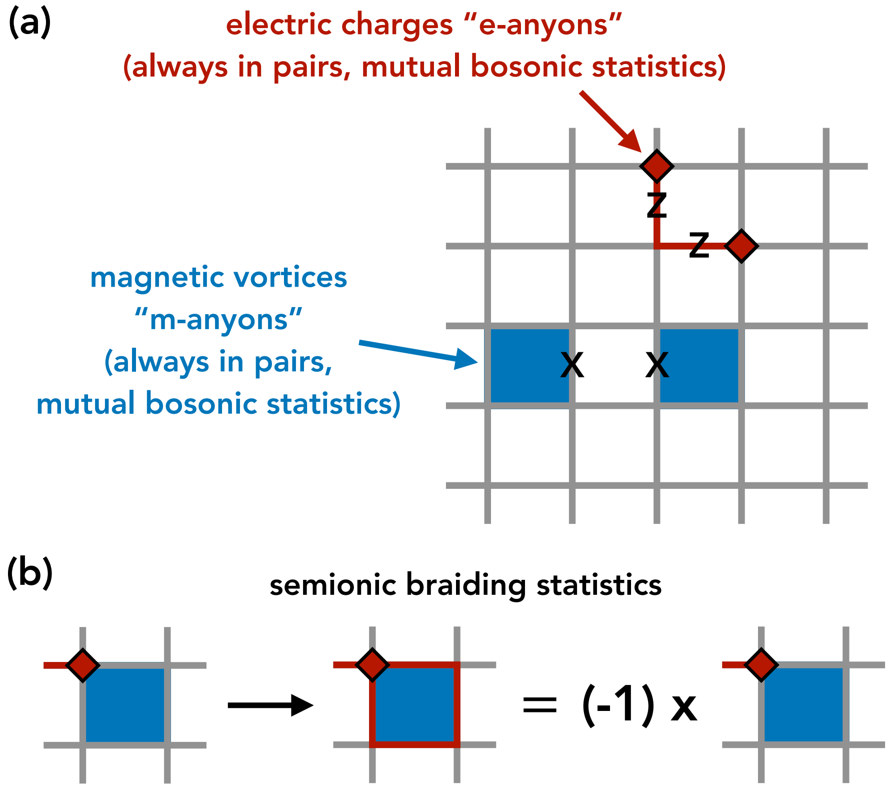

Figure 2.2: **Anyons in the toric code**. (a) We show e-aynons (star-excitations, red) and m-anyons (plaquette-excitations, blue). When anyons are braided around the same type of anyon, they are mutually bosonic. (b) When braiding an e-anyon around an m-anyon, the particle exchange statistics are fermionic.

toric code ($h = \lambda = 0$) can be solved exactly; its ground state is a topological and long-range entangled $\mathbb{Z}_2$ gapped quantum spin liquid. It is an equal superposition of all configurations satisfying $B_\square = A_+ = 1\ \forall\square, +$ (quantum loop gas). The von Neumann entropy $S(\rho) = -\mathrm{tr}\rho \log \rho$ of the reduced density operator ρ of a simply connected disc of circumference L with smooth boundaries, where the exterior degrees of freedom are traced out, reads [75]

$$S(\rho) = \alpha L - \gamma, \quad \gamma = \ln 2, \tag{2.19}$$

where γ is the non-zero topological entanglement entropy, i.e., the ground state features *long-range* entanglement.[5] It is a characteristic of the topology of the ground state and is non-zero irrespective of the boundary conditions.

The toric code features two types of topological defects, e- and m-anyons, which are excitations of the star operator $\propto \mu$ and the plaquette operator $\propto J$, respectively, see Fig. 2.2a. The name

---

[5] This is different from the short-range entanglement of SPT phases.

anyon comes from the fact that these excitations are neither purely fermionic nor bosonic, but instead can pick up *any* phase Θ when exchanging two particles $|\psi_1\psi_2\rangle = e^{i\Theta}|\psi_2\psi_1\rangle$. In the case of the toric code, the anyons fulfill semionic statistics: they are bosonic when braided around the same anyon type, but the composition (e+m) is fermionic, see Fig. 2.2b. In [P4], we show that for the triangular and honeycomb lattice, at zero temperature[6], the ground state is topological iff *both* e- and m-anyons are deconfined. We further show that there are phases where one of the two anyons is deconfined in a topologically trivial phase, meaning that even at zero temperature, one must make a distinction between topology and deconfinement.

When introducing fields h, λ, the topological phase of the two-dimensional toric code survives until a finite critical field, where it has a continuous phase transition to the trivial phase in the (2+1)D Ising universality class. In [P4], we map out the topological phase diagrams for the triangular, honeycomb, and cubic lattices for the first time with a numerically exact method, substantially improving previous approximations of the phase diagram.

2.5 Quantum Monte Carlo for the extended toric code

We first explain Markov chain Monte Carlo in the context of classical Monte Carlo simulations at finite temperature in Sec. 2.5.1. We will then present the path-integral expansion that is fundamental to the QMC algorithm to discuss the emergence of the sign-problem in the context of the extended toric code.

2.5.1 Markov chain Monte Carlo

The central object in statistical physics to describe macroscopic physics is the canonical partition function

$$Z = \sum_s e^{-\beta E(s)}, \tag{2.20}$$

where β is the inverse temperature and s are the microcanonical states with energy $E(s)$. The *Boltzmann weight*

$$P(s) = e^{-\beta E(s)}/Z. \tag{2.21}$$

is the probability that the canonical (thermal) system is in the microcanonical state s. The expectation value of a macroscopic observable O is given by

$$\langle O \rangle = \sum_s O(s)P(s). \tag{2.22}$$

The goal of statistical physics, and numerical Monte Carlo simulations in particular, is to calculate these expectation values. However, summing over all microcanonical states s quickly becomes intractable because of the exponential configuration space (quantum mechanics: Hilbert space)

---

[6] At any non-zero temperature, the two-dimensional toric code is in a topologically trivial phase [76].

growth. The goal of all *Markov chain* Monte Carlo methods is to effectively sample $\langle O \rangle$ by only summing over a subset of states s', which, however, still represent the Boltzmann distribution. This technique is called *importance sampling*. The states s' are determined by constructing a (first-order) Markov chain [77], which is a sequence of states in which every state depends only on the previous state. Starting from an initial state, we define a transition rate $W(s_{\text{new}}|s_{\text{old}})$ to determine the next state s_{new} in the Markov chain, given the current state s_{old}. It can be written as

$$W(s_{\text{new}}|s_{\text{old}}) = T(s_{\text{new}}|s_{\text{old}}) \times A(s_{\text{new}}, s_{\text{old}}), \tag{2.23}$$

where $T(s_{\text{new}}|s_{\text{old}})$ is the *trial distribution* to propose the next element s_{new} given s_{old}, and $A(s_{\text{new}}, s_{\text{old}})$ is the probability to accept the new element s_{new} as the next element in the Markov chain (in case it is rejected, the next element in the Markov chain is again s_{old}). In physics, we typically require *ergodicity* and *detailed balance*, which ensure that the Markov chain represents an ensemble in equilibrium [78].

Ergodicity means that every possible physical state s is in principle reachable by the Markov chain[7] and that the Markov chain is aperiodic. The *balance* condition states that

$$\frac{\mathrm{d}P(s_{\text{old}})}{\mathrm{d}t} = -\sum_{s_{\text{new}}} W(s_{\text{new}}|s_{\text{old}})P(s_{\text{old}}) + \sum_{s_{\text{new}}} W(s_{\text{old}}|s_{\text{new}})P(s_{\text{new}}) = 0 \tag{2.24}$$

is required to represent a stationary ensemble. The discrete time t serves as an index for elements in the Markov chain. The first (second) term represents the outgoing (incoming) probability. In physics, one typically imposes the even stricter detailed balance condition, which locally fulfills Eq. (2.24):

$$W(s_{\text{new}}|s_{\text{old}})P(s_{\text{old}}) = W(s_{\text{old}}|s_{\text{new}})P(s_{\text{new}}). \tag{2.25}$$

The famous algorithm by Metropolis [79] with the extension of Hastings [80] chooses the acceptance ratio

$$A(s_{\text{new}}, s_{\text{old}} = \min\left(1, \frac{P(s_{\text{new}})}{P(s_{\text{old}})} \frac{T(s_{\text{old}}|s_{\text{new}})}{T(s_{\text{new}}|s_{\text{old}})}\right) \tag{2.26}$$

which satisfies Eq. (2.25). This relatively simple algorithm has proven to be extremely successful and is still the backbone of modern Monte Carlo simulations in physics more than seven decades after its first formulation.

2.5.2 QMC algorithm

Wu, Deng, and Prokof'ev developed a continuous-time QMC algorithm for simulating the extended toric code (2.18) [81]. The first step is to split the Hamiltonian into two non-commuting parts, i.e., group it into one part that depends on $\hat{\sigma}^x$, and another part that depends on $\hat{\sigma}^z$. Here,

---

[7] This does, however, not mean that every state will likely be reached in practice. In fact, importance sampling relies on the fact that most states are effectively irrelevant.

we will choose the $\hat{\sigma}^z$-eigenbasis and refer to $\hat{\sigma}^z$-terms ($\hat{\sigma}^x$-terms) as diagonal (off-diagonal) terms.[8] The diagonal term $\hat{U}$ and the off-diagonal term $\hat{K}$ read:

$$\begin{aligned} \hat{U} &= -J \sum_{\square} \hat{B}_{\square} - \lambda \sum_{l} \hat{\sigma}_l^z, \\ \hat{K} &= -\mu \sum_{+} \hat{A}_{+} - h \sum_{l} \hat{\sigma}_l^x. \end{aligned} \tag{2.27}$$

The partition function can be expressed as a path-integral [81]

$$\begin{aligned} Z &= \mathrm{tr}(\exp -\beta \hat{H}) \\ &= \sum_{n=0}^{\infty} \int_{0<\tau_1<\tau_2<\ldots<\tau_n}^{\beta} \mathrm{d}\tau_1 \ldots \mathrm{d}\tau_n \\ &\quad \sum_{\alpha_0, \alpha_1, \ldots, \alpha_{n-1}, \alpha_n = \alpha_0} (-1)^n K_{\alpha_n, \alpha_{n-1}} K_{\alpha_{n-1}, \alpha_{n-2}} \ldots K_{\alpha_1, \alpha_0} \\ &\quad \exp\left(- \int_0^{\beta} \mathrm{d}\tau \, U(\tau) \right), \end{aligned} \tag{2.28}$$

where α_j denominate $\hat{\sigma}^z$-eigenstates, i.e. classical variables $s^z \in \{-1, +1\}$; τ_j is the imaginary time when the off-diagonal term $K_{\alpha_j, \alpha_{j-1}} = \langle \alpha_j | \hat{K} | \alpha_{j-1} \rangle$ changes α_{j-1} to α_j; The multi-link operator $\hat{A}_+$ (four links on the square lattice) flips multiple spins at the same imaginary time, the operator $\hat{\sigma}_l^x$ only flips the imaginary time on one link l. The diagonal energy in the exponent is piecewise-constant: $U(\tau) = U_{\alpha_i}$ for $\tau \in (\tau_i, \tau_{i+1})$.

The algorithm is sign-problem free with fields in $\hat{\sigma}^x$- and $\hat{\sigma}^z$-direction, because every K interaction includes a global minus sign of the Hamiltonian. Introducing a field in $\hat{\sigma}^y$-direction leads to complex weights. This is an example of the infamous sign-problem [25, 82, 83]; An important property is the stoquasticity: many non-stoquastic Hamiltonians (i.e., they have positive/complex off-diagonal elements in a given basis) have a sign-problem [84].[9]

The construction of the Metropolis updates is rather cumbersome and is detailed in [81]. In [P1], we implement the algorithm by Wu, Deng, and Prokof'ev in both the $\hat{\sigma}^x$- and $\hat{\sigma}^z$-basis. We also implement a wide range of common observables and provide interfaces to C, C++, and Python, making the integration into other projects in different programming languages straightforward. The complete documentation of the public application programming interface (API), performance benchmarks, and instructions on how to use the code can be found in [P1]. The package is called ParaToric because it implements the **toric** code in a **para**llel field. Earlier versions of the code were used in the publications [P2, P3, P4, P5], and without ParaToric, these works would not have been possible.[10]

---

[8] However, we could do it the other way around; we implement both bases in [P1].

[9] Stoquasticity is a basis-dependent property, choosing a smart basis can sometimes remove the sign-problem entirely.

[10] The public repository with the up-to-date code is on Github: https://github.com/palmbart/ParaToric.

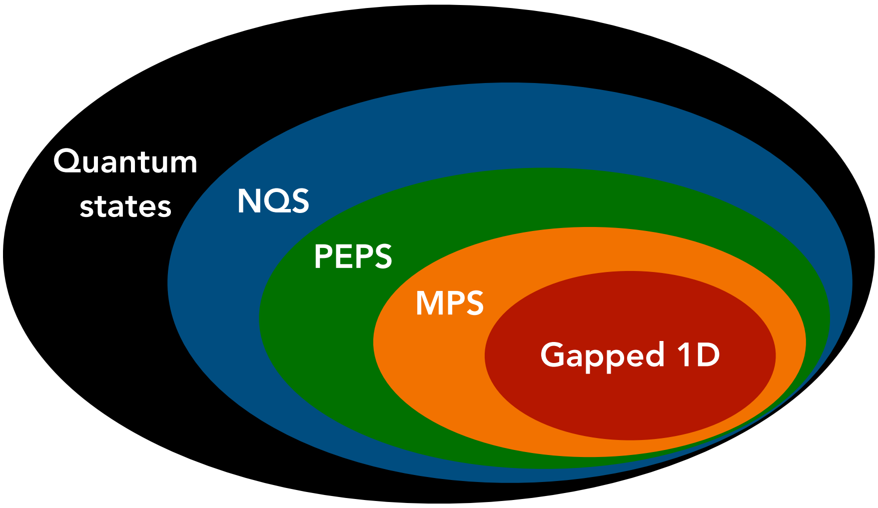

Figure 2.3: **Expressivity of variational quantum states**. Neural quantum states (NQS) have been shown to have the same or higher expressivity than polynomially tractable tensor networks, including matrix product states (MPS) and projected entangled pair states (PEPS) [86]. Polynomially tractable means that a tensor network representing N degrees of freedom (e.g., spins) with bond dimension χ can be approximately (or exactly) contracted in a time $\mathrm{poly}(N, \chi)$. An example where the expressivity of NQS is indispensable for efficient representation is volume-law entangled quantum states. Figure adapted from [86].

2.6 Neural quantum states

A quantum state can generally be written as

$$|\psi\rangle = \sum_{\mathcal{S}} \psi(\mathcal{S}) |\mathcal{S}\rangle, \tag{2.29}$$

where $\psi(\mathcal{S})$ are complex numbers and $|\mathcal{S}\rangle$ are many-body basis states. As an example, for N spins of the classical Ising model (local Hilbert space dimension 2), we would have $\mathcal{S} = (\mathcal{S}_0, \mathcal{S}_1, \dots, \mathcal{S}_{N-1})$ with $\mathcal{S}_i \in \{-1, 1\}$.

NQS were originally proposed by Carleo and Troyer [85] and represent the complex coefficients $\psi(\mathcal{S})$ using neural networks. They take inputs $\mathcal{S}$ and map them through the neural network with parameters $\mathcal{W}$ to the output $\psi(\mathcal{S})$.

The main advantage of neural networks is their expressivity, i.e., their capability to efficiently represent quantum states even for highly entangled systems such as volume-law entangled states [87]. In that regard, neural networks can efficiently represent more quantum states than competing variational methods such as matrix product state (introduced in Sec. 3.3) or projected entangled pair states (PEPS) [86], see Fig. 2.3. Another advantage of NQS is that many architectures work for non-stoquastic Hamiltonians [87], thus circumventing the infamous sign-problem, which sets strict bounds to the applicability of quantum Monte Carlo methods [25, 82, 83]. NQS have a wide range of applications, including ground states, excited states, thermal states, time-evolutions, and open quantum systems [87].

The main challenge of NQS, and at the same time the main drawback of their expressivity, is the training process, which typically features non-convex optimization landscapes and is not guaranteed to converge. There have been several ideas on how to tackle this problem. One option among many [87] is to incorporate (gauge) symmetries of the Hamiltonian into the network architecture [88–91], which reduces the number of parameters without reducing expressivity. Quantum spin liquids often have emergent gauge symmetries or other highly symmetric regions in parameter space, but in many adjacent parameter regimes, the (gauge) symmetry is not exactly fulfilled. For a long time, it was unclear whether these approximate symmetries could be practically exploited. In [P5], we present an NQS network architecture incorporating approximate symmetries into the training process. We map out the phase diagram of a Hamiltonian with a sign-problem beyond the reach of quantum Monte Carlo, i.e., the extended toric code (2.18) with an additional field in $\hat{\sigma}^y$-direction, thus demonstrating that the network architecture also works in parameter regions far away from symmetric regions and correctly captures phase transitions. We also apply the architecture to the PXP Rydberg Hamiltonian [92], highlighting its applicability to other models.

2.7 Publication 1: ParaToric 1.0: Continuous-time quantum Monte Carlo for the toric code in a parallel field

In this section, the following publication is reprinted:

P1 *ParaToric 1.0: Continuous-time quantum Monte Carlo for the toric code in a parallel field*,
Simon M. Linsel and Lode Pollet,
submitted to Scipost Physics Codebases,
doi: 10.48550/arXiv.2506.03146.
Reprinted on pages 16–54.

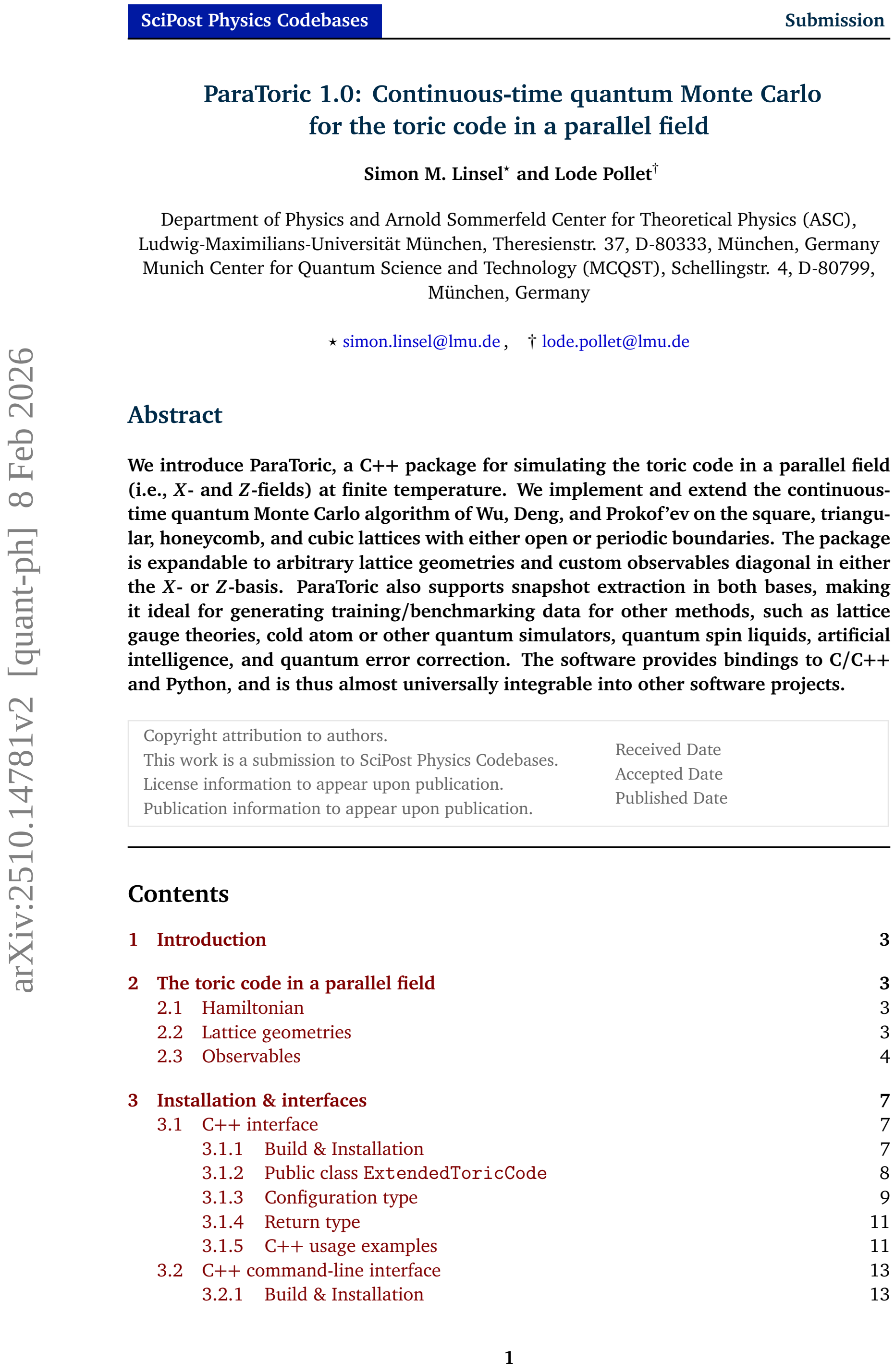

SciPost Physics Codebases
Submission

ParaToric 1.0: Continuous-time quantum Monte Carlo for the toric code in a parallel field

Simon M. Linsel[⋆] **and Lode Pollet**[†]

Department of Physics and Arnold Sommerfeld Center for Theoretical Physics (ASC),
Ludwig-Maximilians-Universität München, Theresienstr. 37, D-80333, München, Germany
Munich Center for Quantum Science and Technology (MCQST), Schellingstr. 4, D-80799,
München, Germany

⋆ simon.linsel@lmu.de , † lode.pollet@lmu.de

Abstract

We introduce ParaToric, a C++ package for simulating the toric code in a parallel field (i.e., X- and Z-fields) at finite temperature. We implement and extend the continuous-time quantum Monte Carlo algorithm of Wu, Deng, and Prokof'ev on the square, triangular, honeycomb, and cubic lattices with either open or periodic boundaries. The package is expandable to arbitrary lattice geometries and custom observables diagonal in either the X- or Z-basis. ParaToric also supports snapshot extraction in both bases, making it ideal for generating training/benchmarking data for other methods, such as lattice gauge theories, cold atom or other quantum simulators, quantum spin liquids, artificial intelligence, and quantum error correction. The software provides bindings to C/C++ and Python, and is thus almost universally integrable into other software projects.

Publication information to appear upon publication.

Received Date
Accepted Date
Published Date

Contents

1 Introduction

The toric code is one of the most fundamental and most-studied models in modern condensed matter physics. It was first written down by Kitaev [1] and is the simplest example of a model hosting a topological phase (a gapped $\mathbb{Z}_2$ quantum spin liquid) and anyonic excitations. The toric code is also the foundational model for error-correcting codes [2,3] and has deep connections to the Ising gauge theory [4].

The toric code can be extended with fields which, when strong enough, destroy the topological order. This model is sign-problem-free, thus making quantum Monte Carlo the method of choice. Wu, Deng, and Prokof'ev developed a continuous-time quantum Monte Carlo algorithm [5]. ParaToric implements and extends this algorithm with new updates which enable ergodicity at large temperatures and at zero off-diagonal field, thus significantly improving the applicability of the algorithm.

ParaToric implements a wide range of lattices, boundary conditions, and observables. It is also possible to extend ParaToric with new interactions, observables, and lattices. We provide documented interfaces in C, C++, and Python as well as command-line interfaces, making the integration of ParaToric into other projects and programming languages straightforward. ParaToric will save simulation results to HDF5 files and snapshots to GraphML files (XML-based), with a focus on interoperability with other packages. ParaToric comes with an MIT license.

2 The toric code in a parallel field

2.1 Hamiltonian

ParaToric implements and extends the continuous-time quantum Monte Carlo (QMC) algorithm by Wu, Deng, and Prokof'ev [5] to simulate the toric code in a parallel field (also called perturbed toric code or extended toric code)

$$\hat{\mathcal{H}} = -\mu\sum_{v}\hat{A}_v - J\sum_{p}\hat{B}_p - h\sum_{l}\hat{\sigma}^x_l - \lambda\sum_{l}\hat{\sigma}^z_l, \tag{1}$$

where $J,\lambda > 0$ in the $\hat{\sigma}^x$-basis and $\mu, h > 0$ in the $\hat{\sigma}^z$-basis (otherwise the model has a sign-problem). $\hat{\sigma}^x_l$ and $\hat{\sigma}^z_l$ are Pauli matrices defined on the links of the underlying lattice. The star term $\hat{A}_v$ contains all links adjacent to lattice site v, the plaquette term $\hat{B}_p$ contains all links that belong to the same elementary plaquette p of the underlying lattice. The temperature $T = 1/\beta$ is finite. For readers interested in extending the code, we note that it is relatively straightforward to add interactions that are diagonal in the chosen basis, such as (long-range) Ising interactions. Off-diagonal interactions require a more careful review and extension of the Monte Carlo updates to ensure ergodicity. However, diagonal interactions can also lead to sampling problems, especially when they introduce frustration.

2.2 Lattice geometries

We implement the square, honeycomb, triangular, and cubic lattices, see Fig. 1. On the cubic lattice, the plaquettes contain the four links of cube faces, *not* the twelve links of the cube

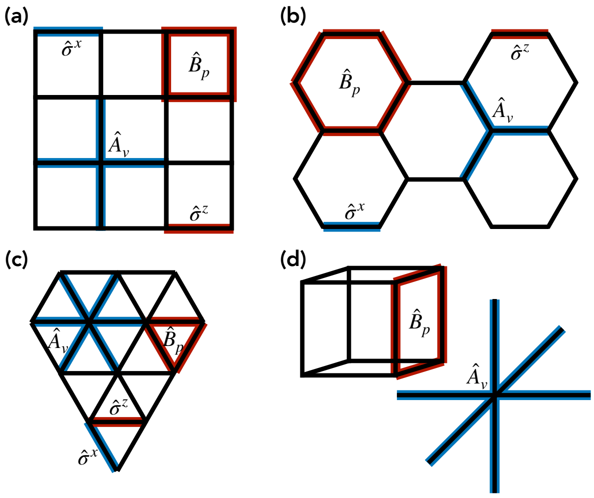

Figure 1: **Implemented lattices**. We implement the extended toric code (1) on the square (a), honeycomb (b), triangular (c), and cubic lattices (d). For each lattice, we show the star ($\hat{A}_v$) and plaquette ($\hat{B}_p$) terms. The cubic lattice importantly features star interactions of six links and plaquette interactions of four links on the faces of cubes.

(that model has a different m-anyon structure). We implement open and periodic boundaries, respectively. New lattices can be added in `src/lattice/lattice.cpp`.

2.3 Observables

Here we list all observables that ParaToric implements for the extended toric code. Custom observables can be added in `src/mcmc/extended_toric_code_qmc.hpp`. For each observable $\hat{O}$, we calculate the expectation value $\langle \hat{O} \rangle$ and the Binder ratio $U_O = \frac{\langle \hat{O}^4 \rangle}{\langle \hat{O}^2 \rangle^2}$ with error bars obtained from bootstrapping (see below), respectively.

`anyon_count` The number of e-anyons ($\hat{\sigma}^x$-basis) or m-anyons ($\hat{\sigma}^z$-basis) in the system.

`anyon_density` $\hat{\sigma}^x$-basis: The number of e-anyons divided by the number of lattice sites. $\hat{\sigma}^z$-basis: The number of m-anyons divided by the number of plaquettes.

`delta` The difference between the star and plaquette expectation values: $\Delta = \langle \hat{A}_v \rangle - \langle \hat{B}_p \rangle$.

`energy` The total energy $E = \langle \hat{\mathcal{H}} \rangle$.

`energy_h` The electric field term $E_h = \langle -h \sum_l \hat{\sigma}_l^x \rangle$.

`energy_lmbda` The gauge field term $E_\lambda = \langle -\lambda \sum_l \hat{\sigma}_l^z \rangle$. We write λ as `lmbda` because some programming languages feature `lambda` as a keyword.

`energy_J` The plaquette term $E_J = \langle -J \sum_p \hat{B}_p \rangle$.

`energy_mu` The star term $E_\mu = \langle -\mu \sum_v \hat{A}_v \rangle$.

`fredenhagen_marcu` The equal-time Fredenhagen-Marcu loop operator [6–8]:

$$O_{\mathrm{FM}}^{x/z} = \lim_{L\to\infty} \frac{\langle \prod_{l\in C_{1/2}^{x/z}} \hat{\sigma}_l^{x/z} \rangle}{\sqrt{|\langle \prod_{l\in C^{x/z}} \hat{\sigma}_l^{x/z} \rangle|}}, \tag{2}$$

$C_{1/2}^{x/z}$ is half, $C^{x/z}$ is a full Wilson loop in the $\hat{\sigma}^x$-basis ('t Hooft loop in the $\hat{\sigma}^z$-basis). The loop is automatically constructed for all supported lattices, and the perimeter scales with $\mathcal{O}(L)$, where L is the linear system size. When probing perimeter/area laws, the user should change L. We currently do not support off-diagonal loop operators, e.g., measuring products of $\hat{\sigma}^x$-operators in the $\hat{\sigma}^z$-basis.

`largest_cluster` The largest connected cluster of neighboring bonds with $\hat{\sigma}^x = -1$ ($\hat{\sigma}^z = -1$) in the $\hat{\sigma}^x$-basis ($\hat{\sigma}^z$-basis). This observable is used to calculate the percolation strength, see [9].

`largest_plaquette_cluster` The largest connected cluster of neighboring elementary plaquettes that share a bond with $\hat{\sigma}^x = -1$ ($\hat{\sigma}^z = -1$) in the $\hat{\sigma}^x$-basis ($\hat{\sigma}^z$-basis). This observable is used to calculate the plaquette percolation strength.

`percolation_probability` Measures the bond percolation probability, i.e. if we can wind around the system while only traversing bonds with $\hat{\sigma}^x = -1$ ($\hat{\sigma}^z = -1$) in the $\hat{\sigma}^x$-basis ($\hat{\sigma}^z$-basis). Formally, it is the expectation value $\langle \hat{\Pi}^{x/z} \rangle$ of the projector

$$\hat{\Pi}^{x/z} = \sum_{W(j)\neq 0} |\{\hat{\sigma}^{x/z}\}_j\rangle\langle\{\hat{\sigma}^{x/z}\}_j|, \tag{3}$$

over all possible configurations $\{\hat{\sigma}^{x/z}\}_j$ with non-zero winding number $W(j)$ of connected link clusters of neighboring $\hat{\sigma}^{x/z} = -1$. These clusters are called percolating clusters. For details, see [9–11].

`percolation_strength` If a snapshot does not have a percolating cluster, the percolation strength is 0. If a snapshot has a percolating cluster, the percolation strength is `largest_cluster` divided by the total number of links in the system. For details, see [9, 11].

`plaquette_percolation_probability` Similar to the percolation probability of bonds. Two plaquettes are in the same cluster if they share a link l with $\hat{\sigma}_l^x = -1$. For details, see [11].

`plaquette_percolation_strength` If a snapshot does not have a plaquette-percolating cluster, the plaquette percolation strength is 0. If a snapshot has a plaquette-percolating cluster, the plaquette percolation strength is `largest_plaquette_cluster` divided by the total number of elementary plaquettes in the system.

`plaquette_z` The plaquette expectation value $\langle \hat{B}_p \rangle$.

`sigma_x` The electric field expectation value $\langle \hat{\sigma}^x \rangle$.

`sigma_x_static_susceptibility` The static susceptibility

$$\chi_x^{\text{stat}} = \int_0^{\beta} \langle \hat{\sigma}^x(0)\,\hat{\sigma}^x(\tau)\rangle_{\text{c}}\,\mathrm{d}\tau, \tag{4}$$

where $\langle ... \rangle_{\text{c}}$ is the connected correlator, and the integral is over the imaginary time τ. Importantly, χ_x^{stat} can be calculated in both the $\hat{\sigma}^x$- and $\hat{\sigma}^z$-basis.

`sigma_x_dynamical_susceptibility` The dynamical (fidelity) susceptibility

$$\chi_x^{\text{dyn}} = \int_0^{\beta/2} \tau\langle \hat{\sigma}^x(0)\,\hat{\sigma}^x(\tau)\rangle_{\text{c}}\,\mathrm{d}\tau, \tag{5}$$

where $\langle ... \rangle_{\text{c}}$ is the connected correlator, and the integral is over the imaginary time τ[1]. Importantly, χ_x^{dyn} can be calculated in both the $\hat{\sigma}^x$- and $\hat{\sigma}^z$-basis.

`sigma_z` The gauge field expectation value $\langle \hat{\sigma}^z \rangle$.

`sigma_z_static_susceptibility` The static susceptibility

$$\chi_z^{\text{stat}} = \int_0^{\beta} \langle \hat{\sigma}^z(0)\,\hat{\sigma}^z(\tau)\rangle_{\text{c}}\,\mathrm{d}\tau, \tag{6}$$

where $\langle ... \rangle_{\text{c}}$ is the connected correlator, and the integral is over the imaginary time τ. Importantly, χ_z^{stat} can be calculated in both the $\hat{\sigma}^x$- and $\hat{\sigma}^z$-basis.

`sigma_z_dynamical_susceptibility` The dynamical (fidelity) susceptibility

$$\chi_z^{\text{dyn}} = \int_0^{\beta/2} \tau\langle \hat{\sigma}^z(0)\,\hat{\sigma}^z(\tau)\rangle_{\text{c}}\,\mathrm{d}\tau, \tag{7}$$

where $\langle ... \rangle_{\text{c}}$ is the connected correlator, and the integral is over the imaginary time τ. Importantly, χ_z^{dyn} can be calculated in both the $\hat{\sigma}^x$- and $\hat{\sigma}^z$-basis.

`staggered_imaginary_times` Order parameter from [5]. It is defined as

$$\begin{aligned} O_{\text{SI}}^{x/z} =& \frac{1}{\beta}\Big[(\tau_1^k - 0) - (\tau_2^k - \tau_1^k) + ... + (-1)^{N(k)-1} \\ & (\tau_{N(k)}^k - \tau_{N(k)-1}^k) + (-1)^{N(k)}(\beta - \tau_{N(k)}^k)\Big], \end{aligned} \tag{8}$$

where τ_n^k is the imaginary time of the n-th tuple spin flip of type k. k is a plaquette p (star s) of links in the $\hat{\sigma}^x$-basis ($\hat{\sigma}^z$-basis). This order parameter can neither be evaluated from snapshots, nor from any other method that does not have access to imaginary time.

`star_x` The star expectation value $\langle \hat{A}_v \rangle$.

`string_number` The total number of links with $\hat{\sigma}^x = -1$ in the $\hat{\sigma}^x$-basis ($\hat{\sigma}^z = -1$ in the $\hat{\sigma}^z$-basis).

---

[1] Compared to the static susceptibility, the dynamical (fidelity) susceptibility contains an extra τ dependency in the integral.

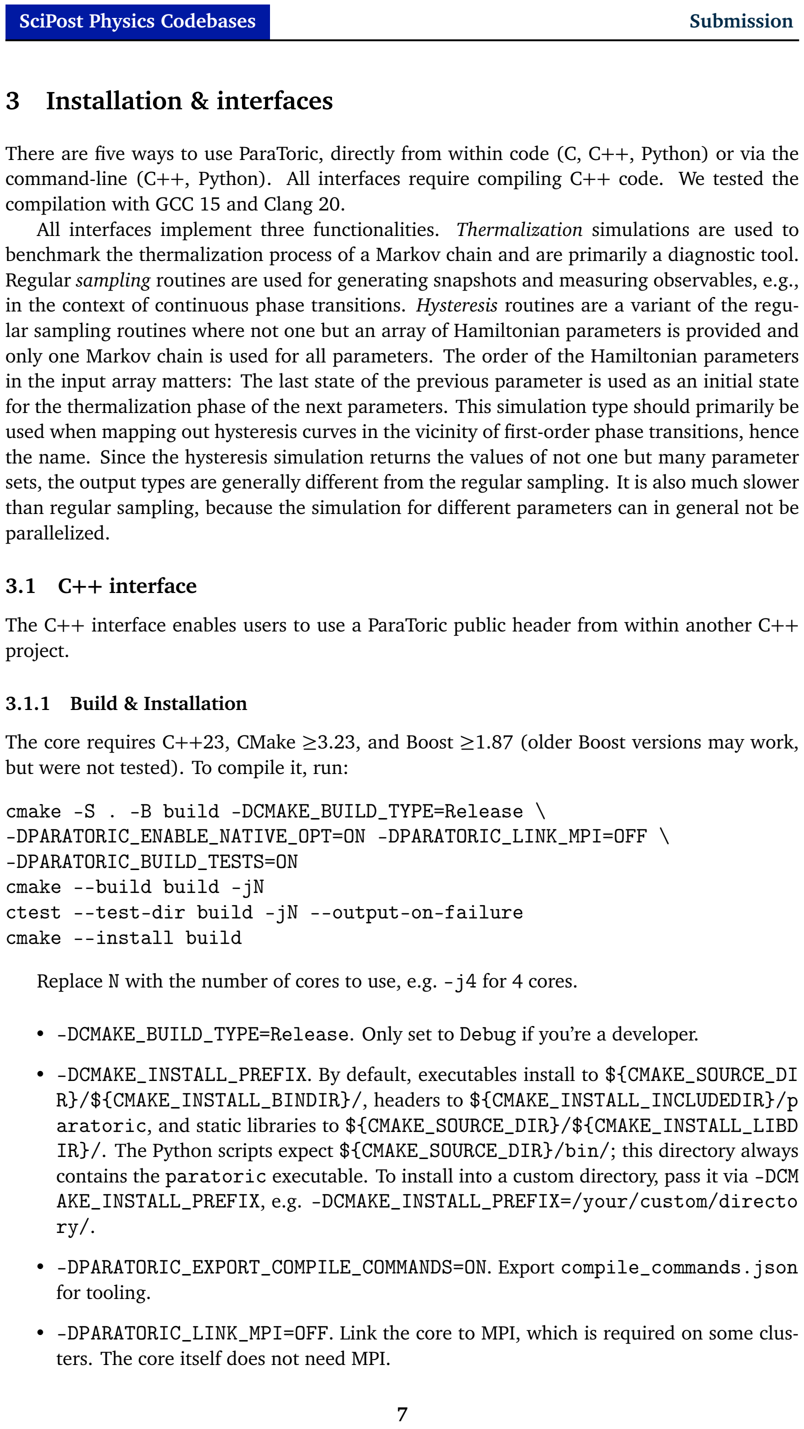

3 Installation & interfaces

There are five ways to use ParaToric, directly from within code (C, C++, Python) or via the command-line (C++, Python). All interfaces require compiling C++ code. We tested the compilation with GCC 15 and Clang 20.

All interfaces implement three functionalities. *Thermalization* simulations are used to benchmark the thermalization process of a Markov chain and are primarily a diagnostic tool. Regular *sampling* routines are used for generating snapshots and measuring observables, e.g., in the context of continuous phase transitions. *Hysteresis* routines are a variant of the regular sampling routines where not one but an array of Hamiltonian parameters is provided and only one Markov chain is used for all parameters. The order of the Hamiltonian parameters in the input array matters: The last state of the previous parameter is used as an initial state for the thermalization phase of the next parameters. This simulation type should primarily be used when mapping out hysteresis curves in the vicinity of first-order phase transitions, hence the name. Since the hysteresis simulation returns the values of not one but many parameter sets, the output types are generally different from the regular sampling. It is also much slower than regular sampling, because the simulation for different parameters can in general not be parallelized.

3.1 C++ interface

The C++ interface enables users to use a ParaToric public header from within another C++ project.

3.1.1 Build & Installation

The core requires C++23, CMake ≥3.23, and Boost ≥1.87 (older Boost versions may work, but were not tested). To compile it, run:

```
cmake -S . -B build -DCMAKE_BUILD_TYPE=Release \
-DPARATORIC_ENABLE_NATIVE_OPT=ON -DPARATORIC_LINK_MPI=OFF \
-DPARATORIC_BUILD_TESTS=ON
cmake --build build -jN
ctest --test-dir build -jN --output-on-failure
cmake --install build
```

Replace `N` with the number of cores to use, e.g. `-j4` for 4 cores.

- `-DCMAKE_BUILD_TYPE=Release`. Only set to `Debug` if you're a developer.
- `-DCMAKE_INSTALL_PREFIX`. By default, executables install to `${CMAKE_SOURCE_DIR}/${CMAKE_INSTALL_BINDIR}/`, headers to `${CMAKE_INSTALL_INCLUDEDIR}/paratoric`, and static libraries to `${CMAKE_SOURCE_DIR}/${CMAKE_INSTALL_LIBDIR}/`. The Python scripts expect `${CMAKE_SOURCE_DIR}/bin/`; this directory always contains the `paratoric` executable. To install into a custom directory, pass it via `-DCMAKE_INSTALL_PREFIX`, e.g. `-DCMAKE_INSTALL_PREFIX=/your/custom/directory/`.
- `-DPARATORIC_EXPORT_COMPILE_COMMANDS=ON`. Export `compile_commands.json` for tooling.
- `-DPARATORIC_LINK_MPI=OFF`. Link the core to MPI, which is required on some clusters. The core itself does not need MPI.

- `-DPARATORIC_ENABLE_NATIVE_OPT=OFF`. Use `-march=native` on GCC and Clang.
- `-DPARATORIC_ENABLE_AVX2=OFF`. Use AVX2 (Haswell New Instructions). Requires a CPU which supports AVX2.
- `-DPARATORIC_ENABLE_FAST_MATH=ON`. Use `-ffast-math` on GCC and Clang.
- `-DPARATORIC_BUILD_TESTS=PROJECT_IS_TOP_LEVEL`. Compile the tests (recommended).

CMake usage (installed package)

```
cmake_minimum_required(VERSION 3.23)
project(my_qmc_app CXX)

find_package(paratoric CONFIG REQUIRED)   # provides paratoric::core

add_executable(myapp main.cpp)
target_link_libraries(myapp PRIVATE paratoric::core)
```

CMake usage (as subdirectory)

If the core lives in `deps/paratoric`, add it and link to the same target:

```
add_subdirectory(deps/paratoric)
add_executable(myapp main.cpp)
target_link_libraries(myapp PRIVATE paratoric::core)
```

3.1.2 Public class `ExtendedToricCode`

The interface class `ExtendedToricCode` lives in the public header `#include<paratoric/mcmc/extended_toric_code.hpp>`. All symbols are in the `paratoric` namespace. All methods are static, take a single `Config` object and return a `Result` object. The required fields in config are documented for each method within the docstrings.

`Result ExtendedToricCode::get_thermalization(Config config)` Run thermalization only. Required fields: `lat_spec.{basis,lattice_type,system_size,beta,boundaries,default_spin}`, `param_spec.{mu,h,J,lmbda,h_therm,lmbda_therm}`, `sim_spec.{N_thermalization,N_resamples,custom_therm,observables,seed}`, `out_spec.{path_out,save_snapshots}`.

`Result ExtendedToricCode::get_sample(Config config)` Run a production measurement pass. Returns the observables selected in `config`. Required fields: `lat_spec.{basis,lattice_type,system_size,beta,boundaries,default_spin}`, `param_spec.{mu,h,J,lmbda}`, `sim_spec.{N_samples,N_thermalization,N_between_samples,N_resamples,observables,seed}`, `out_spec.{path_out,save_snapshots}`.

`Result ExtendedToricCode::get_hysteresis(Config config)` Perform a hysteresis sweep, where the last state of the previous parameter is used as the initial state of the following parameter in `h_hys` & `lmbda_hys`. Required fields: `lat_spec.{basis,lattice_type,system_size,beta,boundaries,default_spin}`, `param_spec.{mu,J,h_hys,lmbda_hys}`, `sim_spec.{N_samples,N_thermalization,N_between_samples,N_resamples,observables,seed}`, `out_spec.{paths_out,save_snapshots}`.

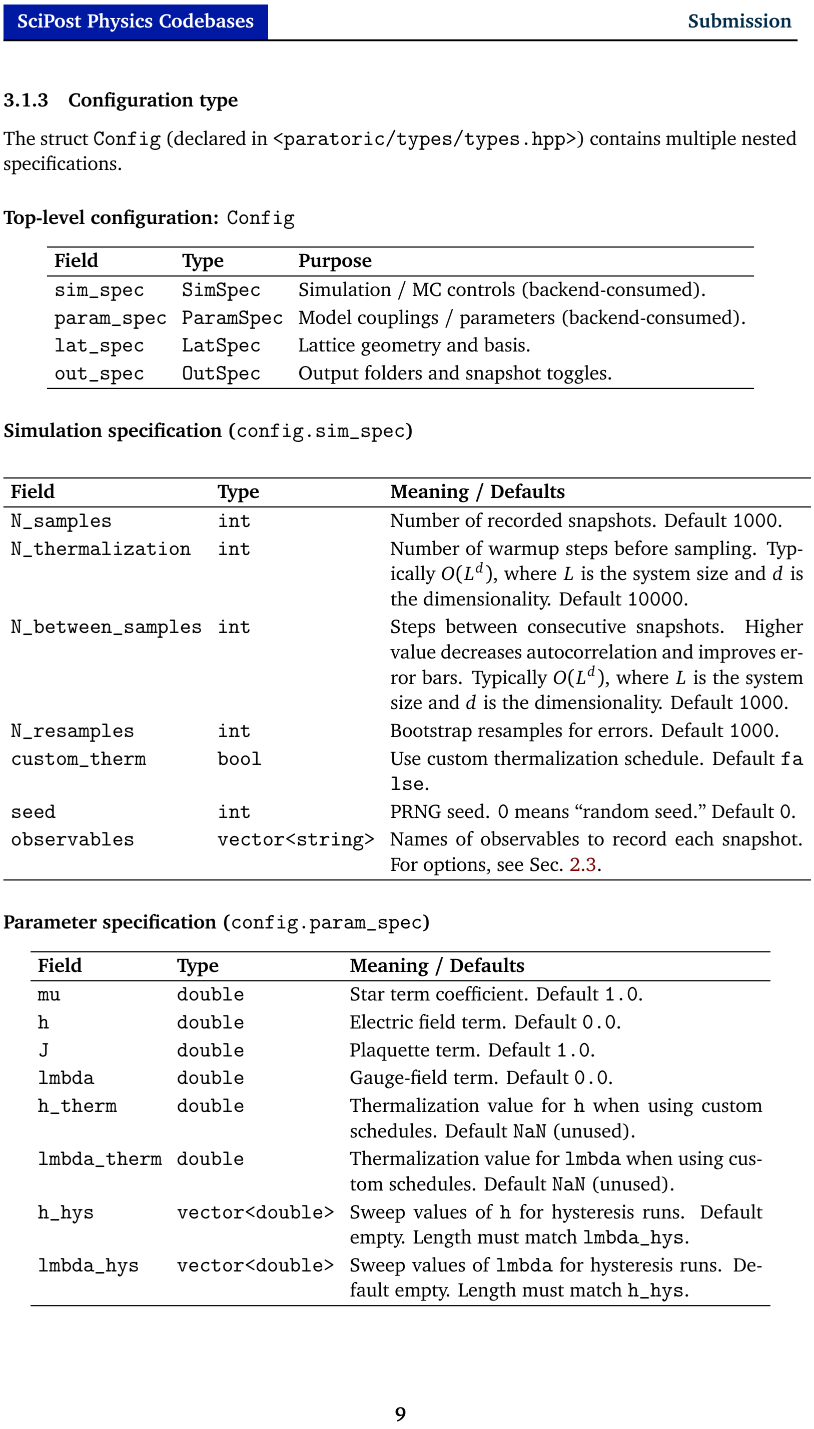

3.1.3 Configuration type

The struct `Config` (declared in `<paratoric/types/types.hpp>`) contains multiple nested specifications.

Top-level configuration: `Config`

Field	Type	Purpose
`sim_spec`	`SimSpec`	Simulation / MC controls (backend-consumed).
`param_spec`	`ParamSpec`	Model couplings / parameters (backend-consumed).
`lat_spec`	`LatSpec`	Lattice geometry and basis.
`out_spec`	`OutSpec`	Output folders and snapshot toggles.

Simulation specification (`config.sim_spec`)

Field	Type	Meaning / Defaults
`N_samples`	`int`	Number of recorded snapshots. Default 1000.
`N_thermalization`	`int`	Number of warmup steps before sampling. Typically $O(L^d)$, where L is the system size and d is the dimensionality. Default 10000.
`N_between_samples`	`int`	Steps between consecutive snapshots. Higher value decreases autocorrelation and improves error bars. Typically $O(L^d)$, where L is the system size and d is the dimensionality. Default 1000.
`N_resamples`	`int`	Bootstrap resamples for errors. Default 1000.
`custom_therm`	`bool`	Use custom thermalization schedule. Default `false`.
`seed`	`int`	PRNG seed. 0 means “random seed.” Default 0.
`observables`	`vector<string>`	Names of observables to record each snapshot. For options, see Sec. 2.3.

Parameter specification (`config.param_spec`)

Field	Type	Meaning / Defaults
`mu`	`double`	Star term coefficient. Default `1.0`.
`h`	`double`	Electric field term. Default `0.0`.
`J`	`double`	Plaquette term. Default `1.0`.
`lmbda`	`double`	Gauge-field term. Default `0.0`.
`h_therm`	`double`	Thermalization value for `h` when using custom schedules. Default `NaN` (unused).
`lmbda_therm`	`double`	Thermalization value for `lmbda` when using custom schedules. Default `NaN` (unused).
`h_hys`	`vector<double>`	Sweep values of `h` for hysteresis runs. Default empty. Length must match `lmbda_hys`.
`lmbda_hys`	`vector<double>`	Sweep values of `lmbda` for hysteresis runs. Default empty. Length must match `h_hys`.

Lattice specification (`config.lat_spec`)

Field	Type	Meaning / Valid values
`basis`	`char`	Spin eigenbasis for the simulation. Must be `'x'` or `'z'`.
`lattice_type`	`string`	The lattice (`"square"`, `"triangular"`, `"honeycomb"` or `"cubic"`).
`system_size`	`int`	Linear system size (per dimension).
`beta`	`double`	Inverse temperature $\beta > 0$.
`boundaries`	`string`	Boundary condition: `"periodic"` or `"open"`.
`default_spin`	`int`	Initial link spin, must be $+1$ or -1.

Output specification (`config.out_spec`)

Field	Type	Meaning
`path_out`	`string`	Primary output folder name.
`paths_out`	`vector<string>`	Hysteresis subfolder names. Length must match `h_hys`.
`save_snapshots`	`bool`	Save snapshots toggle. Default `false`.

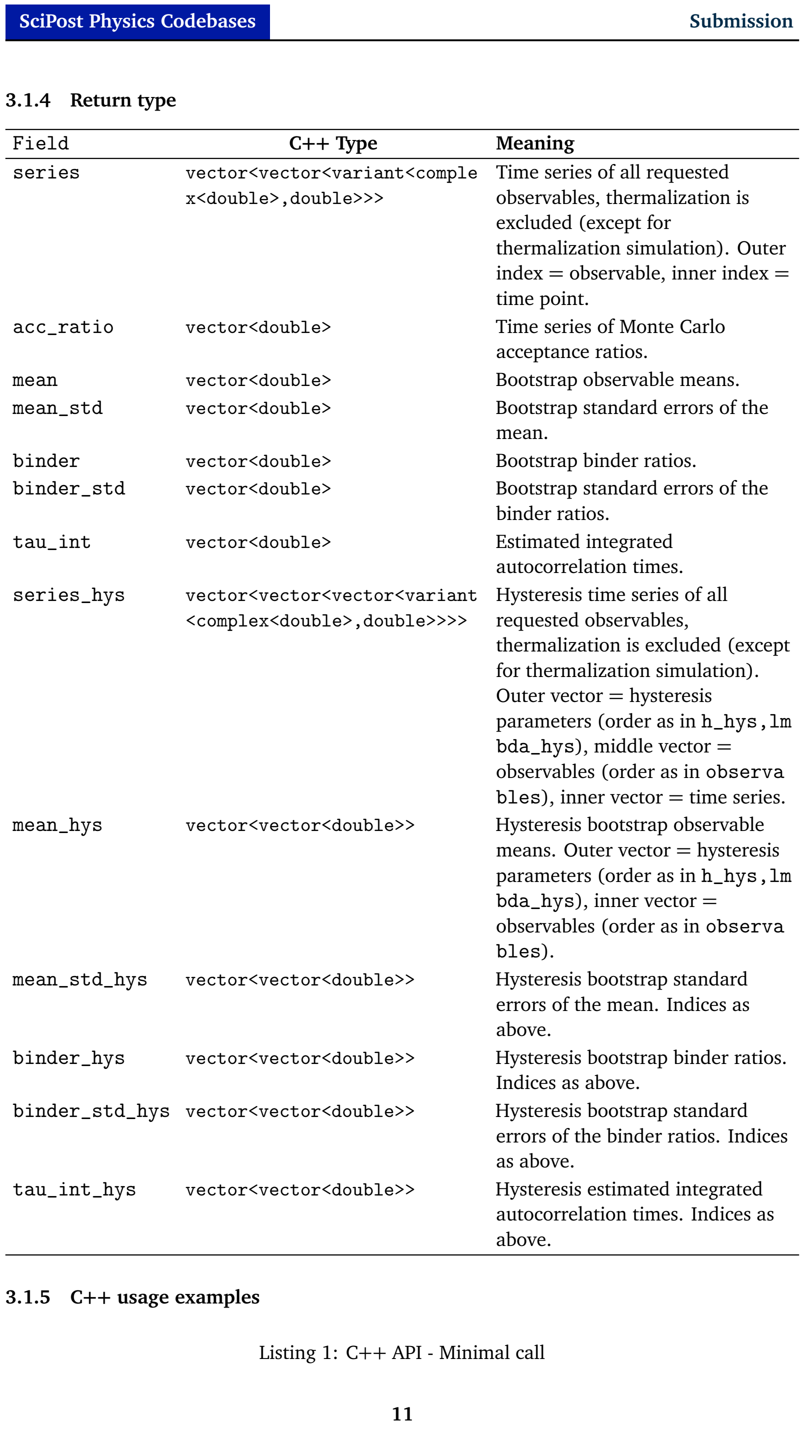

3.1.4 Return type

`Field`	C++ Type	Meaning
`series`	`vector<vector<variant<complex<double>,double>>>`	Time series of all requested observables, thermalization is excluded (except for thermalization simulation). Outer index = observable, inner index = time point.
`acc_ratio`	`vector<double>`	Time series of Monte Carlo acceptance ratios.
`mean`	`vector<double>`	Bootstrap observable means.
`mean_std`	`vector<double>`	Bootstrap standard errors of the mean.
`binder`	`vector<double>`	Bootstrap binder ratios.
`binder_std`	`vector<double>`	Bootstrap standard errors of the binder ratios.
`tau_int`	`vector<double>`	Estimated integrated autocorrelation times.
`series_hys`	`vector<vector<vector<variant<complex<double>,double>>>>`	Hysteresis time series of all requested observables, thermalization is excluded (except for thermalization simulation). Outer vector = hysteresis parameters (order as in `h_hys,lmbda_hys`), middle vector = observables (order as in `observables`), inner vector = time series.
`mean_hys`	`vector<vector<double>>`	Hysteresis bootstrap observable means. Outer vector = hysteresis parameters (order as in `h_hys,lmbda_hys`), inner vector = observables (order as in `observables`).
`mean_std_hys`	`vector<vector<double>>`	Hysteresis bootstrap standard errors of the mean. Indices as above.
`binder_hys`	`vector<vector<double>>`	Hysteresis bootstrap binder ratios. Indices as above.
`binder_std_hys`	`vector<vector<double>>`	Hysteresis bootstrap standard errors of the binder ratios. Indices as above.
`tau_int_hys`	`vector<vector<double>>`	Hysteresis estimated integrated autocorrelation times. Indices as above.

3.1.5 C++ usage examples

Listing 1: C++ API - Minimal call

```
// C++23
#include <iostream>
#include <print>
#include <vector>
#include <string>
#include <paratoric/mcmc/extended_toric_code.hpp>
#include <paratoric/types/types.hpp>

int main() {
  using namespace paratoric;

  Config cfg{};

  // ---- lattice sub-config (required) ----
  cfg.lat_spec.basis = 'z'; // or 'x'
  cfg.lat_spec.lattice_type = "square"; // or "cubic", "honeycomb", ...
  cfg.lat_spec.system_size = 16;
  cfg.lat_spec.beta = 8.0;
  cfg.lat_spec.boundaries = "periodic"; // or "open"
  cfg.lat_spec.default_spin = 1;

  // ---- Hamiltonian parameters ----
  cfg.param_spec.mu = 1.0; // star term
  cfg.param_spec.J = 1.0; // plaquette term
  cfg.param_spec.h = 0.20; // electric field term
  cfg.param_spec.lmbda = 0.00; // gauge-field term

  // Optional thermalization schedule values (used if custom_therm = true)
  cfg.param_spec.h_therm = std::numeric_limits<double>::quiet_NaN();
  cfg.param_spec.lmbda_therm = std::numeric_limits<double>::quiet_NaN();

  // (Optional) Hysteresis sweep grids - only read by get_hysteresis(...)
  cfg.param_spec.h_hys = {}; // e.g. {0.0, 0.1, 0.2, 0.3, 0.2, 0.1, 0.0}
  cfg.param_spec.lmbda_hys = {}; // e.g. {0.0, 0.1, 0.2, 0.3, 0.2, 0.1, 0.0}

  // ---- Simulation (MC) controls ----
  cfg.sim_spec.N_samples = 0; // 0 => thermalization-only
  cfg.sim_spec.N_thermalization = 5000; // warmup steps
  cfg.sim_spec.N_between_samples = 10; // thinning between snapshots
  cfg.sim_spec.N_resamples = 1000; // bootstrap
  cfg.sim_spec.custom_therm = false; // set true to use *_therm values
  cfg.sim_spec.seed = 12345; // 0 => random seed

  // Observables to record each snapshot (backend-recognized names)
  cfg.sim_spec.observables = {
    "energy", // total energy
    "plaquette_z", // plaquette energy
    "anyon_count", // number of anyons (x-basis: e-anyons, z-basis: m-anyons
       )
    "fredenhagen_marcu" // example: Wilson/'t Hooft loop proxy
  };

  // ---- Output / I/O policy ----
  cfg.out_spec.path_out = "runs/sample"; // single-run output dir
  cfg.out_spec.paths_out = {}; // filled only for hysteresis
  cfg.out_spec.save_snapshots = false; // set true to dump every snapshot
```

```
  cfg.out_spec.full_time_series = true; // save full time series (FCS)

  // 1) Check thermalization
  Result warmup = ExtendedToricCode::get_thermalization(cfg);
  std::print("Thermalization␣series:␣{}", warmup.series);

  // 2) Production sample (set N_samples > 0 and call get_sample)
  cfg.sim_spec.N_samples = 2000;
  Result out = ExtendedToricCode::get_sample(cfg);
  std::print("Production␣autocorrelations:␣{}", out.tau_int);

  return 0;
}
```

3.2 C++ command-line interface

ParaToric ships a C++ command-line interface `${CMAKE_INSTALL_PREFIX}/${CMAKE_INSTALL_BINDIR}/paratoric` that orchestrates C++ backends, runs sweeps, and writes HDF5 (observables) and XML (snapshots) outputs.

3.2.1 Build & Installation

The command-line interface requires HDF5 ≥1.14.3 (older HDF5 versions may work, but were not tested). The core requires C++23, CMake ≥3.23, and Boost ≥1.87 (older Boost versions may work, but were not tested). To compile it, run:

```
cmake -S . -B build -DCMAKE_BUILD_TYPE=Release \
-DPARATORIC_ENABLE_NATIVE_OPT=ON -DPARATORIC_LINK_MPI=OFF \
-DPARATORIC_BUILD_TESTS=ON -DPARATORIC_BUILD_CLI=ON
cmake --build build -jN
ctest --test-dir build -jN --output-on-failure
cmake --install build
```

Replace `N` with the number of cores to use, e.g. `-j4` for 4 cores.

- `-DCMAKE_BUILD_TYPE=Release`. Only set to `Debug` if you're a developer.
- `-DCMAKE_INSTALL_PREFIX`. By default, executables install to `${CMAKE_SOURCE_DIR}/${CMAKE_INSTALL_BINDIR}/`, headers to `${CMAKE_INSTALL_INCLUDEDIR}/paratoric`, and static libraries to `${CMAKE_SOURCE_DIR}/${CMAKE_INSTALL_LIBDIR}/`. The Python scripts expect `${CMAKE_SOURCE_DIR}/bin/`; this directory always contains the `paratoric` executable. To install into a custom directory, pass it via `-DCMAKE_INSTALL_PREFIX`, e.g. `-DCMAKE_INSTALL_PREFIX=/your/custom/directory/`.
- `-DPARATORIC_EXPORT_COMPILE_COMMANDS=ON`. Export `compile_commands.json` for tooling.
- `-DPARATORIC_LINK_MPI=OFF`. Link the core to MPI, which is required on some clusters. The core itself does not need MPI.
- `-DPARATORIC_ENABLE_NATIVE_OPT=OFF`. Use `-march=native` on GCC and Clang.

- `-DPARATORIC_ENABLE_AVX2=OFF`. Use AVX2 (Haswell New Instructions). Requires a CPU which supports AVX2.
- `-DPARATORIC_ENABLE_FAST_MATH=ON`. Use `-ffast-math` on GCC and Clang.
- `-DPARATORIC_BUILD_TESTS=PROJECT_IS_TOP_LEVEL`. Compile the tests (recommended).
- `-DPARATORIC_BUILD_CLI=PROJECT_IS_TOP_LEVEL` Required for both the C++ and Python command line interface.

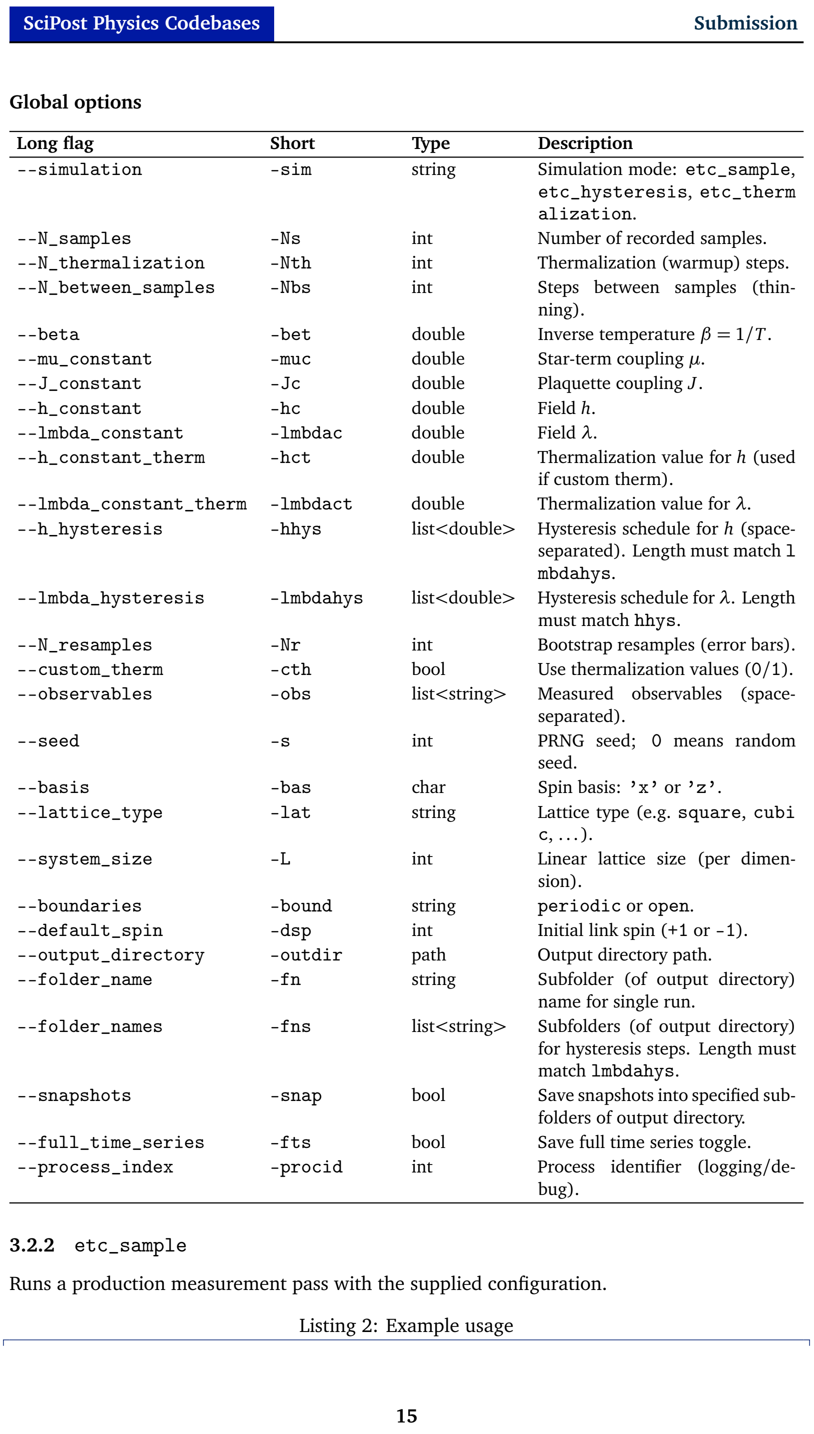

Global options

Long flag	Short	Type	Description
`--simulation`	`-sim`	string	Simulation mode: `etc_sample`, `etc_hysteresis`, `etc_thermalization`.
`--N_samples`	`-Ns`	int	Number of recorded samples.
`--N_thermalization`	`-Nth`	int	Thermalization (warmup) steps.
`--N_between_samples`	`-Nbs`	int	Steps between samples (thinning).
`--beta`	`-bet`	double	Inverse temperature $\beta = 1/T$.
`--mu_constant`	`-muc`	double	Star-term coupling μ.
`--J_constant`	`-Jc`	double	Plaquette coupling J.
`--h_constant`	`-hc`	double	Field h.
`--lmbda_constant`	`-lmbdac`	double	Field λ.
`--h_constant_therm`	`-hct`	double	Thermalization value for h (used if custom therm).
`--lmbda_constant_therm`	`-lmbdact`	double	Thermalization value for λ.
`--h_hysteresis`	`-hhys`	list<double>	Hysteresis schedule for h (space-separated). Length must match `lmbdahys`.
`--lmbda_hysteresis`	`-lmbdahys`	list<double>	Hysteresis schedule for λ. Length must match `hhys`.
`--N_resamples`	`-Nr`	int	Bootstrap resamples (error bars).
`--custom_therm`	`-cth`	bool	Use thermalization values (0/1).
`--observables`	`-obs`	list<string>	Measured observables (space-separated).
`--seed`	`-s`	int	PRNG seed; 0 means random seed.
`--basis`	`-bas`	char	Spin basis: `'x'` or `'z'`.
`--lattice_type`	`-lat`	string	Lattice type (e.g. `square`, `cubic`, ...).
`--system_size`	`-L`	int	Linear lattice size (per dimension).
`--boundaries`	`-bound`	string	`periodic` or `open`.
`--default_spin`	`-dsp`	int	Initial link spin (+1 or -1).
`--output_directory`	`-outdir`	path	Output directory path.
`--folder_name`	`-fn`	string	Subfolder (of output directory) name for single run.
`--folder_names`	`-fns`	list<string>	Subfolders (of output directory) for hysteresis steps. Length must match `lmbdahys`.
`--snapshots`	`-snap`	bool	Save snapshots into specified subfolders of output directory.
`--full_time_series`	`-fts`	bool	Save full time series toggle.
`--process_index`	`-procid`	int	Process identifier (logging/debug).

3.2.2 `etc_sample`

Runs a production measurement pass with the supplied configuration.

Listing 2: Example usage

```
./paratoric -sim etc_sample -Ns 2000 -Nth 5000 -Nbs 10 -Nr 1000 -bet 16.0 -
   muc 1 -Jc 1 -hc 0.2 -lmbdac 0.0 -obs energy plaquette_z anyon_count -bas
    z -lat square -L 16 -bound periodic -dsp 1 -outdir ./runs/sample -snap
   =0 -fts=1
```

3.2.3 `etc_hysteresis`

Runs a parameter sweep where the last state of step i initializes step $i+1$. Provide `--h_hysteresis` and `--lmbda_hysteresis` as space-separated lists, and `--folder_names` for per-step outputs.

Listing 3: Example usage

```
./paratoric -sim etc_hysteresis -Ns 1000 -Nth 2000 -Nbs 50 -Nr 500 -bet
   12.0 -muc 1 -Jc 1 -lmbdahys 0.2 0.2 0.2 0.2 0.2 0.2 0.2 -hhys 0.0 0.1
   0.2 0.3 0.2 0.1 0.0 -obs energy fredenhagen_marcu -bas x -lat square -L
   12 -bound periodic -dsp 1 -outdir ./runs/hys -fns step0 step1 step2
   step3 step4 step5 step6
```

3.2.4 `etc_thermalization`

Performs thermalization only (no production sampling).

Listing 4: Example usage

```
./paratoric -sim etc_thermalization -Ns 0 -Nth 5000 -Nbs 10 -Nr 500 -bet
   10.0 -muc 1 -Jc 1 -hc 0.3 -lmbdac 0.1 -hct 0.4 -lmbdact 0.2 -cth 1 -obs
   energy anyon_density -bas z -lat square -L 10 -bound open -dsp 1 -outdir
    ./runs/therm -snap=1
```

3.2.5 HDF5 structure

The output HDF5 has the structure `simulation/results/acc_ratio` for an array of the acceptance ratios (only for thermalization), `simulation/results/observable_name/series` for the time series (if it was enabled), and `simulation/results/observable_name/{mean,mean_error,binder,binder_error,autocorrelation_time}`. For the regular sampling, `mean`, `mean_error`, `binder`, `binder_error` and `autocorrelation_time` contain doubles. For the hysteresis, they contain an array of values for the hysteresis parameters (in the order of `h_hysteresis` and `lmbda_hysteresis`).

3.3 C interface

The C interface enables users to use a ParaToric public header from within another C project or another programming language that supports a C-style interface. The C interface exposes a stable ABI. It mirrors the C++ interface. Include the public header `#include<paratoric/mcmc/extended_toric_code_c.h>`. All functions return `ptc_status_t`.

3.3.1 Build & Installation

The code can be compiled in exactly the same fashion as for the C++ interface.

CMake usage (installed package).

```
cmake_minimum_required(VERSION 3.23)
project(my_qmc_c C)
find_package(paratoric CONFIG REQUIRED)   # provides paratoric::core
add_executable(cdemo main.c)
target_link_libraries(cdemo PRIVATE paratoric::core)
```

CMake usage (as subdirectory).

```
add_subdirectory(deps/paratoric)
add_executable(cdemo main.c)
target_link_libraries(cdemo PRIVATE paratoric::core)
```

3.3.2 Status & error handling

Name	C type/values	Meaning
`ptc_status_t`	`{PTC_STATUS_OK=0, PTC_STATUS_INVALID_ARGUMENT=1, PTC_STATUS_RUNTIME_ERROR=2, PTC_STATUS_NO_MEMORY=3, PTC_STATUS_INTERNAL_ERROR=4}`	Return code of every API call.
`ptc_last_error()`	`const char*`	Thread–local error string. Valid until next call.

3.3.3 Opaque handle

Create and destroy the interface instance. Use `ptc_create(ptc_handle_t **out)` and `ptc_destroy(ptc_handle_t *h)`.

3.3.4 Configuration type

Top-level `ptc_config_t` aggregates four nested specs. Field names mirror the C++ `Config`.

Top-level configuration: `ptc_config_t`

Field	Type	Purpose
`sim`	`ptc_sim_spec_t`	Monte Carlo parameters.
`params`	`ptc_param_spec_t`	Hamiltonian parameters.
`lat`	`ptc_lat_spec_t`	Lattice parameters.
`out`	`ptc_out_spec_t`	Output paths and snapshot toggle.

Simulation specification (`config.sim`)

Field	Type	Meaning
`N_samples`	`int`	Number of snapshots.
`N_thermalization`	`int`	Thermalization steps.
`N_between_samples`	`int`	Thinning between snapshots.
`N_resamples`	`int`	Bootstrap resamples.
`custom_therm`	`bool`	Custom thermalization schedule.
`seed`	`int`	PRNG seed (0 = random).
`observables`	`const char* const*`	Array of observable names (nullable).
`N_observables`	`size_t`	Length of `observables`.

Parameter specification (`config.params`)

Field	Type	Meaning
`mu,h,J,lmbda`	`double`	Couplings (star, electric, plaquette, gauge).
`h_therm`	`double`	Thermalization value for `h` if `custom_therm=true`.
`lmbda_therm`	`double`	Thermalization value for `lmbda` if `custom_therm=true`.
`h_hys`	`const double*`	Hysteresis schedule for `h` (nullable).
`h_hys_len`	`size_t`	Length of `h_hys`. Must match `lmbda_hys_len`.
`lmbda_hys`	`const double*`	Hysteresis schedule for `lmbda` (nullable).
`lmbda_hys_len`	`size_t`	Length of `lmbda_hys`. Must match `h_hys_len`.

Lattice specification (`config.lat`)

Field	Type	Meaning / Valid values
`basis`	`char`	Spin basis: `'x'` or `'z'`.
`lattice_type`	`const char*`	E.g. `"triangular"`, `"square"`, …
`system_size`	`int`	Linear system size per dimension.
`beta`	`double`	Inverse temperature.
`boundaries`	`const char*`	`"periodic"` or `"open"`.
`default_spin`	`int`	Initial link spin: +1 or -1.

Output specification (`config.out`)

Field	Type	Meaning
`path_out`	`const char*`	Single output directory (nullable).
`paths_out`	`const char* const*`	Output directories for hysteresis steps (nullable).
`N_paths_out`	`size_t`	Length of `paths_out`. Must match `h_hys_len` and `lmbda_hys_len`.
`save_snapshots`	`bool`	Toggle snapshot dumping.

3.3.5 Return type

All outputs are owned by the caller. Call `ptc_result_destroy(&r)` to free and zero.

Field	C type	Meaning
`series`	`ptc_series_t`	Time series (real/complex) of all requested observables, thermalization is excluded (except for thermalization simulation). Outer index = observable, inner index = time point.
`acc_ratio`	`ptc_dvec_t`	MC acceptance ratios for each update (thermalization).
`mean`, `mean_std`	`ptc_dvec_t`	Bootstrap mean and standard error (order as in `observables`).
`binder`, `binder_std`	`ptc_dvec_t`	Binder ratios and standard error (order as in `observables`).
`tau_int`	`ptc_dvec_t`	Integrated autocorrelation time (order as in `observables`).
`series_hys`	`ptc_series_blocks_t`	Hysteresis time series. Outer index = hysteresis parameters (order as in `h_hys`,`lmbda_hys`), middle index = observables (order as in `observables`), inner vector = time series.
`mean_hys`, `mean_std_hys`, `binder_hys`, `binder_std_hys`, `tau_int_hys`	`ptc_dmat_t`	Outer index = hysteresis parameters (order as in `h_hys`,`lmbda_hys`), inner index = observables (order as in `observables`).

3.3.6 Procedures (mirror the C++ API)

All fill a `ptc_result_t *out` on success. Return `PTC_STATUS_OK` on success.

`ptc_get_thermalization(ptc_handle_t *h, const ptc_config_t *cfg, ptc_result_t *out)` Run thermalization only. **Required fields:** `cfg->lat.{basis,lattice_type,system_size,beta,boundaries,default_spin}`, `cfg->params.{mu,h,J,lmbda}`, `cfg->sim.{N_thermalization,N_resamples,observables,N_observables,seed}`, `cfg->out.{path_out,save_snapshots}`.

`ptc_get_sample(ptc_handle_t *h, const ptc_config_t *cfg, ptc_result_t *out)` Run a production measurement pass. **Required fields:** `cfg->lat.{basis,lattice_type,system_size,beta,boundaries,default_spin}`, `cfg->params.{mu,h,J,lmbda,h_therm,lmbda_therm}`, `cfg->sim.{N_samples,N_thermalization,N_between_samples,N_resamples,custom_therm,observables,N_observables,seed}`, `cfg->out.{path_out,save_snapshots}`.

`ptc_get_hysteresis(ptc_handle_t *h, const ptc_config_t *cfg, ptc_result_t *out)` Run a hysteresis sweep over `h_hys` and/or `lmbda_hys`. The last state of step `i` initializes step `i+1`. **Required fields:** `cfg->lat.{basis,lattice_type,system_size,beta,boundaries,default_spin}`, `cfg->params.{mu,h_hys,h_hys_len,J,lmbda_hys,lmbda_hys_len}`, `cfg->sim.{N_samples,N_thermalization,N_between_samples,N_resamples,observables,N_observables,seed}`, `cfg->out.{paths_out,N_paths_out,save_snapshots}`.

3.3.7 C usage example

Listing 5: C API - Minimal call

```
#include <stdio.h>
#include <math.h>
#include <paratoric/mcmc/extended_toric_code_c.h>

int main(void) {
  ptc_handle_t* h = NULL;
  if (ptc_create(&h) != PTC_STATUS_OK) { puts("create␣failed"); return 1; }

  ptc_lat_spec_t lat = {
    .basis = 'z',
    .lattice_type = "square",
    .system_size = 16,
    .beta = 8.0,
    .boundaries = "periodic",
    .default_spin = 1
  };

  ptc_param_spec_t ps = {
    .mu = 1.0, .h = 0.2, .J = 1.0, .lmbda = 0.0,
    .h_therm = NAN, .lmbda_therm = NAN,
    .h_hys = NULL, .h_hys_len = 0,
    .lmbda_hys = NULL, .lmbda_hys_len = 0
  };

  const char* obs[] = {"energy","plaquette_z","anyon_count"};
  ptc_sim_spec_t sim = {
    .N_samples = 0, /* thermalization-only initially */
    .N_thermalization = 5000,
    .N_between_samples = 10,
    .N_resamples = 1000,
    .custom_therm = false,
    .seed = 12345,
    .observables = obs,
    .N_observables = sizeof(obs)/sizeof(obs[0])
  };

  ptc_out_spec_t outspec = {
    .path_out = "runs/sample",
    .paths_out = NULL, .N_paths_out = 0,
    .save_snapshots = false
  };

  ptc_config_t cfg = { .sim = sim, .params = ps, .lat = lat, .out = outspec
      };

  ptc_result_t warm = {0};
  ptc_status_t st = ptc_get_thermalization(h, &cfg, &warm);
  if (st != PTC_STATUS_OK) { puts(ptc_last_error()); ptc_destroy(h); return
      2; }
  ptc_result_destroy(&warm);

  cfg.sim.N_samples = 2000;
  ptc_result_t res = {0};
  st = ptc_get_sample(h, &cfg, &res);
  if (st != PTC_STATUS_OK) { puts(ptc_last_error()); ptc_destroy(h); return
      3; }
```

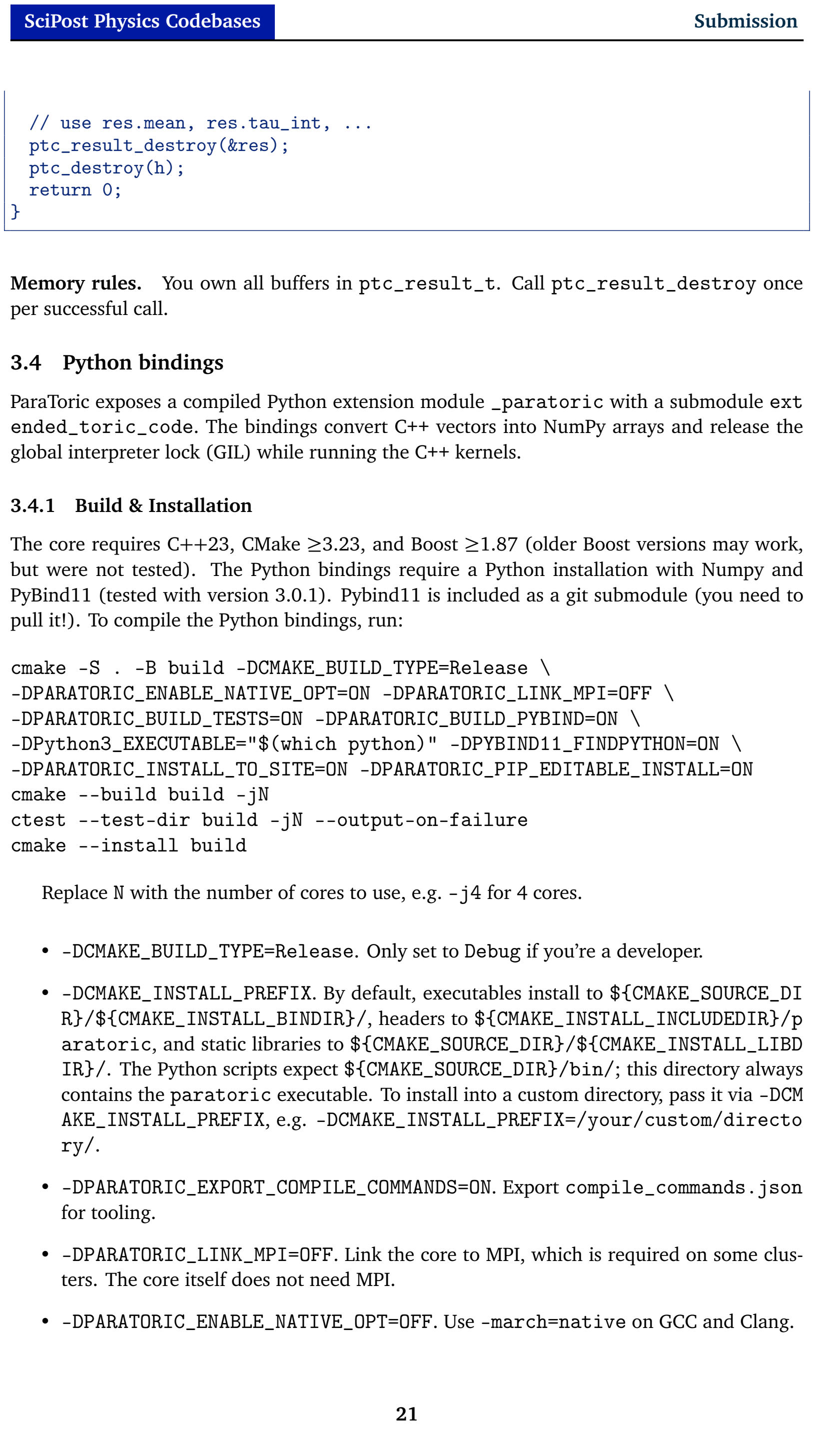

```
  // use res.mean, res.tau_int, ...
  ptc_result_destroy(&res);
  ptc_destroy(h);
  return 0;
}
```

Memory rules. You own all buffers in `ptc_result_t`. Call `ptc_result_destroy` once per successful call.

3.4 Python bindings

ParaToric exposes a compiled Python extension module `_paratoric` with a submodule `extended_toric_code`. The bindings convert C++ vectors into NumPy arrays and release the global interpreter lock (GIL) while running the C++ kernels.

3.4.1 Build & Installation

The core requires C++23, CMake ≥3.23, and Boost ≥1.87 (older Boost versions may work, but were not tested). The Python bindings require a Python installation with Numpy and PyBind11 (tested with version 3.0.1). Pybind11 is included as a git submodule (you need to pull it!). To compile the Python bindings, run:

```
cmake -S . -B build -DCMAKE_BUILD_TYPE=Release \
-DPARATORIC_ENABLE_NATIVE_OPT=ON -DPARATORIC_LINK_MPI=OFF \
-DPARATORIC_BUILD_TESTS=ON -DPARATORIC_BUILD_PYBIND=ON \
-DPython3_EXECUTABLE="$(which python)" -DPYBIND11_FINDPYTHON=ON \
-DPARATORIC_INSTALL_TO_SITE=ON -DPARATORIC_PIP_EDITABLE_INSTALL=ON
cmake --build build -jN
ctest --test-dir build -jN --output-on-failure
cmake --install build
```

Replace `N` with the number of cores to use, e.g. `-j4` for 4 cores.

- `-DCMAKE_BUILD_TYPE=Release`. Only set to `Debug` if you're a developer.
- `-DCMAKE_INSTALL_PREFIX`. By default, executables install to `${CMAKE_SOURCE_DIR}/${CMAKE_INSTALL_BINDIR}/`, headers to `${CMAKE_INSTALL_INCLUDEDIR}/paratoric`, and static libraries to `${CMAKE_SOURCE_DIR}/${CMAKE_INSTALL_LIBDIR}/`. The Python scripts expect `${CMAKE_SOURCE_DIR}/bin/`; this directory always contains the `paratoric` executable. To install into a custom directory, pass it via `-DCMAKE_INSTALL_PREFIX`, e.g. `-DCMAKE_INSTALL_PREFIX=/your/custom/directory/`.
- `-DPARATORIC_EXPORT_COMPILE_COMMANDS=ON`. Export `compile_commands.json` for tooling.
- `-DPARATORIC_LINK_MPI=OFF`. Link the core to MPI, which is required on some clusters. The core itself does not need MPI.
- `-DPARATORIC_ENABLE_NATIVE_OPT=OFF`. Use `-march=native` on GCC and Clang.

- `-DPARATORIC_ENABLE_AVX2=OFF`. Use AVX2 (Haswell New Instructions). Requires a CPU which supports AVX2.
- `-DPARATORIC_ENABLE_FAST_MATH=ON`. Use `-ffast-math` on GCC and Clang.
- `-DPARATORIC_BUILD_TESTS=PROJECT_IS_TOP_LEVEL`. Compile the tests (recommended).
- `-DPARATORIC_BUILD_PYBIND=OFF`. Compile Python bindings.
- `-DPARATORIC_INSTALL_TO_SITE=OFF`. Install ParaToric Python module to site packages.
- `-DPARATORIC_PIP_EDITABLE_INSTALL=OFF`. Install ParaToric Python module via pip as an editable module.
- `-DPARATORIC_PIP_OFFLINE_INSTALL=OFF`. Turn on when installing to pip without internet access. Requires `NumPy` and `setuptools`.

3.4.2 Module layout

- `paratoric._paratoric`: compiled extension (PyBind11). Submodule: `extended_toric_code`.
- `paratoric.extended_toric_code`: convenient alias
- Running `python -m paratoric` enters the package entry point (`__main__.py`).

NumPy return formats

All time series with potentially complex values are returned as `complex128`. Real observables appear with zero imaginary part. Shapes are documented in the function references below.

API reference (`paratoric.extended_toric_code`)

`get_thermalization(...)` Run only the warmup and return per-snapshot observables and MC acceptance ratios. Internally converts `std::variant<complex<double>,double>` to `complex128` and `std::vector<double>` to `float64` arrays. The GIL is released while the C++ routine executes.

Parameter	Type / default	Meaning
`N_thermalization`	`int`	Warmup steps.
`N_resamples`	`int=1000`	Bootstrap resamples.
`observables`	`list[str]`	Names per snapshot.
`seed`	`int=0`	PRNG seed (0 ⇒ random).
`mu,h,J,lmbda`	`float`	Hamiltonian parameters.
`basis`	`{'x','z'}='x'`	Spin eigenbasis.
`lattice_type`	`str`	E.g. `"triangular"`, `"square"`, …
`system_size`	`int`	Linear size per dimension.
`beta`	`float`	Inverse temperature.
`boundaries`	`str="periodic"`	Boundary condition.
`default_spin`	`int=1`	Initial link spin (`+1`/`-1`).
`save_snapshots`	`bool=false`	Enable snapshot files.
`path_out`	`path|None=None`	Output directory (if saving).

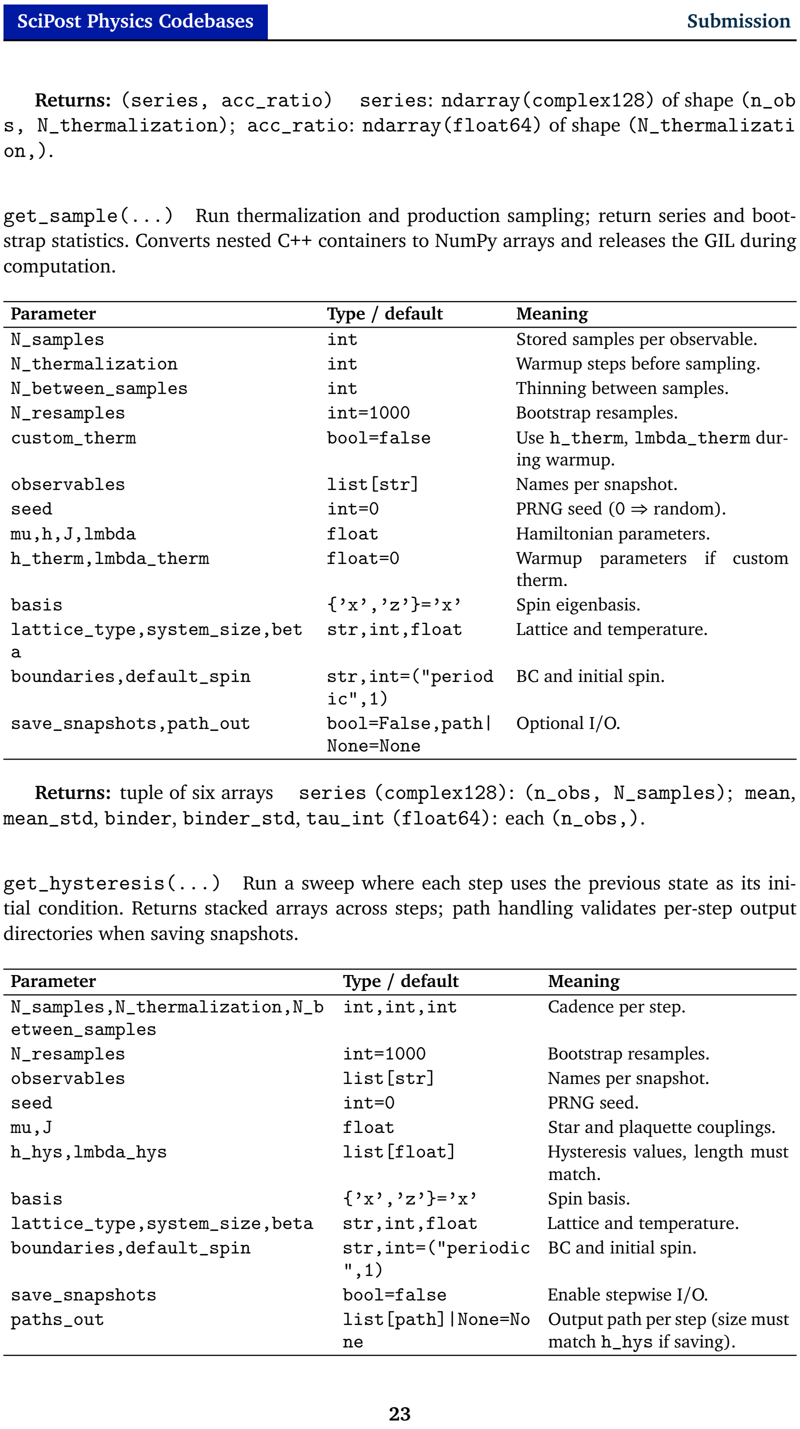

Returns: `(series, acc_ratio)` `series`: `ndarray(complex128)` of shape `(n_obs, N_thermalization)`; `acc_ratio`: `ndarray(float64)` of shape `(N_thermalization,)`.

`get_sample(...)` Run thermalization and production sampling; return series and bootstrap statistics. Converts nested C++ containers to NumPy arrays and releases the GIL during computation.

Parameter	**Type / default**	**Meaning**
`N_samples`	`int`	Stored samples per observable.
`N_thermalization`	`int`	Warmup steps before sampling.
`N_between_samples`	`int`	Thinning between samples.
`N_resamples`	`int=1000`	Bootstrap resamples.
`custom_therm`	`bool=false`	Use `h_therm`, `lmbda_therm` during warmup.
`observables`	`list[str]`	Names per snapshot.
`seed`	`int=0`	PRNG seed (0 ⇒ random).
`mu,h,J,lmbda`	`float`	Hamiltonian parameters.
`h_therm,lmbda_therm`	`float=0`	Warmup parameters if custom therm.
`basis`	`{'x','z'}='x'`	Spin eigenbasis.
`lattice_type,system_size,beta`	`str,int,float`	Lattice and temperature.
`boundaries,default_spin`	`str,int=("periodic",1)`	BC and initial spin.
`save_snapshots,path_out`	`bool=False,path|None=None`	Optional I/O.

Returns: tuple of six arrays `series (complex128): (n_obs, N_samples)`; `mean`, `mean_std`, `binder`, `binder_std`, `tau_int (float64)`: each `(n_obs,)`.

`get_hysteresis(...)` Run a sweep where each step uses the previous state as its initial condition. Returns stacked arrays across steps; path handling validates per-step output directories when saving snapshots.

Parameter	**Type / default**	**Meaning**
`N_samples,N_thermalization,N_between_samples`	`int,int,int`	Cadence per step.
`N_resamples`	`int=1000`	Bootstrap resamples.
`observables`	`list[str]`	Names per snapshot.
`seed`	`int=0`	PRNG seed.
`mu,J`	`float`	Star and plaquette couplings.
`h_hys,lmbda_hys`	`list[float]`	Hysteresis values, length must match.
`basis`	`{'x','z'}='x'`	Spin basis.
`lattice_type,system_size,beta`	`str,int,float`	Lattice and temperature.
`boundaries,default_spin`	`str,int=("periodic",1)`	BC and initial spin.
`save_snapshots`	`bool=false`	Enable stepwise I/O.
`paths_out`	`list[path]|None=None`	Output path per step (size must match `h_hys` if saving).

Returns: tuple of six arrays `series3d (complex128)`: `(n_steps, n_obs, N_samples)`; `mean2d`, `std2d`, `binder2d`, `binder_std2d`, `tau2d (float64)`: each `(n_steps, n_obs)`. The number of steps equals `len(h_hys)` (and `len(lmbda_hys)`).

Array dtypes and shapes (summary)

Function	Name / dtype	Shape
`get_thermalization`	`series` (`complex128`)	`(n_obs, N_thermalization)`
	`acc_ratio` (`float64`)	`(N_thermalization,)`
`get_sample`	`series` (`complex128`)	`(n_obs, N_samples)`
	`mean`, `mean_std`, `binder`, `binder_std`, `tau_int` (`float64`)	each `(n_obs,)`
`get_hysteresis`	`series3d` (`complex128`)	`(n_steps, n_obs, N_samples)`
	`mean2d`, `std2d`, `binder2d`, `binder_std2d`, `tau2d` (`float64`)	each `(n_steps, n_obs)`

Notes on performance

The bindings release the global interpreter lock (GIL) during heavy compute (`py::gil_scoped_release`), enabling multi-threaded C++ execution if the backend uses threads or when calling from multiprocessing workers. Conversions handle 1D/2D/3D containers and enforce consistent inner lengths before copying to NumPy.

3.4.3 Usage example

Listing 6: Importing and calling from Python

```
>>> import numpy as np
>>> from paratoric import extended_toric_code as etc
>>> series, acc_ratio = etc.get_thermalization(
... N_thermalization=2000, N_resamples=500,
... observables=["energy","plaquette_z","anyon_count"],
... seed=0, mu=1.0, h=0.2, J=1.0, lmbda=0.0,
... basis='z', lattice_type="square", system_size=16, beta=8.0,
... boundaries="periodic", default_spin=1,
... save_snapshots=False, path_out=None)
>>> series.shape, series.dtype
((3, 2000), dtype('complex128'))
>>> out = etc.get_sample(
... N_samples=1000, N_thermalization=5000, N_between_samples=10,
... N_resamples=1000, custom_therm=False,
... observables=["energy","plaquette_z"],
... seed=0, mu=1.0, h=0.2, h_therm=0.0,
... J=1.0, lmbda=0.0, lmbda_therm=0.0,
... basis='z', lattice_type="square", system_size=16, beta=8.0,
... boundaries="periodic", default_spin=1,
... save_snapshots=False, path_out=None)
>>> (series_s, mean, mean_std, binder, binder_std, tau_int) = out
```

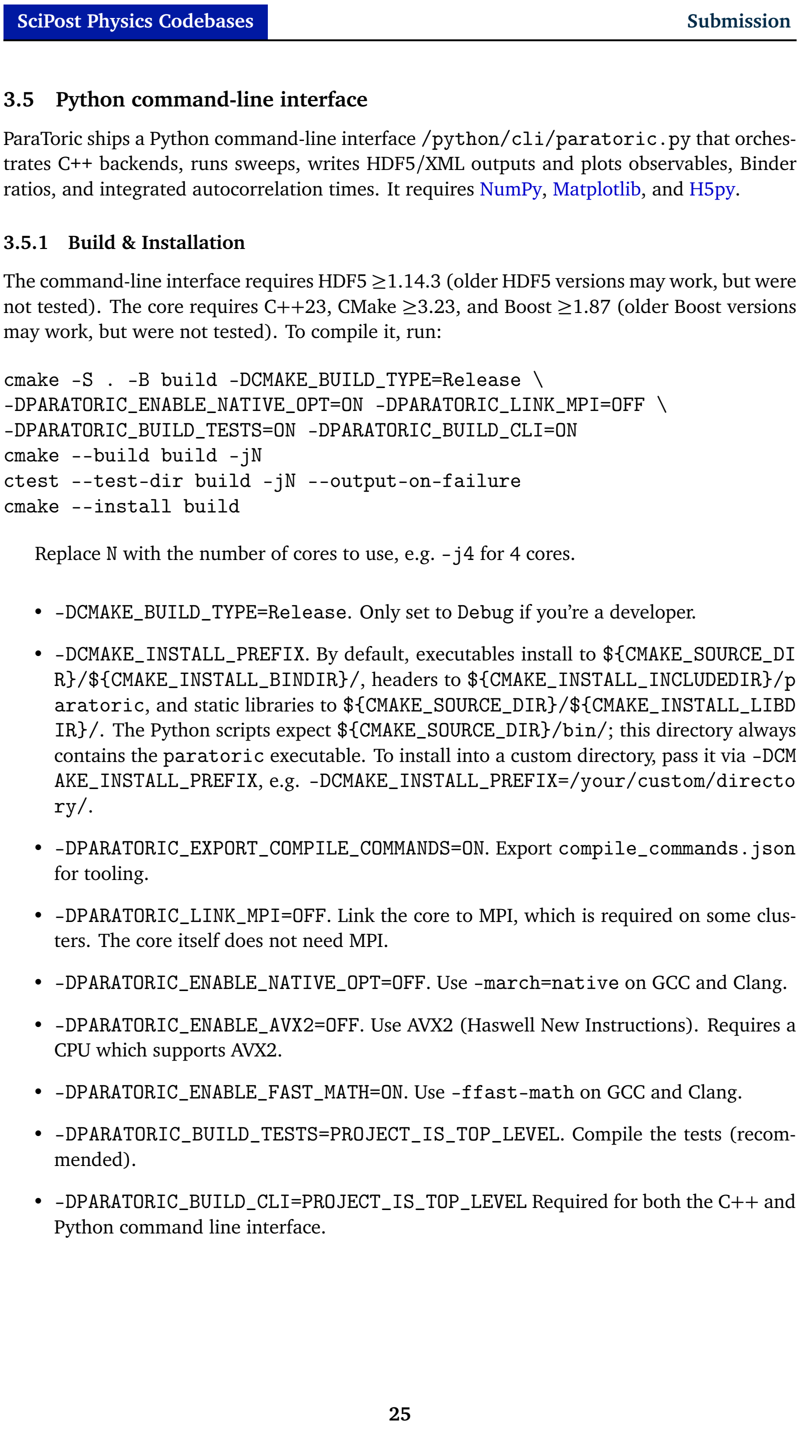

3.5 Python command-line interface

ParaToric ships a Python command-line interface `/python/cli/paratoric.py` that orchestrates C++ backends, runs sweeps, writes HDF5/XML outputs and plots observables, Binder ratios, and integrated autocorrelation times. It requires NumPy, Matplotlib, and H5py.

3.5.1 Build & Installation

The command-line interface requires HDF5 $\geq$1.14.3 (older HDF5 versions may work, but were not tested). The core requires C++23, CMake $\geq$3.23, and Boost $\geq$1.87 (older Boost versions may work, but were not tested). To compile it, run:

```
cmake -S . -B build -DCMAKE_BUILD_TYPE=Release \
-DPARATORIC_ENABLE_NATIVE_OPT=ON -DPARATORIC_LINK_MPI=OFF \
-DPARATORIC_BUILD_TESTS=ON -DPARATORIC_BUILD_CLI=ON
cmake --build build -jN
ctest --test-dir build -jN --output-on-failure
cmake --install build
```

Replace `N` with the number of cores to use, e.g. `-j4` for 4 cores.

- `-DCMAKE_BUILD_TYPE=Release`. Only set to Debug if you're a developer.
- `-DCMAKE_INSTALL_PREFIX`. By default, executables install to `${CMAKE_SOURCE_DIR}/${CMAKE_INSTALL_BINDIR}/`, headers to `${CMAKE_INSTALL_INCLUDEDIR}/paratoric`, and static libraries to `${CMAKE_SOURCE_DIR}/${CMAKE_INSTALL_LIBDIR}/`. The Python scripts expect `${CMAKE_SOURCE_DIR}/bin/`; this directory always contains the `paratoric` executable. To install into a custom directory, pass it via `-DCMAKE_INSTALL_PREFIX`, e.g. `-DCMAKE_INSTALL_PREFIX=/your/custom/directory/`.
- `-DPARATORIC_EXPORT_COMPILE_COMMANDS=ON`. Export `compile_commands.json` for tooling.
- `-DPARATORIC_LINK_MPI=OFF`. Link the core to MPI, which is required on some clusters. The core itself does not need MPI.
- `-DPARATORIC_ENABLE_NATIVE_OPT=OFF`. Use `-march=native` on GCC and Clang.
- `-DPARATORIC_ENABLE_AVX2=OFF`. Use AVX2 (Haswell New Instructions). Requires a CPU which supports AVX2.
- `-DPARATORIC_ENABLE_FAST_MATH=ON`. Use `-ffast-math` on GCC and Clang.
- `-DPARATORIC_BUILD_TESTS=PROJECT_IS_TOP_LEVEL`. Compile the tests (recommended).
- `-DPARATORIC_BUILD_CLI=PROJECT_IS_TOP_LEVEL` Required for both the C++ and Python command line interface.

General options

Long flag	Short	Description
`--help`	`-h`	Show help and exit.
`--simulation`	`-sim`	Simulation type selector.
`--N_thermalization`	`-Nth`	Thermalization steps (proposed updates).
`--N_samples`	`-Ns`	Number of samples/snapshots.
`--N_between_steps`	`-Nbs`	Steps between successive samples (thinning).
`--N_resamples`	`-Nr`	Bootstrap resamples.
`--custom_therm`	`-cth`	Use thermalization values for h, λ (0 or 1).
`--observables`	`-obs`	Space-separated list, e.g. `fredenhagen_marcu` `percolation_probability energy`.
`--seed`	`-seed`	PRNG seed; 0 means random seed.
`--mu_constant`	`-muc`	Value of μ.
`--J_constant`	`-Jc`	Value of J.
`--h_constant`	`-hc`	Value of h.
`--h_constant_therm`	`-hct`	Thermalization value of h.
`--lmbda_constant`	`-lmbdac`	Value of λ.
`--lmbda_constant_therm`	`-lmbdact`	Thermalization value of λ.
`--output_directory`	`-outdir`	Output directory.
`--snapshots`	`-snap`	Save snapshots toggle (0/1).
`--full_time_series`	`-fts`	Save full time series toggle (0/1).
`--processes`	`-proc`	Logical CPU count for Python multiprocessing. 0 means all available cores. Negative numbers $-x$ mean use all cores minus x. Default is -4.

Lattice-specific options

Long flag	Short	Description
`--help`	`-h`	Show help and exit.
`--basis`	`-bas`	Spin basis: `x` or `z`.
`--lattice_type`	`-lat`	`square`, `cubic`, `triangular`, `honeycomb`, …
`--system_size`	`-L`	Linear size; in 2D, 30 yields a 30×30 lattice (unit cells).
`--temperature`	`-T`	Temperature $T = 1/\beta > 0$.
`--boundaries`	`-bound`	`periodic` or `open`.
`--default_spin`	`-dsp`	Initial edge spin: `1` or `-1`.

The command line interface offers several sweep modes. All are embarrassingly parallel; set `--processes` close to the number of steps when possible.

3.5.2 T-sweep

Runs `T_steps` independent Markov chains for evenly spaced temperatures in $[T\_\text{lower}, T\_\text{upper}]$ and plots all requested observables.

Listing 7: Example usage

```
python3 ./python/cli/paratoric.py -sim etc_T_sweep -Nbs 8000 -Ns 1000 -muc
    1 -Nth 50000 -Tl 0.1 -Tu 10 -Ts 15 -hc 0.5 -Jc 1 -lmbdac 0.2 -Nr 1000 -
    obs percolation_strength percolation_probability largest_cluster
    largest_plaquette_cluster string_number energy energy_h energy_mu
    energy_J energy_lmbda sigma_x sigma_z star_x plaquette_z
    staggered_imaginary_times delta anyon_count anyon_density
    fredenhagen_marcu sigma_x_static_susceptibility
    sigma_x_dynamical_susceptibility sigma_z_static_susceptibility
    sigma_z_dynamical_susceptibility -bas x -lat square -L 6 -bound periodic
     -dsp 1 -outdir /your/output/directory
```

Sweep-specific flags.

Long flag	Short	Description
`--simulation`	`-sim`	Use `etc_T_sweep`.
`--T_lower`	`-Tl`	Lower bound of T.
`--T_upper`	`-Tu`	Upper bound of T.
`--T_steps`	`-Ts`	Number of temperatures between bounds.

3.5.3 h-sweep

Runs `h_steps` independent chains in parallel for evenly spaced h in [h_lower, h_upper].

Listing 8: Example usage

```
python3 ./python/cli/paratoric.py -sim etc_h_sweep -Nbs 8000 -Ns 1000 -muc
    1 -Nth 50000 -hl 0.0 -hu 0.5 -hs 15 -T 0.1 -Jc 1 -lmbdac 0.2 -Nr 1000 -
    obs percolation_strength percolation_probability
    plaquette_percolation_probability plaquette_percolation_strength
    largest_cluster largest_plaquette_cluster string_number energy energy_h
    energy_mu energy_J energy_lmbda sigma_x sigma_z star_x plaquette_z
    staggered_imaginary_times delta anyon_count anyon_density
    fredenhagen_marcu sigma_x_static_susceptibility
    sigma_x_dynamical_susceptibility sigma_z_static_susceptibility
    sigma_z_dynamical_susceptibility -bas x -lat square -L 6 -bound periodic
     -dsp 1 -outdir /your/output/directory
```

Sweep-specific flags.

Long flag	Short	Description
`--simulation`	`-sim`	Use `etc_h_sweep`.
`--h_lower`	`-hl`	Lower bound of h.
`--h_upper`	`-hu`	Upper bound of h.
`--h_steps`	`-hs`	Number of field steps between bounds.

3.5.4 λ-sweep

Runs `lmbda_steps` independent chains in parallel for evenly spaced λ in [λ_lower, λ_upper].

Listing 9: Example usage

```
python3 ./python/cli/paratoric.py -sim etc_lmbda_sweep -Nbs 12000 -Ns 1000
    -muc 1 -Nth 100000 -lmbdal 0.1 -lmbdau 0.7 -lmbdas 15 -T 0.1 -hc 0.1 -Jc
     1 -Nr 1000 -obs percolation_strength percolation_probability
    plaquette_percolation_probability plaquette_percolation_strength
    largest_cluster largest_plaquette_cluster string_number energy energy_h
    energy_mu energy_J energy_lmbda sigma_x sigma_z star_x plaquette_z
    staggered_imaginary_times delta anyon_count anyon_density
    fredenhagen_marcu sigma_x_static_susceptibility
    sigma_x_dynamical_susceptibility sigma_z_static_susceptibility
    sigma_z_dynamical_susceptibility -bas z -lat honeycomb -L 6 -bound
    periodic -dsp 1 -outdir /your/output/directory
```

Sweep-specific flags.

Long flag	Short	Description
`--simulation`	`-sim`	Use `etc_lmbda_sweep`.
`--lmbda_lower`	`-lmbdal`	Lower bound of λ.
`--lmbda_upper`	`-lmbdau`	Upper bound of λ.
`--lmbda_steps`	`-lmbdas`	Number of field steps between bounds.

3.5.5 ∘-sweep

Runs `Theta_steps` independent chains in parallel along a circle in (λ, h) centered at `(lmbda_constant,h_constant)` with radius `radius`, for angles $\Theta \in [\Theta\_\mathrm{lower}, \Theta\_\mathrm{upper}]$ (angles measured anti-clockwise from the λ-axis).

Listing 10: Example usage

```
python3 ./python/cli/paratoric.py -sim etc_circle_sweep -Nbs 8000 -Ns 1000
    -muc 1 -Nth 50000 -lmbdac 0.0 -rad 1.0 -Thl 0 -Thu 1.57 -Ths 30 -T 0.1 -
    hc 0.0 -Jc 1 -Nr 1000 -obs percolation_strength percolation_probability
    largest_cluster largest_plaquette_cluster string_number energy energy_h
    energy_mu energy_J energy_lmbda sigma_x sigma_z star_x plaquette_z
    staggered_imaginary_times delta anyon_count anyon_density
    fredenhagen_marcu sigma_x_static_susceptibility
    sigma_x_dynamical_susceptibility sigma_z_static_susceptibility
    sigma_z_dynamical_susceptibility -bas x -lat square -L 6 -bound periodic
     -dsp 1 -outdir /your/output/directory
```

Sweep-specific flags.

Long flag	Short	Description
`--simulation`	`-sim`	Use `etc_circle_sweep`.
`--lmbda_constant`	`-lmbdac`	Circle center in λ.
`--h_constant`	`-hc`	Circle center in h.
`--radius`	`-rad`	Circle radius.
`--Theta_lower`	`-Thl`	Lower bound of Θ.
`--Theta_upper`	`-Thu`	Upper bound of Θ.
`--Theta_steps`	`-Ths`	Number of angles between bounds.

3.5.6 Hysteresis-sweep

Uses the hysteresis schedule specified in `hhys` and `lmbdahys`. This mode will run two Markov chains, one in the original parameter order specified in `hhys` and `lmbdahys`, and one with a reversed parameter order, i.e., it calculates both branches of the hysteresis loop.

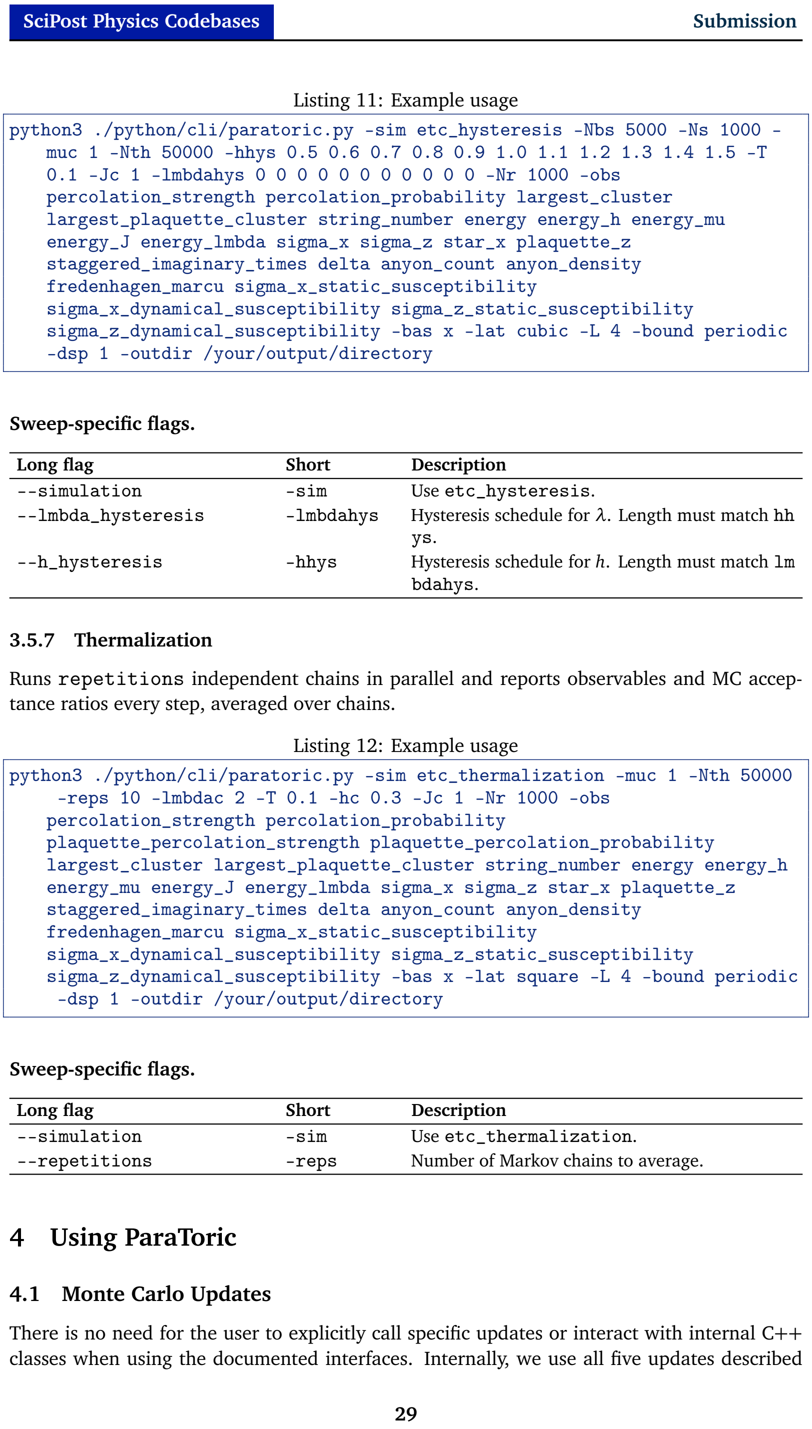

Listing 11: Example usage

```
python3 ./python/cli/paratoric.py -sim etc_hysteresis -Nbs 5000 -Ns 1000 -
   muc 1 -Nth 50000 -hhys 0.5 0.6 0.7 0.8 0.9 1.0 1.1 1.2 1.3 1.4 1.5 -T
   0.1 -Jc 1 -lmbdahys 0 0 0 0 0 0 0 0 0 0 0 -Nr 1000 -obs
   percolation_strength percolation_probability largest_cluster
   largest_plaquette_cluster string_number energy energy_h energy_mu
   energy_J energy_lmbda sigma_x sigma_z star_x plaquette_z
   staggered_imaginary_times delta anyon_count anyon_density
   fredenhagen_marcu sigma_x_static_susceptibility
   sigma_x_dynamical_susceptibility sigma_z_static_susceptibility
   sigma_z_dynamical_susceptibility -bas x -lat cubic -L 4 -bound periodic
   -dsp 1 -outdir /your/output/directory
```

Sweep-specific flags.

Long flag	Short	Description
`--simulation`	`-sim`	Use `etc_hysteresis`.
`--lmbda_hysteresis`	`-lmbdahys`	Hysteresis schedule for λ. Length must match `hhys`.
`--h_hysteresis`	`-hhys`	Hysteresis schedule for h. Length must match `lmbdahys`.

3.5.7 Thermalization

Runs `repetitions` independent chains in parallel and reports observables and MC acceptance ratios every step, averaged over chains.

Listing 12: Example usage

```
python3 ./python/cli/paratoric.py -sim etc_thermalization -muc 1 -Nth 50000
    -reps 10 -lmbdac 2 -T 0.1 -hc 0.3 -Jc 1 -Nr 1000 -obs
   percolation_strength percolation_probability
   plaquette_percolation_strength plaquette_percolation_probability
   largest_cluster largest_plaquette_cluster string_number energy energy_h
   energy_mu energy_J energy_lmbda sigma_x sigma_z star_x plaquette_z
   staggered_imaginary_times delta anyon_count anyon_density
   fredenhagen_marcu sigma_x_static_susceptibility
   sigma_x_dynamical_susceptibility sigma_z_static_susceptibility
   sigma_z_dynamical_susceptibility -bas x -lat square -L 4 -bound periodic
    -dsp 1 -outdir /your/output/directory
```

Sweep-specific flags.

Long flag	Short	Description
`--simulation`	`-sim`	Use `etc_thermalization`.
`--repetitions`	`-reps`	Number of Markov chains to average.

4 Using ParaToric

4.1 Monte Carlo Updates

There is no need for the user to explicitly call specific updates or interact with internal C++ classes when using the documented interfaces. Internally, we use all five updates described in the original algorithm by Wu, Deng, and Prokof'ev [5]. These must furthermore be supplemented with the following two updates: Because for high temperatures and for zero off-diagonal fields the spin at imaginary time $0 = \beta$ cannot be flipped, we allow for flipping the spin on the entire imaginary axis on one bond or on a plaquette (star) in the $\hat{\sigma}^x$-basis ($\hat{\sigma}^z$-basis).

These updates only change the energy terms diagonal in the given basis and are trivial when caching the total integrated diagonal energy (the update locally flips the sign of the total integrated potential energy). Another advantage is that integrated autocorrelation times for observables diagonal in the given basis improve even in regimes that were previously accessible. By default, all seven updates are equally likely to be proposed. The user may manually fine-tune the proposal probabilities when maximizing performance in a very specific parameter regime. We use a 64-bit Mersenne-Twister for pseudorandom numbers [12] with the ability to set the seed externally. Some updates have early exits for input parameters for which they will always be rejected.

4.2 Monte Carlo Diagnostics

There are two compilation modes, `Release` and `Debug`. In production runs, one should always use the `Release` mode; however, it still gives the user enough information to diagnose sampling problems without severe performance impacts.

4.2.1 Thermalization mode

We provide thermalization routines which should be used before production runs to ensure proper thermalization (also known as burn-in). Thermalization times can vary drastically between different observables and initial conditions. We provide an example of sufficient and insufficient thermalization in Fig. 2. We recommend using the provided Python command-line interface, which will also plot the thermalization of all measured observables for the user.

In thermalization runs, we also return the Monte Carlo acceptance ratio of every update. This can also be used to diagnose freezing (in the measurement phase, use the integrated autocorrelation time instead), e.g., when the acceptance ratio is always identical and/or very low.

In case one suspects experiencing a serious sampling problem, we recommend recompiling the project in the `Debug` mode, which provides a wide array of runtime debug information about the proposed steps, acceptance ratios, and intermediate results. However, do not use the `Debug` mode in production runs, as it negatively impacts performance.

4.2.2 Integrated autocorrelation time

When measuring observables, we first thermalize the system with `N_thermalization` steps, then measure `N_samples` times with `N_between_samples` steps between measurements. The normalized autocorrelation function $\rho_O(k)$ of an observable O_k (observable O measured at time k) applied to a discrete time series of length N is given by:

$$\rho_O(k) = \frac{C(k)}{C(0)}, \qquad C(k) = \frac{1}{N-k}\sum_{i=0}^{N-k-1}(O_i - \bar{O})(O_{i+k} - \bar{O}), \qquad \bar{O} = \frac{1}{N}\sum_{i=0}^{N-1} O_i. \tag{9}$$

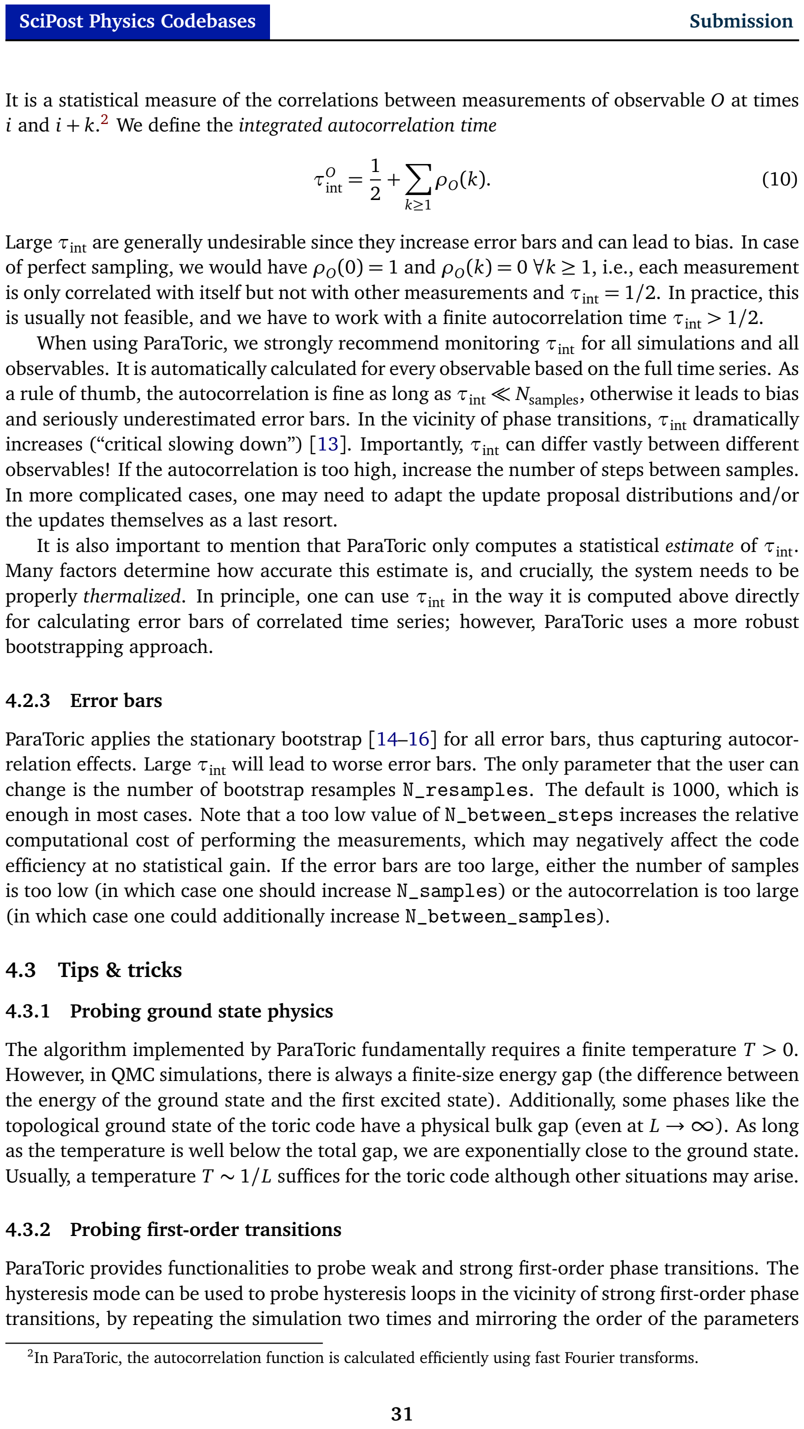

It is a statistical measure of the correlations between measurements of observable O at times i and $i+k$.[2] We define the *integrated autocorrelation time*

$$\tau_{\text{int}}^{O} = \frac{1}{2} + \sum_{k\geq 1} \rho_O(k). \tag{10}$$

Large τ_{int} are generally undesirable since they increase error bars and can lead to bias. In case of perfect sampling, we would have $\rho_O(0) = 1$ and $\rho_O(k) = 0\ \forall k \geq 1$, i.e., each measurement is only correlated with itself but not with other measurements and $\tau_{\text{int}} = 1/2$. In practice, this is usually not feasible, and we have to work with a finite autocorrelation time $\tau_{\text{int}} > 1/2$.

When using ParaToric, we strongly recommend monitoring τ_{int} for all simulations and all observables. It is automatically calculated for every observable based on the full time series. As a rule of thumb, the autocorrelation is fine as long as $\tau_{\text{int}} \ll N_{\text{samples}}$, otherwise it leads to bias and seriously underestimated error bars. In the vicinity of phase transitions, τ_{int} dramatically increases (“critical slowing down”) [13]. Importantly, τ_{int} can differ vastly between different observables! If the autocorrelation is too high, increase the number of steps between samples. In more complicated cases, one may need to adapt the update proposal distributions and/or the updates themselves as a last resort.

It is also important to mention that ParaToric only computes a statistical *estimate* of τ_{int}. Many factors determine how accurate this estimate is, and crucially, the system needs to be properly *thermalized*. In principle, one can use τ_{int} in the way it is computed above directly for calculating error bars of correlated time series; however, ParaToric uses a more robust bootstrapping approach.

4.2.3 Error bars

ParaToric applies the stationary bootstrap [14–16] for all error bars, thus capturing autocorrelation effects. Large τ_{int} will lead to worse error bars. The only parameter that the user can change is the number of bootstrap resamples `N_resamples`. The default is 1000, which is enough in most cases. Note that a too low value of `N_between_steps` increases the relative computational cost of performing the measurements, which may negatively affect the code efficiency at no statistical gain. If the error bars are too large, either the number of samples is too low (in which case one should increase `N_samples`) or the autocorrelation is too large (in which case one could additionally increase `N_between_samples`).

4.3 Tips & tricks

4.3.1 Probing ground state physics

The algorithm implemented by ParaToric fundamentally requires a finite temperature $T > 0$. However, in QMC simulations, there is always a finite-size energy gap (the difference between the energy of the ground state and the first excited state). Additionally, some phases like the topological ground state of the toric code have a physical bulk gap (even at $L \to \infty$). As long as the temperature is well below the total gap, we are exponentially close to the ground state. Usually, a temperature $T \sim 1/L$ suffices for the toric code although other situations may arise.

4.3.2 Probing first-order transitions

ParaToric provides functionalities to probe weak and strong first-order phase transitions. The hysteresis mode can be used to probe hysteresis loops in the vicinity of strong first-order phase transitions, by repeating the simulation two times and mirroring the order of the parameters

---

[2] In ParaToric, the autocorrelation function is calculated efficiently using fast Fourier transforms.

in `h_hysteresis` and `lmbda_hysteresis`. Weak first-order transitions can be detected by plotting a time series histogram of an observable (it exhibits a double-peak structure). Both approaches have been used in the context of the toric code [11].

4.3.3 Choosing the basis

Sometimes, one can work in both the $\hat{\sigma}^x$- and the $\hat{\sigma}^z$-basis. However, the performance can vary drastically! Generally, the $\hat{\sigma}^x$-basis is more efficient for $h/J > \lambda/\mu$ and vice versa.

4.3.4 Choosing `N_thermalization`

Based on our experience, we can say that $N_{\text{thermalization}} = 500L^d/T$ is a sensible choice for small fields, where d is the dimensionality of the system. Nevertheless, one should make use of the provided tools to benchmark thermalization, see Sec. 4.2, and rather err on the side of safety.

4.3.5 Choosing `N_samples`

Neglecting autocorrelation effects, the error of an observable ΔO scales as $\Delta O \sim 1/\sqrt{N_{\text{samples}}}$. More samples are, in principle, always better and lead to lower error bars. Smoothness of a curve of statistical results also requires that error bars be small in relation to the parameter grid size. If one increases the parameter resolution (e.g., in the field h), then one typically also increases `N_samples`.

4.3.6 Choosing `N_between_samples`

The optimal choice for `N_samples` is the integrated autocorrelation time of the time series (where a measurement is taken after every update). A good guess of the autocorrelation time based on previous simulations for smaller system sizes or nearby parameter points can result in substantial computational saving costs in production runs for large system sizes. Near continuous phase transitions, the integrated autocorrelation time has an additional dependence $\tau_{\text{int}} \sim L^z$, where z is the dynamical exponent of the universality class of the transition. For a 2D system in the vicinity of a continuous phase transition, a sensible scaling for `N_between_samples` could be $\mathcal{O}(L^2 \times \beta \times L^z)$ ($\mathcal{O}(L^2)$ links, each has off-diagonal spin flips $\mathcal{O}(\beta)$).

4.3.7 Choosing `N_resamples`

As with `N_samples`, more is better (but also more costly). Usually `N_resamples` ≈ 1000 is a sensible choice.

4.3.8 Extracting snapshots

When the option `save_snapshots` is enabled, ParaToric will write the snapshots into the directory specified in `path_out` (or in the paths `paths_out` for hysteresis sweeps). The snapshots are saved in the GraphML format (XML-based), which is supported by many major graph libraries. One snapshot will be saved for every measurement of observables, i.e., `N_samples` snapshots in total. All snapshots are written into a single file to save disk space and simultaneously offer a structured, self-documenting format. Every edge stores a list of spins. The first spin belongs to the first snapshot, the second one to the second snapshot, and so on. There are no special requirements for disks or memory bandwidth; the snapshots are kept in RAM and are only written to disk after the simulation has finished.

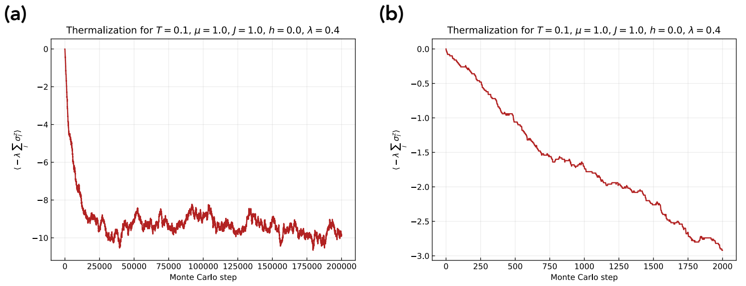

Figure 2: **Good and bad thermalization** plots produced by the Python command-line interface. We show the gauge field energy $\propto \lambda$. (a) The system is well thermalized; after its initial drop, the energy fluctuates around the expectation value. (b) The system is not yet thermalized; the floating average is still decreasing.

4.3.9 Adding new observables/lattices/updates

After adding features to the code, *always* benchmark them using analytical results, other numerical methods (exact diagonalization, tensor networks, ...), and unit tests. We advise using a fixed seed during development, e.g., when checking whether two methods produce the exact same result. The code has some built-in features to check self-consistency, e.g., at the end of each simulation, the code checks whether the cached total energy is numerically close to the total energy calculated from scratch. Do not turn off these features, as they will point you toward bugs!

4.4 Benchmarks

4.4.1 Thermalization

In Fig. 2 (which we already discussed before and repeat here for completeness) we plot the gauge field energy $\propto \lambda$ for two systems: the left one is sufficiently thermalized, the right one is not. The plots are direct outputs of the Python command-line interface. Always make sure the system is well thermalized.

4.4.2 Integrated autocorrelation time

Here, we demonstrate how the integrated autocorrelation time τ_{int} grows with decreasing `N_between_samples`. We use the following setup:

Listing 13: `N_between_samples` benchmarking setup

```
>>> import numpy as np
>>> from paratoric import extended_toric_code as etc
>>> series, mean, std, binder, binder_std, tau_int = etc.get_sample(
    N_samples=100000, N_thermalization=10000, N_between_samples=1,
    N_resamples=1000, custom_therm=False, observables=["energy"], seed=0, mu
    =1.0, h=0.0, h_therm=0.0, J=1.0, lmbda=0, lmbda_therm=0.0, basis='x',
    lattice_type="square", system_size=4, beta=10, boundaries="periodic",
    default_spin=1, save_snapshots=False)
```

We only run the simulation once per `N_between_samples`. The results are:

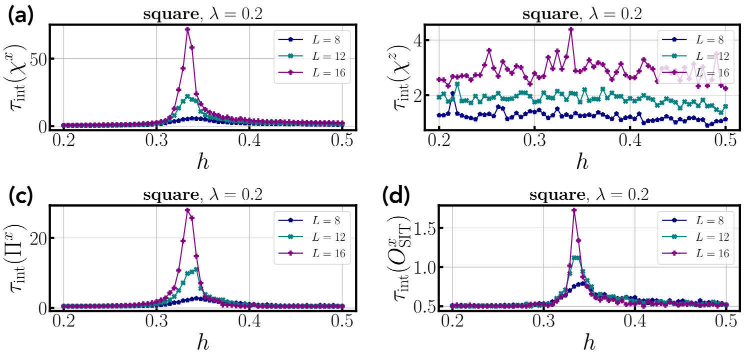

Figure 3: **Critical slowing down** of the integrated autocorrelation times in the vicinity of a continuous (topological) phase transition. We simulate the extended toric code (1) on the square lattice in the $\hat{\sigma}^x$-basis around the critical field $h_c(\lambda = 0.2) \approx 0.33$ [5,9]. (a) The susceptibility χ^x features a maximum around the critical field. The growth of τ_{int} with L is superlinear: we observe critical slowing down. (b) The susceptibility χ^z does not have a maximum near the critical field and does not exhibit critical slowing down because the phase transition is driven by h/J (not λ/μ). (c) The percolation probability Π^x is an order parameter and exhibits critical slowing down. (d) The staggered imaginary time order parameter O^x_{SI} also exhibits critical slowing down, albeit with *much* smaller τ_{int} than Π^x.

`N_between_samples`	**1**	**10**	**100**	**500**	**1000**
τ_{int} (energy)	1895	141.4	19.7	3.24	1.64

For very small `N_between_samples`, τ_{int} is very high: in cases where the update is rejected, the configuration is identical to the one measured before! A choice of `N_between_samples` between 500 and 1000 would be a good tradeoff between τ_{int} and runtime for this example. Increasing `N_between_samples` to well over 1000 would be a waste of CPU time.

The second setup illustrates critical slowing down. We use the Python CLI and sweep across a continuous topological phase transition on the square lattice for $L \in \{8, 12, 16\}$ (see Sec. 4.4.4):

Listing 14: Critical slowing down benchmarking setup

```
python3 -u ./python/cli/paratoric.py -sim etc_h_sweep -Ns 100000 -Nbs 160*L
    ^2 -Nth 10000*L^2 -T 1/L -muc 1 -hl 0.2 -hu 0.5 -hs 64 -hct 0.0 -Jc 1 -
    lmbdac 0.2 -lmbdact 0.2 -Nr 1000 -cth 0 -obs percolation_strength
    percolation_probability plaquette_percolation_strength
    plaquette_percolation_probability largest_cluster
    largest_plaquette_cluster string_number energy energy_h energy_mu
    energy_J energy_lmbda sigma_x sigma_z star_x plaquette_z
    staggered_imaginary_times delta anyon_count anyon_density
    fredenhagen_marcu sigma_x_static_susceptibility
    sigma_x_dynamical_susceptibility sigma_z_static_susceptibility
    sigma_z_dynamical_susceptibility -s 0 -bas x -lat square -L 16 -bound
    periodic -dsp 1 -proc 64 -snap 0 -fts 0 -outdir /scratch/s/Simon.Linsel/
    toric_code/out
```

In Fig. 3, we show τ_{int} of χ^x (a), χ^z (b), Π^x (c), and O^x_{SI} (d). All observables except χ^z can probe the phase transition. Unfortunately, they also exhibit critical slowing down, signaled by a maximum of τ_{int} (around the critical field) which grows superlinearly with L. Our results nicely demonstrate how different observables can have vastly different τ_{int}. In particular, O^x_{SI} has a very low τ_{int}, which is very convenient for run-times.

χ^z cannot probe the phase transition as it is driven by h/J (not λ/μ). It does neither exhibit critical slowing down, nor even a maximum of τ_{int} around the critical field. τ_{int} has an approximately linear increase with L for χ^z (and for χ^x far away from the phase transition) because in `N_between_samples` we did not take into account the growth of the imaginary time dimension ($\beta = L$). The susceptibilities are integrals over the imaginary time, so the autocorrelation gets worse. A simple fix is to add an additional β-dependency to `N_between_samples`.

4.4.3 Run-time

We benchmark the run-time for two realistic parameter sets on the square lattice and varying system size. The first setup simulates the toric code without fields:[3]

Listing 15: L benchmarking setup 1

```
>>> import numpy as np
>>> from paratoric import extended_toric_code as etc
>>> L=20
>>> series, mean, std, binder, binder_std, tau_int = etc.get_sample(
    N_samples=10000, N_thermalization=500*L*L*L, N_between_samples=8*L*L*L,
    N_resamples=1000, custom_therm=False, observables=["energy", "sigma_x",
    "sigma_z"], seed=0, mu=1.0, h=0.0, h_therm=0.0, J=1.0, lmbda=0,
    lmbda_therm=0.0, basis='x', lattice_type="square", system_size=L, beta=L
    , boundaries="periodic", default_spin=1, save_snapshots=False)
```

We only run one test per system size. The results are:

L	4	8	12	16	20
Runtime (s)	3.1	21.3	75	197	379

From our experience, for large L the update complexity is approximately $\mathcal{O}(L^3 \log \beta)$, owing to the chosen cubic dependency of `N_thermalization` and `N_between_samples` and a $\mathcal{O}(\log \beta)$ dependence of operations on the imaginary time axis, see β benchmark below. The system size itself does not impact the performance, as the interactions are local. On computing clusters, we have realized system sizes of up to $L = 80$ for the square lattice; this number will only increase in the future as CPUs get faster.

The second setup simulates the toric code with fields in both $\hat{\sigma}^x$ and $\hat{\sigma}^z$-direction:

Listing 16: L benchmarking setup 2

```
>>> import numpy as np
>>> from paratoric import extended_toric_code as etc
>>> L=20
>>> series, mean, std, binder, binder_std, tau_int = etc.get_sample(
    N_samples=10000, N_thermalization=500*L*L*L, N_between_samples=8*L*L*L,
    N_resamples=1000, custom_therm=False, observables=["energy", "sigma_x",
    "sigma_z"], seed=0, mu=1.0, h=0.2, J=1.0, lmbda=0.2, basis='x',
    lattice_type="square", system_size=L, beta=L, boundaries="periodic",
    default_spin=1, save_snapshots=False)
```

---

[3] All tests were run on a laptop; some conditions, like the CPU temperature, were not identical for all simulations. The benchmarks are therefore only an approximation.

We only run one test per system size. The results are:

L	**4**	**8**	**12**	**16**	**20**
Runtime (s)	3.9	34.1	133	323	689

We also test the run-time dependence of the inverse temperature β, with the following setup:

Listing 17: β benchmarking setup

```
>>> import numpy as np
>>> from paratoric import extended_toric_code as etc
>>> series, mean, std, binder, binder_std, tau_int = etc.get_sample(
    N_samples=10000, N_thermalization=20000, N_between_samples=2000,
    N_resamples=1000, custom_therm=False, observables=["energy", "sigma_x",
    "sigma_z"], seed=0, mu=1.0, h=0.2, J=1.0, lmbda=0.2, basis='x',
    lattice_type="square", system_size=10, beta=20, boundaries="periodic",
    default_spin=1, save_snapshots=False)
```

We only run one test per β. The results are:

β	**4**	**8**	**12**	**16**	**20**
Runtime (s)	14.9	17.2	19.1	20.0	22.1

This benchmark illustrates an appealing feature of our implementation: there is almost no slowing down when increasing β implying that very low temperatures are within reach with ParaToric. This paradoxical result (because the number n of off-diagonal star/plaquette and magnetic field operators must physically scale linearly in β) is explained by the fact that most searches within the imaginary time axis scale as $\mathcal{O}(\log n)$ by making use of binary searches.

4.4.4 Topological phase transition

We probe the well-known topological phase transition in the ground state of the extended toric code (1) on the square lattice, where we have a gapped $\mathbb{Z}_2$ quantum spin liquid for small fields h, λ and a topologically trivial phase for high fields. We set $J = \mu = 1$, $\lambda = 0.2$ and sweep h over the known critical value $h_c(\lambda = 0.2) \approx 0.33$ [5,9] for $L \in \{10, 20, 40, 80\}$ in the $\hat{\sigma}^x$-basis. The temperature is set to $T = 1/L$ to capture ground state physics. We take 30000 snapshots, with $8L^3$ steps in between snapshots and $500L^3$ thermalization steps.[4]. We confirm that the systems are well thermalized. We show the percolation probability, the Fredenhagen-Marcu string order parameter, and the staggered imaginary time order parameter in Fig. 4. All of them reproduce the known phase boundary.

5 Conclusion & Outlook

We have presented ParaToric, a continuous-time quantum Monte Carlo solver for the toric code in a parallel field. ParaToric builds on the existing work by Wu, Deng, and Prokof'ev [5] and is also applicable to high temperature and low off-diagonal couplings.

ParaToric can store snapshots, which makes it ideally suited to generate training/benchmarking data for applications in other fields, such as lattice gauge theories, cold atom or other

---

[4] If we were interested in quantities like critical exponents and we need to go very close to the critical field, we should take into account the dynamical exponent z ($\tau_{\text{int}} \sim L^z$) in the number of steps between snapshots to account for critical slowing down. Now the error bars are just larger near the critical field.

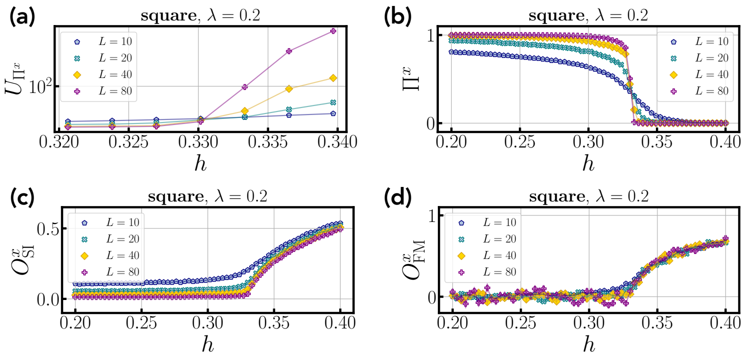

Figure 4: **Topological phase transition** of the extended toric code (1) on the square lattice. The critical field is known and located at $h_c(\lambda = 0.2) \approx 0.33$ [5, 9]. Our results agree with the value published in the literature, within error bars. (a) The percolation probability Binder ratio U_{Π^x} [9] features a crossing point around $h = 0.33$. (b) The percolation probability Π^x is non-zero in the topological phase and zero in the trivial phase. The transition gets sharper with increasing system size. (c) The staggered imaginary time order parameter O^x_{SI} is zero in the topological phase and non-zero in the trivial phase. (d) The Fredenhagen-Marcu order parameter O^x_{FM} is zero in the topological phase and non-zero in the trivial phase. The loop length grows with $\mathcal{O}(L)$. Compared to the other order parameters, it is very noisy because it is a multi-body correlator and on top of that a division of two exponentially small numbers.

quantum simulators, quantum spin liquids, artificial intelligence, and quantum error correction. We believe it also serves a pedagogical purpose. Another strength of ParaToric is its interoperability with other programming languages. The C interface is compatible with virtually all programming languages, thus ParaToric can be seamlessly integrated into other projects.

ParaToric comes with an MIT license. For future release of ParaToric we plan extensions along the following lines:

- Additional lattices such as the kagome and the ruby lattice. Given the underlying graph structure used in ParaToric, such extensions are straightforward.
- Additional observables: we think here of, for instance, the finite temperature extension of the fidelity susceptibility to diagnose the phase transitions in the absence of a local order parameter. It would be worthwhile to have additional off-diagonal observables such as the off-diagonal Fredenhagen-Marcu string operators, or correlation functions between off-diagonal operators in space and or time. Measurements of the Rényi entropy are also high on the to-do list. The latter two classes require however major changes to the code, and testing.
- Additional interaction types. There are many classes of models in which topological order may be emergent instead of explicit as in the toric code. Such models typically have additional interactions than the ones covered in ParaToric, such as longer-range Ising interactions, and miss some others (typically the plaquette type interactions, and sometimes even the star terms). It is in general an open problem how to efficiently

simulate such models at the lowest temperatures (even for sign-free models). Extending ParaToric to dealing with other types of interactions can thus serve as an additional tool for benchmarking purposes and algorithmic exploration.

Acknowledgements

The authors acknowledge fruitful discussions with A. Bohrdt, G. De Paciani, G. Dünnweber, F. Grusdt, L. Homeier, and N. V. Prokof'ev.

Author contributions SML did the main coding and planning work with input from LP. All authors contributed to the writing of the manuscript.

Funding information This research was funded by the European Research Council (ERC) under the European Union's Horizon 2020 research and innovation program – ERC Starting Grant SimUcQuam (Grant Agreement No. 948141), and by the Deutsche Forschungsgemeinschaft (DFG, German Research Foundation) under Germany's Excellence Strategy – EXC-2111 – project number 390814868. The project/research is part of the Munich Quantum Valley, which is supported by the Bavarian state government with funds from the Hightech Agenda Bayern Plus. L.P. acknowledges financial support from ANR-23-CE30-0018.

References

[1] A. Kitaev, *Fault-tolerant quantum computation by anyons*, Annals of Physics **303**(1), 2 (2003), doi:https://doi.org/10.1016/S0003-4916(02)00018-0.

[2] E. Dennis, A. Kitaev, A. Landahl and J. Preskill, *Topological quantum memory*, Journal of Mathematical Physics **43**(9), 4452 (2002), doi:10.1063/1.1499754, https://pubs.aip.org/aip/jmp/article-pdf/43/9/4452/19183135/4452_1_online.pdf.

[3] A. G. Fowler, M. Mariantoni, J. M. Martinis and A. N. Cleland, *Surface codes: Towards practical large-scale quantum computation*, Phys. Rev. A **86**, 032324 (2012), doi:10.1103/PhysRevA.86.032324.

[4] J. B. Kogut, *An introduction to lattice gauge theory and spin systems*, Rev. Mod. Phys. **51**, 659 (1979), doi:10.1103/RevModPhys.51.659.

[5] F. Wu, Y. Deng and N. Prokof'ev, *Phase diagram of the toric code model in a parallel magnetic field*, Phys. Rev. B **85**, 195104 (2012), doi:10.1103/PhysRevB.85.195104.

[6] K. Fredenhagen and M. Marcu, *Charged states in z2 gauge theories*, Communications in Mathematical Physics **92**(1), 81 (1983), doi:10.1007/BF01206315.

[7] K. Fredenhagen and M. Marcu, *Confinement criterion for qcd with dynamical quarks*, Phys. Rev. Lett. **56**, 223 (1986), doi:10.1103/PhysRevLett.56.223.

[8] K. Fredenhagen and M. Marcu, *Dual interpretation of order parameters for lattice gauge theories with matter fields*, Nuclear Physics B - Proceedings Supplements **4**, 352 (1988), doi:https://doi.org/10.1016/0920-5632(88)90124-7.

[9] S. M. Linsel, A. Bohrdt, L. Homeier, L. Pollet and F. Grusdt, *Percolation as a confinement order parameter in z2 lattice gauge theories*, Phys. Rev. B **110**, L241101 (2024), doi:10.1103/PhysRevB.110.L241101.

[10] G. Dünnweber, S. M. Linsel, A. Bohrdt and F. Grusdt, *Percolation renormalization group analysis of confinement in z2 lattice gauge theories*, Phys. Rev. B **111**, 024314 (2025), doi:10.1103/PhysRevB.111.024314.

[11] S. M. Linsel, L. Pollet and F. Grusdt, *Independent e- and m-anyon confinement in the parallel field toric code on non-square lattices*, doi:10.48550/arXiv.2504.03512 (2025).

[12] M. Matsumoto and T. Nishimura, *Mersenne twister: a 623-dimensionally equidistributed uniform pseudo-random number generator*, ACM Trans. Model. Comput. Simul. **8**, 3 (1998).

[13] U. Wolff, *Critical slowing down*, Nuclear Physics B - Proceedings Supplements **17**, 93 (1990), doi:https://doi.org/10.1016/0920-5632(90)90224-I.

[14] D. N. Politis and J. P. Romano, *The stationary bootstrap*, Journal of the American Statistical Association **89**(428), 1303 (1994), doi:10.1080/01621459.1994.10476870.

[15] D. N. Politis and H. White, *Automatic block-length selection for the dependent bootstrap*, Econometric Reviews **23**(1), 53 (2004), doi:10.1081/ETC-120028836.

[16] A. Patton, D. N. Politis and H. White, *Correction to "automatic block-length selection for the dependent bootstrap" by d. politis and h. white*, Econometric Reviews **28**(4), 372 (2009), doi:10.1080/07474930802459016.

2.8 Publication 2: Percolation as a confinement order parameter in $\mathbb{Z}_2$ lattice gauge theories

In this section, the following publication is reprinted:

P2 *Percolation as a confinement order parameter in $\mathbb{Z}_2$ lattice gauge theories*,
Simon M. Linsel, Annabelle Bohrdt, Lukas Homeier, Lode Pollet, and Fabian Grusdt,
Physical Review B **110**, L241101 (2024), ©2024 American Physical Society,
doi: 10.1103/PhysRevB.110.L241101.
Reprinted on pages 56–71.

PHYSICAL REVIEW B **110**, L241101 (2024)

Letter

Percolation as a confinement order parameter in $\mathbb{Z}_2$ lattice gauge theories

Simon M. Linsel,[1,2,*] Annabelle Bohrdt,[2,3] Lukas Homeier,[1,2] Lode Pollet,[1,2] and Fabian Grusdt[1,2,†]

[1]*Department of Physics and Arnold Sommerfeld Center for Theoretical Physics (ASC), Ludwig-Maximilians-Universität München, Theresienstr. 37, München D-80333, Germany*

[2]*Munich Center for Quantum Science and Technology (MCQST), Schellingstr. 4, D-80799 München, Germany*

[3]*Institute of Theoretical Physics, University of Regensburg, D-93053, Germany*

(Received 29 January 2024; accepted 15 November 2024; published 2 December 2024)

Lattice gauge theories (LGTs) were introduced in 1974 by Wilson to study quark confinement. These models have been shown to exhibit (de)confined phases, yet it remains challenging to define experimentally accessible order parameters. Here we propose percolation-inspired order parameters (POPs) to probe confinement of dynamical matter in $\mathbb{Z}_2$ LGTs using electric field basis snapshots accessible to quantum simulators. We apply the POPs to study a classical $\mathbb{Z}_2$ LGT and find a confining phase up to temperature $T = \infty$ in two dimensions (critical T_c, i.e., finite-T phase transition, in three dimensions) for any nonzero density of $\mathbb{Z}_2$ charges. Further, using quantum Monte Carlo we demonstrate that the POPs reproduce the square lattice Fradkin-Shenker phase diagram at $T = 0$ and explore the phase diagram at $T > 0$. The correlation length exponent coincides with the one of the three-dimensional Ising universality class and we determine the POP critical exponent characterizing percolation. Our proposed POPs provide a geometric perspective of confinement and are directly accessible to snapshots obtained in quantum simulators, making them suitable as a probe for quantum spin liquids.

DOI: 10.1103/PhysRevB.110.L241101

Introduction. Lattice gauge theories (LGTs) have been widely studied in the fields of high-energy [1], condensed matter [2–4], and biophysics [5]. In 1979, Fradkin and Shenker proved in their groundbreaking work [6] the existence of two phases in their model, where $\mathbb{Z}_2$ charged particles are confined or deconfined, respectively. Ever since, researchers have found intimate connections of $\mathbb{Z}_2$ LGTs to other physical effects, including topological order [7,8], quantum spin liquids [9,10], and even quantum information [11]. In the light of quantum simulation, LGTs with finite-dimensional local Hilbert spaces, e.g., $\mathbb{Z}_2$ LGTs and quantum link models [12], gain particular attention because of their experimental feasibility [13].

Despite experimental progress, it remains a challenging problem to define order parameters for deconfined (e.g., topological) phases that are accessible to both numerical simulations and cold-atom experiments. Wegner-Wilson loops (WWL) [1,2] are nonlocal order parameters allowing us to probe (de)confinement in pure gauge theories, i.e., without matter. They measure the fluctuation of the magnetic field and feature an area (perimeter) law in the (de)confined phase. However, they are not suitable for $\mathbb{Z}_2$ LGTs with matter [6]. The Fredenhagen-Marcu order parameter [14–16] partly solves this problem by relating a full to a half WWL, measuring the response of the system when spatially separating two matter particles [17]. However, being a ratio of two small numbers, the Fredenhagen-Marcu order parameter suffers insurmountably from noise in some regimes [18,19]; nevertheless it was used experimentally for systems with a strong Rydberg blockade [20,21].

Much physical intuition of confinement of matter comes from electric field lines connecting gauge charges, creating a linear confining potential [22]. In the electric field basis, accessible to state-of-the-art quantum simulators [13,23–28], a picture of fluctuating electric fields is appealing, analogous to fluctuating magnetic fields in WWL: if the electric field lines are fluctuating so strongly that one cannot distinguish whether two charges are connected or not, the picture of confining electric strings breaks down. As will be shown in this Letter, this physical intuition can be formalized with the help of percolation theory, which has been used extensively to study phase transitions geometrically [29].

Bernoulli percolation theory was introduced by Broadbent and Hammersley [30], where they studied the random flow of a fluid through a medium. A prime example of the use of percolation theory in physics is the random cluster model, which was successfully used to study many physical systems, e.g., the Potts model [31,32]. More recently, percolation theory was applied in the context of quantum monopole motion in spin ice [33], quantum error correction [34], and gauge theories [35].

In this Letter, we show that percolation can also serve as a nonlocal order parameter to probe confinement. In the confined phase, analogous to quarks in a confining potential, two charges are being held together by $\mathbb{Z}_2$ electric strings and form a $\mathbb{Z}_2$-neutral meson [27]. In the deconfined phase, in our picture matter particles move essentially independently through the system and the $\mathbb{Z}_2$ electric strings form a global cluster spanning over the entire lattice, see Fig. 1. We study a classical and a quantum model using classical (quantum) Monte Carlo (MC/QMC). We show that the phase

---

[*] Contact author: simon.linsel@physik.uni-muenchen.de

[†] Contact author: fabian.grusdt@physik.uni-muenchen.de

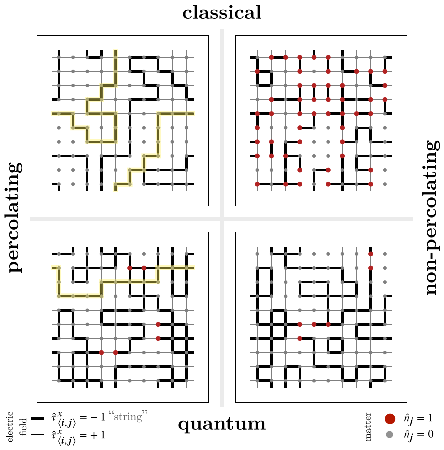

FIG. 1. Classical and quantum snapshots of (non)percolating strings. We show periodic classical/quantum snapshots of (non)percolating strings ($\hat{\tau}^x = -1$) obtained from MC simulations in the electric field basis. Here, percolation refers to a cluster of electric fields winding around the periodic system and connecting to itself in at least one dimension, see Ref. [18], Sec. I. The (non)percolating phase is associated with a deconfined (confined) phase. Top: The classical snapshots are obtained from Hamiltonian (2). The percolating snapshot is captured at high temperature for a system without matter excitations. Introducing matter prevents the formation of a percolating string cluster, as can be observed in the confined snapshot. Bottom: The ground state quantum snapshots are obtained from equal imaginary time slices of Hamiltonian (8), inside (percolating) and outside (nonpercolating) the topological phase. Here, a nonzero matter density does not necessarily prohibit percolation.

boundary in the celebrated Fradkin-Shenker model (extended toric code) [6] can be reproduced by percolation-inspired order parameters (POPs), paving the way for the application of POPs in related models.

Classical $\mathbb{Z}_2$ *LGT.* The complex nature of percolation in $\mathbb{Z}_2$ LGTs emerges from the local $\mathbb{Z}_2$ symmetry generator

$$\hat{G}_j = (-1)^{\hat{n}_j} \prod_{l \in + j} \hat{\tau}^x_l, \tag{1}$$

where $\hat{n}_j = \hat{a}^\dagger_j \hat{a}_j$ is the number operator for (hard-core, Higgs) matter on site $\boldsymbol{j}$ and the Pauli matrix $\hat{\tau}^x_l$ defines the electric field on a link l adjacent to site $\boldsymbol{j}$. This leads to an extensive set of conserved quantities $\{g_j\}$, which fulfill Gauss's law $\hat{G}_j|\psi\rangle = g_j|\psi\rangle$. The choice of $\{g_j\}$ defines a gauge sector. In the following, we only consider $g_j = 1$, i.e., no background charges.

To demonstrate the viability of the POPs, we first perform MC simulations of the $\mathbb{Z}_2$-symmetric classical Hamiltonian

$$\hat{\mathcal{H}}_{\text{can}} = -h \sum_l \hat{\tau}^x_l \tag{2}$$

in the canonical regime, i.e. we fix the number of matter particles $N = \sum_j \hat{n}_j$. We assume $h > 0$.

Due to Gauss's law, each matter particle has to be connected to a cluster Σ of neighboring strings where $\hat{\tau}^x_l = -1\ \forall l \in \Sigma$. This cluster costs an energy $2h\ell$, where ℓ is the number of neighboring strings in the cluster. At low temperature T and low matter density, this results in matter particles forming mesonic bound states, where matter particles on neighboring sites are connected by one string [27]. At higher temperatures, there is a competition between the entropy $S(\ell)$ and the energy $E(\ell)$ of strings (in linear approximation). When $TS > E$, a global string network forms that winds around the system for periodic boundaries while matter particles become free $\mathbb{Z}_2$ charges [37]. We describe this as a percolation transition of the strings from a nonpercolating bound mesonic regime to a percolating regime with incoherent but free charges.

To probe this transition, we define two POPs. Percolation probability is the probability that a string cluster percolates, i.e., winds around the system and connects to itself, see Ref. [18], Sec. I A. Given an electric field snapshot j, we calculate how many times $W^i_c(j)$ every connected string cluster c winds around the system in dimension i and define the total winding number $W(j) = \sum_i W^i_c(j)$ [38]. The percolation probability $\Pi = \langle \Theta(W) \rangle$, where Θ is the Heaviside step function, is obtained by averaging over the ensemble. More generally, it can also be written as a Hermitian projector $\hat{\Pi} = \sum_{\Theta(W(j))>0} |\{\hat{\tau}^x\}_j\rangle\langle\{\hat{\tau}^x\}_j|$ onto all possible percolating string configurations $\{\hat{\tau}^x\}_j$. In the literature, this concept is sometimes also referred to as the wrapping probability [39] or the winding number [40]. Further, we define the percolation strength $P = \Theta(\Pi) \max_c |c|/N_{\text{links}}$ as the number of strings $|c|$ in the largest string cluster divided by the total number of links N_{links} given that the system percolates [27]. We probe the transition on a periodic square lattice with system sizes $L^2 = 20^2, 30^2, 40^2, 50^2$. In the following we distinguish the cases for (i) zero matter density $d = 0$ and (ii) nonzero matter density $d = N/L^2 > 0$.

(i) Hamiltonian (2) can be mapped to the classical two-dimensional (2D) Ising model on the dual lattice [2,3], where the confined phase corresponds to the ferromagnetic ordered phase. The POPs can be viewed as a disorder parameter detecting domain walls in the ferromagnet, see Ref. [18], Sec. III. Via a finite-size scaling analysis, we confirm that the percolation transition we find takes place exactly at the Ising critical temperature $(T/h)_c|_{\text{Ising}} = 2/\log(1+\sqrt{2}) \approx 2.27$ [41] [see Fig. 2(a)]. For the correlation length critical exponents, we find $\nu = 1.04(10)$ (2D Ising universality). Hence, one divergent length scale for percolation and Ising spins fixes ν. This is consistent with previous studies, where the exponent ν of the confinement length [42] and wrapping probabilities [38] was found to be of Ising universality. For the percolation strength critical exponent, we find $\beta = 0.58(10)$. We are unaware of a direct relation of the percolation strength critical exponent β to the 2D Ising critical exponent. The percolation probability can also serve as an order parameter but it is impossible to extract a corresponding β since the percolation probability jumps from zero to one in the thermodynamic limit (TDL). The phase diagram is reminiscent of [43].

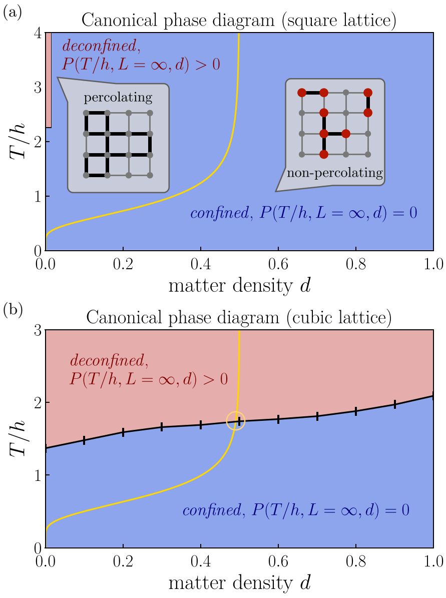

FIG. 2. Canonical thermal deconfinement phase diagrams at nonzero matter density. We show two temperature-density phase diagrams of the classical Hamiltonian (2) for (a) the square and (b) the cubic lattice. In the confined phase (blue), the percolation strength $P(T/h, L = \infty, d)$ vanishes while strings percolate $P(T/h, L = \infty, d) > 0$ in the deconfined phase (red). The yellow lines are the exactly solvable $\mu = 0$ case of Hamiltonian (3), see Eqs. (4) and (5). (a) We find a thermal deconfinement transition only at zero matter density. The critical temperature $(T/h)_c = 2.27(1)$, extracted via a finite-size scaling analysis, is identical to the Ising critical temperature. At nonzero matter density, the system is confining for all temperatures. (b) In contrast to the square lattice, a finite-temperature thermal deconfinement transition exists for arbitrary matter density. At the $\mu = 0$ line, the phase transition to the deconfined phase (yellow circle) matches the Bernoulli percolation threshold $p_{\mathrm{c,cu}} = 0.247(5)$ [36] (note that we show d, not p).

(ii) We numerically find no thermal deconfinement transition, i.e., the presence of matter prevents the formation of a percolating string cluster and is thus always confined in the TDL, see Ref. [18], Sec. II A. To unravel this behavior analytically, we study the grand-canonical version of Hamiltonian (2),

$$\hat{\mathcal{H}}_{\mathrm{gc}} = -h \sum_{l} \hat{\tau}_l^x - \mu \sum_{j} \hat{n}_j$$
$$= -h \sum_{l} \hat{\tau}_l^x - \mu \sum_{j} \frac{1}{2}\left(1 - \prod_{l \in +_j} \hat{\tau}_l^x\right), \tag{3}$$

where we used the Gauss law constraint $\hat{G}_j = +1$, Eq. (1), to express $\hat{n}_j$ by $\hat{\tau}_l^x$ in the second line. The chemical potential μ serves as a Lagrange multiplier for the matter density. Eq. (3) is a generalized Ising model with four-spin interactions $\propto \mu$.

At $\mu = 0$, the electric fields are completely independent resembling standard Bernoulli bond percolation. From independent thermal distributions at each bond l, the corresponding probability p to host a string ($\hat{\tau}_l^x = -1$) is

$$p = e^{-\beta h}/[2\cosh(\beta h)] \tag{4}$$

with $\beta = 1/T$. Hence, $0 \leqslant p < 1/2$ for $\mu = 0$, which we find to correspond to average matter densities

$$d = \tfrac{1}{2}[1 - (2p - 1)^z] \tag{5}$$

for a lattice with even coordination number z. Importantly, all values of p remain below the Bernoulli percolation threshold $p_{\mathrm{c,sq}} = 0.5$ on the square lattice [36,44]. Hence, for $\mu = 0$ (corresponding to $d = 1/2$ for $T/h \to \infty$) we analytically proved that the presence of matter prohibits percolation, i.e., there is no finite-T percolation phase transition, see Fig. 2(a). Notably, the percolation threshold is reached when $T/h \to \infty$, indicating a deconfined, critically percolating state at infinite temperature.

Conversely, the percolation threshold for the cubic lattice is $p_{\mathrm{c,cu}} = 0.247(5)$ [36], implying that a thermal deconfinement phase transition at finite T can exist at any matter density d since $p \to 1/2$ for $T \to \infty$. We simulate the periodic cubic lattice with system sizes $L^3 = 10^3, 12^3, 14^3$ and show the phase diagram in Fig. 2(b). As expected, and in contrast to the square lattice, the deconfined phase persists for arbitrary matter density and sufficiently high temperatures.

Quantum $\mathbb{Z}_2$ LGT: Extended toric code. We start with a generalization of Hamiltonian (3) by adding magnetic fluctuations $\propto J$ and dynamical matter $\propto \lambda$:

$$\hat{\mathcal{H}}_{\mathrm{qLGT}} = -\mu \sum_{j} \hat{n}_j - h \sum_{l} \hat{\tau}_l^x - J \sum_{\square} \prod_{l \in \square} \hat{\tau}_l^z$$
$$- \lambda \sum_{\langle i,j \rangle} (\hat{a}_i^\dagger + \hat{a}_i)\, \hat{\tau}_l^z\, (\hat{a}_j^\dagger + \hat{a}_j). \tag{6}$$

This quantum Hamiltonian fulfills $[\hat{\mathcal{H}}_{\mathrm{qLGT}}, \hat{G}_j] = 0$ and is thus a $\mathbb{Z}_2$ LGT. To study this Hamiltonian with QMC, we restrict ourselves to the gauge sector $g_j = +1$. We integrate out the matter fields and write

$$\hat{n}_j = \frac{1}{2}\left(1 - \prod_{l \in +_j} \hat{\tau}_l^x\right), \tag{7}$$

i.e., the configuration $\{\hat{\tau}_l^x\}$ uniquely determines the state of the hard-core matter. Using Eq. (7) in Hamiltonian (6) yields

$$\hat{\mathcal{H}}_{\mathrm{eTC}} = -\mu \sum_{+} \prod_{l \in +} \hat{\tau}_l^x - J \sum_{\square} \prod_{l \in \square} \hat{\tau}_l^z$$
$$- h \sum_{l} \hat{\tau}_l^x - \lambda \sum_{l} \hat{\tau}_l^z, \tag{8}$$

exactly and without local constraints. This is the extended toric code where in LGT language, h acts as a confining potential and λ can be viewed as a gauge-breaking perturbation in the pure gauge theory. This model was originally studied

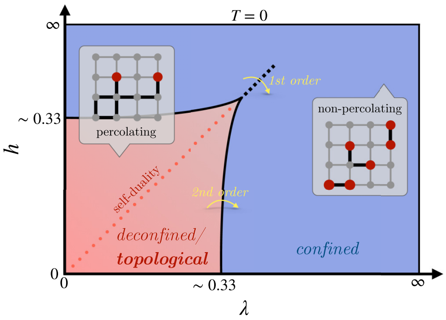

FIG. 3. Fradkin-Shenker phase diagram. We show that percolation identifies the same phase boundaries for the Fradkin-Shenker phase diagram of the extended toric code ($\mu = J = 1$) [6,45] on the square lattice, see Hamiltonian (8): in the deconfined phase (red) electric strings percolate while the percolation strength vanishes in the confined phase (blue). The confinement transition is continuous (solid lines) while there is a first-order line (dashed line) extending into the confined phase [45].

by Fradkin and Shenker [6], featuring a $T = 0$ phase diagram with a deconfined topological phase for small fields and a confined phase for large fields h, λ [6,45], see Fig. 3. Fradkin and Shenker [6] proved that the confined ($h \gg 1$) and Higgs phase ($\lambda \gg 1$) are adiabatically connected and thus identical. In the following, we fix $\mu = J = 1$.

In order to study percolation in the quantum $\mathbb{Z}_2$ LGT, we adapt the continuous-time QMC algorithm from Wu *et al.* [45] to the $\hat{\tau}^x$ basis to extract snapshots of strings (see Fig. 1) from equal-imaginary-time slices in the path-integral representation and set $T = 1/L$ to gain insights into the ground-state phase diagram, see Ref. [18], Sec. II B and Refs. [46–53]. Our analysis of such data leads us to the main result of this Letter: we conjecture that confinement in the quantum $\mathbb{Z}_2$ LGT with dynamical matter can be directly probed through percolation of $\mathbb{Z}_2$ electric strings.

The extended toric code features a self-duality ($h \leftrightarrow \lambda$) and the pure gauge model ($\lambda = 0$) can be mapped to the 2D transverse-field Ising model on the dual lattice [2,4,18] where the quantum critical point is in the 3D Ising universality class. Above the self-duality line, i.e., $h > \lambda$, we find that the POPs reproduce the well-known phase transition from a deconfined (percolating) regime to a confined (nonpercolating) phase for the entire phase boundary. We perform a finite-size scaling analysis to extract the critical temperature and the critical exponents. We illustrate a crossing-point analysis of the percolation strength Binder cumulant at $\lambda = 0.3$ in Fig. 4(a). The correlation length critical exponent $\nu = 0.65(27)$ matches the 3D Ising universality class. This is akin to the phenomenology we found for the classical $\mathbb{Z}_2$ LGT above. For the percolation strength critical exponent we find $\beta = 0.05(4)$. We were unable to provide a good estimate of the Fredenhagen-Marcu order parameter in the confined phase for $h > \lambda$ due to high noise in the data.

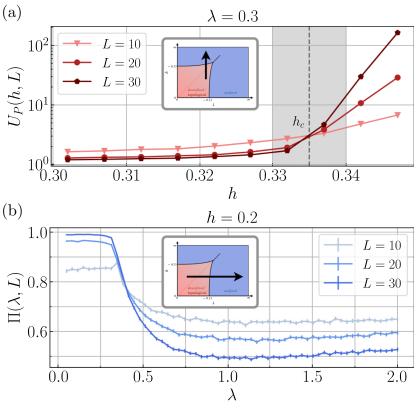

FIG. 4. QMC results of the extended toric code. We show results for the POPs in the square lattice toric code Hamiltonian (8) at $T = 1/L$. (a) We present a crossing-point analysis of the percolation strength Binder cumulant U_P above the self-duality line at $\lambda = 0.3$, i.e., at nonzero charge density. The critical electric field $h_c = 0.335(2)$ is in very good agreement with previous studies of the extended toric code [45]. (b) We present the percolation probability $\Pi(\lambda)$ for different system sizes at $h = 0.2$. At large couplings λ, we observe a clear decrease in Π with higher system sizes, and we conjecture that in the confined phase Π approaches zero in the TDL.

Below the self-duality line, i.e., $h < \lambda$, the $\hat{\tau}^x$ basis is numerically less efficient in sampling snapshots than the $\hat{\tau}^z$ basis (since spins tend to be more aligned in the $\hat{\tau}^z$ basis), however, we still find a percolation transition in the $\hat{\tau}^x$ basis in this regime. From self-duality, we know that the physical phase transition is at $\lambda_c \approx 0.335$. For $h = 0.2$, we find Binder cumulant crossing points at $\lambda \approx 0.4$ that shift toward lower λ for increasing system size. We argue that this behavior is a finite-size effect and can be traced back to the finite-size gap, see Ref. [18], Sec. II B. This view is supported by the decrease of the percolation probability we observe with increasing system size, see Fig. 4(b), although it does not yet extrapolate to zero for the simulated system sizes up to $L^2 = 30^2$. For Bernoulli percolation, Kolmogorov's zero-one law [54] restricts the percolation probability to either zero or one in the TDL. Even though the percolation of electric strings is correlated, we conjecture that the percolation probability in the confined phase approaches zero in the TDL. We are also able to probe the transition with the Fredenhagen-Marcu operator, see Ref. [18], Sec. II B.

At $h = \lambda = 0.2$ (deconfined, topological ground state), we find a percolating phase at low but finite temperatures and a nonpercolating phase at higher temperatures. We trace this back to the bulk gap, where due to exponential suppression of thermal matter excitations the topological ground state stays robust against a nonzero temperature in finite-size systems, see Ref. [18], Sec. II B. At temperatures well above the bulk gap, we observe a clear decrease in the percolation strength with higher system sizes. We conjecture that the percolation probability approaches zero in the TDL for any $T > 0$. We were unable to provide a good estimate of the Fredenhagen-Marcu order parameter for finite temperatures due to high noise in the data. In the literature, confinement at finite temperature is also probed using Polyakov loops [55] or by explicitly violating the gauge symmetry [56].

Our results for the quantum $\mathbb{Z}_2$ LGT can be interpreted by drawing connections with the classical $\mathbb{Z}_2$ LGT studied above. On the pure gauge axis, without matter, both support finite-T percolation transitions, which can be related to standard WWL. In the square lattice classical theory we find a complete breakdown of percolation at any nonvanishing matter density and for any T: Likewise, percolation breaks down in the Higgs phase (large λ) where $\mathbb{Z}_2$ charges accumulate and condense. In contrast, the $T = 0$ deconfined phase in the quantum theory sustains percolation, because $\mathbb{Z}_2$ charges are gapped and only appear virtually as correlated pairs in the ground state. This picture changes once again when thermal fluctuations are included: these lead to a nonzero density of thermally activated but free $\mathbb{Z}_2$-charged excitations at any $T > 0$, where the classical theory explains the breakdown of string percolation.

Discussion and outlook. We have introduced new POPs to probe the confinement of matter excitations in $\mathbb{Z}_2$ LGTs. We have applied it to study a classical model where we demonstrated the substantial influence of matter and the lattice geometry on the existence of a percolating, i.e., deconfined, phase. Further, using snapshots generated from continuous-time QMC, we demonstrated that the phase boundaries of the square lattice Fradkin-Shenker model, one of the textbook examples featuring confinement and topological order, can be reproduced by our POPs. The correlation length critical exponent falls into the 3D Ising universality class. We also demonstrated the potential of the POPs at finite temperature. Another task, left for future research, will be to check for a first-order percolation transition across the self-duality line at the tip of the deconfined phase.

While we only discuss $\mathbb{Z}_2$ LGTs on the square and the cubic lattice, we also envision future applications of the POPs in other LGTs, where different interactions, lattice geometries, or higher symmetries can be realized. Percolation was already used in the context of quantum error correcting codes [57]. Since percolation can be directly measured from snapshots in the electric field basis, the order parameter is readily accessible to state-of-the-art quantum simulators [13,23–28], and extends the geometric perspective on confinement beyond one-dimensional systems [58,59].

Acknowledgments. We thank M. Aidelsburger, D. Banerjee, G. Dünnweber, M. Kebrič, F. Palm, G. Semeghini, T. Wang, and H. Zhao for fruitful discussions. This research was funded by theEuropean Research Council (ERC) under the European Union's Horizon 2020 research and innovation program (Grant Agreement No. 948141)–ERC Starting Grant SimUcQuam, and by the Deutsche Forschungsgemeinschaft (DFG, German Research Foundation) under Germany's Excellence Strategy–EXC-2111–390814868 and via Research Unit FOR 2414 under Project No. 277974659. L.H. acknowledges support from the Studienstiftung des deutschen Volkes.

---

[1] K. G. Wilson, Confinement of quarks, Phys. Rev. D **10**, 2445 (1974).
[2] F. J. Wegner, Duality in generalized ising models and phase transitions without local order parameters, J. Math. Phys. **12**, 2259 (1971).
[3] E. Fradkin and L. Susskind, Order and disorder in gauge systems and magnets, Phys. Rev. D **17**, 2637 (1978).
[4] J. B. Kogut, An introduction to lattice gauge theory and spin systems, Rev. Mod. Phys. **51**, 659 (1979).
[5] P. E. Lammert, D. S. Rokhsar, and J. Toner, Topology and nematic ordering, Phys. Rev. Lett. **70**, 1650 (1993).
[6] E. Fradkin and S. H. Shenker, Phase diagrams of lattice gauge theories with Higgs fields, Phys. Rev. D **19**, 3682 (1979).
[7] X.-G. Wen, *Quantum Field Theory of Many-Body Systems: From the Origin of Sound to an Origin of Light and Electrons* (Oxford University Press, Oxford, 2007), p. 520.
[8] R. Verresen, U. Borla, A. Vishwanath, S. Moroz, and R. Thorngren, Higgs condensates are symmetry-protected topological phases: I. Discrete symmetries, arXiv:2211.01376.
[9] N. Read and S. Sachdev, Large-N expansion for frustrated quantum antiferromagnets, Phys. Rev. Lett. **66**, 1773 (1991).
[10] S. Sachdev, Topological order, emergent gauge fields, and Fermi surface reconstruction, Rep. Prog. Phys. **82**, 014001 (2019).
[11] A. Kitaev, Fault-tolerant quantum computation by anyons, Ann. Phys. (NY) **303**, 2 (2003).
[12] U.-J. Wiese, Ultracold quantum gases and lattice systems: Quantum simulation of lattice gauge theories, Ann. Phys. (NY) **525**, 777 (2013).
[13] J. C. Halimeh, M. Aidelsburger, F. Grusdt, P. Hauke, and B. Yang, Cold-atom quantum simulators of gauge theories, arXiv:2310.12201.
[14] K. Fredenhagen and M. Marcu, Charged states in $\mathbb{Z}_2$ gauge theories, Commun. Math. Phys. **92**, 81 (1983).
[15] K. Fredenhagen and M. Marcu, Confinement criterion for QCD with dynamical quarks, Phys. Rev. Lett. **56**, 223 (1986).
[16] K. Fredenhagen and M. Marcu, Dual interpretation of order parameters for lattice gauge theories with matter fields, Nucl. Phys. B **4**, 352 (1988).
[17] K. Gregor, D. A. Huse, R. Moessner, and S. L. Sondhi, Diagnosing deconfinement and topological order, New J. Phys. **13**, 025009 (2011).
[18] See Supplemental Material at http://link.aps.org/supplemental/10.1103/PhysRevB.110.L241101 for details on the Monte Carlo simulations.
[19] W.-T. Xu, F. Pollmann, and M. Knap, Critical behavior of Fredenhagen-Marcu string order parameters at topological phase transitions with emergent higher-form symmetries, arXiv:2402.00127.

[20] G. Semeghini, H. Levine, A. Keesling, S. Ebadi, T. T. Wang, D. Bluvstein, R. Verresen, H. Pichler, M. Kalinowski, R. Samajdar, A. Omran, S. Sachdev, A. Vishwanath, M. Greiner, V. Vuletić, and M. D. Lukin, Probing topological spin liquids on a programmable quantum simulator, Science **374**, 1242 (2021).

[21] R. Verresen, M. D. Lukin, and A. Vishwanath, Prediction of toric code topological order from rydberg blockade, Phys. Rev. X **11**, 031005 (2021).

[22] W.-Y. Zhang, Y. Liu, Y. Cheng, M.-G. He, H.-Y. Wang, T.-Y. Wang, Z.-H. Zhu, G.-X. Su, Z.-Y. Zhou, Y.-G. Zheng, H. Sun, B. Yang, P. Hauke, W. Zheng, J. C. Halimeh, Z.-S. Yuan, and J.-W. Pan, Observation of microscopic confinement dynamics by a tunable topological θ-angle, arXiv:2306.11794.

[23] E. Zohar, A. Farace, B. Reznik, and J. I. Cirac, Digital quantum simulation of $\mathbb{Z}_2$ lattice gauge theories with dynamical fermionic matter, Phys. Rev. Lett. **118**, 070501 (2017).

[24] L. Barbiero, C. Schweizer, M. Aidelsburger, E. Demler, N. Goldman, and F. Grusdt, Coupling ultracold matter to dynamical gauge fields in optical lattices: From flux attachment to $\mathbb{Z}_2$ lattice gauge theories, Sci. Adv. **5**, eaav7444 (2019).

[25] C. Schweizer, F. Grusdt, M. Berngruber, L. Barbiero, E. Demler, N. Goldman, I. Bloch, and M. Aidelsburger, Floquet approach to $\mathbb{Z}_2$ lattice gauge theories with ultracold atoms in optical lattices, Nature Phys. **15**, 1168 (2019).

[26] L. Homeier, C. Schweizer, M. Aidelsburger, A. Fedorov, and F. Grusdt, $\mathbb{Z}_2$ lattice gauge theories and kitaev's toric code: A scheme for analog quantum simulation, Phys. Rev. B **104**, 085138 (2021).

[27] L. Homeier, A. Bohrdt, S. Linsel, E. Demler, J. C. Halimeh, and F. Grusdt, Realistic scheme for quantum simulation of $\mathbb{Z}_2$ lattice gauge theories with dynamical matter in (2 + 1)D, Commun. Phys. **6**, 127 (2023).

[28] J. Mildenberger, W. Mruczkiewicz, J. C. Halimeh, Z. Jiang, and P. Hauke, Probing confinement in a $\mathbb{Z}_2$ lattice gauge theory on a quantum computer, arXiv:2203.08905.

[29] J. W. Essam, Percolation theory, Rep. Prog. Phys. **43**, 833 (1980).

[30] S. R. Broadbent and J. M. Hammersley, Percolation processes: I. crystals and mazes, Math. Proc. Cambridge Philos. Soc. **53**, 629 (1957).

[31] G. R. Grimmett, *The Random-Cluster Model* (Springer, Berlin, 2006).

[32] R. J. Baxter, *Exactly Solved Models in Statistical Mechanics* (Academic Press, New York, 1982).

[33] M. Stern, C. Castelnovo, R. Moessner, V. Oganesyan, and S. Gopalakrishnan, Quantum percolation of monopole paths and the response of quantum spin ice, Phys. Rev. B **104**, 115114 (2021).

[34] M. B. Hastings, G. H. Watson, and R. G. Melko, Self-correcting quantum memories beyond the percolation threshold, Phys. Rev. Lett. **112**, 070501 (2014).

[35] F. Gliozzi, S. Lottini, M. Panero, and A. Rago, Random percolation as a gauge theory, Nucl. Phys. B **719**, 255 (2005).

[36] M. F. Sykes and J. W. Essam, Critical percolation probabilities by series methods, Phys. Rev. **133**, A310 (1964).

[37] L. Hahn, A. Bohrdt, and F. Grusdt, Dynamical signatures of thermal spin-charge deconfinement in the doped ising model, Phys. Rev. B **105**, L241113 (2022).

[38] C.-J. Huang, L. Liu, Y. Jiang, and Y. Deng, Worm-algorithm-type simulation of the quantum transverse-field ising model, Phys. Rev. B **102**, 094101 (2020).

[39] X. Feng, Y. Deng, and H. W. J. Blöte, Percolation transitions in two dimensions, Phys. Rev. E **78**, 031136 (2008).

[40] D. Banerjee, E. Huffman, and L. Rammelmüller, Exploring bosonic and fermionic link models on $(3+1)$D tubes, Phys. Rev. Res. **4**, 033174 (2022).

[41] L. Onsager, Crystal statistics. I. A two-dimensional model with an order-disorder transition, Phys. Rev. **65**, 117 (1944).

[42] S. Trebst, P. Werner, M. Troyer, K. Shtengel, and C. Nayak, Breakdown of a topological phase: Quantum phase transition in a loop gas model with tension, Phys. Rev. Lett. **98**, 070602 (2007).

[43] Z. Nussinov, Derivation of the fradkin-shenker result from duality: Links to spin systems in external magnetic fields and percolation crossovers, Phys. Rev. D **72**, 054509 (2005).

[44] H. Kesten, The critical probability of bond percolation on the square lattice equals $1/2$, Commun. Math. Phys. **74**, 41 (1980).

[45] F. Wu, Y. Deng, and N. Prokof'ev, Phase diagram of the toric code model in a parallel magnetic field, Phys. Rev. B **85**, 195104 (2012).

[46] M. Matsumoto and T. Nishimura, Mersenne twister: A 623-dimensionally equidistributed uniform pseudo-random number generator, ACM Trans. Model. Comput. Simul. **8**, 3 (1998).

[47] S. Even, *Graph Algorithms*, 2nd ed., edited by G. Even (Cambridge University Press, Cambridge, 2011).

[48] A. W. Sandvik and J. Kurkijärvi, Quantum monte carlo simulation method for spin systems, Phys. Rev. B **43**, 5950 (1991).

[49] M. E. J. Newman and G. T. Barkema, *Monte Carlo Methods in Statistical Physics* (Oxford University Press, Oxford, 1999).

[50] K. Binder and D. W. Heermann, *Monte Carlo Simulation in Statistical Physics* (Springer, Berlin, 2010).

[51] F. J. Wegner, Duality in generalized Ising models, arXiv:1411.5815.

[52] M. S. L. du Croo de Jongh and J. M. J. van Leeuwen, Critical behavior of the two-dimensional ising model in a transverse field: A density-matrix renormalization calculation, Phys. Rev. B **57**, 8494 (1998).

[53] H. W. J. Blöte and Y. Deng, Cluster monte carlo simulation of the transverse ising model, Phys. Rev. E **66**, 066110 (2002).

[54] R. Lyons, Random walks and percolation on trees, Ann. Probab. **18**, 931 (1990).

[55] A. Banerjee, D. Banerjee, G. Kanwar, A. Mariani, T. Rindlisbacher, and U.-J. Wiese, Broken symmetry and fractionalized flux strings in a staggered $u(1)$ pure gauge theory, Phys. Rev. D **109**, 014506 (2024).

[56] D. Banerjee, F.-J. Jiang, P. Widmer, and U.-J. Wiese, The (2 + 1)-D U(1) quantum link model masquerading as deconfined criticality, J. Stat. Mech. (2013) P12010.

[57] T. Botzung, M. Buchhold, S. Diehl, and M. Müller, Robustness and measurement-induced percolation of the surface code, arXiv:2311.14338.

[58] M. Kebrič, L. Barbiero, C. Reinmoser, U. Schollwöck, and F. Grusdt, Confinement and mott transitions of dynamical charges in one-dimensional lattice gauge theories, Phys. Rev. Lett. **127**, 167203 (2021).

[59] M. Kebrič, J. C. Halimeh, U. Schollwöck, and F. Grusdt, Confinement in (1+1)-dimensional $\mathbb{Z}_2$ lattice gauge theories at finite temperature, Phys. Rev. B **109**, 245110 (2024).

Supplemental Material: Percolation as a confinement order parameter in $\mathbb{Z}_2$ lattice gauge theories

Simon M. Linsel,[1, 2, *] Annabelle Bohrdt,[2, 3] Lukas Homeier,[1, 2] Lode Pollet,[1, 2] and Fabian Grusdt[1, 2, †]
[1]*Department of Physics and Arnold Sommerfeld Center for Theoretical Physics (ASC),*
Ludwig-Maximilians-Universität München, Theresienstr. 37, München D-80333, Germany
[2]*Munich Center for Quantum Science and Technology (MCQST), Schellingstr. 4, D-80799 München, Germany*
[3]*Institute of Theoretical Physics, University of Regensburg, D-93053, Germany*

(Dated: November 25, 2024)

I. CLASSICAL MONTE CARLO SAMPLING

Here we present the numerical details of the classical MC sampling and related algorithms used to obtain snapshots, from which the observables for characterizing percolation are evaluated.

A. Canonical Monte Carlo Sampling

We simulate the classical Hamiltonian (2)

$$\hat{\mathcal{H}}_{\text{can}} = -h \sum_{l} \hat{\tau}_l^x$$

on the square and the cubic lattice. Since we consider a canonical ensemble, we fix the number of matter particles $N = \sum_{\boldsymbol{j}} \hat{n}_{\boldsymbol{j}}$, with $(-1)^{\hat{n}_{\boldsymbol{j}}} = \prod_{l \in +_{\boldsymbol{j}}} \hat{\tau}_l^x$, in the system and all chemical potential terms are irrelevant. The size of the lattice determines the matter density resolution that can be achieved.

The MC simulations are implemented in C++ using the Boost C++ libraries. The lattice is represented by a graph. To generate (pseudo-)random numbers, we use the Mersenne Twister [46]. For I/O operations, multiprocessing and postprocessing, we use Python (NumPy, SciPy, Python multiprocessing, Matplotlib, h5py).

At the beginning of each simulation, we initialize the system in a state with the desired number of matter particles that fulfills Gauss's law. Matter particles can only be put into the system in pairs since Gauss's law would otherwise not be fulfilled. This is easily achieved by initializing matter in pairs connected by one string ("dimers"). We then start the thermalization by repeatedly applying MC updates to this state.

A naive way to perform an MC update would be to choose a random matter particle and try to move it to a random nearest neighbor (NN) while flipping the electric field between the old site and the target site if the move is accepted to account for Gauss's law. If the target lattice site is already occupied, the move would be rejected because of the hard-core constraint. Because choosing any matter particle and any NN is equally likely (disregarding boundary effects), detailed balance would be trivially fulfilled. However, this approach becomes inefficient for large matter density, as a random matter particle is unlikely to be movable to *any* NN (see Fig. S1a). Moreover, even if a matter particle is movable, it may be only movable to one NN which makes it highly likely that the move is rejected because of the randomness of the NNs in the trial probability distribution (TPD), see Eq. (S1). For this reason, the naive approach is not suitable for studying systems with a high matter density.

A better approach takes into account 1) only movable matter particles (i.e. matter with at least one unoccupied NN) and 2) only directions where no other matter particle is sitting. Hence, a move is never rejected because of the hard-core constraint (although it may be rejected because of the acceptance probability). This approach is orders of magnitude more efficient than the naive way, but it comes at the cost of a more complicated procedure to fulfill detailed balance.

Firstly, the number of movable matter particles can change after a move (illustrated in Fig. S1a), which makes the TPD asymmetric. Secondly, the number of empty NNs of one given matter particle can change when it moves

---

[*] simon.linsel@physik.uni-muenchen.de

[†] fabian.grusdt@physik.uni-muenchen.de

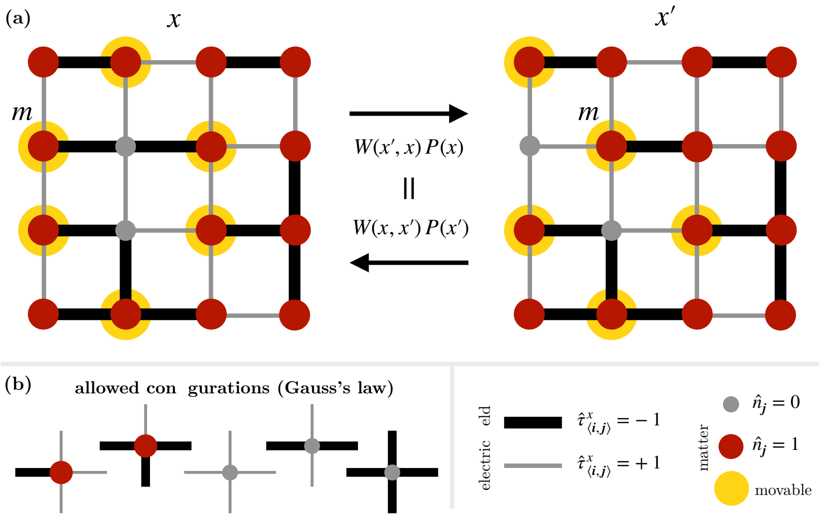

FIG. S1. **Ergodicity condition in canonical sampling.** **(a)** We plot exemplary Metropolis-Hastings updates of a matter excitation m moving between states x and x'. The Boltzmann distribution $P(x)$ and the transition rate $W(x', x)$ from x to x' must fulfill the detailed balance condition $W(x', x)P(x) = W(x, x')P(x')$ to represent a physical state in equilibrium. Hence, the number of unoccupied NN of m and the total number of movable matter particles (marked in yellow) have to be included in the acceptance probability (see Eq. (S2)). **(b)** We illustrate the constraints introduced by Gauss's law. Adapted from [27].

(illustrated in Fig. S1a), which again makes the TPD asymmetric. Hence, we need the Metropolis-Hastings algorithm and the simpler Metropolis algorithm is *not* suited.

Let us suppose we propose a move of a matter particle h from state x to x'. The TPD of this move is given by

$$T(x' \,|\, x) = \frac{1}{\#(\text{movable matter at}\, x)} \times \frac{1}{\#(\text{NNs of matter}\, h\, \text{at}\, x)} \tag{S1}$$

while the TPD for a move from x' to x is given by

$$T(x \,|\, x') = \frac{1}{\#(\text{movable matter at}\, x')} \times \frac{1}{\#(\text{NNs of matter}\, h\, \text{at}\, x')}.$$

Hence, the Metropolis-Hastings acceptance probability reads

$$\begin{aligned} A(x', x) &= \min\left(1, \frac{e^{-\beta E(x')}}{e^{-\beta E(x)}} \frac{T(x \,|\, x')}{T(x' \,|\, x)}\right) \\ &= \min\left(1, \frac{e^{-\beta E(x')}}{e^{-\beta E(x)}} \times \frac{\#(\text{NNs of matter}\, h\, \text{at}\, x)}{\#(\text{NNs of matter}\, h\, \text{at}\, x')} \times \frac{\#(\text{movable matter at}\, x)}{\#(\text{movable matter at}\, x')}\right). \end{aligned} \tag{S2}$$

For efficiency reasons, we store the "movability" of every matter particle and update this information after every successful move update. Only matter particles in the neighborhood of the move update must get a movability check, otherwise, there would be no point in storing the information altogether.

If we only used the move update, we would face two problems: 1) It does not work for the cases where we have no matter or every lattice site is occupied by a matter particle (density $d = 1$), since in both cases no matter particle is movable, and 2) it can be slow for high temperatures since only one string is created (or removed) for every

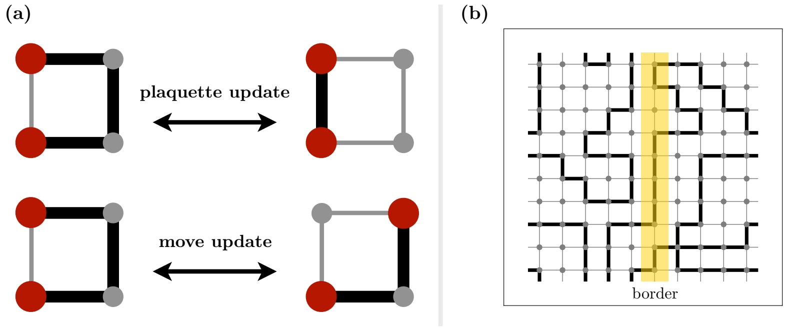

FIG. S2. **MC updates and percolation detection. (a)** We show the update procedures for the Metropolis-Hastings sampling on the square lattice. A plaquette update flips all electric fields in a plaquette. In a move update, a matter particle moves to an unoccupied lattice site and flips the electric field along its way. All updates conserve the number of matter particles and Gauss's law. **(b)** We sketch the algorithm to detect percolation in x-direction (horizontal). The algorithm tries to find a path that winds around the lattice while only traversing strings. In this example, the strings percolate. When crossing the border, sites get assigned a higher/lower winding number, see Alg. 1. Adapted from [27].

successful MC update. For this reason, we introduce plaquette updates (see Fig. S2a), which flip all electric fields in an elementary plaquette. Plaquette updates can create string clusters up to the size of the plaquette and thus speed up the simulations for high temperatures, where higher excited states with more strings are more likely. In the TPD, every elementary plaquette is equally likely to be tried. Hence, we have a symmetric TPD and Metropolis sampling is sufficient. In every MC update, there is a 50% chance to propose either a plaquette update or a move update (except at zero or maximal matter density, where we only use plaquette updates).

We thermalize the system with $100 \times L^2$ MC updates and perform $2 \times L^2$ MC updates between samples, see Fig. S3. We confirmed that the system is thermalized and the autocorrelation is low enough for every simulated parameter set. We take the autocorrelation between snapshots into account for every error bar.

For each sample, we measure the percolation probability, the percolation strength, the largest string cluster and the total number of strings in the system. For the case where we put only two matter particles into the system, we additionally measure the distance between those two matter particles.

The algorithm to measure the percolation probability/strength in a system with periodic boundaries is presented in Alg. 1. The algorithm tries to find a path that winds around the system in at least one dimension, i.e. one can traverse the strings only visiting every string once and come back to the orginal lattice site while winding around the system at least once. In more technical terms, the algorithm starts a depth-first search from lattice sites in the starting point list S while only traversing links that are strings. We assign a winding number to every vertex which changes when crossing over a cut through the system (in one dimension). When vertices with two distinct winding numbers (e.g. 0 and 1) "meet", the system is percolating in this specific dimension, since the path connecting the two vertices winds around the system and was thus assigned a different winding number. In the case of two or more dimensions, the percolation search is repeated for every dimension. The system is percolating when it is percolating in at least one dimension.

We use periodic systems only because the conventional percolation definition for open boundaries has an error that scales as $\mathcal{O}(1/L)$ in comparison to this definition where the error scales as $\mathcal{O}(1/L^2)$. This greatly improves the finite-size scaling.

Since the percolation search is repeated many times (a typical number of samples is $\sim 10^5$) and we want to simulate as large systems as possible, the algorithm must be designed efficiently. In principle, a new depth-first search (see e.g. [47]) is performed for every starting point. Thus, the complexity would be $\mathcal{O}(D \times L^{D-1} \times L^D)$ since for every dimension we have $\mathcal{O}(L^{D-1})$ starting points from which we would start a depth-first search with complexity $\mathcal{O}(L^D)$. In practice, we can heavily reduce the complexity by storing visited lattice sites. In case we visit such a lattice site, the search stops. If we detect percolation, the search also stops.

For measuring the largest string cluster, we use a built-in function of the Boost C++ library that clusters the graph

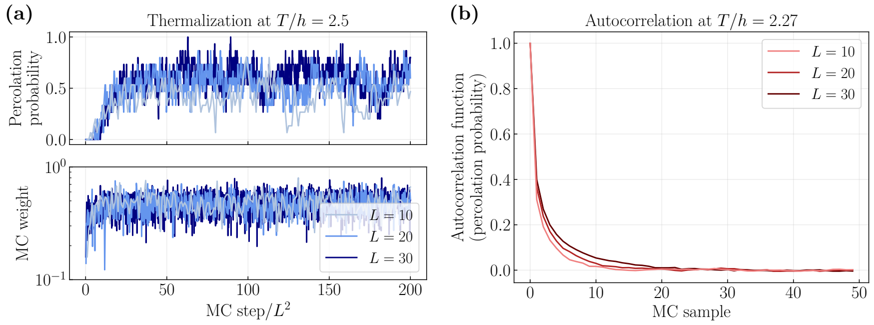

FIG. S3. **MC thermalization & autocorrelation.** We show results for MC simulations of Hamiltonian (2) for exactly two matter excitations on the square lattice. **(a)** We show the thermalization of the percolation probability (top) and the MC weights averaged over 15 runs (bottom) at $T/h = 2.5$, i.e. slightly above the phase transition in the percolating phase. For clarity reasons, we only show every 100th measurement. We have confirmed that in our simulations the system thermalizes after $200 \times L^2$ steps for all T/h. **(b)** We show the autocorrelation of the percolation probability at $T/h = 2.27$, i.e. approximately at the phase transition. We plot the average over 15 runs with 10^4 samples, respectively. Between each sample, we perform $2 \times L^2$ steps. We find only small autocorrelation between samples.

into its connected components only considering strings based on a depth-first search approach.

B. Grand Canonical Monte Carlo Sampling

We simulate the classical Hamiltonian (3)

$$\hat{\mathcal{H}}_{\mathrm{gc}} = -h \sum_{l} \hat{\tau}^x_l - \mu \sum_{\boldsymbol{j}} \hat{n}_{\boldsymbol{j}}$$

on the square and the cubic lattice. Since we are in a grand canonical ensemble, we fix the chemical potential μ in the system. The size of the lattice determines the matter density resolution that can be achieved by tuning the chemical potential.

Since we fix the gauge sector to $g_{\boldsymbol{j}} = +1$ and we only consider hard-core bosons, we can rewrite $\hat{n}_{\boldsymbol{j}}$ in terms of electric fields $\hat{\tau}^x_{\langle \boldsymbol{i},\boldsymbol{j}\rangle}$. For hard-core bosons, we have

$$\hat{n}_{\boldsymbol{j}} = \frac{1}{2}\left(1 - (-1)^{\hat{n}_{\boldsymbol{j}}}\right). \tag{S3}$$

Plugging in Gauss's law yields

$$\hat{n}_{\boldsymbol{j}} = \frac{1}{2}\left(1 - \prod_{l \in +_{\boldsymbol{j}}} \hat{\tau}^x_l\right). \tag{S4}$$

Finally, the grand canonical Hamiltonian reads

$$\hat{\mathcal{H}}_{\mathrm{gc}} = -h \sum_{l} \hat{\tau}^x_l - \mu \sum_{\boldsymbol{j}} \frac{1}{2}\left(1 - \prod_{l \in +_{\boldsymbol{j}}} \hat{\tau}^x_l\right). \tag{S5}$$

To compare canonical results with matter particle number N to grand canonical results, we have to tune μ and β such that

$$N = \sum_{\boldsymbol{j}} \frac{1}{2}\left(1 - \left\langle \prod_{l \in +_{\boldsymbol{j}}} \hat{\tau}^x_l \right\rangle\right). \tag{S6}$$

Algorithm 1 Percolation detection (x-direction).

Input: Graph representation of lattice with adjacency list Adj, starting point list S, x-coordinate list x, x-value x_{cut} which separates the system

Output: Percolation boolean (true ≡ percolating; false ≡ non-percolating)

```
function IsPercolating($Adj, S, E$)
    discovered ← {false}                                        ▷ No vertex is discovered in the beginning
    for $v_s \in S$ do
        winding_number_storage ← {INT_MAX}
        v_stack ← {}
        winding_number_stack ← {}
        top ← 0
        v_stack[top] ← $v_s$                                    ▷ Starting point of search
        winding_number_stack[top] ← 0
        while top $\geq 0$ do
            $v_{\text{top}}$ ← v_stack[top]
            $w_{\text{top}}$ ← winding_number_stack[top]
            top ← top $- 1$
            if discovered[$v_{\text{top}}$] = true then
                Continue with next iteration                    ▷ Abandon search
            end if
            discovered[$v_{\text{top}}$] ← true
            winding_number_storage[$v_{\text{top}}$] ← $w_{\text{top}}$
            for $v_{\text{n}} \in Adj[v_{\text{top}}]$ do
                if string between $v_{\text{top}}$ and $v_{\text{n}}$ then
                    $w_{\text{new}} \leftarrow w_{\text{top}}$
                    if $x[v_{\text{n}}] > x_{\text{cut}}$ and $x[v_{\text{top}}] = x_{\text{cut}}$ then
                        $w_{\text{new}} \leftarrow w_{\text{top}} + 1$
                    else if $x[v_{\text{top}}] > x_{\text{cut}}$ and $x[v_{\text{n}}] = x_{\text{cut}}$ then
                        $w_{\text{new}} \leftarrow w_{\text{top}} - 1$
                    end if
                    if discovered[$v_{\text{n}}$] = false then
                        top ← top $+ 1$
                        v_stack[top] ← $v_{\text{n}}$
                        winding_number_stack[top] ← $w_{\text{new}}$
                    else if winding_number_storage[$v_{\text{n}}$] $\neq w_{\text{new}}$ then
                        return true                             ▷ Algorithm has found percolating string cluster
                    end if
                end if
            end for
        end while
    end for
    return false                                                ▷ Algorithm has not found percolating string cluster
end function
```

Hamiltonian (S5) does only depend on the electric field configuration $\{\hat{\tau}_l^x\}$ and is a generalized Ising model with four-spin-interactions $\propto \mu$ in a longitudinal magnetic field.

The procedure for an MC update is much simpler than in the canonical case. In the first update procedure (which can change the number of matter particles), a random link is chosen and we propose a flip to that link. If the move is accepted, the electric field on the link is flipped and the matter particle numbers at the neighboring lattice sites are updated to satisfy Gauss's law. As the canonical plaquette update does not change the number of matter particles, it can be used here as well. Neither of the two updates has asymmetric TPDs and thus we can use Metropolis sampling. In every MC update, there is a 50% chance to propose either a plaquette update or an electric field flip update.

We thermalize the system with $500 \times L^2$ MC updates and perform $5 \times L^2$ MC updates between samples. We confirmed that the system is thermalized and the autocorrelation is low enough for every simulated parameter set. We take the autocorrelation between snapshots into account for every error bar.

As in the canonical case, we measure the percolation probability, the percolation strength, the largest string cluster and the total number of strings in the system for each sample. We use the same algorithms as in the canonical case.

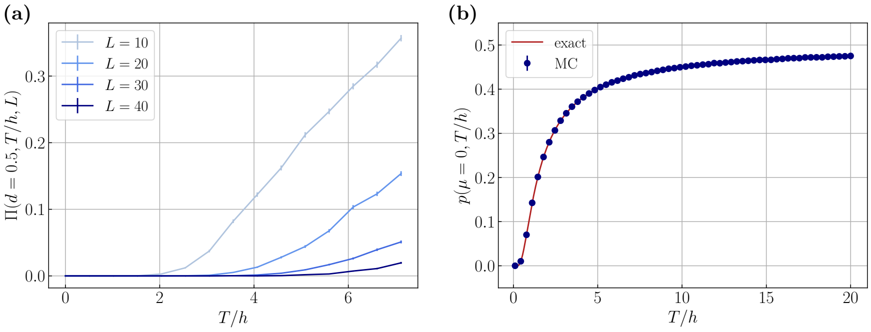

FIG. S4. **Finite-density regime.** We demonstrate the non-existence of thermal deconfinement at non-zero matter density. **(a)** We show results for Hamiltonian (2) at density $d = 0.5$. For increasing system size, the percolation probability Π decreases in magnitude and the first non-zero shifts to higher temperatures T/h. **(b)** We show results for Hamiltonian (3) at $\mu = 0$. The error bars are too small to be visible. With increasing T/h, the probability p for a bond to host a string approaches the percolation threshold $p_{\text{c,square}} = 0.5$ from below confirming the exact result $p = e^{-\beta h}/2\cosh(\beta h)$. Because the percolation threshold is only reached at $T/h \to \infty$, non-zero percolation at $\mu = 0$ in finite systems is only a finite-size effect and there is no thermal deconfinement phase transition.

II. (QUANTUM) MONTE CARLO RESULTS

Here we provide supplementary results supporting the claims in the main part of the paper, and details on the procedure used to extract the critical exponents.

A. Classical finite-density regime on the square lattice

We simulate Hamiltonian (2) at non-zero matter density $d = 0.5$ for $L^2 = 10^2, 20^2, 30^2, 40^2$ and show the percolation probability $\Pi(T)$ in Fig. S4a. While Π is non-zero at high temperatures for every simulated finite-size system, we observe a decrease in Π with increasing system size.

At $\mu = 0$, the electric fields are completely independent and the probability p for a bond to host a string is given by $p = e^{-\beta h}/2\cosh(\beta h)$, i.e. the percolation threshold $p_{\text{c,square}} = 0.5$ is never reached for finite temperatures. We simulate Hamiltonian (3) at $\mu = 0$ and show $p(T/h)$ as a function of temperature T/h in Fig. S4b. p approaches 0.5 from below for $T/h \to \infty$. Hence, we proved that a thermal deconfinement phase transition cannot exist for finite T/h at $\mu = 0$. We conjecture the absence of a phase transition for every non-zero matter density, as indicated by our numerical simulations; we performed T-sweeps for $d = 0.1, 0.2, ..., 1.0$ and find the same qualitative behavior as in Fig. S4a for all simulated densities.

B. Extended toric code QMC

We simulate Hamiltonian (8) on a periodic square lattice using an adaption of the continuous-time QMC algorithm from Wu *et al.* [45]. Unless explicitly stated otherwise, we sample snapshots from equal-imaginary-time-slices in the $\hat{\tau}^x$-basis. We set $\mu = J = 1$. Observables that are diagonal in the $\hat{\tau}^x$-basis can be directly sampled from snapshots analogous to the classical model. Non-diagonal observables cannot be directly extracted from snapshots and are calculated by averaging over the imaginary time (i.e. computing moments of a Poisson process):

$$\lambda\langle\hat{\tau}_l^z\rangle = \langle N_l\rangle/\beta, \tag{S7}$$

$$J\Big\langle\prod_{l\in\square}\hat{\tau}_l^z\Big\rangle = \langle N_\square\rangle/\beta. \tag{S8}$$

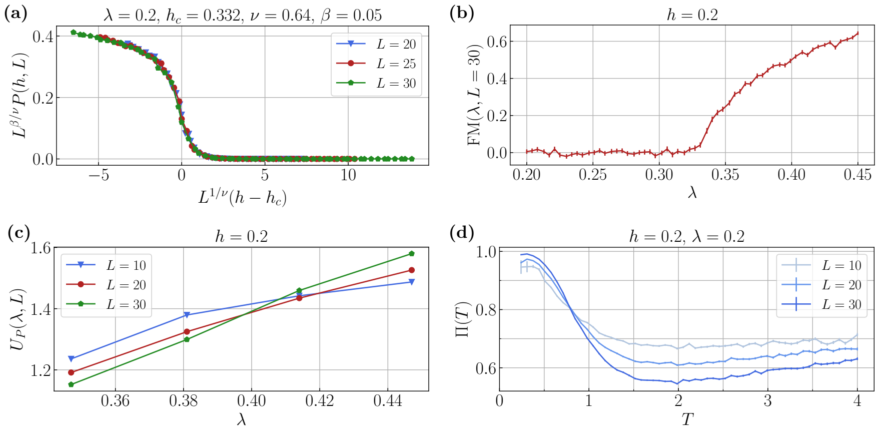

FIG. S5. **QMC finite-size scaling.** We show results for the POPs in the square lattice toric code Hamiltonian (8). **(a)** We present the finite-size data collapse of the percolation strength P for $\lambda = 0.2$. The curves collapse into a well-defined scaling function. **(b)** We present the Fredenhagen-Marcu order parameter $\mathrm{FM}(\lambda, L = 30)$ – obtained from QMC simulations in the $\hat{\tau}^z$-basis – for $h = 0.2$, confirming the known phase boundary at $\lambda_c \sim 0.33$. **(c)** We present the percolation strength Binder cumulant $U_P(\lambda)$ for different system sizes. The shift in the crossing points toward lower λ is a clear sign of strong finite-size effects. We conjecture that the crossing points approach the known critical value $\lambda_c \sim 0.33$ in the TDL. **(d)** We present the percolation probability $\Pi(T)$ for different system sizes. At temperatures well above the bulk gap, we observe a clear decrease in Π with higher system sizes. For Bernoulli percolation, Kolmogorov's zero-one-law [54] restricts the percolation probability to either zero or one in the TDL. We conjecture that Π approaches zero in the TDL for any $T > 0$.

Here, N_l ($N_\Box$) is the number of single (plaquette) spin flips in imaginary time on link l (plaquette $\Box$) [48]. For details on the QMC algorithm, we once again refer to Wu *et al.* [45].

h-sweeps.—We set $T = 1/L$, $\lambda = 0, 0.1, 0.2, 0.3$ and $L^2 = 20^2, 25^2, 30^2$. We extract the critical electric field h_c and the critical exponents ν (correlation length ξ) and β (percolation strength P), defined by

$$\xi(L \to \infty) \sim |h - h_c|^{-\nu} \tag{S9}$$

and

$$P(h, L \to \infty) \sim (h - h_c)^{\beta} \sim \xi^{-\beta/\nu}. \tag{S10}$$

For $L \gg \xi$, the relevant length scale is set by the correlation length. For $L \ll \xi$ however, the relevant length scale is L. Thus, we have

$$\begin{aligned} P(h, L) &\sim \begin{cases} L^{-\beta/\nu} & L \ll \xi \\ \xi^{-\beta/\nu} & L \gg \xi \end{cases} \\ &= \xi^{-\beta/\nu} f\left(\frac{L}{\xi}\right), \end{aligned} \tag{S11}$$

where we defined the *scaling function*

$$f\left(\frac{L}{\xi}\right) \sim \begin{cases} \left(\frac{L}{\xi}\right)^{-\beta/\nu} & L \ll \xi \\ \text{const.} & L \gg \xi. \end{cases} \tag{S12}$$

By introducing $\widetilde{f}(\tilde{x}) \equiv \tilde{x}^{\beta} f(\tilde{x}^{\nu}) \Leftrightarrow f(x) = x^{-\beta/\nu} \widetilde{f}(x^{1/\nu})$ [49, 50] we can write

$$\begin{aligned} P(h,L) &= \xi^{-\beta/\nu} f\Big(\frac{L}{\xi}\Big) \\ &= \xi^{-\beta/\nu} (L/\xi)^{-\beta/\nu} \widetilde{f}\big((L/\xi)^{1/\nu}\big) \\ &= L^{-\beta/\nu} \widetilde{f}\big(L^{1/\nu} \xi^{-1/\nu}\big) \\ &= L^{-\beta/\nu} \widetilde{f}\big(L^{1/\nu}(h-h_c)\big) \end{aligned} \tag{S13}$$

or in terms of fields

$$P(h,L) = |h-h_c|^{\beta} \bar{f}\big(L^{1/\nu}(h-h_c)\big). \tag{S14}$$

We first perform a crossing point analysis of the percolation strength Binder cumulant

$$U_P(h,L) = \frac{\langle P^4(h,L)\rangle}{\langle P^2(h,L)\rangle^2} \tag{S15}$$

to extract an estimate for h_c. Close to h_c the Binder cumulant behaves as

$$\begin{aligned} U_P(h,L) &= \frac{L^{-4\beta/\nu} f_{P^4}\big(L^{1/\nu}(h-h_c)\big)}{\Big[L^{-2\beta/\nu} f_{P^2}\big(L^{1/\nu}(h-h_c)\big)\Big]^2} \\ &= f_{U_P}\big(L^{1/\nu}(h-h_c)\big). \end{aligned} \tag{S16}$$

Therefore, the Binder cumulant is dimensionless and does not depend on β. To extract h_c without knowing ν, we note the following: At h_c, the Binder cumulant takes the value

$$U_P(h_c,L) = f_{U_P}(0) \quad \forall L \tag{S17}$$

independent of L. Hence, we expect that the Binder cumulants for different system sizes “cross” at h_c, see Fig. 4a.

We obtain an estimate for ν by manually collapsing finite-size curves using Eq. (S16). Finally, β can be estimated by manually collapsing finite-size curves with the scaling ansatz

$$P(h,L) = L^{-\beta/\nu} f_P\big(L^{1/\nu}(h-h_c)\big), \tag{S18}$$

see Fig. S5a.

Our estimates serve as the starting point for a reduced χ^2 optimization which converged to the final values $h_c = 0.3301(17)$, $\nu = 0.65(27)$ and $\beta = 0.05(4)$ for $\lambda = 0$. The critical exponents are identical for different λ up to statistical errors as expected. We were unable to provide a good estimate of the Fredenhagen-Marcu order parameter in the confined phase for $h > \lambda$ due to high noise in the data.

λ-sweep.—We set $T = 1/L$, $h = 0.2$ and $L^2 = 10^2, 20^2, 30^2$. We find Binder cumulant crossing points around $\lambda \approx 0.4$ that shift toward lower λ with increasing system size, see Fig. S5c. The gap consists of the bulk gap Δ_{B} and the finite-size gap Δ_L. Because of the self-duality, we know that the true phase transition where the gap closes is at $\lambda_c \sim 0.33$. However, in finite-size systems (i) the gap never completely closes and (ii) the finite-size ground state can *appear* topological because of the finite-size gap. We conjecture that the true critical value of $\lambda_c \sim 0.33$ is reached in the TDL and the strong finite-size effects are caused by a large finite-size gap. In Fig. S5b, we show the Fredenhagen-Marcu order parameter

$$\mathrm{FM} = \frac{\prod_{l\in\mathcal{C}_{1/2}} \hat{\tau}^z_l}{\prod_{l\in\mathcal{C}} \hat{\tau}^z_l}, \tag{S19}$$

where $\mathcal{C}$ is a closed contour of links with length $\sim L$ at equal imaginary time and $\mathcal{C}_{1/2}$ contains half the links of $\mathcal{C}$ and thus forms an open contour. FM was calculated using QMC snapshots in the $\hat{\tau}^z$-basis and confirms the known critical value $\lambda_c \sim 0.33$.

T-sweep.—We set $h = \lambda = 0.2$ and $L^2 = 10^2, 20^2, 30^2$. We find a crossing-point in the percolation strength Binder cumulant at $T > 0$ and a percolating phase extending into $T > 0$, see Fig. S5d. However, the topological order is known to break down for $T > 0$. We trace this behavior back to the bulk gap Δ_{B}. For $T < \Delta_{\mathrm{B}}$ the density of thermal excitations is non-zero in the TDL, however, it is exponentially suppressed and thus not visible in finite-size systems. After all, this is the reason why we can gain insights into the ground state using finite-T QMC schemes. While the true ground state for $T > 0$ is not topological, it *appears* like the topological ground state at $T = 0$ in finite-size systems. This reasoning is supported by the estimated order-of-magnitude of the bulk gap $\Delta_{\mathrm{B}} \simeq J$ at $h = \lambda = 0.2$ which matches the temperature scale below which we observe the percolating (deconfined) ground state features. We were unable to provide a good estimate of the Fredenhagen-Marcu order parameter for finite temperatures due to high noise in the data.

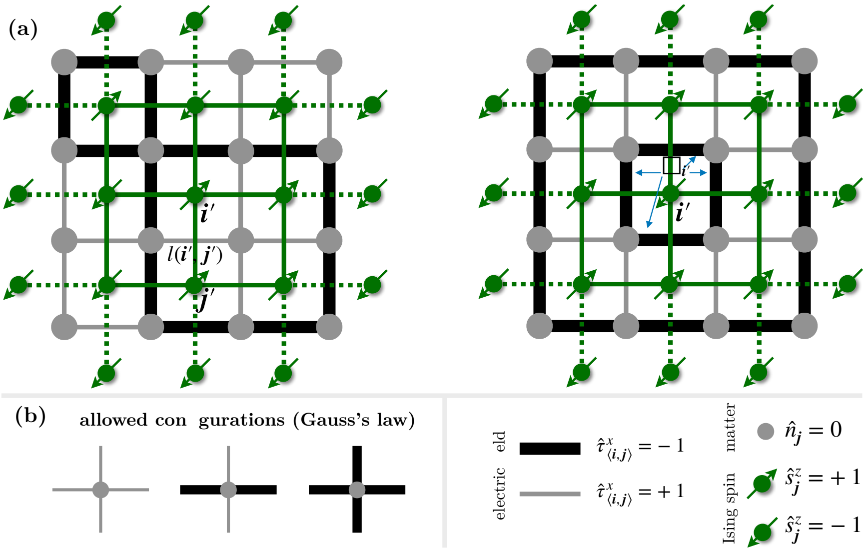

FIG. S6. **Ising mapping of the pure gauge model.** We illustrate the mapping of the pure gauge model Hamiltonian (S20) to the TFIM on the dual lattice. **(a)** We show two configurations of electric strings and the corresponding spin configuration on the dual lattice. The electric strings form closed loops. The electric field on a link l depends on the dual lattice link between $\boldsymbol{i}'$ and $\boldsymbol{j}'$ that intersects l. By flipping a spin on a dual lattice site $\boldsymbol{j}'$, all electric fields in the surrounding plaquette $\square_{\boldsymbol{j}'}$ are flipped. A percolating string cluster corresponds to a domain wall of spins since closed string loops necessarily have spins of the same orientation along their perimeter. Due to Gauss's law, the star term $\propto \mu$ is constant, see **(b)**. Adapted from [51].

III. MAPPING THE PURE GAUGE THEORY TO THE 2D TRANSVERSE-FIELD ISING MODEL

Here we concisely motivate the mapping of the pure gauge extended toric code Hamiltonian (8), where $\lambda = 0$ (i.e. without matter), to the 2D transverse-field Ising model (TFIM) [2]. The starting point is the pure gauge model

$$\hat{\mathcal{H}} = -\mu \sum_{+} \prod_{l\in +} \hat{\tau}^x_l - J \sum_{\square} \prod_{l\in\square} \hat{\tau}^z_l - h \sum_l \hat{\tau}^x_l \,. \tag{S20}$$

Since we have no matter, the $\mathbb{Z}_2$ electric strings can only form closed loops. If we define Ising spins $\hat{s}^z \in \{\pm 1\}$ on the dual lattice sites, a string loop on an elementary plaquette can be thought of as one spin with $\hat{s}^z = +1$ in a background of spins with $\hat{s}^z = -1$. The operator $\hat{s}^x$ flips the spin $\hat{s}^z$ in the dual lattice and thus the electric fields on the surrounding plaquette in the LGT: it creates/destroys string loops. This intuition can be formalized with the definition of the dual-lattice site variables:

$$\hat{s}^z_{\boldsymbol{i}'} \hat{s}^z_{\boldsymbol{j}'} = \hat{\tau}^x_{l(\boldsymbol{i}',\boldsymbol{j}')}, \tag{S21}$$

$$\hat{s}^x_{\boldsymbol{j}'} = \prod_{l\in\square_{\boldsymbol{j}'}} \hat{\tau}^z_l, \tag{S22}$$

where $l(\boldsymbol{i}', \boldsymbol{j}')$ is the link that intersects with the dual link between dual lattice sites $\boldsymbol{i}', \boldsymbol{j}'$ and $\square_{\boldsymbol{j}'}$ is the plaquette of links surrounding the dual lattice site $\boldsymbol{j}'$, see Fig. S6a. Plugging into Hamiltonian (S20) yields the TFIM:

$$\hat{\mathcal{H}}'_{\mathrm{TFIM}} = -h \sum_{\langle \boldsymbol{i}',\boldsymbol{j}'\rangle} \hat{s}^z_{\boldsymbol{i}'} \hat{s}^z_{\boldsymbol{j}'} - J \sum_{\boldsymbol{i}'} \hat{s}^x_{\boldsymbol{i}'}. \tag{S23}$$

The star term $\propto \mu$ vanishes due to Gauss's law, see Fig. S6b. The square lattice TFIM has a quantum critical point at $(h/J)_c \approx 1/3.044 \approx 0.33$ [52, 53] (3D Ising universality) and a critical temperature $(T/h)_c = 2/\log(1+\sqrt{2}) \approx 2.27$ [41] (2D Ising universality). We identify the (non-)percolating phase of the extended toric code with the unmagnetized (magnetized) phase of the TFIM. Percolating strings in the deconfined phase correspond to domain walls in the paramagnetic phase in the dual TFIM since closed string loops necessarily have spins of the same orientation along their perimeter.

2.9 Publication 3: Percolation renormalization group analysis of confinement in $\mathbb{Z}_2$ lattice gauge theories

In this section, the following publication is reprinted:

P3 *Percolation renormalization group analysis of confinement in* $\mathbb{Z}_2$ *lattice gauge theories*,
Gesa Dünnweber, Simon M. Linsel, Annabelle Bohrdt, and Fabian Grusdt,
Physical Review B **111**, 024314 (2025), ©2025 American Physical Society,
doi: 10.1103/PhysRevB.111.024314.
Reprinted on pages 73–86.

PHYSICAL REVIEW B **111**, 024314 (2025)

Percolation renormalization group analysis of confinement in $\mathbb{Z}_2$ lattice gauge theories

Gesa Dünnweber,[1,2,3,4] Simon M. Linsel,[1,2,5] Annabelle Bohrdt,[2,6] and Fabian Grusdt[1,2]
[1]*Faculty of Physics, Arnold Sommerfeld Centre for Theoretical Physics (ASC),*
Ludwig-Maximilians-Universität München, Theresienstr. 37, 80333 München, Germany
[2]*Munich Center for Quantum Science and Technology (MCQST), Schellingstr. 4, 80799 München, Germany*
[3]*Department of Physics, TUM School of Natural Sciences, Technical University of Munich, James-Franck-Str. 1, 85748 Garching, Germany*
[4]*Walther-Meißner-Institut, Bayerische Akademie der Wissenschaften, Walther-Meißner-Str. 8, 85748 Garching, Germany*
[5]*Department of Physics, Harvard University, Cambridge, Massachusetts 02138, USA*
[6]*Institute of Theoretical Physics, University of Regensburg, Universitätsstr. 31, 93053 Regensburg, Germany*

(Received 16 July 2024; revised 20 December 2024; accepted 2 January 2025; published 27 January 2025)

The analytical study of confinement in lattice gauge theories (LGTs) remains a difficult task to this day. Taking a geometric perspective on confinement, we develop a real-space renormalization group (RG) formalism for $\mathbb{Z}_2$ LGTs using percolation probability as a confinement order parameter. The RG flow we analyze is constituted by both the percolation probability and the coupling parameters. We consider a classical $\mathbb{Z}_2$ LGT in two dimensions, with matter and thermal fluctuations, and analytically derive the confinement phase diagram. We find good agreement with numerical and exact benchmark results and confirm that a finite matter density enforces confinement at $T < \infty$ in the model we consider. Our RG scheme enables future analytical studies of $\mathbb{Z}_2$ LGTs with matter and quantum fluctuations and beyond.

DOI: 10.1103/PhysRevB.111.024314

I. INTRODUCTION

The confinement problem is of fundamental interest in a variety of theoretical models, most notably in quantum chromodynamics [1,2]. Lattice gauge theories (LGTs), originally introduced to study quantum chromodynamics nonperturbatively [3], are of vital importance in the study of confinement [4]. A famous example is the Fradkin-Shenker model [5], which features a confined and a deconfined topological phase while hosting a local $\mathbb{Z}_2$ symmetry. It is especially intriguing because of its wide applicability [6,7] and its experimental accessibility in modern quantum simulation platforms [8–12].

It remains challenging to define experimentally, numerically, and analytically accessible order parameters to probe confinement. Well-known examples are Wilson loops [3], Polyakov loops [13], t'Hooft loops [14], and the Fredenhagen-Marcu operator [15,16], of which only the latter is applicable in the presence of dynamical matter. However, even the Fredenhagen-Marcu order parameter suffers from severe numerical instability in certain regimes, due to its definition as a ratio of two exponentially small numbers [17,18]. Recently, a percolation-inspired order parameter has been proposed [18], which can be sampled directly and hence circumvents such instabilities. It further establishes a geometric perspective on confinement where $\mathbb{Z}_2$ electric strings percolate in the deconfined phase. Because of the scale invariance of percolation near phase transitions [19,20], it is possible to construct an effective renormalization group formalism to analytically obtain the phase diagram, which is the main goal of this paper.

The renormalization group (RG) [21,22], originally developed in the context of quantum field theories, has been widely successful in many areas of physics. It was famously used in condensed matter physics to derive scaling laws for the Kondo model [23]. RG was also applied to study the confinement problem in LGTs without dynamical matter [24–26].

In this paper we introduce a real-space RG formalism for $\mathbb{Z}_2$ lattice gauge theories with matter, featuring a simultaneous flow of coupling parameters and percolation probability. We apply the RG formalism to explain the confinement phase diagram of a classical $\mathbb{Z}_2$ LGT with fluctuating matter [see Fig. 1(a)]. Our analytical results are in good agreement with earlier numerical studies of this model [18]. In particular we provide analytical understanding of why any nonzero concentration of matter excitations at finite temperature leads to confinement in this model. Moreover, we go beyond earlier studies [18] by considering the regime of vanishing string tension $h = 0$ (or infinite temperature $T/h = \infty$) where we predict a thermally deconfined state with percolating strings; see Fig. 1(a). We confirm this prediction by numerically exact Monte Carlo simulations.

Our RG method lays the foundation to study percolation-based confinement in more complicated models. For example, the Fradkin-Shenker model [5] could be analyzed and the interplay of thermal and quantum fluctuations can be explored. This adds further analytical understanding of confinement of dynamical charges in $\mathbb{Z}_2$ LGTs and beyond: for instance, the critical exponents associated with the

---

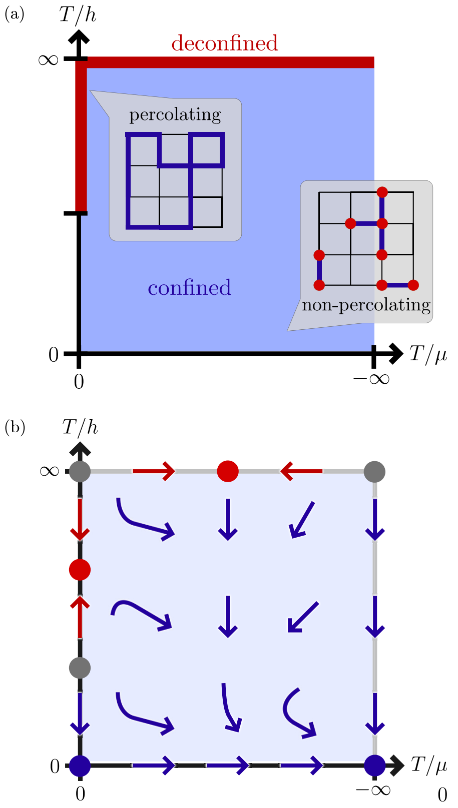

FIG. 1. (a) Confinement phase diagram of the classical $\mathbb{Z}_2$ LGT we study. We show that for positive βh any nonzero particle density, i.e., any $T/\mu \neq 0$, leads to a deconfined system in which no percolating cluster of electric strings is formed. The system is deconfined in the limit $T/h = \infty$. The pure gauge system realized at $T/\mu = 0$ exhibits a confinement phase transition. (b) RG flow in the μ-h plane. The phase diagram in the thermodynamic limit is constructed from this RG flow. (Non)percolating fixed points are marked in red (blue); gray points correspond to unstable fixed points.

confinement-deconfinement transition that we find at unstable fixed points in the RG flow diagram [see Fig. 1(b)] can be analyzed.

II. $\mathbb{Z}_2$ LATTICE GAUGE THEORY

We consider the classical two-dimensional $\mathbb{Z}_2$ lattice gauge theory in the electric field basis

$$\hat{H} = -h \sum_{\langle \mathbf{i},\mathbf{j}\rangle} \hat{\tau}^x_{\langle \mathbf{i},\mathbf{j}\rangle}, \tag{1}$$

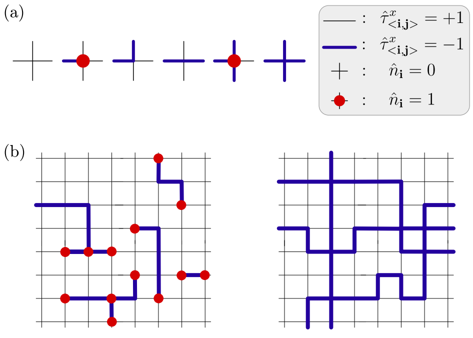

CONFINED / NON-PERCOLATING DECONFINED / PERCOLATING

FIG. 2. (a) $\mathbb{Z}_2$ Gauss's law on the square lattice. We illustrate the allowed configurations under Gauss's law on the square lattice in the electric field basis. (b) Percolation probability as an order parameter for confinement. In the deconfined phase, there exists a percolating cluster of $\mathbb{Z}_2$ electric strings. In the confined regime, matter is bound in local $\mathbb{Z}_2$-neutral clusters (hadrons). We show that any nonzero charge density prohibits thermal deconfinement.

where $\hat{\tau}^x_{\langle \mathbf{i},\mathbf{j}\rangle} = \pm 1$ is the electric field on the bond connecting neighboring sites **i** and **j** on the square lattice. Sites can be locally occupied by hard-core bosonic matter, subject to a $\mathbb{Z}_2$ Gauss law. This defines a classical statistical mechanics problem with Boltzmann weight $w = \frac{1}{Z}e^{-\beta H}$, temperature $T = 1/\beta$, and partition function $Z = \sum e^{-\beta H}$, where the sum is over all gauge-invariant states.

The local $\mathbb{Z}_2$ symmetry generator is given by

$$\hat{G}_{\mathbf{j}} = (-1)^{\hat{n}_{\mathbf{j}}} \prod_{\mathbf{i}:\langle \mathbf{i},\mathbf{j}\rangle} \hat{\tau}^x_{\langle \mathbf{i},\mathbf{j}\rangle}. \tag{2}$$

Choosing a gauge sector yields locally conserved quantities—the charges $g_{\mathbf{j}}$. We choose the *physical sector* with $g_{\mathbf{j}} = 1$ at all sites **j**, which is interpreted as having no background charges. This local constraint is known as *Gauss's law*. Thus the hard-core matter particles with density $\hat{n}_{\mathbf{j}} = \hat{a}^\dagger_{\mathbf{j}}\hat{a}_{\mathbf{j}}$ must have an odd number of adjoining electric strings $\hat{\tau}^x_{\langle \mathbf{i},\mathbf{j}\rangle} = -1$. Figure 2(a) illustrates the $\mathbb{Z}_2$ Gauss law on the square lattice.

To study this model analytically, we use its grand canonical variant

$$\begin{aligned}\hat{H} &= -h \sum_{\langle \mathbf{i},\mathbf{j}\rangle} \hat{\tau}^x_{\langle \mathbf{i},\mathbf{j}\rangle} - \mu \sum_{\mathbf{j}} \hat{n}_{\mathbf{j}} \\ &= -h \sum_{\langle \mathbf{i},\mathbf{j}\rangle} \hat{\tau}^x_{\langle \mathbf{i},\mathbf{j}\rangle} + \mu \sum_{\mathbf{j}} \prod_{\mathbf{i}:\langle \mathbf{i},\mathbf{j}\rangle} \hat{\tau}^x_{\langle \mathbf{i},\mathbf{j}\rangle} + \text{const},\end{aligned} \tag{3}$$

where μ is a chemical potential used to fix the matter density. By Gauss's law the latter can be expressed as $(-1)^{\hat{n}_{\mathbf{j}}} = \prod_{\mathbf{i}:\langle \mathbf{i},\mathbf{j}\rangle} \hat{\tau}^x_{\langle \mathbf{i},\mathbf{j}\rangle}$. We refer to bonds with electric field $\hat{\tau}^x = -1$ as *occupied*. These bonds form (electric) strings ξ where $\hat{\tau}^x_l = -1\ \forall l \in \xi$. We use the convention $h \geqslant 0$ and $\mu \leqslant 0$, i.e., the absence of electric strings and of matter particles is energetically preferred.

We define confinement geometrically in the electric field basis. The percolation probability $\rho = \rho(\beta h, \beta\mu)$ is the probability that there exists a cluster of $\mathbb{Z}_2$ electric strings that extends across opposite ends of the lattice. In the confined regime, matter forms finite-size $\mathbb{Z}_2$ neutral clusters, resembling hadrons; in the deconfined regime, strings form a percolating cluster; see Fig. 2(b). It has been demonstrated that ρ is a suitable order parameter to probe confinement, including in cases with fluctuating matter [18].

III. DERIVATION OF THE CONFINEMENT PHASE DIAGRAM

A. Renormalization group approach

We take a real-space RG approach where we perform a partial trace over the systems' degrees of freedom and assign each possible configuration a new *block* configuration on the renormalized system. Imposing that the total partition sum of the renormalized system is that of the original system,

$$\begin{aligned} Z &= \sum_{\{\hat{\tau}^x_{\langle \mathbf{i},\mathbf{j}\rangle}\}} e^{-\beta H(\{\hat{\tau}^x_{\langle \mathbf{i},\mathbf{j}\rangle}\},h,\mu)} \\ &\overset{!}{=} \sum_{\{\hat{\tau}^x_{\langle \mathbf{I},\mathbf{J}\rangle}\}} e^{-\beta H'(\{\hat{\tau}^x_{\langle \mathbf{I},\mathbf{J}\rangle}\},h',\mu')}, \end{aligned} \tag{4}$$

we obtain a new Hamiltonian H' that must have (approximately) the same structure as the original Hamiltonian. The state $\{\hat{\tau}^x_{\langle \mathbf{i},\mathbf{j}\rangle}\}$ before the RG map is called the microconfiguration and the state $\{\hat{\tau}^x_{\langle \mathbf{I},\mathbf{J}\rangle}\}$ after renormalizing is called the block or macroconfiguration. The RG procedure is repeated ad infinitum and the phase diagram in the thermodynamic limit can be constructed from the resulting parameter flow.

The challenge in constructing such a renormalization scheme for this $\mathbb{Z}_2$ LGT lies in the additional constraints that (i) the block configuration must still satisfy Gauss's law and (ii) the percolation probability must be tractable throughout the renormalization.

Starting with requirement (ii), we mimic the *spanning cluster rule* previously used [19,27] to analyze the Bernoulli percolation, which is the bond percolation on the square lattice. Bernoulli percolation is realized in our model at $\mu = 0$, i.e., for independent links or without Gauss's law constraints. We then adapt this approach such that the density of matter particles obeying Gauss's law are approximately conserved, yielding a renormalized Hamiltonian that indeed takes the same form as the original Hamiltonian (to first order in β). This is the *adjusted spanning cluster rule*.

Step 1. Divide the square lattice into blocks according to Fig. 3(a). One such block is shown in Fig. 3(b) on the left. We use capital letters to label sites in the original configurations and numbers to label sites in the renormalized configuration. Note that the block shape chosen here is not unique and there may be other blocks which produce a similar renormalization scheme. In particular, for other lattice geometries or more complicated interactions it may be necessary to choose larger blocks at this point.

Step 2. For each block, define the macroconfiguration by setting $\hat{\tau}^x_{1,5} = -1$ if and only if there exists a path traversing only occupied bonds from $\{A, B\}$ to $\{L, K\}$. If no such path exists, set $\hat{\tau}^x_{1,5} = +1$. Proceed similarly with paths from $\{C, D\}$ to $\{I, L\}$ giving $\hat{\tau}^x_{2,5}$, from $\{F, E\}$ to $\{L, K\}$ giving $\hat{\tau}^x_{3,5}$, and from $\{G, H\}$ to $\{I, L\}$ giving $\hat{\tau}^x_{4,5}$. Hence the block configuration has a horizontal electric string from vertex 2 to vertex 5 iff there exists a cluster spanning from the center to the right in the original configuration (*spanning cluster rule*).

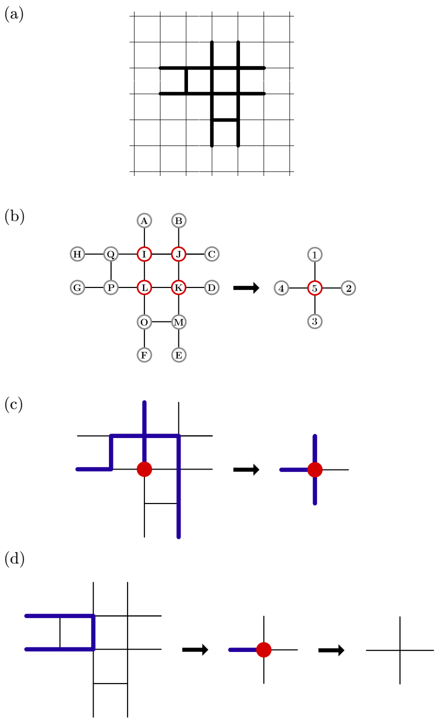

FIG. 3. Adjusted spanning cluster RG scheme. The square lattice is divided into blocks (a) which are each assigned a renormalized/block configuration by checking for spanning clusters in each direction (b). We show the renormalization of an example configuration (c). In the case of a pure gauge configuration, the renormalized configuration is further adjusted to preserve particle number (d).

Step 3. Adjust the block configuration from step 2 to approximately preserve the particle density. Whenever the original configuration is pure gauge, i.e., whenever $n_{\mathbf{j}} = 0$ for the central sites $\mathbf{j} = I, J, K, L$, the block configuration is set to also have zero particles. To do this, note that the block configuration from step 2 corresponds to the nonzero particle number precisely if it has an odd number of incoming electric strings (Gauss's law). Thus there must be either one incoming string or three. In the former case, remove the string and, in the latter case, add the fourth string. Either way, the block now has an even number of occupied bonds and thus no particle at the central site.

Step 4. Introduce particles on the block configuration by following Gauss's law.

B. Coupling parameter flow

Now that the RG procedure is defined, it remains to track the flow of coupling parameters h, μ under this map.

The renormalized Hamiltonian H' is determined via Eq. (4) to be

$$-\beta\hat{H}'\big(\{\hat{\tau}^x_{\langle\mathbf{I},\mathbf{J}\rangle}\}\big) = \ln\left(\sum_{\{\hat{\tau}^x_{\langle\mathbf{i},\mathbf{j}\rangle}\}^*} e^{-\beta\hat{H}(\{\hat{\tau}^x_{\langle\mathbf{i},\mathbf{j}\rangle}\},h,\mu)}\right), \tag{5}$$

where the asterisk indicates that the sum is taken only over those microstates $\{\hat{\tau}^x_{\langle\mathbf{i},\mathbf{j}\rangle}\}$ for which the renormalization procedure yields the specific block state $\{\hat{\tau}^x_{\langle\mathbf{I},\mathbf{J}\rangle}\}$.

Imposing that $\hat{H}'$ takes a similar form to $\hat{H}$, specifically that interactions remain block local, Eq. (5) holds not just for the entire lattice but also for states on a single block. For such a block the original state consists of 18 bonds and the renormalized state of four bonds. The calculation can then be done exactly using symbolic computation to classify the 2^{18} microstates according to their assigned macrostate and evaluating the respective sums. For example,

$\exp\Big(-\beta\hat{H}'\Big($ 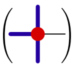 $\Big)\Big) =$

$= \exp\Big(-\beta\hat{H}\Big($ 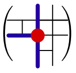 $\Big)\Big) + \exp\Big(-\beta\hat{H}\Big($ 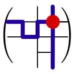 $\Big)\Big) + \dots\ .$

(6)

We thus obtain formulas for the Boltzmann weights $\exp[-\beta\hat{H}'(\{\hat{\tau}^x_1, \hat{\tau}^x_2, \hat{\tau}^x_3, \hat{\tau}^x_4\})]$ of all possible block configurations shown in Fig. 2. Keeping only the highest order terms in orders of β, the renormalized Hamiltonian

$$\hat{H}' = -h'\sum_{\langle\mathbf{I},\mathbf{J}\rangle}\hat{\tau}^x_{\langle\mathbf{I},\mathbf{J}\rangle} - \mu'\sum_{\mathbf{J}}\hat{n}_{\mathbf{J}} + \text{const} \tag{7}$$

again depends only on the coupling parameters h', μ' and the RG map $(\beta h, \beta\mu) \to [(\beta h)', (\beta\mu)']$ is obtained (see Appendix B). Figure 4 shows the resulting flow of the coupling parameters under the RG map.

Figure 1(b) depicts the fixed points of this flow including the limit cases corresponding to the axes of Fig. 4. On the axis $T/h \to 0$, the only energetically allowed state is the state with no electric strings, so the system never percolates. (Alternatively, using the canonical Hamiltonian with fixed particle number or density, the limit $T/h \to 0$ yields a dimer state which also does not percolate.) The flow from points in the plane towards this limit indicates that the percolation probability is zero at all of these points.

In the limit $T/\mu = -\infty$, the $\hat{\tau}^x$ strings are independent; thus the system reduces to Bernoulli percolation. The percolation behavior is then determined by the bond occupation probability p. The critical probability on the square lattice is $p_c = 1/2$ [28,29]. In the model at hand, $p = \frac{e^{-\beta h}}{e^{-\beta h}+e^{\beta h}} < \frac{1}{2}$ for $\beta h > 0$ (this corresponds to a two-level system realized by a single $\hat{\tau}^x$ link in a thermal ensemble). So the percolation probability is 0, except at the point with $\beta h = 0$ (infinite temperature limit) where the percolation probability is 1 and the system exhibits critical percolation. The critical probability depends crucially on the lattice geometry [28,30] and number of spatial dimensions [31], so intuitively one should expect the percolation for finite T/μ to similarly depend on these.

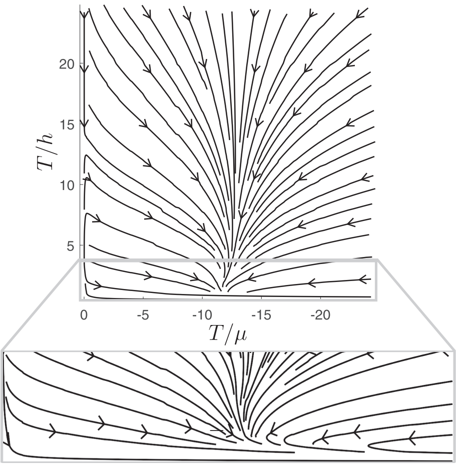

FIG. 4. RG flow, numerical plot. All values of the coupling parameters $T/\mu \neq 0$, $T/h < \infty$ flow towards the nonpercolating fixed point $T/\mu \to -\infty$, $T/h = 0$.

For the axis $T/h = \infty$, the system flows towards some fixed point $(T/\mu, T/h) = (T/\mu^*, \infty)$. In particular, the critically percolating point $(T/\mu, T/h) = (-\infty, \infty)$ flows towards the same fixed point, suggesting that all $(T/\mu, T/h) = (T/\mu, \infty)$ values yield a percolating system. For an intuitive picture of this limit we note that, as βh is zero, there is no difference being made between strings and antistrings. Thus any correlation effects in the string distribution must stem from the preference of closed loops via $\beta\mu \neq 0$.

In the limit of a pure gauge theory with no particles, i.e., $T/\mu \to 0$, the system can be mapped to a classical Ising model on the dual lattice [32,33] with a percolation transition on this axis [18,34]. The coupling parameter flow in Fig. 1 exhibits several fixed points on this axis. We identify a stable, nonpercolating (confined) fixed point at $T = 0$, an unstable, i.e., critical, fixed point at a critical temperature $T_C = 3.48h > 0$ where the percolation transition of the pure gauge theory takes place, a stable, percolating (deconfined) fixed point above T_C, and an unstable, i.e., critical, fixed point at $T = \infty$ flowing towards the percolating (deconfined) state, demonstrating critical percolation at $T = \infty$.

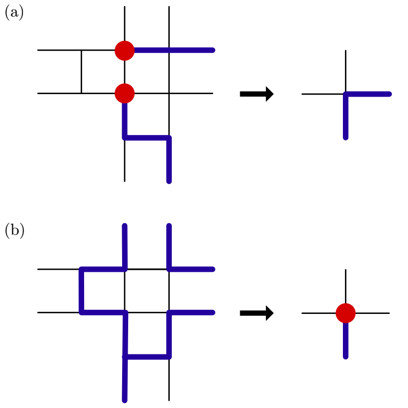

FIG. 5. Percolation corrections. We show that the percolation properties may be altered during an RG step. Nonpercolating microstates are sometimes mapped to percolating macrostates (a) or vice versa (b). The resulting percolation probability flow needs to be tracked alongside the flow of the coupling parameters to obtain the percolation phase diagram.

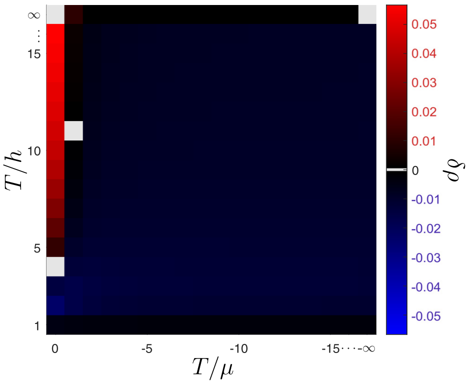

FIG. 6. Numerical values of the percolation corrections. The percolation corrections are negative for $T/\mu \neq 0$, $T/h < \infty$. The percolation transition for the pure gauge theory with $T/\mu = 0$ is emphasized by the sign change of corrections on this axis. Overall, the percolation corrections are relatively small [$\delta\rho < 0.08\ \forall(\beta h, \beta\mu)$], implying that the renormalization scheme can indeed be used to analyze percolation.

C. Percolation probability flow

So far we have only studied the RG flow of the renormalized coupling parameters $\beta\mu$ and βh in the Hamiltonian. However, during each RG step, the percolation properties of the system may be altered by introducing or removing connections between electric string clusters. On the block level this corresponds to mapping a percolating microconfiguration to a nonpercolating macroconfiguration and vice versa. Both of these can happen with the adjusted spanning cluster rule we used (see Fig. 5). Now, to extract the percolation transition, we revisit the implicit assumption made so far that the percolation probability is kept constant throughout the RG flow. In reality, further care must be taken to analyze how the renormalization procedure affects the percolation properties and we will see that this influences the conclusions drawn from the parameter flow.

We track the overall change $\delta\rho$ of the percolation probability ρ which is equal to the average of the percolation change over all possible configurations weighted by the respective Boltzmann factors:

$$\begin{aligned}\delta\rho(\beta h, \beta\mu) &= \rho(\beta h, \beta\mu) - \rho(\beta h', \beta\mu') \\ &= \frac{1}{Z(\beta h, \beta\mu)} \sum_{\text{states } \Phi} e^{-\beta \hat{H}(\Phi)}[\rho(\Phi) - \rho(\Phi')].\end{aligned} \tag{8}$$

It is thus possible that, during the flow from some point $(\beta h, \beta\mu)$ in coupling parameter space to a fixed point, the renormalization procedure has changed the clusters in such a way that a (non)percolating configuration at the fixed point does not imply a (non)percolating configuration at the starting point. Hence it is necessary to construct the flow of percolation probability alongside the RG flow of the coupling parameters.

To obtain the total change in percolation probability during the RG flow to some fixed point with known percolation probability, the changes from each of the RG steps are summed up, i.e.,

$$\begin{aligned}\Delta\rho(\beta h, \beta\mu) &= \rho(\beta h, \beta\mu) - \rho_\infty \\ &= \sum_{n=0}^{\infty}(\rho_n - \rho_{n+1}) \\ &= \sum_{n=0}^{\infty}\delta\rho_n.\end{aligned} \tag{9}$$

Here, ρ_n denotes the percolation probability at the coupling parameters which are reached by applying n RG steps starting from the point $(\beta h, \beta\mu)$. Figure 6 shows the corrections to the percolation obtained during the RG flow for various βh, $\beta\mu$.

We analyze whether these percolation corrections correspond to a genuine change of percolation probability or if they can be neglected: consider the sign of the percolation corrections in various regions of the confinement phase diagram. If we flow towards a percolating fixed point, then positive percolation corrections mean that the initial system is more percolating than the renormalized system. In the case that percolation probability of the fixed point is 1, this implies that the initial system must also be percolating (and that any percolation corrections correspond to errors from dropping higher order terms in the renormalized Hamiltonian). Similarly, a flow towards a nonpercolating fixed point during which negative percolation corrections are attained implies that the starting point in coupling parameter space must be nonpercolating. (Alternatively, the effects of percolation corrections on the confinement phase diagram can be analyzed by comparing to a site-bond percolation problem; see Appendix C).

Recall that for all $T/h < \infty$ with nonzero T/μ the RG flow is towards a nonpercolating fixed point. $\delta\rho$ is positive only in the region with $\mu/T \ll 0$ and large enough T/h [in Fig. 6 we see a point at $(T/\mu, T/h) = (-1, 11)$ near the edge of this region]. The flow from any point $T/h < \infty$ with nonzero T/μ eventually leaves this region and $\Delta\rho$ is negative for any such parameter values. Thus we can conclude that the system does not percolate in these cases.

In the limit $T/h \to \infty$, the flow is towards a percolating fixed point. The percolation corrections then indicate that the system indeed percolates in this case for all T/μ.

For $T/\mu = 0$ the percolation behavior changes with varying T/h. For large T/h, renormalizing the system significantly increases the percolation probability at each step. The percolation probability at these points must thus be greater than zero. Since Kolmogorov's zero-one law implies that the percolation probability in the thermodynamic limit is either zero or one [35,36], the percolation probability in this region must be one. For small T/h, renormalizing leads to the nonpercolating fixed point at $T/h = 0$ and the percolation corrections are negative. We thus conclude that there is a phase transition from a percolating system at large T/h to a nonpercolating system at small T/h.

The combined RG flow of the coupling parameters and the percolation probability can also be considered graphically as a three-dimensional flow (see Fig. 7). We see the percolation transition directly in the two stable fixed points of the flow for $T/\mu = 0$. These fixed points differ in the percolation corrections accumulated during the flow and are thus represented at different heights/levels in the three-dimensional diagram. Note that the fixed point $\delta\rho = 0$ of percolation probability flow is distinct from the fixed point of coupling parameter flow. However, a finite number of steps with negative percolation corrections at the beginning of the RG flow is outweighed by the infinite number of steps with positive percolation corrections that do not tend to zero in the RG flow toward the fixed point. Thus the percolation transition of the pure gauge system occurs at the largest T/h from which the flow ends in the region with positive $\delta\rho$.

D. Phase diagram

The results are summarized in the phase diagram shown in Fig. 1(a). The system exhibits confinement whenever $T/\mu < 0$ and $T/h < \infty$ and is deconfined in the limit $T/h \to \infty$. On the axis $T/|\mu| = 0$ (pure gauge theory), we find a percolation transition with confinement for small T/h and deconfinement for large T/h. This is in good agreement with exact results and the predictions from Monte Carlo simulations [18]. For positive βh, we have in particular confirmed that *any* finite chemical potential $\beta\mu$ (i.e., any nonzero particle density) results in a confined system with no percolating cluster of electric strings.

For the percolation transition of the pure gauge theory, the RG flow gives a critical T/h value of 3.48, which we compare to the exact value of ∼2.27 (the exact value is identical to the Ising critical temperature). In the RG approach, higher order terms generated in the Hamiltonian are neglected at each step. It is thus expected that the RG results are qualitatively but not quantitatively correct. The critical exponents of this phase transition can be obtained by linearizing the RG map around the critical point. For example, we obtain the critical exponent of the correlation length $\nu \approx 1.087$, which is in good quantitative agreement with the exact value $\nu = 1$ of the Ising universality class.

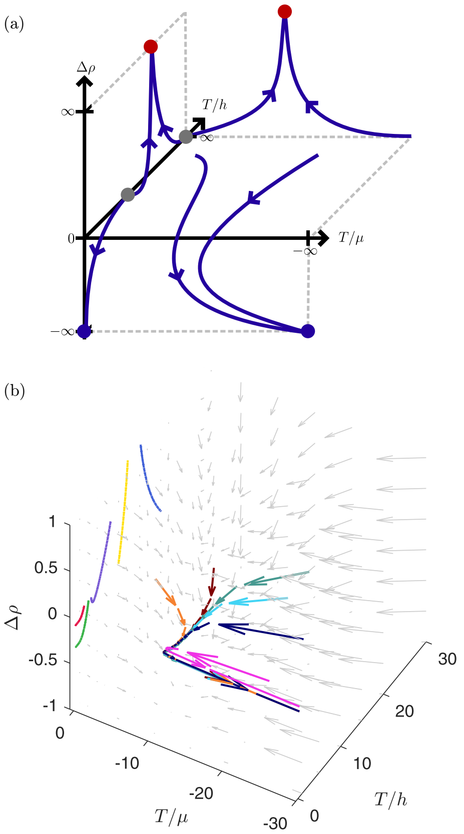

FIG. 7. Three-dimensional RG flow. The flow of the coupling parameters and the percolation probability flow yield a three-dimensional combined RG flow, of which we show a schematic depiction (a) and a numerical plot (b). In the numerical plot, each arrow represents one RG step and the colors correspond to different starting points in parameter space. On the $T/\mu = 0$ axis the RG steps are too small for the arrows to be visible. The percolation transition of the pure gauge theory with $T/\mu = 0$ is demonstrated by two different fixed points to which the flow on this axis leads.

The Hamiltonian (3) has been studied numerically at finite T/h in Ref. [18], with their results being in good qualitative agreement with our analysis. It was shown that any small but finite string tension h leads to a nonpercolating confined phase

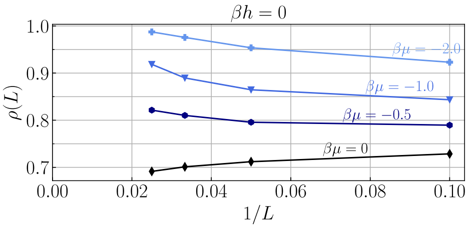

FIG. 8. Monte Carlo at zero string tension. We simulate Hamiltonian (3) at $\beta h = 0$ (i.e., no string tension) using classical Monte Carlo. The error bars are too small to be visible. For $\beta\mu = 0$ it is exactly known that the system is percolating in the thermodynamic limit [18]. In this case we have $\rho(L \to \infty) \to 1/2$ since the system is *directly at* the Bernoulli percolation threshold. For $\beta\mu < 0$ the percolation probability $\rho(L, \beta\mu)$ clearly increases with L and $\rho(L, \beta\mu < 0) > \rho(L, \beta\mu = 0)$. We conjecture that $\rho(L \to \infty, \beta\mu < 0) \to 1$ due to Kolmogorov's zero-one law. These numerical results support our RG result that the system is percolating for $\beta h = 0$, $\beta\mu \leqslant 0$.

at finite doping. Here, we apply the classical Monte Carlo algorithm from [18] at $T/h = \infty$, i.e., at zero string tension, to confirm our RG result that the system is percolating in that regime. In Fig. 8, we show the percolation probability $\rho(\beta h = 0, L)$ for system sizes $L^2 = 10^2, 20^2, 30^2, 40^2$ with open boundaries. This result can be related to previous 1D LGT results [37], where it has been shown that any small nonzero string tension h leads to confinement, i.e., an exponential decay of the Green's function, while at $h = 0$ the system is deconfined.

Another way to analyze the RG flow is by directly renormalizing snapshots obtained from the Monte Carlo simulations. For coupling parameters at or near the RG fixed points, the renormalized snapshots should be statistically similar to nonrenormalized snapshots of the lattice. We present some results from training a neural network to distinguish renormalized and nonrenormalized snapshots in Appendix E.

IV. CONCLUSION AND OUTLOOK

We have introduced a real-space RG scheme to probe confinement in $\mathbb{Z}_2$ LGTs using percolation probability as an order parameter. We successfully reproduced the confinement phase diagram of a classical $\mathbb{Z}_2$ LGT and found good agreement with exact and numerical benchmark results. In particular, we confirm the numerical result that a finite matter density prohibits a thermally deconfined phase on the 2D square lattice. In addition, we extended the phase diagram to regions not previously considered, including the case of vanishing string tension, and supported our RG results with Monte Carlo simulations.

The RG flow was considered as a simultaneous flow of the percolation probability alongside the coupling parameters. We envision that this RG ansatz can be generalized to other lattice geometries, to $\mathbb{Z}_N$ gauge symmetries, and to other models such as the Fradkin-Shenker model featuring quantum fluctuations in the future. We believe that our RG scheme has the potential to advance the analytical studies of confinement in $\mathbb{Z}_2$ LGTs and beyond.

ACKNOWLEDGMENTS

We thank L. Homeier and L. Pollet for insightful discussions. This research was funded by the European Research Council (ERC) under the European Union's Horizon 2020 research and innovation program (Grant Agreement No. 948141), ERC Starting Grant SimUcQuam, and by the Deutsche Forschungsgemeinschaft (DFG, German Research Foundation) under Germany's Excellence Strategy, EXC-2111 Grant No. 390814868 and via Research Unit FOR 2414 under Project No. 277974659. This work was supported by the QuantERA grant DYNAMITE, by the Deutsche Forschungsgemeinschaft (DFG, German Research Foundation) under Project No. 499183856. This project was funded within the QuantERA II Programme that has received funding from the European Union's Horizon 2020 research and innovation programme under Grant Agreement No. 101017733. G.D. acknowledges funding from the Munich Quantum Valley, supported by the Bavarian state government with funds from the Hightech Agenda Bayern Plus.

APPENDIX A: RENORMALIZATION PROCEDURE—ADJUSTED SPANNING CLUSTER RULE

See Table I for the adjusted spanning cluster rule.

APPENDIX B: DETAILS OF RG FLOW

To determine the renormalized Hamiltonian $\hat{H}'$, we classify all allowed microconfigurations $\{\hat{\tau}_1^x, \dots, \hat{\tau}_{18}^x\}$ of a block according to the assigned block configuration $\{\hat{\tau}_{\mathrm{I}}^x, \hat{\tau}_{\mathrm{II}}^x, \hat{\tau}_{\mathrm{III}}^x \hat{\tau}_{\mathrm{IV}}^x\}$. Taking a specific block state and adding the Boltzmann weights of all microstates which are renormalized to this gives the expectation value

$$\exp[-\beta\hat{H}'(\{\hat{\tau}_{\mathrm{I}}^x, \hat{\tau}_{\mathrm{II}}^x, \hat{\tau}_{\mathrm{III}}^x \hat{\tau}_{\mathrm{IV}}^x\})] = \sum_{\text{resp. microstates}} \exp\left[-\beta\hat{H}\left(\{\hat{\tau}_1^x, \dots, \hat{\tau}_{18}^x\}, h, \mu\right)\right]. \tag{B1}$$

Using symbolic computation to calculate these sums exactly, we obtain the following results:

$$c \cdot e^{4\beta h'} \overset{!}{=} e^{-\beta\hat{H}'(1,1,1,1)}$$
$$= 293\,\mathrm{e}^{-2\beta h} + 1165\,\mathrm{e}^{2\beta h} + 62\,\mathrm{e}^{-4\beta h} + 1160\,\mathrm{e}^{4\beta h} + 6\,\mathrm{e}^{-6\beta h} + 815\,\mathrm{e}^{6\beta h} + 442\,\mathrm{e}^{8\beta h} + 185\,\mathrm{e}^{10\beta h} + 60\,\mathrm{e}^{12\beta h}$$

TABLE I. Adjusted spanning cluster rule. We apply the adjusted spanning cluster renormalization to some example configurations.

micro-configuration	Boltzmann weight	renormalized block configuration
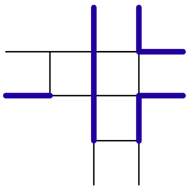	$e^{2\beta h}$	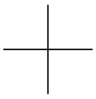
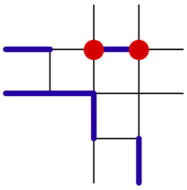	$e^{6\beta h+2\beta\mu}$	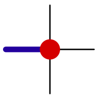
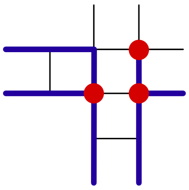	$e^{3\beta\mu-4\beta h}$	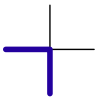
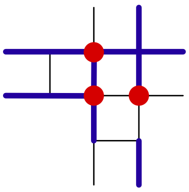	$e^{3\beta\mu-4\beta h}$	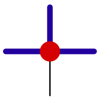
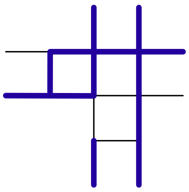	$e^{-8\beta h}$	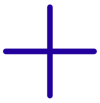

$$
\begin{aligned}
&+19\,e^{14\beta h}+6\,e^{16\beta h}+e^{18\beta h}+124\,e^{\beta\mu}+158\,e^{2\beta\mu}+68\,e^{3\beta\mu}+8\,e^{4\beta\mu}+12\,e^{-2\beta h}\,e^{\beta\mu}+480\,e^{2\beta h}\,e^{\beta\mu}\\
&+15\,e^{-2\beta h}\,e^{2\beta\mu}+663\,e^{2\beta h}\,e^{2\beta\mu}+900\,e^{4\beta h}\,e^{\beta\mu}+4\,e^{-2\beta h}\,e^{3\beta\mu}+392\,e^{2\beta h}\,e^{3\beta\mu}+80\,e^{2\beta h}\,e^{4\beta\mu}+1464\,e^{4\beta h}\,e^{2\beta\mu}\\
&+1032\,e^{6\beta h}\,e^{\beta\mu}+1044\,e^{4\beta h}\,e^{3\beta\mu}+278\,e^{4\beta h}\,e^{4\beta\mu}+1858\,e^{6\beta h}\,e^{2\beta\mu}+808\,e^{8\beta h}\,e^{\beta\mu}+1456\,e^{6\beta h}\,e^{3\beta\mu}\\
&+424\,e^{6\beta h}\,e^{4\beta\mu}+1484\,e^{8\beta h}\,e^{2\beta\mu}+456\,e^{10\beta h}\,e^{\beta\mu}+1168\,e^{8\beta h}\,e^{3\beta\mu}+332\,e^{8\beta h}\,e^{4\beta\mu}+784\,e^{10\beta h}\,e^{2\beta\mu}
\end{aligned}
$$

$$
\begin{aligned}
&+ 192\,\mathrm{e}^{12\beta h}\,\mathrm{e}^{\beta\mu} + 552\,\mathrm{e}^{10\beta h}\,\mathrm{e}^{3\beta\mu} + 138\,\mathrm{e}^{10\beta h}\,\mathrm{e}^{4\beta\mu} + 268\,\mathrm{e}^{12\beta h}\,\mathrm{e}^{2\beta\mu} + 56\,\mathrm{e}^{14\beta h}\,\mathrm{e}^{\beta\mu} + 144\,\mathrm{e}^{12\beta h}\,\mathrm{e}^{3\beta\mu}\\
&+ 28\,\mathrm{e}^{12\beta h}\,\mathrm{e}^{4\beta\mu} + 52\,\mathrm{e}^{14\beta h}\,\mathrm{e}^{2\beta\mu} + 8\,\mathrm{e}^{16\beta h}\,\mathrm{e}^{\beta\mu} + 16\,\mathrm{e}^{14\beta h}\,\mathrm{e}^{3\beta\mu} + 2\,\mathrm{e}^{14\beta h}\,\mathrm{e}^{4\beta\mu} + 4\,\mathrm{e}^{16\beta h}\,\mathrm{e}^{2\beta\mu} + 754,
\end{aligned}
$$

$$
\begin{aligned}
c \cdot^{2\beta h'} e^{\beta\mu'} &\overset{!}{=} e^{-\beta\hat{H}'(-1,1,1,1)} = e^{-\beta\hat{H}'(1,-1,1,1)} = e^{-\beta\hat{H}'(1,1,-1,1)} = e^{-\beta\hat{H}'(1,1,1,-1)}\\
&= 578\,\mathrm{e}^{\beta\mu} + 840\,\mathrm{e}^{2\beta\mu} + 542\,\mathrm{e}^{3\beta\mu} + 133\,\mathrm{e}^{4\beta\mu} + 174\,\mathrm{e}^{-2\beta h}\,\mathrm{e}^{\beta\mu} + 1002\,\mathrm{e}^{2\beta h}\,\mathrm{e}^{\beta\mu} + 277\,\mathrm{e}^{-2\beta h}\,\mathrm{e}^{2\beta\mu}\\
&\quad + 1454\,\mathrm{e}^{2\beta h}\,\mathrm{e}^{2\beta\mu} + 26\,\mathrm{e}^{-4\beta h}\,\mathrm{e}^{\beta\mu} + 1044\,\mathrm{e}^{4\beta h}\,\mathrm{e}^{\beta\mu} + 186\,\mathrm{e}^{-2\beta h}\,\mathrm{e}^{3\beta\mu} + 958\,\mathrm{e}^{2\beta h}\,\mathrm{e}^{3\beta\mu} + 45\,\mathrm{e}^{-2\beta h}\,\mathrm{e}^{4\beta\mu}\\
&\quad + 234\,\mathrm{e}^{2\beta h}\,\mathrm{e}^{4\beta\mu} + 44\,\mathrm{e}^{-4\beta h}\,\mathrm{e}^{2\beta\mu} + 1502\,\mathrm{e}^{4\beta h}\,\mathrm{e}^{2\beta\mu} + 702\,\mathrm{e}^{6\beta h}\,\mathrm{e}^{\beta\mu} + 38\,\mathrm{e}^{-4\beta h}\,\mathrm{e}^{3\beta\mu} + 972\,\mathrm{e}^{4\beta h}\,\mathrm{e}^{3\beta\mu}\\
&\quad + 9\,\mathrm{e}^{-4\beta h}\,\mathrm{e}^{4\beta\mu} + 239\,\mathrm{e}^{4\beta h}\,\mathrm{e}^{4\beta\mu} + 6\,\mathrm{e}^{-6\beta h}\,\mathrm{e}^{2\beta\mu} + 948\,\mathrm{e}^{6\beta h}\,\mathrm{e}^{2\beta\mu} + 304\,\mathrm{e}^{8\beta h}\,\mathrm{e}^{\beta\mu} + 584\,\mathrm{e}^{6\beta h}\,\mathrm{e}^{3\beta\mu}\\
&\quad + 2\,\mathrm{e}^{-6\beta h}\,\mathrm{e}^{4\beta\mu} + 141\,\mathrm{e}^{6\beta h}\,\mathrm{e}^{4\beta\mu} + 370\,\mathrm{e}^{8\beta h}\,\mathrm{e}^{2\beta\mu} + 84\,\mathrm{e}^{10\beta h}\,\mathrm{e}^{\beta\mu} + 212\,\mathrm{e}^{8\beta h}\,\mathrm{e}^{3\beta\mu} + 45\,\mathrm{e}^{8\beta h}\,\mathrm{e}^{4\beta\mu}\\
&\quad + 87\,\mathrm{e}^{10\beta h}\,\mathrm{e}^{2\beta\mu} + 16\,\mathrm{e}^{12\beta h}\,\mathrm{e}^{\beta\mu} + 44\,\mathrm{e}^{10\beta h}\,\mathrm{e}^{3\beta\mu} + 6\,\mathrm{e}^{10\beta h}\,\mathrm{e}^{4\beta\mu} + 10\,\mathrm{e}^{12\beta h}\,\mathrm{e}^{2\beta\mu} + 2\,\mathrm{e}^{14\beta h}\,\mathrm{e}^{\beta\mu} + 4\,\mathrm{e}^{12\beta h}\,\mathrm{e}^{3\beta\mu},
\end{aligned}
$$

$$
\begin{aligned}
c &\overset{!}{=} e^{-\beta\hat{H}'(-1,-1,1,1)} = e^{-\beta\hat{H}'(1,-1,-1,1)} = e^{-\beta\hat{H}'(1,1,-1,-1)} = e^{-\beta\hat{H}'(-1,1,1,-1)}\\
&= 232\,\mathrm{e}^{-2\beta h} + 266\,\mathrm{e}^{2\beta h} + 104\,\mathrm{e}^{-4\beta h} + 146\,\mathrm{e}^{4\beta h} + 25\,\mathrm{e}^{-6\beta h} + 54\,\mathrm{e}^{6\beta h} + 4\,\mathrm{e}^{-8\beta h} + 14\,\mathrm{e}^{8\beta h} + \mathrm{e}^{-10\beta h} + 2\,\mathrm{e}^{10\beta h}\\
&\quad + 1224\,\mathrm{e}^{\beta\mu} + 1846\,\mathrm{e}^{2\beta\mu} + 1280\,\mathrm{e}^{3\beta\mu} + 332\,\mathrm{e}^{4\beta\mu} + 894\,\mathrm{e}^{-2\beta h}\,\mathrm{e}^{\beta\mu} + 1030\,\mathrm{e}^{2\beta h}\,\mathrm{e}^{\beta\mu} + 1343\,\mathrm{e}^{-2\beta h}\,\mathrm{e}^{2\beta\mu}\\
&\quad + 1597\,\mathrm{e}^{2\beta h}\,\mathrm{e}^{2\beta\mu} + 392\,\mathrm{e}^{-4\beta h}\,\mathrm{e}^{\beta\mu} + 560\,\mathrm{e}^{4\beta h}\,\mathrm{e}^{\beta\mu} + 934\,\mathrm{e}^{-2\beta h}\,\mathrm{e}^{3\beta\mu} + 1034\,\mathrm{e}^{2\beta h}\,\mathrm{e}^{3\beta\mu} + 258\,\mathrm{e}^{-2\beta h}\,\mathrm{e}^{4\beta\mu}\\
&\quad + 246\,\mathrm{e}^{2\beta h}\,\mathrm{e}^{4\beta\mu} + 616\,\mathrm{e}^{-4\beta h}\,\mathrm{e}^{2\beta\mu} + 836\,\mathrm{e}^{4\beta h}\,\mathrm{e}^{2\beta\mu} + 118\,\mathrm{e}^{-6\beta h}\,\mathrm{e}^{\beta\mu} + 186\,\mathrm{e}^{6\beta h}\,\mathrm{e}^{\beta\mu} + 416\,\mathrm{e}^{-4\beta h}\,\mathrm{e}^{3\beta\mu}\\
&\quad + 504\,\mathrm{e}^{4\beta h}\,\mathrm{e}^{3\beta\mu} + 108\,\mathrm{e}^{-4\beta h}\,\mathrm{e}^{4\beta\mu} + 106\,\mathrm{e}^{4\beta h}\,\mathrm{e}^{4\beta\mu} + 159\,\mathrm{e}^{-6\beta h}\,\mathrm{e}^{2\beta\mu} + 263\,\mathrm{e}^{6\beta h}\,\mathrm{e}^{2\beta\mu} + 20\,\mathrm{e}^{-8\beta h}\,\mathrm{e}^{\beta\mu}\\
&\quad + 28\,\mathrm{e}^{8\beta h}\,\mathrm{e}^{\beta\mu} + 114\,\mathrm{e}^{-6\beta h}\,\mathrm{e}^{3\beta\mu} + 146\,\mathrm{e}^{6\beta h}\,\mathrm{e}^{3\beta\mu} + 20\,\mathrm{e}^{-6\beta h}\,\mathrm{e}^{4\beta\mu} + 24\,\mathrm{e}^{6\beta h}\,\mathrm{e}^{4\beta\mu} + 26\,\mathrm{e}^{-8\beta h}\,\mathrm{e}^{2\beta\mu}\\
&\quad + 54\,\mathrm{e}^{8\beta h}\,\mathrm{e}^{2\beta\mu} + 12\,\mathrm{e}^{-8\beta h}\,\mathrm{e}^{3\beta\mu} + 20\,\mathrm{e}^{8\beta h}\,\mathrm{e}^{3\beta\mu} + 2\,\mathrm{e}^{-8\beta h}\,\mathrm{e}^{4\beta\mu} + 2\,\mathrm{e}^{8\beta h}\,\mathrm{e}^{4\beta\mu} + 3\,\mathrm{e}^{-10\beta h}\,\mathrm{e}^{2\beta\mu}\\
&\quad + 7\,\mathrm{e}^{10\beta h}\,\mathrm{e}^{2\beta\mu} + 312,
\end{aligned}
$$

$$
\begin{aligned}
c &\overset{!}{=} e^{-\beta\hat{H}'(-1,1,-1,1)} = e^{-\beta\hat{H}'(1,-1,1,-1)}\\
&= 219\,\mathrm{e}^{-2\beta h} + 261\,\mathrm{e}^{2\beta h} + 95\,\mathrm{e}^{-4\beta h} + 149\,\mathrm{e}^{4\beta h} + 22\,\mathrm{e}^{-6\beta h} + 60\,\mathrm{e}^{6\beta h} + 2\,\mathrm{e}^{-8\beta h} + 16\,\mathrm{e}^{8\beta h} + 2\,\mathrm{e}^{10\beta h} + 1116\,\mathrm{e}^{\beta\mu}\\
&\quad + 1604\,\mathrm{e}^{2\beta\mu} + 992\,\mathrm{e}^{3\beta\mu} + 210\,\mathrm{e}^{4\beta\mu} + 849\,\mathrm{e}^{-2\beta h}\,\mathrm{e}^{\beta\mu} + 903\,\mathrm{e}^{2\beta h}\,\mathrm{e}^{\beta\mu} + 1241\,\mathrm{e}^{-2\beta h}\,\mathrm{e}^{2\beta\mu} + 1242\,\mathrm{e}^{2\beta h}\,\mathrm{e}^{2\beta\mu}\\
&\quad + 368\,\mathrm{e}^{-4\beta h}\,\mathrm{e}^{\beta\mu} + 464\,\mathrm{e}^{4\beta h}\,\mathrm{e}^{\beta\mu} + 789\,\mathrm{e}^{-2\beta h}\,\mathrm{e}^{3\beta\mu} + 721\,\mathrm{e}^{2\beta h}\,\mathrm{e}^{3\beta\mu} + 182\,\mathrm{e}^{-2\beta h}\,\mathrm{e}^{4\beta\mu} + 153\,\mathrm{e}^{2\beta h}\,\mathrm{e}^{4\beta\mu}\\
&\quad + 570\,\mathrm{e}^{-4\beta h}\,\mathrm{e}^{2\beta\mu} + 564\,\mathrm{e}^{4\beta h}\,\mathrm{e}^{2\beta\mu} + 89\,\mathrm{e}^{-6\beta h}\,\mathrm{e}^{\beta\mu} + 139\,\mathrm{e}^{6\beta h}\,\mathrm{e}^{\beta\mu} + 400\,\mathrm{e}^{-4\beta h}\,\mathrm{e}^{3\beta\mu} + 292\,\mathrm{e}^{4\beta h}\,\mathrm{e}^{3\beta\mu}\\
&\quad + 105\,\mathrm{e}^{-4\beta h}\,\mathrm{e}^{4\beta\mu} + 69\,\mathrm{e}^{4\beta h}\,\mathrm{e}^{4\beta\mu} + 139\,\mathrm{e}^{-6\beta h}\,\mathrm{e}^{2\beta\mu} + 146\,\mathrm{e}^{6\beta h}\,\mathrm{e}^{2\beta\mu} + 10\,\mathrm{e}^{-8\beta h}\,\mathrm{e}^{\beta\mu} + 18\,\mathrm{e}^{8\beta h}\,\mathrm{e}^{\beta\mu}\\
&\quad + 135\,\mathrm{e}^{-6\beta h}\,\mathrm{e}^{3\beta\mu} + 63\,\mathrm{e}^{6\beta h}\,\mathrm{e}^{3\beta\mu} + 41\,\mathrm{e}^{-6\beta h}\,\mathrm{e}^{4\beta\mu} + 18\,\mathrm{e}^{6\beta h}\,\mathrm{e}^{4\beta\mu} + 18\,\mathrm{e}^{-8\beta h}\,\mathrm{e}^{2\beta\mu} + 22\,\mathrm{e}^{8\beta h}\,\mathrm{e}^{2\beta\mu}\\
&\quad + 22\,\mathrm{e}^{-8\beta h}\,\mathrm{e}^{3\beta\mu} + 6\,\mathrm{e}^{8\beta h}\,\mathrm{e}^{3\beta\mu} + 12\,\mathrm{e}^{-8\beta h}\,\mathrm{e}^{4\beta\mu} + 2\,\mathrm{e}^{8\beta h}\,\mathrm{e}^{4\beta\mu} + 2\,\mathrm{e}^{-10\beta h}\,\mathrm{e}^{2\beta\mu} + 2\,\mathrm{e}^{10\beta h}\,\mathrm{e}^{2\beta\mu}\\
&\quad + 2\,\mathrm{e}^{-10\beta h}\,\mathrm{e}^{4\beta\mu} + 302,
\end{aligned}
$$

$$
\begin{aligned}
c \cdot e^{-2\beta h'} e^{\beta\mu'} &\overset{!}{=} e^{-\beta\hat{H}'(-1,-1,-1,1)} = e^{-\beta\hat{H}'(-1,-1,1,-1)} = e^{-\beta\hat{H}'(-1,1,-1,-1)} = e^{-\beta\hat{H}'(1,-1,-1,-1)}\\
&= 732\,\mathrm{e}^{\beta\mu} + 1166\,\mathrm{e}^{2\beta\mu} + 760\,\mathrm{e}^{3\beta\mu} + 182\,\mathrm{e}^{4\beta\mu} + 1161\,\mathrm{e}^{-2\beta h}\,\mathrm{e}^{\beta\mu} + 301\,\mathrm{e}^{2\beta h}\,\mathrm{e}^{\beta\mu} + 1785\,\mathrm{e}^{-2\beta h}\,\mathrm{e}^{2\beta\mu}\\
&\quad + 420\,\mathrm{e}^{2\beta h}\,\mathrm{e}^{2\beta\mu} + 1116\,\mathrm{e}^{-4\beta h}\,\mathrm{e}^{\beta\mu} + 82\,\mathrm{e}^{4\beta h}\,\mathrm{e}^{\beta\mu} + 1259\,\mathrm{e}^{-2\beta h}\,\mathrm{e}^{3\beta\mu} + 267\,\mathrm{e}^{2\beta h}\,\mathrm{e}^{3\beta\mu} + 325\,\mathrm{e}^{-2\beta h}\,\mathrm{e}^{4\beta\mu}\\
&\quad + 57\,\mathrm{e}^{2\beta h}\,\mathrm{e}^{4\beta\mu} + 1720\,\mathrm{e}^{-4\beta h}\,\mathrm{e}^{2\beta\mu} + 62\,\mathrm{e}^{4\beta h}\,\mathrm{e}^{2\beta\mu} + 657\,\mathrm{e}^{-6\beta h}\,\mathrm{e}^{\beta\mu} + 11\,\mathrm{e}^{6\beta h}\,\mathrm{e}^{\beta\mu} + 1200\,\mathrm{e}^{-4\beta h}\,\mathrm{e}^{3\beta\mu}\\
&\quad + 58\,\mathrm{e}^{4\beta h}\,\mathrm{e}^{3\beta\mu} + 331\,\mathrm{e}^{-4\beta h}\,\mathrm{e}^{4\beta\mu} + 8\,\mathrm{e}^{4\beta h}\,\mathrm{e}^{4\beta\mu} + 1078\,\mathrm{e}^{-6\beta h}\,\mathrm{e}^{2\beta\mu} + 274\,\mathrm{e}^{-8\beta h}\,\mathrm{e}^{\beta\mu} + 703\,\mathrm{e}^{-6\beta h}\,\mathrm{e}^{3\beta\mu}
\end{aligned}
$$

$$+ 7\,\mathrm{e}^{6\beta h}\,\mathrm{e}^{3\beta\mu} + 189\,\mathrm{e}^{-6\beta h}\,\mathrm{e}^{4\beta\mu} + 406\,\mathrm{e}^{-8\beta h}\,\mathrm{e}^{2\beta\mu} + 82\,\mathrm{e}^{-10\beta h}\,\mathrm{e}^{\beta\mu} + 266\,\mathrm{e}^{-8\beta h}\,\mathrm{e}^{3\beta\mu} + 56\,\mathrm{e}^{-8\beta h}\,\mathrm{e}^{4\beta\mu}$$
$$+ 88\,\mathrm{e}^{-10\beta h}\,\mathrm{e}^{2\beta\mu} + 12\,\mathrm{e}^{-12\beta h}\,\mathrm{e}^{\beta\mu} + 56\,\mathrm{e}^{-10\beta h}\,\mathrm{e}^{3\beta\mu} + 9\,\mathrm{e}^{-10\beta h}\,\mathrm{e}^{4\beta\mu} + 12\,\mathrm{e}^{-12\beta h}\,\mathrm{e}^{2\beta\mu} + 4\,\mathrm{e}^{-12\beta h}\,\mathrm{e}^{3\beta\mu}$$
$$+ \mathrm{e}^{-12\beta h}\,\mathrm{e}^{4\beta\mu} + \mathrm{e}^{-14\beta h}\,\mathrm{e}^{2\beta\mu},$$

$$c \cdot e^{-4\beta h'} \overset{!}{=} e^{-\beta\hat{H}'(-1,-1,-1,-1)}$$
$$= 1087\,\mathrm{e}^{-2\beta h} + 199\,\mathrm{e}^{2\beta h} + 1184\,\mathrm{e}^{-4\beta h} + 26\,\mathrm{e}^{4\beta h} + 891\,\mathrm{e}^{-6\beta h} + 482\,\mathrm{e}^{-8\beta h} + 191\,\mathrm{e}^{-10\beta h} + 60\,\mathrm{e}^{-12\beta h} + 19\,\mathrm{e}^{-14\beta h}$$
$$+ 6\,\mathrm{e}^{-16\beta h} + \mathrm{e}^{-18\beta h} + 52\,\mathrm{e}^{\beta\mu} + 210\,\mathrm{e}^{2\beta\mu} + 68\,\mathrm{e}^{3\beta\mu} + 32\,\mathrm{e}^{4\beta\mu} + 360\,\mathrm{e}^{-2\beta h}\,\mathrm{e}^{\beta\mu} + 693\,\mathrm{e}^{-2\beta h}\,\mathrm{e}^{2\beta\mu}$$
$$+ 27\,\mathrm{e}^{2\beta h}\,\mathrm{e}^{2\beta\mu} + 948\,\mathrm{e}^{-4\beta h}\,\mathrm{e}^{\beta\mu} + 444\,\mathrm{e}^{-2\beta h}\,\mathrm{e}^{3\beta\mu} + 128\,\mathrm{e}^{-2\beta h}\,\mathrm{e}^{4\beta\mu} + 4\,\mathrm{e}^{2\beta h}\,\mathrm{e}^{4\beta\mu} + 1332\,\mathrm{e}^{-4\beta h}\,\mathrm{e}^{2\beta\mu}$$
$$+ 1240\,\mathrm{e}^{-6\beta h}\,\mathrm{e}^{\beta\mu} + 1100\,\mathrm{e}^{-4\beta h}\,\mathrm{e}^{3\beta\mu} + 294\,\mathrm{e}^{-4\beta h}\,\mathrm{e}^{4\beta\mu} + 1724\,\mathrm{e}^{-6\beta h}\,\mathrm{e}^{2\beta\mu} + 944\,\mathrm{e}^{-8\beta h}\,\mathrm{e}^{\beta\mu} + 1360\,\mathrm{e}^{-6\beta h}\,\mathrm{e}^{3\beta\mu}$$
$$+ 374\,\mathrm{e}^{-6\beta h}\,\mathrm{e}^{4\beta\mu} + 1516\,\mathrm{e}^{-8\beta h}\,\mathrm{e}^{2\beta\mu} + 516\,\mathrm{e}^{-10\beta h}\,\mathrm{e}^{\beta\mu} + 984\,\mathrm{e}^{-8\beta h}\,\mathrm{e}^{3\beta\mu} + 260\,\mathrm{e}^{-8\beta h}\,\mathrm{e}^{4\beta\mu} + 832\,\mathrm{e}^{-10\beta h}\,\mathrm{e}^{2\beta\mu}$$
$$+ 224\,\mathrm{e}^{-12\beta h}\,\mathrm{e}^{\beta\mu} + 456\,\mathrm{e}^{-10\beta h}\,\mathrm{e}^{3\beta\mu} + 90\,\mathrm{e}^{-10\beta h}\,\mathrm{e}^{4\beta\mu} + 268\,\mathrm{e}^{-12\beta h}\,\mathrm{e}^{2\beta\mu} + 64\,\mathrm{e}^{-14\beta h}\,\mathrm{e}^{\beta\mu} + 128\,\mathrm{e}^{-12\beta h}\,\mathrm{e}^{3\beta\mu}$$
$$+ 12\,\mathrm{e}^{-12\beta h}\,\mathrm{e}^{4\beta\mu} + 48\,\mathrm{e}^{-14\beta h}\,\mathrm{e}^{2\beta\mu} + 8\,\mathrm{e}^{-16\beta h}\,\mathrm{e}^{\beta\mu} + 16\,\mathrm{e}^{-14\beta h}\,\mathrm{e}^{3\beta\mu} + 4\,\mathrm{e}^{-16\beta h}\,\mathrm{e}^{2\beta\mu} + 630.$$

We set

$$\hat{H}' \overset{!}{=} -h' \sum_{\langle \mathbf{I},\mathbf{J}\rangle} \hat{\tau}^x_{\langle \mathbf{I},\mathbf{J}\rangle} - \mu' \sum_{\mathbf{J}} \hat{n}_{\mathbf{J}}$$

and solve for $\beta \cdot h'$ and $\beta \cdot \mu'$ (neglecting constant terms in the Hamiltonian). This gives

$$\beta\mu' = \frac{1}{2}\ln\left(\frac{ce^{2\beta h'}e^{\beta\mu'} \cdot ce^{-2\beta h'}e^{\beta\mu'}}{c \cdot c}\right) = \frac{1}{2}\ln\left(\frac{e^{-\beta\hat{H}'(-1,1,1,1)} \cdot e^{-\beta\hat{H}'(-1,-1,-1,1)}}{e^{-\beta\hat{H}'(-1,-1,1,1)} \cdot e^{-\beta\hat{H}'(-1,1,-1,1)}}\right)$$

and

$$\beta h' = \frac{1}{8}\ln\left(\frac{c \cdot e^{4\beta h'}}{c \cdot e^{-4\beta h'}}\right) = \frac{1}{8}\ln\left(\frac{e^{-\beta\hat{H}'(1,1,1,1)}}{e^{-\beta\hat{H}'(-1,-1,-1,-1)}}\right). \tag{B2}$$

The difference between the approximate Hamiltonian obtained in this way and the exactly renormalized Hamiltonian—i.e., the effect of dropping the higher order terms in Eq. (7)—is evaluated by comparing the respective Boltzmann factors (normalized by the corresponding partition sums) as follows:

$$\epsilon\left(\left\{\hat{\tau}^x_{\langle \mathbf{I},\mathbf{J}\rangle}\right\}, \beta h, \beta\mu\right) := \frac{\exp\left[-\beta\hat{H}'\left(\left\{\hat{\tau}^x_{\langle \mathbf{I},\mathbf{J}\rangle}\right\}, h, \mu\right)\right]}{\exp\left(-\beta\hat{H}'[(1,1,1,1), h, \mu]\right) + \cdots + \exp\left(-\beta\hat{H}'[(1,1,1,1), h, \mu]\right)} \tag{B3}$$
$$- \frac{\exp\left(\beta h' \sum_{\langle \mathbf{I},\mathbf{J}\rangle} \hat{\tau}^x_{\langle \mathbf{I},\mathbf{J}\rangle} + \beta\mu' \sum_{\mathbf{J}} \hat{n}_{\mathbf{J}}\right)}{\exp\left[\beta h' \cdot (1+1+1+1) + \beta\mu' \cdot 0\right] + \cdots + \exp\left[\beta h' \cdot (-1-1-1-1) + \beta\mu' \cdot 0\right]}. \tag{B4}$$

The numerical value of these higher order terms depends on the chosen macrostate and on the coupling parameters. However, plugging in the formulas above, we note that the absolute value of these terms is small in all cases

$$\left|\epsilon\left(\left\{\hat{\tau}^x_{\langle \mathbf{I},\mathbf{J}\rangle}\right\}, \beta h, \beta\mu\right)\right| \leqslant 10^{-4} \quad \text{for all } \left\{\hat{\tau}^x_{\langle \mathbf{I},\mathbf{J}\rangle}\right\}, \beta h, \beta\mu \tag{B5}$$

and thus the higher-order corrections scale to zero with each subsequent RG step. We conclude that the higher order corrections are negligible for the RG transformation and the qualitative phase diagram.

This results in the flow diagram shown in Figs. 4 and 1. In particular, all $(\beta h, \beta\mu)$ with $\beta\mu > -\infty$ and $\beta h > 0$ flow to the nonpercolating fixed point at $\beta\mu = 0$, $\beta h = \infty$.

We can analytically take limits of the flow equations to derive the behavior on each of the axes. In the limit $\beta h = 0$ we get

$$\beta h' = \frac{1}{8}\ln\left(\frac{4068\,\mathrm{e}^{\beta\mu} + 6750\,\mathrm{e}^{2\beta\mu} + 4844\,\mathrm{e}^{3\beta\mu} + 1290\,\mathrm{e}^{4\beta\mu} + 4968}{4356\,\mathrm{e}^{\beta\mu} + 6654\,\mathrm{e}^{2\beta\mu} + 4556\,\mathrm{e}^{3\beta\mu} + 1194\,\mathrm{e}^{4\beta\mu} + 4776}\right)$$

and

$$\beta\mu' = \frac{1}{2}\ln\left(\frac{4\,\mathrm{e}^{2\beta\mu}\,(2769\,\mathrm{e}^{\beta\mu} + 1770\,\mathrm{e}^{2\beta\mu} + 427\,\mathrm{e}^{3\beta\mu} + 1966)\,(3369\,\mathrm{e}^{\beta\mu} + 2290\,\mathrm{e}^{2\beta\mu} + 579\,\mathrm{e}^{3\beta\mu} + 2214)}{\begin{array}{r}(3956\,\mathrm{e}^{\beta\mu} + 5550\,\mathrm{e}^{2\beta\mu} + 3420\,\mathrm{e}^{3\beta\mu} + 794\,\mathrm{e}^{4\beta\mu} + 1128)\\ \times\,(4452\,\mathrm{e}^{\beta\mu} + 6750\,\mathrm{e}^{2\beta\mu} + 4460\,\mathrm{e}^{3\beta\mu} + 1098\,\mathrm{e}^{4\beta\mu} + 1160)\end{array}}\right).$$

Thus we (approximately) stay on this axis and flow towards the fixed point $(\beta h, \beta\mu) = (0, -0.077)$. The system percolates at the point $(\beta h, \beta\mu) = (0, 0)$ and flows from there to this fixed point, implying percolation for all $(\beta h, \beta\mu) = (0, \beta\mu)$.

In the limit $\beta\mu = -\infty$ (pure gauge) we get $\beta\mu' = -\infty$ and

$$\beta h' = \frac{1}{8}\ln\left(\frac{\begin{array}{r}\mathrm{e}^{12\beta h}\,(56\,\mathrm{e}^{2\beta h} + 237\,\mathrm{e}^{4\beta h} + 517\,\mathrm{e}^{6\beta h} + 648\,\mathrm{e}^{8\beta h} + 512\,\mathrm{e}^{10\beta h} + 303\,\mathrm{e}^{12\beta h}\\ + 139\,\mathrm{e}^{14\beta h} + 46\,\mathrm{e}^{16\beta h} + 14\,\mathrm{e}^{18\beta h} + 5\,\mathrm{e}^{20\beta h} + \mathrm{e}^{22\beta h} + 6)\end{array}}{\begin{array}{r}(5\,\mathrm{e}^{2\beta h} + 14\,\mathrm{e}^{4\beta h} + 46\,\mathrm{e}^{6\beta h} + 145\,\mathrm{e}^{8\beta h} + 337\,\mathrm{e}^{10\beta h} + 554\,\mathrm{e}^{12\beta h}\\ + 630\,\mathrm{e}^{14\beta h} + 457\,\mathrm{e}^{16\beta h} + 173\,\mathrm{e}^{18\beta h} + 26\,\mathrm{e}^{20\beta h} + 1)\end{array}}\right).$$

Thus for $\beta h > 0.29$ and for $\beta h < 0.074$ we have $\beta h' > \beta h$ and for $0.074 < \beta h < 0.29$ we have $\beta h' < \beta h$.

In the limit $\beta\mu = 0$ (Bernoulli percolation), the flow equations give

$$\beta h' = \frac{1}{8}\ln\left(\frac{\begin{array}{r}324\,\mathrm{e}^{-2\beta h} + 2780\,\mathrm{e}^{2\beta h} + 62\,\mathrm{e}^{-4\beta h} + 4846\,\mathrm{e}^{4\beta h} + 6\,\mathrm{e}^{-6\beta h} + 5585\,\mathrm{e}^{6\beta h}\\ + 4234\,\mathrm{e}^{8\beta h} + 2115\,\mathrm{e}^{10\beta h} + 692\,\mathrm{e}^{12\beta h} + 145\,\mathrm{e}^{14\beta h} + 18\,\mathrm{e}^{16\beta h} + \mathrm{e}^{18\beta h} + 1112\end{array}}{\begin{array}{r}2712\,\mathrm{e}^{-2\beta h} + 230\,\mathrm{e}^{2\beta h} + 4858\,\mathrm{e}^{-4\beta h} + 26\,\mathrm{e}^{4\beta h} + 5589\,\mathrm{e}^{-6\beta h} + 4186\,\mathrm{e}^{-8\beta h}\\ + 2085\,\mathrm{e}^{-10\beta h} + 692\,\mathrm{e}^{-12\beta h} + 147\,\mathrm{e}^{-14\beta h} + 18\,\mathrm{e}^{-16\beta h} + \mathrm{e}^{-18\beta h} + 992\end{array}}\right)$$

and thus $\beta h' > \beta h$ for all $\beta h > 0$ on this axis. For the limit $\beta h \to \infty$ there is only one allowed configuration—the configuration with zero electric strings. Thus the RG flow is not uniquely defined in this limit. Because the flow equations give $|\beta\mu'| < |\beta\mu|$ for large enough βh, we define the flow in this limit the same way, e.g., $\beta\mu' := \beta\mu + 1$.

Altogether we obtain the RG flow depicted in Figs. 1(b) and 4.

APPENDIX C: CORRESPONDENCE TO SITE-BOND PERCOLATION

We give a rough bound of the consequences which percolation corrections have on the confinement phase diagram by comparing to a site-bond percolation problem.

Note that $|\delta\rho| \lesssim 0.08$ for all $(\beta h, \beta\mu)$ with the maximum value being attained at $(\beta h, \beta\mu) \to (0, -\infty)$. In the uncorrelated limit, the effect on the confinement phase diagram corresponds to a site-bond percolation problem. The site-bond percolation problem considers a lattice on which both sites and bonds can be randomly occupied [38]. The correspondence is then established by assigning occupancy to macrosites in a given RG step according to whether the percolation carries through the corresponding microconfiguration. Specifically, we say for a bond-percolating block configuration that the central site is occupied if and only if the microconfiguration percolates. (Note that the occupation of sites defined here is distinct from the charges defined above.) In the worst case we thus have a site occupation probability of $1 - \delta\rho \approx 0.92$. On the curve of critical Bernoulli site-bond percolation this corresponds to a bond occupation probability of 0.56 [39,40].

It follows that the critical bond occupation probability is shifted in the uncorrelated system by at most 0.06. Assuming that the effect is similar in the correlated system, we can conclude that the percolation corrections do not affect the RG flow for large enough βh (small T/h).

APPENDIX D: DETAILS OF PERCOLATION FLOW

The percolation change is defined by the difference in percolation probabilities of the the renormalized configuration and the original configuration. To calculate this, we check for each microconfiguration on a block whether or not it percolates and compare this to the percolation of the assigned macroconfiguration.

The percolation flow depends on the path with respect to which we define percolation, e.g., from left to right or from the bottom to the right. To simplify, we take the average over all such paths, shown in Fig. 9.

The resulting percolation change is

$$\begin{aligned}\delta\rho(\beta h, \beta\mu) = \frac{1}{Z(\beta h, \beta\mu)} \cdot \frac{1}{6}\big(&2470\,\mathrm{e}^{-2\beta h} - 68\,\mathrm{e}^{2\beta h} + 2630\,\mathrm{e}^{-4\beta h} - 418\,\mathrm{e}^{4\beta h} + 1712\,\mathrm{e}^{-6\beta h} - 277\,\mathrm{e}^{6\beta h} + 682\,\mathrm{e}^{-8\beta h}\\
&- 124\,\mathrm{e}^{8\beta h} + 170\,\mathrm{e}^{-10\beta h} - 44\,\mathrm{e}^{10\beta h} + 36\,\mathrm{e}^{-12\beta h} - 10\,\mathrm{e}^{12\beta h} + 6\,\mathrm{e}^{-14\beta h} - \mathrm{e}^{14\beta h} - 1712\,\mathrm{e}^{\beta\mu} - 1108\,\mathrm{e}^{2\beta\mu}\\
&- 126\,\mathrm{e}^{3\beta\mu} + 220\,\mathrm{e}^{4\beta\mu} - 1360\,\mathrm{e}^{-2\beta h}\,\mathrm{e}^{\beta\mu} - 1646\,\mathrm{e}^{2\beta h}\,\mathrm{e}^{\beta\mu} - 977\,\mathrm{e}^{-2\beta h}\,\mathrm{e}^{2\beta\mu} - 1517\,\mathrm{e}^{2\beta h}\,\mathrm{e}^{2\beta\mu}\\
&- 808\,\mathrm{e}^{-4\beta h}\,\mathrm{e}^{\beta\mu} - 1290\,\mathrm{e}^{4\beta h}\,\mathrm{e}^{\beta\mu} - 170\,\mathrm{e}^{-2\beta h}\,\mathrm{e}^{3\beta\mu} - 208\,\mathrm{e}^{2\beta h}\,\mathrm{e}^{3\beta\mu} + 120\,\mathrm{e}^{-2\beta h}\,\mathrm{e}^{4\beta\mu} + 156\,\mathrm{e}^{2\beta h}\,\mathrm{e}^{4\beta\mu}\\
&- 1172\,\mathrm{e}^{-4\beta h}\,\mathrm{e}^{2\beta\mu} - 1316\,\mathrm{e}^{4\beta h}\,\mathrm{e}^{2\beta\mu} - 396\,\mathrm{e}^{-6\beta h}\,\mathrm{e}^{\beta\mu} - 786\,\mathrm{e}^{6\beta h}\,\mathrm{e}^{\beta\mu} - 400\,\mathrm{e}^{-4\beta h}\,\mathrm{e}^{3\beta\mu} - 260\,\mathrm{e}^{4\beta h}\,\mathrm{e}^{3\beta\mu}\\
&- 64\,\mathrm{e}^{-4\beta h}\,\mathrm{e}^{4\beta\mu} + 26\,\mathrm{e}^{4\beta h}\,\mathrm{e}^{4\beta\mu} - 933\,\mathrm{e}^{-6\beta h}\,\mathrm{e}^{2\beta\mu} - 645\,\mathrm{e}^{6\beta h}\,\mathrm{e}^{2\beta\mu} - 138\,\mathrm{e}^{-8\beta h}\,\mathrm{e}^{\beta\mu} - 318\,\mathrm{e}^{8\beta h}\,\mathrm{e}^{\beta\mu}\\
&- 580\,\mathrm{e}^{-6\beta h}\,\mathrm{e}^{3\beta\mu} - 194\,\mathrm{e}^{6\beta h}\,\mathrm{e}^{3\beta\mu} - 170\,\mathrm{e}^{-6\beta h}\,\mathrm{e}^{4\beta\mu} - 26\,\mathrm{e}^{6\beta h}\,\mathrm{e}^{4\beta\mu} - 400\,\mathrm{e}^{-8\beta h}\,\mathrm{e}^{2\beta\mu} - 184\,\mathrm{e}^{8\beta h}\,\mathrm{e}^{2\beta\mu}\\
&- 22\,\mathrm{e}^{-10\beta h}\,\mathrm{e}^{\beta\mu} - 70\,\mathrm{e}^{10\beta h}\,\mathrm{e}^{\beta\mu} - 470\,\mathrm{e}^{-8\beta h}\,\mathrm{e}^{3\beta\mu} - 76\,\mathrm{e}^{8\beta h}\,\mathrm{e}^{3\beta\mu} - 132\,\mathrm{e}^{-8\beta h}\,\mathrm{e}^{4\beta\mu} - 14\,\mathrm{e}^{8\beta h}\,\mathrm{e}^{4\beta\mu}\end{aligned}$$

$$\begin{aligned}
&- 86\,\mathrm{e}^{-10\beta h}\,\mathrm{e}^{2\beta\mu} - 34\,\mathrm{e}^{10\beta h}\,\mathrm{e}^{2\beta\mu} - 6\,\mathrm{e}^{12\beta h}\,\mathrm{e}^{\beta\mu} - 188\,\mathrm{e}^{-10\beta h}\,\mathrm{e}^{3\beta\mu} - 12\,\mathrm{e}^{10\beta h}\,\mathrm{e}^{3\beta\mu} - 66\,\mathrm{e}^{-10\beta h}\,\mathrm{e}^{4\beta\mu}\\
&- 2\,\mathrm{e}^{10\beta h}\,\mathrm{e}^{4\beta\mu} - 8\,\mathrm{e}^{-12\beta h}\,\mathrm{e}^{2\beta\mu} - 4\,\mathrm{e}^{12\beta h}\,\mathrm{e}^{2\beta\mu} - 28\,\mathrm{e}^{-12\beta h}\,\mathrm{e}^{3\beta\mu} - 24\,\mathrm{e}^{-12\beta h}\,\mathrm{e}^{4\beta\mu} - 4\,\mathrm{e}^{-14\beta h}\,\mathrm{e}^{4\beta\mu}\\
&+ 1168\Big)
\end{aligned}$$

and is normalized by the partition sum

$$\begin{aligned}
Z(\beta h, \beta\mu) = {}& 2796\,\mathrm{e}^{-2\beta h} + 2796\,\mathrm{e}^{2\beta h} + 1924\,\mathrm{e}^{-4\beta h} + 1924\,\mathrm{e}^{4\beta h} + 1086\,\mathrm{e}^{-6\beta h} + 1086\,\mathrm{e}^{6\beta h} + 512\,\mathrm{e}^{-8\beta h} + 512\,\mathrm{e}^{8\beta h}\\
&+ 194\,\mathrm{e}^{-10\beta h} + 194\,\mathrm{e}^{10\beta h} + 60\,\mathrm{e}^{-12\beta h} + 60\,\mathrm{e}^{12\beta h} + 19\,\mathrm{e}^{-14\beta h} + 19\,\mathrm{e}^{14\beta h} + 6\,\mathrm{e}^{-16\beta h} + 6\,\mathrm{e}^{16\beta h}\\
&+ \mathrm{e}^{-18\beta h} + \mathrm{e}^{18\beta h} + 12336\,\mathrm{e}^{\beta\mu} + 18360\,\mathrm{e}^{2\beta\mu} + 11904\,\mathrm{e}^{3\beta\mu} + 2832\,\mathrm{e}^{4\beta\mu} + 11072\,\mathrm{e}^{-2\beta h}\,\mathrm{e}^{\beta\mu}\\
&+ 11072\,\mathrm{e}^{2\beta h}\,\mathrm{e}^{\beta\mu} + 16444\,\mathrm{e}^{-2\beta h}\,\mathrm{e}^{2\beta\mu} + 16444\,\mathrm{e}^{2\beta h}\,\mathrm{e}^{2\beta\mu} + 7936\,\mathrm{e}^{-4\beta h}\,\mathrm{e}^{\beta\mu} + 7936\,\mathrm{e}^{4\beta h}\,\mathrm{e}^{\beta\mu}\\
&+ 10800\,\mathrm{e}^{-2\beta h}\,\mathrm{e}^{3\beta\mu} + 10800\,\mathrm{e}^{2\beta h}\,\mathrm{e}^{3\beta\mu} + 2646\,\mathrm{e}^{-2\beta h}\,\mathrm{e}^{4\beta\mu} + 2646\,\mathrm{e}^{2\beta h}\,\mathrm{e}^{4\beta\mu} + 11848\,\mathrm{e}^{-4\beta h}\,\mathrm{e}^{2\beta\mu}\\
&+ 11848\,\mathrm{e}^{4\beta h}\,\mathrm{e}^{2\beta\mu} + 4480\,\mathrm{e}^{-6\beta h}\,\mathrm{e}^{\beta\mu} + 4480\,\mathrm{e}^{6\beta h}\,\mathrm{e}^{\beta\mu} + 8032\,\mathrm{e}^{-4\beta h}\,\mathrm{e}^{3\beta\mu} + 8032\,\mathrm{e}^{4\beta h}\,\mathrm{e}^{3\beta\mu}\\
&+ 2084\,\mathrm{e}^{-4\beta h}\,\mathrm{e}^{4\beta\mu} + 2084\,\mathrm{e}^{4\beta h}\,\mathrm{e}^{4\beta\mu} + 6900\,\mathrm{e}^{-6\beta h}\,\mathrm{e}^{2\beta\mu} + 6900\,\mathrm{e}^{6\beta h}\,\mathrm{e}^{2\beta\mu} + 2016\,\mathrm{e}^{-8\beta h}\,\mathrm{e}^{\beta\mu}\\
&+ 2016\,\mathrm{e}^{8\beta h}\,\mathrm{e}^{\beta\mu} + 4816\,\mathrm{e}^{-6\beta h}\,\mathrm{e}^{3\beta\mu} + 4816\,\mathrm{e}^{6\beta h}\,\mathrm{e}^{3\beta\mu} + 1282\,\mathrm{e}^{-6\beta h}\,\mathrm{e}^{4\beta\mu} + 1282\,\mathrm{e}^{6\beta h}\,\mathrm{e}^{4\beta\mu}\\
&+ 3232\,\mathrm{e}^{-8\beta h}\,\mathrm{e}^{2\beta\mu} + 3232\,\mathrm{e}^{8\beta h}\,\mathrm{e}^{2\beta\mu} + 768\,\mathrm{e}^{-10\beta h}\,\mathrm{e}^{\beta\mu} + 768\,\mathrm{e}^{10\beta h}\,\mathrm{e}^{\beta\mu} + 2240\,\mathrm{e}^{-8\beta h}\,\mathrm{e}^{3\beta\mu}\\
&+ 2240\,\mathrm{e}^{8\beta h}\,\mathrm{e}^{3\beta\mu} + 568\,\mathrm{e}^{-8\beta h}\,\mathrm{e}^{4\beta\mu} + 568\,\mathrm{e}^{8\beta h}\,\mathrm{e}^{4\beta\mu} + 1180\,\mathrm{e}^{-10\beta h}\,\mathrm{e}^{2\beta\mu} + 1180\,\mathrm{e}^{10\beta h}\,\mathrm{e}^{2\beta\mu}\\
&+ 256\,\mathrm{e}^{-12\beta h}\,\mathrm{e}^{\beta\mu} + 256\,\mathrm{e}^{12\beta h}\,\mathrm{e}^{\beta\mu} + 752\,\mathrm{e}^{-10\beta h}\,\mathrm{e}^{3\beta\mu} + 752\,\mathrm{e}^{10\beta h}\,\mathrm{e}^{3\beta\mu} + 166\,\mathrm{e}^{-10\beta h}\,\mathrm{e}^{4\beta\mu}\\
&+ 166\,\mathrm{e}^{10\beta h}\,\mathrm{e}^{4\beta\mu} + 312\,\mathrm{e}^{-12\beta h}\,\mathrm{e}^{2\beta\mu} + 312\,\mathrm{e}^{12\beta h}\,\mathrm{e}^{2\beta\mu} + 64\,\mathrm{e}^{-14\beta h}\,\mathrm{e}^{\beta\mu} + 64\,\mathrm{e}^{14\beta h}\,\mathrm{e}^{\beta\mu} + 160\,\mathrm{e}^{-12\beta h}\,\mathrm{e}^{3\beta\mu}\\
&+ 160\,\mathrm{e}^{12\beta h}\,\mathrm{e}^{3\beta\mu} + 28\,\mathrm{e}^{-12\beta h}\,\mathrm{e}^{4\beta\mu} + 28\,\mathrm{e}^{12\beta h}\,\mathrm{e}^{4\beta\mu} + 52\,\mathrm{e}^{-14\beta h}\,\mathrm{e}^{2\beta\mu} + 52\,\mathrm{e}^{14\beta h}\,\mathrm{e}^{2\beta\mu} + 8\,\mathrm{e}^{-16\beta h}\,\mathrm{e}^{\beta\mu}\\
&+ 8\,\mathrm{e}^{16\beta h}\,\mathrm{e}^{\beta\mu} + 16\,\mathrm{e}^{-14\beta h}\,\mathrm{e}^{3\beta\mu} + 16\,\mathrm{e}^{14\beta h}\,\mathrm{e}^{3\beta\mu} + 2\,\mathrm{e}^{-14\beta h}\,\mathrm{e}^{4\beta\mu} + 2\,\mathrm{e}^{14\beta h}\,\mathrm{e}^{4\beta\mu} + 4\,\mathrm{e}^{-16\beta h}\,\mathrm{e}^{2\beta\mu}\\
&+ 4\,\mathrm{e}^{16\beta h}\,\mathrm{e}^{2\beta\mu} + 3188.
\end{aligned}$$

To estimate the total percolation change $\Delta\rho(\beta h, \beta\mu) = \sum_{n=0}^{\infty} \delta\rho_n$ for the flow starting at some point in parameter space, we sum over the percolation change from the RG steps starting at this point.

We note that $\delta\rho$ is positive only in the region with $\beta\mu \ll 0$ and βh small enough. Because the flow from any point $(\beta h, \beta\mu) \neq (\beta h, -\infty)$ eventually leaves this region, $\Delta\rho$ cannot be positive for any such parameter values. For $\beta\mu = -\infty$ we find the percolation transition point $[\Delta\rho(\beta h, -\infty) = 0]$ to be the largest βh from which the flow ends in the region with positive $\delta\rho$. The transition thus occurs at $(\beta h, \beta\mu) = (1/3.48\dots, -\infty)$. The exact critical point is at $(\beta h, \beta\mu) = (1/2.27\dots, -\infty)$.

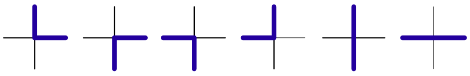

FIG. 9. Percolating paths through a block. There are several percolating paths through a block with respect to which the percolation change can be defined. In our calculations, we take the average over all such paths.

APPENDIX E: DATA ANALYSIS WITH MONTE CARLO SNAPSHOTS

In this section, we consider another method to analyze the renormalization group flow.

We first perform Monte Carlo simulations of the model (3). The RG steps are then applied directly on the resulting snapshots which yields a data set of smaller, renormalized snapshots. For coupling strengths βh, $\beta\mu$ in the vicinity of a fixed point, there should be little change in the snapshots generated this way when compared to Monte Carlo snapshots with no RG step applied. For coupling parameters far from any fixed point, the RG step significantly changes the lattice configurations. This effect is more prominent after several RG steps are applied.

In order to define an objective metric of similarity in sets of lattice snapshots, we train a neural network to distinguish these data sets. The change from applying an RG step is then quantified by the success rate of this neural network in distinguishing the data sets.

Table II shows the results for a set of 10 000 Monte Carlo snapshots with system size 75×75. The renormalization procedure from Sec. III A asymptotically halves the system length at each step, but the block covering has constant losses at the edges. Thus applying an RG step to a state

TABLE II. Distinction accuracies of the neural network. We generate 10 000 Monte Carlo snapshots with system size 75 × 75 and open boundary conditions. To combat boundary effects, a square of size 45 × 45 from the center of these snapshots is used. We apply two RG steps to the first 5000 snapshots. The resulting 9 × 9 lattice configurations are compared to same size cutouts from applying one RG step to the remaining 5000 snapshots. A neural network with three hidden layers is trained on 80% of the data and tested on the remaining 20%. We show the distinction accuracies of the trained neural network between the data sets with two RG steps and with one RG step.

Percolating phase $T/h = +\infty, T/\mu = -0.5$	Nonpercolating phase $T/h = 1.0, T/\mu = -0.5$	Near RG fixed point $T/h = 3.48, T/\mu = -3.48 \times 10^{-4}$	Near exact fixed point $T/h = 2.27, T/\mu = -2.27 \times 10^{-4}$
80.45%	49.45%	72.50%	77.10%

of size $(4k+1) \times (4k+1)$ yields a configuration with size $(2k-1) \times (2k-1)$. We can see that the effect of the RG step is indiscernible for the nonpercolating configurations, i.e., the neural network accuracy is no better than a random guess. At the chosen parameters, most of the configurations are empty and so the renormalization has little effect. We recognize this as the trivial nonpercolating fixed point at $T/h = 0$. In the percolating phase at $T/h = +\infty$, the high accuracy shows that a single RG step strongly affects the system, indicating that the flow has not yet reached a fixed point. The accuracies near the critical fixed point at $T/h = 3.48$, $T/\mu = 0$ are harder to interpret and we would have expected lower accuracies in this case. It is possible that the results are due to the smaller system size, effects from the open boundaries, or T/μ being nonzero.

Overall this method yields no striking results for the model at hand. It is however interesting since it could easily be applied to analyze other models where snapshots are available, e.g., from quantum Monte Carlo simulations or experimental data.

---

[1] J. Greensite, *An Introduction to the Confinement Problem* (Springer, Berlin, 2011).

[2] R. Pasechnik and M. Šumbera, Different faces of confinement, Universe **7**, 330 (2021).

[3] K. G. Wilson, Confinement of quarks, Phys. Rev. D **10**, 2445 (1974).

[4] J. B. Kogut, The lattice gauge theory approach to quantum chromodynamics, Rev. Mod. Phys. **55**, 775 (1983).

[5] E. Fradkin and S. H. Shenker, Phase diagrams of lattice gauge theories with Higgs fields, Phys. Rev. D **19**, 3682 (1979).

[6] P. E. Lammert, D. S. Rokhsar, and J. Toner, Topology and nematic ordering. I. A gauge theory, Phys. Rev. E **52**, 1778 (1995).

[7] A. Kitaev, Fault-tolerant quantum computation by anyons, Ann. Phys. (NY) **303**, 2 (2003).

[8] K. J. Satzinger, Y.-J. Liu, A. Smith, C. Knapp, M. Newman, C. Jones, Z. Chen, C. Quintana, X. Mi, A. Dunsworth, C. Gidney, I. Aleiner, F. Arute, K. Arya, J. Atalaya *et al.*, Realizing topologically ordered states on a quantum processor, Science **374**, 1237 (2021).

[9] G. Semeghini, H. Levine, A. Keesling, S. Ebadi, T. T. Wang, D. Bluvstein, R. Verresen, H. Pichler, M. Kalinowski, R. Samajdar, A. Omran, S. Sachdev, A. Vishwanath, M. Greiner, V. Vuletić *et al.*, Probing topological spin liquids on a programmable quantum simulator, Science **374**, 1242 (2021).

[10] L. Barbiero, C. Schweizer, M. Aidelsburger, E. Demler, N. Goldman, and F. Grusdt, Coupling ultracold matter to dynamical gauge fields in optical lattices: From flux attachment to $\mathbb{Z}_2$ lattice gauge theories, Sci. Adv. **5**, eaav7444 (2019).

[11] C. Schweizer, F. Grusdt, M. Berngruber, L. Barbiero, E. Demler, N. Goldman, I. Bloch, and M. Aidelsburger, Floquet approach to $\mathbb{Z}_2$ lattice gauge theories with ultracold atoms in optical lattices, Nat. Phys. **15**, 1168 (2019).

[12] L. Homeier, A. Bohrdt, S. Linsel, E. Demler, J. C. Halimeh, and F. Grusdt, Realistic scheme for quantum simulation of $\mathbb{Z}_2$ lattice gauge theories with dynamical matter in (2+1)D, Commun. Phys. **6**, 127 (2023).

[13] A. Polyakov, Compact gauge fields and the infrared catastrophe, Phys. Lett. B **59**, 82 (1975).

[14] G. 't Hooft, On the phase transition towards permanent quark confinement, Nucl. Phys. B **138**, 1 (1978).

[15] K. Fredenhagen and M. Marcu, Charged states in $\mathbb{Z}_2$ gauge theories, Commun. Math. Phys. **92**, 81 (1983).

[16] K. Fredenhagen and M. Marcu, Confinement criterion for qcd with dynamical quarks, Phys. Rev. Lett. **56**, 223 (1986).

[17] W.-T. Xu, F. Pollmann, and M. Knap, Critical behavior of the Fredenhagen-Marcu order parameter at topological phase transitions, arXiv:2402.00127.

[18] S. M. Linsel, A. Bohrdt, L. Homeier, L. Pollet, and F. Grusdt, Percolation as a confinement order parameter in $\mathbb{Z}_2$ lattice gauge theories, Phys. Rev. B **110**, L241101 (2024).

[19] P. J. Reynolds, H. E. Stanley, and W. Klein, A real-space renormalization group for site and bond percolation, J. Phys. C **10**, L167 (1977).

[20] J. W. Essam, Percolation theory, Rep. Prog. Phys. **43**, 833 (1980).

[21] K. G. Wilson, Renormalization group and critical phenomena. I. Renormalization group and the Kadanoff scaling picture, Phys. Rev. B **4**, 3174 (1971).

[22] L. P. Kadanoff, Scaling laws for Ising models near T_c, Phys. Phys. Fiz. **2**, 263 (1966).

[23] P. W. Anderson, A poor man's derivation of scaling laws for the Kondo problem, J. Phys. C **3**, 2436 (1970).

[24] E. T. Tomboulis, Long distance dynamics and confinement via RG decimations, Mod. Phys. Lett. A **24**, 2717 (2009).

[25] J. Braun, H. Gies, and J. M. Pawlowski, Quark confinement from colour confinement, Phys. Lett. B **684**, 262 (2010).

[26] M. C. Ogilvie, Quark confinement and the renormalization group, Philos. Trans. R. Soc. A **369**, 2718 (2011).

[27] J. Bernasconi, Real-space renormalization of bond-disordered conductance lattices, Phys. Rev. B **18**, 2185 (1978).

[28] M. F. Sykes and J. W. Essam, Critical percolation probabilities by series methods, Phys. Rev. **133**, A310 (1964).

[29] H. Kesten, The critical probability of bond percolation on the square lattice equals 1/2, Commun. Math. Phys. **74**, 41 (1980).

[30] M. F. Sykes and J. W. Essam, Exact critical percolation probabilities for site and bond problems in two dimensions, J. Math. Phys. **5**, 1117 (1964).

[31] J. Wang, Z. Zhou, W. Zhang, T. M. Garoni, and Y. Deng, Bond and site percolation in three dimensions, Phys. Rev. E **87**, 052107 (2013).

[32] E. Fradkin and L. Susskind, Order and disorder in gauge systems and magnets, Phys. Rev. D **17**, 2637 (1978).

[33] F. J. Wegner, Duality in generalized Ising models and phase transitions without local order parameters, J. Math. Phys. **12**, 2259 (1971).

[34] M. B. Hastings, G. H. Watson, and R. G. Melko, Self-correcting quantum memories beyond the percolation threshold, Phys. Rev. Lett. **112**, 070501 (2014).

[35] A. Kolmogoroff, Über die summen durch den zufall bestimmter unabhängiger größen, Math. Ann. **99**, 309 (1928).

[36] G. Grimmett, *Percolation* (Springer, Berlin, 1999).

[37] M. Kebrič, L. Barbiero, C. Reinmoser, U. Schollwöck, and F. Grusdt, Confinement and mott transitions of dynamical charges in one-dimensional lattice gauge theories, Phys. Rev. Lett. **127**, 167203 (2021).

[38] H. L. Frisch and J. M. Hammersley, Percolation processes and related topics, J. Soc. Ind. Appl. Math. **11**, 894 (1963).

[39] M. Yanuka and R. Englman, Bond-site percolation: empirical representation of critical probabilities, J. Phys. A: Math. Gen. **23**, L339 (1990).

[40] Y. Y. Tarasevich and S. C. van der Marck, An investigation of site-bond percolation on many lattices, Int. J. Mod. Phys. C **10**, 1193 (1999).

2.10 Publication 4: Independent e- and m-Anyon Confinement in the Parallel Field Toric Code on Non-Square Lattices

In this section, the following publication is reprinted:

P4 *Independent e- and m-Anyon Confinement in the Parallel Field Toric Code on Non-Square Lattices*,
Simon M. Linsel, Lode Pollet, and Fabian Grusdt,
PRX Quantum **7**, 010332 (2026), ©2026 American Physical Society,
doi: 10.1103/gtth-cclr.
Reprinted on pages 88–99.

PRX QUANTUM **7,** 010332 (2026)

Independent e- and m-Anyon Confinement in the Parallel Field Toric Code on Non-Square Lattices

Simon M. Linsel,[1,2,*] Lode Pollet,[1,2] and Fabian Grusdt[1,2]

[1] *Department of Physics and Arnold Sommerfeld Center for Theoretical Physics (ASC), Ludwig-Maximilians-Universität München, Theresienstr. 37, München D-80333, Germany*
[2] *Munich Center for Quantum Science and Technology (MCQST), Schellingstr. 4, D-80799 München, Germany*

(Received 10 April 2025; revised 1 October 2025; accepted 5 December 2025; published 13 February 2026)

Kitaev's toric code has become one of the most studied models in physics and is highly relevant to the fields of both quantum error correction and condensed matter physics. Most notably, it is the simplest known model hosting an extended, deconfined topological bulk phase. To this day, it remains challenging to reliably and robustly probe topological phases, as many state-of-the-art order parameters are sensitive to specific models and even specific parameter regimes. With the emergence of powerful quantum simulators which are approaching the regimes of topological bulk phases, there is a timely need for experimentally accessible order parameters. Here we study the ground state physics of the parallel field toric code on the honeycomb, triangular, and cubic lattices using continuous-time quantum Monte Carlo. By extending the concept of experimentally accessible percolation-inspired order parameters (POPs) we show that electric and magnetic anyons are independently confined on the honeycomb and triangular lattices, unlike on the square lattice. Our work manifestly demonstrates that, even in the ground state, we must make a distinction between topological order and (de-)confinement. Moreover, we report multicritical points in the aforementioned confinement phase diagrams. Finally, we map out the topological phase diagrams on the honeycomb, triangular, and cubic lattices and compare the performance of the POPs with other topological order parameters. Our work paves the way for studies of confinement involving dynamical matter and the associated multicritical points in contemporary quantum simulation platforms for $\mathbb{Z}_2$ lattice gauge theories.

DOI: 10.1103/gtth-cclr

I. INTRODUCTION

Quantum models featuring topological order [1–3] are one of the main research directions in modern condensed matter physics. They are highly relevant for the study of the integer [4] and fractional [5] quantum Hall effect, quantum spin liquids [6], and quantum error correction [7]. Topological phases have intriguing features such as degenerate, long-range entangled ground states and point-like excitations ("anyons") in two-dimensional systems, which fulfill neither fermionic nor bosonic statistics but can instead pick up *any* phase (hence the name) when braiding two anyons [8,9]. As a result, the topological phases remain stable against local perturbations and thus constitute an important class of models for fault-tolerant quantum computing [7,10].

The toric code, originally studied by Kitaev [7], is generally regarded as the simplest model featuring $\mathbb{Z}_2$ topological order and anyons. Fradkin and Shenker [11] famously studied the extended toric code, i.e., the toric code in a parallel field, on the square lattice. At zero temperature, it features two phases separated by a continuous phase transition: an extended topological deconfined phase for small fields and a trivial confined phase for large fields which encloses a first-order line that ends at a multicritical point [11,12] whose universality class is still a topic of debate [7,13–21]. Other recent studies suggest that the qualitative structure of the phase diagram also holds on the honeycomb, triangular, and cubic lattices [22,23], yet numerically exact studies have not been reported.

There is a timely need for experimentally accessible order parameters due to the emergence of quantum simulators enabling snapshot measurements [24–30] and moving toward the regimes of quantum spin liquids [31]. Topological phases inherently involve nonlocal entanglement and importantly cannot be probed using local order parameters

---

[*] Contact author: simon.linsel@lmu.de

known from the Ginzburg-Landau paradigm. In the last few decades, a plethora of methods have been established to probe topological phases, ranging from topological entanglement entropy [32–34] to string-loop order operators derived from Wegner-Wilson [35,36] and 't Hooft loops [37]. A fundamental challenge is that most topology probes are tailored to specific analytical, numerical or experimental frameworks and are not easily accessible to other methods. For example, the topological entanglement entropy can usually be extracted with the density matrix renormalization group [38] or wavefunction-based approaches; however, it requires a gap and is challenging to extract from both quantum Monte Carlo (QMC) (requiring the replica trick [39]) and experiments [40].

Here we map out the topological and confinement phase diagrams of the extended toric code on the honeycomb, triangular, and cubic lattices using a numerically exact state-of-the-art continuous-time QMC algorithm [12]. We demonstrate that e-anyons and m-anyons are independently confined on the triangular and honeycomb lattices. To this end, we generalize the recently proposed percolation-inspired order parameters (POPs) [41,42]—which are experimentally accessible to snapshot measurements and were shown to capture the phases of the Fradkin-Shenker model—from e-anyons to m-anyons. The topological phase is identified with the phase where both e- and m-anyons are deconfined [11] (see Fig. 1). We find a set of multicritical points in the topological and confinement phase diagrams that closely resemble the structure of the Fradkin-Shenker phase diagram. Finally, we compare the POP performance with two other order parameters: a staggered imaginary times observable (SIT) and the Fredenhagen-Marcu loop operator (FM).

II. EXTENDED TORIC CODE

We study the extended toric code, described by the Hamiltonian

$$\hat{\mathcal{H}} = -\sum_v \hat{A}_v - \sum_p \hat{B}_p - h_x \sum_l \hat{\tau}_l^x - h_z \sum_l \hat{\tau}_l^z, \tag{1}$$

where Pauli matrices $\hat{\tau}_l^x$ and $\hat{\tau}_l^z$ are defined on the links l of the underlying lattice. The star term $\hat{A}_v = \prod_{l\in v} \hat{\tau}_l^x$ describes the interaction of all links l connected to a vertex v and the magnetic term $\hat{B}_p = \prod_{l\in p} \hat{\tau}_l^z$ describes the interaction of links on an elementary plaquette p of the respective lattice. The terms $\propto h_x, h_z$ are external fields. In this work, we only consider $h_x, h_z \geq 0$ and periodic boundaries.

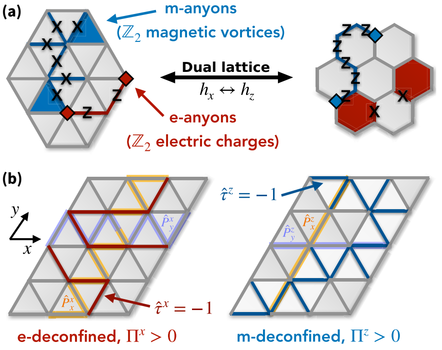

FIG. 1. Link- and plaquette percolation as confinement order parameters for e- and m-anyons in the extended toric code (1). (a) On the left, we start with a triangular lattice in the ground state of the bare toric code ($h_x = h_z = 0$), i.e., $\hat{A}_v = \hat{B}_p = 1$ everywhere. Applying $\hat{\tau}^z$-perturbations ("Z") on a cluster of neighboring links creates a pair of frustrated stars ($\hat{A}_v = -1$) at the open ends of the cluster, which are associated with pointlike e-anyons living on lattice sites (red). Applying $\hat{\tau}^x$-perturbations ("X") on a cluster of links connecting neighboring plaquettes creates a pair of frustrated plaquettes ($\hat{B}_p = -1$) at the open ends of the cluster, which are associated with pointlike m-anyons living on plaquettes (blue). The problem can be mapped to the dual lattice (here: honeycomb lattice) where the meaning of e- and m-anyons is swapped along with the fields ($h_x \leftrightarrow h_z$). (b) In the e-deconfined phase a percolating cluster of links with $\hat{\tau}^x = -1$ winds around the periodic lattice in at least one spatial dimension (here $\hat{P}^x_x = \hat{P}^x_y = -1$), corresponding to a nonzero percolation probability $\Pi^x > 0$. In the m-deconfined phase a percolating plaquette cluster connected by links with $\hat{\tau}^z = -1$ winds around the periodic lattice in at least one spatial dimension (here $\hat{P}^z_x = 1, \hat{P}^z_y = -1$), corresponding to a nonzero plaquette percolation probability $\Pi^z > 0$.

The bare toric code, i.e., $h_x = h_z = 0$, features an exactly solvable topological ground state with $\hat{A}_v = \hat{B}_p = 1 \ \forall \ v, p$ which is an equal superposition of closed loops of connected links with $\hat{\tau}^x = -1$ ($\hat{\tau}^z = -1$) on the (dual) lattice, typically referred to as a "quantum loop gas." The four topological sectors of the ground state can be equally distinguished in the $\hat{\tau}^x$- or $\hat{\tau}^z$-basis by the expectation values of noncontractible loop operators, measuring the winding number parity in x- or y-direction,

$$\hat{P}^x_{x/y} = \prod_{l\in\tilde{\gamma}_{y/x}} \hat{\tau}^x_l, \tag{2}$$

$$\hat{P}^z_{x/y} = \prod_{l\in\gamma_{y/x}} \hat{\tau}^z_l, \tag{3}$$

where γ_α ($\tilde{\gamma}_\alpha$) is a noncontractible loop winding around the α-direction ($\alpha \in \{x, y\}$) of the (dual) lattice. We illustrate the winding number parity in Fig. 1(b).

Two-dimensional toric codes feature two types of anyonic excitations [illustrated in Fig. 1(a)]: e-anyons ($\mathbb{Z}_2$ electric charges) are pointlike excitations on a frustrated star ($\hat{A}_v = -1$). They can be created in pairs by applying $\hat{\tau}^z$-perturbations on neighboring links on the bare toric code ground state with $\hat{A}_v = \hat{B}_p = 1$ everywhere, thus creating a cluster of links with $\hat{\tau}^x = -1$. m-anyons ($\mathbb{Z}_2$ magnetic vortices) are pointlike excitations associated with a frustrated plaquette ($\hat{B}_p = -1$). They can be created in pairs by applying $\hat{\tau}^x$-perturbations on links connecting elementary plaquettes on the ground state, thus creating a plaquette cluster connected by links with $\hat{\tau}^z = -1$. For the bare toric code $h_x, h_z = 0$, anyons are thermal excitations of the ground state.

When performing a duality mapping [35], i.e., identifying plaquettes with sites, e-anyons on a two-dimensional lattice can be identified with m-anyons on the dual lattice and vice versa [see Fig. 1(a)]. In the case of the self-dual Fradkin-Shenker model [11], i.e., the extended toric code on the square lattice, e-anyons behave identically to m-anyons upon changing $h_x \leftrightarrow h_z$. This is reflected in the naming of the model's two phases, the confined (topological) phase where both e- and m-anyons are confined (deconfined). Crucially, this is not the case for the toric code on the triangular and the honeycomb lattice which are instead dual to each other. Later we will show that e- and m-anyons are independently confined on the triangular and honeycomb lattices.

Different classes of order parameters are commonly used in the literature to probe topological order. The first class are string-loop order operators derived from Wegner-Wilson [35,36] and 't Hooft loops [37]. A prominent example is the FM, which was introduced in the context of $\mathbb{Z}_2$ lattice gauge theories [43–45]. Its equal-time variant is defined as

$$O^{x/z}_{\text{FM}} = \lim_{L\to\infty} \frac{\langle \prod_{l\in\mathcal{C}^{x/z}_{1/2}} \hat{\tau}_l^{x/z}\rangle}{\sqrt{|\langle \prod_{l\in\mathcal{C}^{x/z}} \hat{\tau}_l^{x/z}\rangle|}}, \qquad (4)$$

where $\mathcal{C}^{x/z}$ is a closed contour of links with perimeter $\mathcal{O}(L)$ at equal imaginary time on the lattice ($\hat{\tau}^z$-basis; "Wegner-Wilson loop") or the dual lattice ($\hat{\tau}^x$-basis; "'t Hooft loop"); $\mathcal{C}^{x/z}_{1/2}$ is an open contour with two open ends that contains half the links of $\mathcal{C}^{x/z}$. The FM order parameter measures the response of the system when two e-anyons (m-anyons) are spatially separated and relates it to the response of the bulk, thus circumventing the problem that for nonzero h_z (h_x) regular Wegner-Wilson ('t Hooft) loops follow a perimeter (area) law in both the trivial and the topological phase [46,47]. Another variant that circumvents the above problem is locally error-corrected decoration [48], where a renormalization group procedure is used to remove anyons from snapshots before measuring the string-loop operators.

In the context of continuous-time QMC, a SIT order parameter local in space but nonlocal in imaginary time has shown some success [12]. It can be defined as

$$O^{x/z}_{\text{SIT}} = \frac{1}{\beta}\Big[(\tau_1^k - 0) - (\tau_2^k - \tau_1^k) + \cdots + (-1)^{N(k)-1} (\tau^k_{N(k)} - \tau^k_{N(k)-1}) + (-1)^{N(k)}(\beta - \tau^k_{N(k)})\Big], \qquad (5)$$

where τ_n^k is the imaginary time of the nth tuple spin flip of type k. k is an elementary plaquette p (star s) of links when sampling in the $\hat{\tau}^x$-basis ($\hat{\tau}^z$-basis) [49]. For details, see Ref. [12].

Recently, POPs have been proposed in the context of e-confinement in $\mathbb{Z}_2$ lattice gauge theories [41]. They measure the winding number of connected clusters C of adjacent links l with $\hat{\tau}_l^x = -1\ \forall\ l \in C$. The physical intuition comes from the picture of fluctuating $\hat{\tau}^x$-fields which connect pairs of e-anyons in local clusters in the confined phase and form global percolating clusters in the deconfined (topological) phase [see Fig. 1(b)]. In its simplest form, the *percolation probability* can be written as the expectation value $\langle\hat{\Pi}^x\rangle$ of the projector

$$\hat{\Pi}^x = \sum_{W(j)\neq 0} |\{\hat{\tau}^x\}_j\rangle\langle\{\hat{\tau}^x\}_j| \qquad (6)$$

over all possible configurations $\{\hat{\tau}^x\}_j$ with nonzero winding number $W(j)$, i.e., configurations with zero winding number have $\Pi^x = 0$. Pictorially, $\hat{\Pi}^x$ measures whether it is possible to traverse the system only on links l with $\hat{\tau}_l^x = -1$, hence the name "percolation probability." Similar order parameters have been used in the context of quantum chromodynamics [50–52].

Here, we not only measure percolation in the $\hat{\tau}^x$-basis to probe the confinement of e-anyons but also extend the definition, by analogy, to the $\hat{\tau}^z$-basis to measure the confinement of m-anyons. Instead of bond percolation, we calculate the *plaquette percolation probability* Π^z where two neighboring plaquettes p_1 and p_2 are part of the same cluster iff they share a link $l \in p_1, p_2$ with $\hat{\tau}_l^z = -1$ [see Fig. 1(b)].

For the quantum loop gas, i.e., the fourfold degenerate ground state of the bare toric code, only noncontractible, percolating loops lead to $\hat{P}^x_{x/y} = -1$ ($\hat{P}^z_{x/y} = -1$) since all contractible loops contribute an overall factor of $+1$ to the winding number parity by construction [see Fig. 1(b)]. The topological sector with $\hat{P}^x_x = \hat{P}^x_y = 1$ ($\hat{P}^z_x = \hat{P}^z_y = 1$) is compatible with percolating loops, hosting, e.g., two percolating clusters or one percolating cluster with an even, nonzero winding number. Thus the topological quantum loop gas has the necessary condition $\Pi^x, \Pi^z > 0$ as a *direct consequence of its topological degeneracy*, underlining that percolation is a very natural quantity to probe in the context of topological phases. We will demonstrate that this conjecture also holds for the toric code subject to a finite external field. Even the absence of percolation in one basis, i.e., the confinement of either e- or m-anyons, already implies a topologically trivial phase.

We will measure and compare the FM, SIT, and POPs to gain insights into the ground state phase diagram of the extended toric code (1) on various lattices. All three order parameters are basis-dependent and it is practically impossible to reproduce results from the $\hat{\tau}^x$-basis in the $\hat{\tau}^z$-basis and vice versa, reflecting the absence of a local order parameter. Therefore, we will study both and combine their total information to understand the phase diagrams.

III. PHASE DIAGRAMS

A. Honeycomb lattice

On the honeycomb lattice, we simulate periodic systems up to $L^2 = 32^2$ in terms of unit cells at $T = 1/L$ and take up to 3×10^4 snapshots for every data point. A recent work [23] provides a good starting point for interesting parameter ranges. We repeat our parameter scans in both the $\hat{\tau}^x$- and $\hat{\tau}^z$-bases and calculate the FM, SIT, POPs, and other observables like the energy for every QMC snapshot. Here and in the following, all error bars are calculated using either the integrated autocorrelation time or the stationary bootstrap [53–55].

We show the e-confinement phase diagram in Fig. 2(a). We observe an extended e-deconfined phase with $\Pi^x > 0$ that is persistent for finite fields $h_x, h_z > 0$ and an e-confined phase with $\Pi^x = 0$ for large fields. For h_x-scans at small h_z, we find a continuous phase transition to the e-confined regime. At $h_z = 0$, the model can be exactly mapped to the transverse-field Ising model (TFIM) on the *triangular* lattice [23], whose phase transition is known to be in the $(2+1)$D Ising universality class [implying $(2+1)$D Ising* for the extended toric code]. Our critical field $h_{x,c} = 0.210(2)$ is in good agreement with TFIM QMC studies which yield $h_{x,c}^{\mathrm{TFIM}} \approx 0.209$ [56]. We repeat the finite-size scaling for the SIT and the results agree with the POPs. The FM order parameter does capture the phase transition from the e-deconfined phase into the e-confined phase ($h_x \gg 1$) but not into the Higgs phase ($h_z \gg 1$), where it is too noisy to be evaluated. The QMC sampling in the $\hat{\tau}^x$-basis becomes vastly inefficient for high h_z because spins are more aligned with the perpendicular $\hat{\tau}^z$-operator. As a result, the observables in this range tend to be noisy and a high number of snapshots is required. For larger fields $h_z \geq 0.3$, the POP Binder cumulants do not show a crossing point for the simulated system sizes, but we still observe a clear drop to $\Pi^x = 0$ for large fields h_x, h_z, see inset. Similarly, for h_z-scans we do not find SIT Binder cumulant crossing points for the simulated system sizes, but we observe an abrupt rise in O^{SIT} at the critical fields (known from the duality to the triangular lattice). We also study a classical limit of the extended toric code (1) on the honeycomb lattice in Appendix A.

In Fig. 2(b), we show the m-confinement phase diagram. For h_z-scans, we observe a transition from an m-deconfined regime with $\Pi^z > 0$ to an m-confined regime with $\Pi^z = 0$. At $h_x = 0$ the critical value is $h_{z,c} = 0.475(5)$ obtained by a crossing-point analysis. This value is confirmed by the SIT and FM order parameters. In stark contrast to the e-confinement, we do not observe a transition into an m-confined regime for large h_x but small h_z. The system remains m-deconfined and $\Pi^z > 0$, while it is e-confined and $\Pi^x = 0$, hence, e- and m-anyons can be independently confined at zero temperature. For details, see Appendix B.

Another interesting feature of the m-confinement phase diagram in Fig. 2(b) is the existence of a first-order phase boundary between the m-deconfined and m-confined phase which starts at a multicritical point around the tip of the e-deconfined phase in Fig. 2(a) at $(h_z, h_x) = (0.485(5), 0.225(5))$ and ends at a multicritical point $(h_z, h_x) = (0.61(1), 0.34(1))$ after which we find a percolation transition (dashed line). This transition is a feature of POPs and important for confinement, but crucially does not signal a topological phase transition, i.e., it is compatible with the Fradkin-Shenker theorem [11]. The first-order nature is signaled by a double-peak structure of the histogram of the probability distribution of observables obtained from QMC snapshots, indicating the coexistence of two phases. We find the double-peak structure not only in Π^z but also in the energy which is a clear sign that this first-order line is indeed physical. An exemplary histogram is shown in the inset of Fig. 2(c). Crucially, the first-order line is not visible in Π^x.

We identify the topological phase with the phase where both e- and m-anyons are deconfined and show the resulting topological phase diagram on the honeycomb lattice in Fig. 3(a). The phase diagram is constructed using the FM, SIT, and POPs in the $\hat{\tau}^x$- ($\hat{\tau}^z$-) basis for h_x- (h_z-) sweeps and all order parameters agree. It is reminiscent of previous studies [23] and qualitatively similar to the square lattice [12]. Interestingly, it exhibits a first-order line akin to the Fradkin-Shenker phase diagram.

B. Triangular lattice

Our approach on the triangular lattice is similar to the honeycomb lattice. We simulate periodic systems up to $L^2 = 32^2$ in terms of unit cells at $T = 1/L$ and take up to 3×10^4 snapshots for every data point. We use the duality between the triangular and honeycomb lattice toric code to identify interesting parameter regimes. We repeat our parameter scans in both the $\hat{\tau}^x$- and $\hat{\tau}^z$-bases and calculate the FM, SIT, POPs, and other observables like the energy for every QMC snapshot.

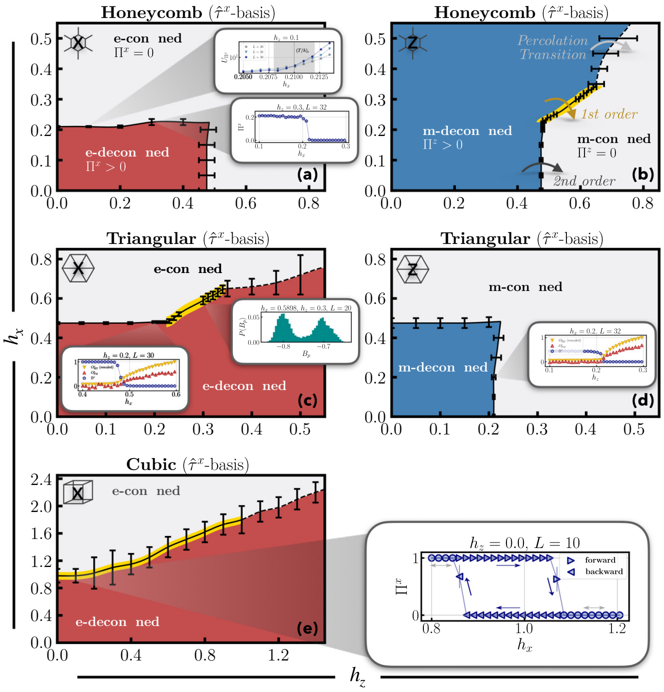

FIG. 2. e- and m-confinement phase diagram of the extended toric code (1) on the honeycomb, triangular, and cubic lattices. We apply continuous-time quantum Monte Carlo at temperature $T = 1/L$ to gain insights into the ground state phase diagram and use a crossing-point analysis of Binder cumulants U to extract the critical fields [see inset of (a)]. On the left (right), we sample in the $\hat{\tau}^x$-basis ($\hat{\tau}^z$-basis) and measure the percolation probability Π^x (plaquette percolation probability Π^z), the Fredenhagen-Marcu loop operator, and the staggered imaginary times observable order parameters. (a) and (b) The honeycomb lattice features an extended e-deconfined region with $\Pi^x > 0$ for small h_x, h_z and an e-confined region with $\Pi^x = 0$ for larger h_x, h_z which are separated by a continuous phase transition. m-anyons are always deconfined ($\Pi^z > 0$) for small h_z, giving rise to an e-confined, m-deconfined regime. For large h_z, m-anyons feature a confined phase. The phase boundary features two multicritical points between which the phase transition is of first-order type. For even higher fields, Π^z has a percolation transition (dashed line) which is not relevant for topology. (c) and (d) The toric code on the triangular lattice is dual to the honeycomb lattice, and the phase diagram is identical to the honeycomb lattice when exchanging the basis $\hat{\tau}^x \leftrightarrow \hat{\tau}^z$ and $h_x \leftrightarrow h_z$. We identify an m-confined, e-deconfined regime for large h_z. (e) On the cubic lattice, the confinement of e-anyons is qualitatively similar to the triangular lattice but features a first-order phase transition (yellow phase boundary, see inset for hysteresis curve) between the e-deconfined (e-confined) region at small (large) h_x. The first-order line ends at a multicritical point around $(h_z, h_x) = (1.0(1), 1.8(2))$ after which we find a percolation transition (dashed line). (a)–(e) We identify the topological phase with the regime where both e- and m-anyons are deconfined. The Fredenhagen-Marcu loop operator and the staggered imaginary times observable order parameters can generally probe the topological phase transition in the $\hat{\tau}^z$-basis ($\hat{\tau}^x$-basis) for h_z-scans (h_x-scans) [see insets in (c) and (d)]. In the other two cases, i.e., in the $\hat{\tau}^x$-basis ($\hat{\tau}^z$-basis) for h_z-scans (h_x-scans) the staggered imaginary times observable features crossover behavior and the Fredenhagen-Marcu loop operator is too noisy to be evaluated. Additional data are presented in Appendix B.

We show the e-confinement phase diagram in Fig. 2(c). Due to the duality to the honeycomb lattice, it is identical to Fig. 2(b) when exchanging $h_x \leftrightarrow h_z$. We observe an extended e-deconfined phase with $\Pi^x > 0$ that is persistent for finite fields $h_x, h_z > 0$. For h_x-scans, we observe a continuous phase transition to an e-confined regime where $\Pi^x = 0$. The critical fields have been extracted using a Binder cumulant crossing-point analysis. At $h_z = 0$, the

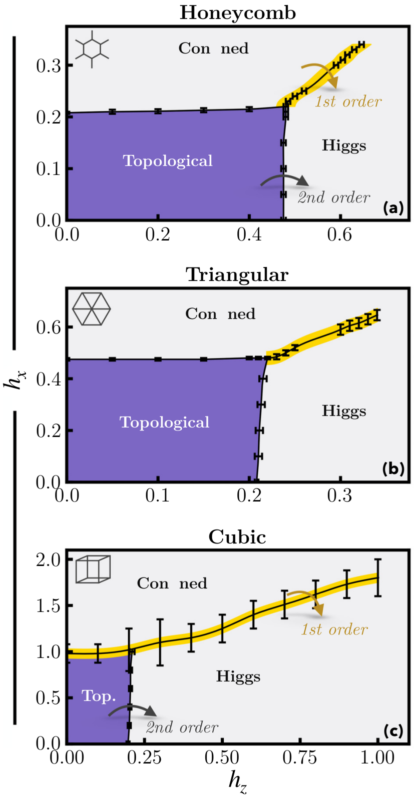

FIG. 3. Topological phase diagram of the extended toric code (1) on the honeycomb, triangular, and cubic lattices. We construct the topological phase diagram using ground state quantum Monte Carlo calculations for the FM, SIT, and POPs which are partially shown in Fig. 2. The general structure of the phase diagram is remarkably similar to the Fradkin-Shenker model [11] for all lattices: the system features an extended topological phase that is persistent for finite fields $h_x, h_z > 0$. The critical line $h_{x,c}(h_z)$ ($h_{z,c}(h_x)$)—extracted using a finite-size scaling analysis—is convex, i.e., it slightly shifts up for increasing h_z (h_x). A first-order line starts at a multicritical point at the tip of the topological phase and ends at a multicritical point in the trivial phase. (a) Honeycomb lattice: a continuous phase transition separates the topological from the trivial regime ($h_x, h_z \gg 1$). (b) Triangular lattice: the honeycomb lattice is dual to the triangular lattice, which is reflected in the topological phase diagram ($h_x \leftrightarrow h_z$). (c) Cubic lattice: the system features a first-order phase transition as we increase h_x while fixing h_z (yellow phase boundary). The phase boundary where h_x is kept constant is associated with a continuous phase transition (solid line).

model can be exactly mapped to the TFIM on the *honeycomb* lattice [35], whose phase transition is in the $(2+1)$D Ising universality class. Our critical field $h_{x,c} = 0.475(5)$ is in good agreement with TFIM QMC studies which yield $h_{x,c}^{\mathrm{TFIM}} \approx 0.469$ [56]. We repeat the finite-size scaling for the SIT and the results agree with the POPs (see inset for FM and SIT results). As on the honeycomb lattice, we observe the first-order line between the multicritical points $(h_z, h_x) = (0.225(5), 0.485(5))$ and $(h_z, h_x) = (0.34(1), 0.61(1))$.

For even higher h_z, we find a percolation transition (dashed line). We can explain this transition by looking at the limit $h_x = 0, h_z \to \infty$ where all spins are magnetized in $\hat{\tau}^z$-direction, see Appendix B. In the $\hat{\tau}^x$-basis, the spins are completely random and independent, i.e., we have Bernoulli bond percolation with a probability $p = 0.5$ which is larger than the Bernoulli bond percolation threshold on the triangular lattice, $p_{c,\mathrm{tri}} \approx 0.35$ [57,58], hence $\Pi^x > 0$. In the other limit $h_z = 0, h_x \to \infty$, all spins are magnetized in $\hat{\tau}^x$-direction, hence $\Pi^x = 0$. The dashed line is the percolation transition between these two limits. On the cubic lattice, the Bernoulli bond percolation threshold is $p_{c,\mathrm{cu}} = 0.247(5)$ [57], indicating a similar situation as on the triangular lattice [see discussion, Fig. 2(e)]. On the honeycomb lattice, however, the Bernoulli bond percolation threshold is $p_{c,\mathrm{hon}} \approx 0.65$ [57,58], thus both limits are e-confined, confirming our numerical result in Fig. 2(a).

In Fig. 2(d), we show the m-confinement phase diagram. The phase diagram is identical to the e-confinement phase diagram of the honeycomb lattice when exchanging $h_x \leftrightarrow h_z$. An extended m-deconfined phase for small fields $h_x, h_z > 0$ has a continuous phase transition to an m-confined phase for larger fields. For large h_z, the system is e-deconfined but m-confined. The SIT Binder cumulant crossing points confirm the phase boundaries of Π^z (see inset for FM and SIT results). The (physical) first-order line cannot be probed using Π^z.

We show the resulting topological phase diagram on the triangular lattice in Fig. 3(b). The duality between the toric code on the triangular and honeycomb lattice is reflected in the topological phase diagram ($h_x \leftrightarrow h_z$).

C. Cubic lattice

We study the cubic lattice toric code with plaquette interactions, i.e., the interaction of 4 links on cube faces but crucially *not* with cubic interactions of 12 links. The star interaction is a 6-qubit term involving all links in three spatial dimensions connected to a given site. In general, the correct definition of a POP in three dimensions heavily depends on the details of the model. For example, cube interactions lead to a different excitation structure than plaquette interactions. For this reason, we do not study m-confinement with percolation but instead rely on the SIT and FM to map out the topological phase boundaries.

We simulate periodic systems up to $L^3 = 16^3$ in terms of unit cells at $T = 1/L$ and take up to 10^4 snapshots for every data point. An earlier work [22] provides a good starting point for interesting parameter ranges. We repeat our parameter scans in both the $\hat{\tau}^x$- and $\hat{\tau}^z$-bases and calculate the FM, SIT, POPs, and other observables like the energy for every QMC snapshot.

We show the e-confinement phase diagram in Fig. 2(e). We detect an extended e-deconfined phase with $\Pi^x > 0$ that is persistent for finite fields $h_x, h_z > 0$. For h_x-scans, we observe a first-order phase transition to an e-confined regime, where $\Pi^x = 0$. To obtain the hysteresis curve, we used the state from the previous data point as the initial state, respectively. We observe an enormous hysteresis area (yellow phase boundaries), which we show for $h_z = 0$ in the inset. At $h_z = 0$, the model is equivalent to Wegner's 4D lattice gauge theory [35] which features a first-order transition [59,60] around the critical field $h_{x,c}^{\text{self-duality}} = 1$ [23] obtained from self-duality. Our critical field $h_{x,c} = 0.98(10)$ (the error bars are the hysteresis interval) is consistent with this result. The hysteresis is also visible in other observables like energy. The first-order phase boundary ends at a multicritical point $(h_z, h_x) = (1.0(1), 1.8(2))$. For even higher fields, Π^x has a percolation transition (dashed line).

For h_z-scans at small h_x, the system remains e-deconfined. However, it features a phase transition to the topologically trivial phase signaled by the SIT and FM in the $\hat{\tau}^z$-basis. At $h_x = 0$, the model can be exactly mapped to the TFIM on the *cubic* lattice [61], whose phase transition is in the $(3+1)$D Ising universality class (implying $(3+1)$D Ising* for the extended toric code). The critical field $h_{z,c}^{\text{TFIM}} \approx 0.194$ [62] is in good agreement with our SIT result $h_{z,c} = 0.197(05)$.

We show the resulting topological phase diagram for the cubic lattice in Fig. 3(c). It is structurally identical to the Fradkin-Shenker phase diagram except for one crucial difference: It features a first-order phase transition between the topological and trivial phase for small h_z which leads to strong hysteresis in all observables. The topological phase diagram also features a multicritical point at $(h_z, h_x) = (0.210(08), 1.0(2))$, the tip of the topological phase, and at $(h_z, h_x) = (1.0(1), 1.8(2))$, the end of the first-order line.

D. Order parameter comparison

Using the SIT, we can reliably perform a finite-size scaling analysis for the topological phase transition for h_z-scans (h_x-scans) in the $\hat{\tau}^z$-basis ($\hat{\tau}^x$-basis). In the other two cases, i.e., h_x-scans (h_z-scans) in the $\hat{\tau}^z$-basis ($\hat{\tau}^x$-basis), the SIT shows crossover behavior but it is crucially able to signal the rough phase boundary. However, it is inaccessible not only to other numerical methods without easy access to imaginary time, like tensor networks, but also to experiments. In its current definition in imaginary time, it further lacks a clear physical meaning. Like for the other order parameters, it is necessary to measure both in the $\hat{\tau}^x$- and the $\hat{\tau}^z$-basis to perform a crossing-point analysis for all topological phase boundaries, requiring separate QMC snapshots, respectively.

In contrast to the SIT, both the FM and the POPs are accessible to quantum simulators. Both can reliably probe the topological phase transition for h_z-scans (h_x-scans) in the $\hat{\tau}^z$-basis ($\hat{\tau}^x$-basis). However, the parameter range for the finite-size scaling is typically larger for the POPs, as the FM is a ratio of two exponentially small numbers which generally results in large statistical errors even for small fields h_x, h_z. In addition, the FM exhibits extreme levels of noise for h_x-scans (h_z-scans) in the $\hat{\tau}^z$-basis ($\hat{\tau}^x$-basis), rendering it practically unusable. In a recent tensor network study [47], the FM was further found to host unphysical singularities in the flux-condensing confined region ($h_x \gg 1$). The exact form of the string-loop operator has to be adapted to the problem at hand. Similarly, the POP has to be adapted for other Hamiltonians and lattices, too (e.g., for the toric code on the three-dimensional cubic lattice).

All order parameters studied in this work are basis-dependent and no single order parameter captures all phase boundaries in its Binder cumulant using only one basis. Vice versa, given one basis and all order parameters in that basis, it is impossible to faithfully calculate the full phase diagram using Binder cumulants thus far, underlining the importance of measuring in different bases. The SIT is more robust than the FM and POPs; however, the SIT is not accessible to quantum simulators, ruling it out for experimental studies.

IV. DISCUSSION AND OUTLOOK

We mapped out the phase diagrams of the extended toric code on the triangular, honeycomb, and cubic lattices using numerically exact continuous-time quantum Monte Carlo simulations, precisely determining their phase boundaries and the order of their transitions, going beyond previous work [22,23]. Our work manifestly demonstrates that, even in the ground state, we must make a distinction between topological order and (de-)confinement. Whereas topological order coincides with deconfinement of e- and m-anyons together, the probing of confinement of e- and m- anyons separately depends on the choice of basis and quantity of interest, a situation which is exacerbated for lattices that are not self-dual. In particular, choosing percolation, which has the advantage of being experimentally accessible in current-generation quantum simulators [24–30], we see that e-confinement agrees with a topologically trivial state on the honeycomb lattice in the $\hat{\tau}^x$-basis. The same is true for m-confinement on the triangular lattice in the $\hat{\tau}^z$-basis. In contrast, m-deconfinement on the honeycomb lattice in the $\hat{\tau}^z$-basis is found over a much larger area in the phase diagram compared to the topological order (and the same is true for the triangular lattice in the $\hat{\tau}^x$-basis). Other quantities, such as the SIT, which is susceptible to dynamical effects, lead to qualitatively similar but quantitatively different behavior. Conceptually similar issues were previously reported for the FM order parameter [47]. All these observations are ultimately related to the nonexistence of a local order parameter for such Ising-like transitions. Note that our results remain fully compatible with the Fradkin-Shenker argument. Our work also connects to the recently popular *PXP* model on the ruby lattice with an emergent odd $\mathbb{Z}_2$ lattice gauge theory where e- and m-deconfinement were likewise found in topologically trivial phases [63,64].

We leave for future work the detailed understanding of the universality class at the multicritical points, which recently gathered a lot of attention on the square lattice, and a more detailed study of the SIT to probe the dynamical aspects of (de-)confinement.

ACKNOWLEDGMENTS

We thank G. Dünnweber and L. Homeier for fruitful discussions. We used the open-source library PARATORIC for the continuous-time QMC simulations [65]. This research was funded by the European Research Council (ERC) under the European Union's Horizon 2020 research and innovation program—ERC Starting Grant SimUcQuam (Grant Agreement No. 948141) and QuantERA II (Grand Agreement No. 101017733), by the QuantERA grant DYNAMITE, and by the Deutsche Forschungsgemeinschaft (DFG, German Research Foundation) under Project No. 499183856 and under Germany's Excellence Strategy—EXC-2111—Project No. 390814868.

DATA AVAILABILITY

The data that support the findings of this article are not publicly available. The data are available from the authors upon reasonable request.

APPENDIX A: CLASSICAL LIMIT OF THE TORIC CODE

We perform classical Monte Carlo simulations of a classical limit of the extended toric code (1)

$$\hat{\mathcal{H}}_{\text{can}} = -h_x \hat{\mathcal{P}} \left[\sum_l \hat{\tau}^x_l\right] \hat{\mathcal{P}} \tag{A1}$$

at a finite temperature T/h_x and $h_x > 0$. We define hard-core bosons $\hat{n}_{\boldsymbol{j}}$ on lattice sites $\boldsymbol{j}$. The projector $\hat{\mathcal{P}}$ fixes the total number of hard-core bosons $N = \sum_{\boldsymbol{j}} \hat{n}_{\boldsymbol{j}}$. This highly nontrivial model has deep connections to Hamiltonian (1) and has been studied numerically [41] and analytically [42] in earlier studies. An interesting feature is the local $\mathbb{Z}_2$ gauge symmetry with the generator

$$\hat{G}_{\boldsymbol{j}} = (-1)^{\hat{n}_{\boldsymbol{j}}} \prod_{l\in +_{\boldsymbol{j}}} \hat{\tau}^x_l. \tag{A2}$$

The property $[\hat{\mathcal{H}}_{\text{can}}, \hat{G}_{\boldsymbol{j}}] = 0$ directly results in a set of locally conserved eigenvalues $\hat{G}_{\boldsymbol{j}} |\Psi\rangle = g_{\boldsymbol{j}} |\Psi\rangle$ ("background charges") which we set to $g_{\boldsymbol{j}} = +1 \ \forall\, \boldsymbol{j}$, defining a so-called "gauge sector." The eigenvalue equation is known as Gauss's law and restricts the physical Hilbert space. Note that the physics of the model depends on the choice of these background charges, it is not to be confused with a gauge transformation that leaves the physics unchanged.

In this canonical formulation, the density of matter particles d is externally fixed. Matter can be introduced into the toric code by identifying an open end of a cluster Σ of neighboring links with $\hat{\tau}^x_l = -1 \ \forall\, l \in \Sigma$, i.e., a site with an uneven number of $\hat{\tau}^x = -1$ attached to it, with a hard-core boson.

Hamiltonian (A1) can equally be formulated in a grand-canonical form where the density of bosons is controlled via a chemical potential μ,

$$\begin{aligned} \hat{\mathcal{H}}_{\text{gc}} &= -h_x \sum_l \hat{\tau}^x_l - \mu \sum_{\boldsymbol{j}} \hat{n}_{\boldsymbol{j}} \\ &= -h_x \sum_l \hat{\tau}^x_l - \mu \sum_{\boldsymbol{j}} \frac{1}{2} \left(1 - \prod_{l\in +_{\boldsymbol{j}}} \hat{\tau}^x_l\right). \end{aligned} \tag{A3}$$

Note that the chemical potential term resembles the star term in the extended toric code (1).

At $\mu = 0$, crucially without fixing the matter density, the probability p for a given link l to have $\hat{\tau}^x_l = -1$ is given by

$$p = e^{-\beta h}/[2\cosh(\beta h)], \tag{A4}$$

independently of other links, thus reducing to a Bernoulli percolation problem. An important observation is that $p \to 1/2$ as $\beta \to 0$, independent of the underlying lattice.

According to Gauss's law, matter particles are connected to a cluster Σ of neighboring links with $\hat{\tau}^x_l = -1 \ \forall\ l \in \Sigma$, where the energy cost $2h_x\ell$ grows linearly with the number of neighboring links ℓ in the cluster (note that clusters can also form closed loops without any matter). At low temperatures, matter particles form mesonic pair states, where matter particles on neighboring sites are connected by a cluster of size one ("confined phase"). At higher temperatures, as a consequence of the competition between energy and entropy, a global cluster that winds around periodic boundaries can form, where matter particles are incoherent, free $\mathbb{Z}_2$ charges ("deconfined phase") [67]. This transition is associated with a percolation transition from a nonpercolating confined regime at low temperatures to a deconfined regime at high temperatures [41]. As a finite-T phase in two dimensions, the deconfined phase is not topological but connects to the $T = 0$ topological phase of the toric code (which is also deconfined).

We simulate the periodic honeycomb lattice with system size up to $L^2 = 40^2$ and take up to 10^4 snapshots. The phase diagram is shown in Fig. 4(a). At zero matter density, the model can be mapped to the two-dimensional classical Ising model on the dual lattice [35], i.e., the triangular lattice. The critical temperature is the *triangular* lattice Ising critical temperature $(T/h_x)_c \approx 3.64$ [66]. This critical temperature is confirmed by the Monte Carlo, where we observe thermal deconfinement and a percolating phase for high temperatures. At a nonzero matter density, we do not find a thermal deconfinement transition in the thermodynamic limit, i.e., the presence of matter prohibits the formation of a percolating cluster. This behavior can be easily understood for $\mu = 0$ [golden line in Fig. 4(a)], where $p \to 1/2$ for $T/h_x \to \infty$, thus never reaching the Bernoulli (bond) percolation threshold on the honeycomb lattice, $p_{c,\text{hon}} \approx 0.65$ [57,58]. The phase diagram is structurally identical to the one of the square lattice [41], where the structure of the phase diagram was confirmed using an analytical renormalization group study [42].

The phase diagram on the triangular lattice is shown in Fig. 4(b). We simulate periodic systems up to $L^2 = 40^2$ and take up to 10^4 snapshots. At zero matter density, the critical temperature is the *honeycomb* lattice Ising critical temperature $(T/h_x)_c \approx 1.52$ [66]. In contrast to the honeycomb lattice, we find a thermal deconfinement phase transition and thus a deconfined phase at nonzero matter density. We extract the critical temperatures using a finite-size scaling analysis. Looking again at the $\mu = 0$ [golden line in Fig. 4(b)], we have $p \to 1/2$ for $T/h_x \to \infty$, thus reaching the Bernoulli (bond) percolation threshold on the triangular lattice, $p_{c,\text{tri}} \approx 0.35$ [57,58] at a finite temperature. The phase diagram is structurally identical to the one on the cubic lattice [41].

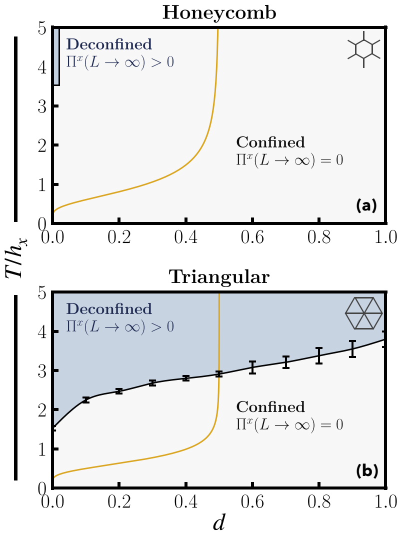

FIG. 4. Classical confinement phase diagram of Hamiltonian (A1) at finite matter density d on the honeycomb and triangular lattices. At zero matter density, the model can be mapped to the two-dimensional classical Ising model on the dual lattice [35], respectively. The golden lines correspond to Hamiltonian (A3) at $\mu = 0$. We use the percolation probability Π^x in the $\hat{\tau}^x$-basis as a confinement order parameter. (a) Honeycomb lattice: we find a thermal deconfinement transition at zero matter density. The critical temperature is the *triangular* lattice Ising critical temperature $(T/h_x)_c \approx 3.64$ [66]. At finite matter densities, the system is always nonpercolating. (b) Triangular lattice: the critical temperature at zero density is the *honeycomb* lattice Ising critical temperature $(T/h_x)_c \approx 1.52$ [66]. In contrast to the honeycomb lattice, we observe an extended region with $\Pi^x > 0$ for finite matter densities. The cubic lattice phase diagram is qualitatively similar to the triangular lattice [41].

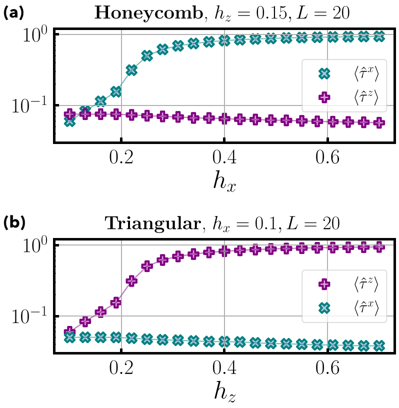

FIG. 5. Magnetizations in x- and z-direction of the extended toric code (1). We apply continuous-time quantum Monte Carlo at temperature $T = 1/L$ for $L = 20$. We calculate the x-magnetization $\langle \hat{\tau}^x \rangle$ and the z-magnetization $\langle \hat{\tau}^z \rangle$. (a) For large h_x the system is magnetized in x-direction and completely paramagnetic in z-direction, here shown for the honeycomb lattice. (b) The opposite is true for large h_z, where the system is magnetized in z-direction and paramagnetic in x-direction, here shown for the triangular lattice.

Our results can be directly related to the full quantum model studied in the main text. The topological ground states of the extended toric code (1) feature percolating clusters since charges (associated with open ends j of a cluster with $\prod_{l\in +j}\hat{\tau}_l^x = -1$) are gapped excitations and only appear in virtual pairs as a consequence of quantum fluctuations. In the Higgs phase ($h_z \gg 1$) on the other hand, charges condense and accumulate, leading to a finite density of free charges. Depending on the lattice geometry, this may prohibit percolation. On the triangular and cubic lattice [see Figs. 2(c) and 2(e)] with larger coordination number, we observe $\Pi^x > 0$ in the Higgs phase since the accumulation of charges does *not* prohibit the formation of a percolating cluster, which is directly related to the fact that the percolating phase of the classical model (A1) is persistent for a finite matter density [see Fig. 4(b)]. Conversely, on the square and honeycomb lattice with smaller coordination number we find $\Pi^x = 0$ in the Higgs phase (extrapolated on the square lattice, see Ref. [41]), since any finite matter density prohibits percolation, as evident from Fig. 4(a). Thus the classical finite-T phase diagram is deeply connected to the behavior observed in the full quantum model and explains the qualitative differences between the lattices. Our work also connects to Ref. [68], where a POP was applied at finite temperature in the context of quantum error correction.

APPENDIX B: ADDITIONAL DETAILS ON THE CONFINEMENT PHASE DIAGRAM

In Fig. 5, we show the x-magnetization $\langle\hat{\tau}^x\rangle$ and the z-magnetization $\langle\hat{\tau}^z\rangle$ with respect to the fields h_x and h_z. For high h_x (h_z) the system is magnetized in the x-direction (z-direction) and paramagnetic in the z-direction (x-direction). Thus, for high h_z the fields τ^x are completely independent and resemble Bernoulli percolation, where each bond is occupied with a probability $p = 0.5$. Depending on the lattice geometry, this probability is below (honeycomb, $p_{c,\text{hon}} \approx 0.65$ [57,58]), at (square, $p_{c,\text{sq}} = 1/2$ [57,69]), or above (triangular, $p_{c,\text{tri}} \approx 0.35$ [57,58]; cubic, $p_{c,\text{cu}} = 0.247(5)$ [57]) the percolation threshold. If $p_c < 0.5$ for a given lattice, then the system is e-deconfined for small h_x and $h_z \to \infty$. For plaquette percolation, the percolation threshold on the *dual* lattice is decisive: the system is m-deconfined for small h_z and $h_x \to \infty$ if $p_c > 0.5$ for a given lattice. The special case $p_c = 1/2$ for the square lattice is discussed in Ref. [41].

In Fig. 6, we show additional details supporting the phase diagram presented in Fig. 2. In Fig. 6(a), we show the plaquette percolation probability Π^z and tune h_x across the e-confinement transition at $h_{x,c} = 0.210(2)$. On both sides of the e-confinement transition and even for high fields h_x, the m-anyons are m-deconfined with $\Pi^z = 1$.

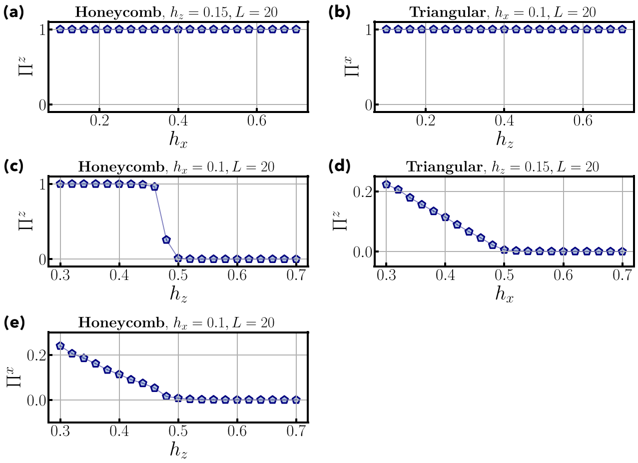

FIG. 6. (Plaquette) percolation probabilities supporting the confinement phase diagram Fig. 2 of the extended toric code (1). We apply continuous-time quantum Monte Carlo at temperature $T = 1/L$ for $L = 20$. We calculate the percolation probability Π^x ($\hat{\tau}^x$-basis) and the plaquette percolation probability Π^z ($\hat{\tau}^z$-basis), respectively. (a) For small h_z the system is m-deconfined ($\Pi^z \neq 0$) on the honeycomb lattice even for large h_x, where the system is e-confined. Hence, e- and m-anyons are independently confined in this regime. (b) Similarly, for small h_x the system is e-deconfined ($\Pi^x \neq 0$) on the triangular lattice even for large h_z, where the system is m-confined. (c)–(e) We show data for the phase boundaries for which no inset is included in Fig. 2.

Thus, e- and m-anyons are independently confined. In Fig. 6(b), we show the analog on the triangular lattice. Here, e-anyons remain deconfined for high fields h_z while m-anyons are simultaneously confined. In the topological phase at small fields h_x, h_z, both e- and m-anyons are deconfined. In Figs. 6(c)–6(e), we show exemplary plots of Π^x, Π^z for the phase boundaries for which no inset is included in Fig. 2.

[1] X.-G. Wen, Vacuum degeneracy of chiral spin states in compactified space, Phys. Rev. B **40**, 7387 (1989).

[2] X.-G. Wen, Topological orders in rigid states, Int. J. Mod. Phys. B **04**, 239 (1990).

[3] X.-G. Wen, *Quantum Field Theory of Many-Body Systems: From the Origin of Sound to an Origin of Light and Electrons* (Oxford University, Oxford, 2007), p. 520.

[4] K. v. Klitzing, G. Dorda, and M. Pepper, New method for high-accuracy determination of the fine-structure constant based on quantized Hall resistance, Phys. Rev. Lett. **45**, 494 (1980).

[5] R. B. Laughlin, Anomalous quantum Hall effect: An incompressible quantum fluid with fractionally charged excitations, Phys. Rev. Lett. **50**, 1395 (1983).

[6] L. Balents, Spin liquids in frustrated magnets, Nature **464**, 199 (2010).

[7] A. Kitaev, Fault-tolerant quantum computation by anyons, Ann. Phys. **303**, 2 (2003).

[8] J. M. Leinaas and J. Myrheim, On the theory of identical particles, Il Nuovo Cimento B (1971–1996) **37**, 1 (1977).

[9] F. Wilczek, Magnetic flux, angular momentum, and statistics, Phys. Rev. Lett. **48**, 1144 (1982).

[10] C. Nayak, S. H. Simon, A. Stern, M. Freedman, and S. Das Sarma, Non-Abelian anyons and topological quantum computation, Rev. Mod. Phys. **80**, 1083 (2008).

[11] E. Fradkin and S. H. Shenker, Phase diagrams of lattice gauge theories with Higgs fields, Phys. Rev. D **19**, 3682 (1979).

[12] F. Wu, Y. Deng, and N. Prokof'ev, Phase diagram of the toric code model in a parallel magnetic field, Phys. Rev. B **85**, 195104 (2012).

[13] J. Vidal, S. Dusuel, and K. P. Schmidt, Low-energy effective theory of the toric code model in a parallel magnetic field, Phys. Rev. B **79**, 033109 (2009).

[14] I. S. Tupitsyn, A. Kitaev, N. V. Prokof'ev, and P. C. E. Stamp, Topological multicritical point in the phase diagram of the toric code model and three-dimensional lattice gauge Higgs model, Phys. Rev. B **82**, 085114 (2010).

[15] S. Gazit, F. F. Assaad, S. Sachdev, A. Vishwanath, and C. Wang, Confinement transition of $\mathbb{Z}_2$ gauge theories coupled to massless fermions: Emergent quantum chromodynamics and SO(5) symmetry, Proc. Natl. Acad. Sci. U.S.A. **115**, E6987 (2018).

[16] A. M. Somoza, P. Serna, and A. Nahum, Self-dual criticality in three-dimensional $\mathbb{Z}_2$ gauge theory with matter, Phys. Rev. X **11**, 041008 (2021).

[17] C. Bonati, A. Pelissetto, and E. Vicari, Multicritical point of the three-dimensional $\mathbb{Z}_2$ gauge Higgs model, Phys. Rev. B **105**, 165138 (2022).

[18] C. Bonati, A. Pelissetto, and E. Vicari, Scalar gauge-Higgs models with discrete Abelian symmetry groups, Phys. Rev. E **105**, 054132 (2022).

[19] N. Iqbal and J. McGreevy, Mean string field theory: Landau-Ginzburg theory for 1-form symmetries, SciPost Phys. **13**, 114 (2022).

[20] N. Manoj and V. B. Shenoy, Arboreal topological and fracton phases, Phys. Rev. B **107**, 165136 (2023).

[21] L. Oppenheim, M. Koch-Janusz, S. Gazit, and Z. Ringel, Machine learning the operator content of the critical self-dual Ising-Higgs lattice gauge theory, Phys. Rev. Res. **6**, 043322 (2024).

[22] D. A. Reiss and K. P. Schmidt, Quantum robustness and phase transitions of the 3D Toric Code in a field, SciPost Phys. **6**, 078 (2019).

[23] V. Kott, M. Mühlhauser, J. A. Koziol, and K. P. Schmidt, Quantum robustness of the toric code in a parallel field on the honeycomb and triangular lattice, SciPost Phys. **17**, 053 (2024).

[24] E. Zohar, A. Farace, B. Reznik, and J. I. Cirac, Digital quantum simulation of $\mathbb{Z}_2$ lattice gauge theories with dynamical fermionic matter, Phys. Rev. Lett. **118**, 070501 (2017).

[25] L. Barbiero, C. Schweizer, M. Aidelsburger, E. Demler, N. Goldman, and F. Grusdt, Coupling ultracold matter to dynamical gauge fields in optical lattices: From flux attachment to $\mathbb{Z}_2$ lattice gauge theories, Sci. Adv. **5**, eaav7444 (2019).

[26] C. Schweizer, F. Grusdt, M. Berngruber, L. Barbiero, E. Demler, N. Goldman, I. Bloch, and M. Aidelsburger, Floquet approach to $\mathbb{Z}_2$ lattice gauge theories with ultracold atoms in optical lattices, Nat. Phys. **15**, 1168 (2019).

[27] L. Homeier, C. Schweizer, M. Aidelsburger, A. Fedorov, and F. Grusdt, $\mathbb{Z}_2$ lattice gauge theories and Kitaev's toric code: A scheme for analog quantum simulation, Phys. Rev. B **104**, 085138 (2021).

[28] L. Homeier, A. Bohrdt, S. Linsel, E. Demler, J. C. Halimeh, and F. Grusdt, Realistic scheme for quantum simulation of $\mathbb{Z}_2$ lattice gauge theories with dynamical matter in $(2+1)$D, Commun. Phys. **6**, 127 (2023).

[29] J. Mildenberger, W. Mruczkiewicz, J. C. Halimeh, Z. Jiang, and P. Hauke, Confinement in a $\mathbb{Z}_2$ lattice gauge theory on a quantum computer, Nat. Phys. **21**, 312 (2025).

[30] J. C. Halimeh, M. Aidelsburger, F. Grusdt, P. Hauke, and B. Yang, Cold-atom quantum simulators of gauge theories, Nat. Phys. **21**, 25 (2025).

[31] G. Semeghini, H. Levine, A. Keesling, S. Ebadi, T. T. Wang, D. Bluvstein, R. Verresen, H. Pichler, M. Kalinowski, R. Samajdar, A. Omran, S. Sachdev, A. Vishwanath, M. Greiner, V. Vuletić, and M. D. Lukin, Probing topological spin liquids on a programmable quantum simulator, Science **374**, 1242 (2021).

[32] A. Kitaev and J. Preskill, Topological entanglement entropy, Phys. Rev. Lett. **96**, 110404 (2006).

[33] M. Levin and X.-G. Wen, Detecting topological order in a ground state wave function, Phys. Rev. Lett. **96**, 110405 (2006).

[34] X. Chen, Z.-C. Gu, and X.-G. Wen, Local unitary transformation, long-range quantum entanglement, wave function renormalization, and topological order, Phys. Rev. B **82**, 155138 (2010).

[35] F. J. Wegner, Duality in generalized Ising models and phase transitions without local order parameters, J. Math. Phys. **12**, 2259 (1971).

[36] K. G. Wilson, Confinement of quarks, Phys. Rev. D **10**, 2445 (1974).

[37] G. 't Hooft, On the phase transition towards permanent quark confinement, Nucl. Phys. B **138**, 1 (1978).

[38] U. Schollwöck, The density-matrix renormalization group in the age of matrix product states, Ann. Phys. **326**, 96 (2011).January 2011 Special Issue.

[39] R. G. Melko, A. B. Kallin, and M. B. Hastings, Finite-size scaling of mutual information in Monte Carlo simulations: Application to the spin-$\frac{1}{2}$ xxz model, Phys. Rev. B **82**, 100409(R) (2010).

[40] R. Ott, T. V. Zache, N. Maskara, M. D. Lukin, P. Zoller, and H. Pichler, Probing topological entanglement on large scales, Phys. Rev. Lett. **135**, 090401 (2025).

[41] S. M. Linsel, A. Bohrdt, L. Homeier, L. Pollet, and F. Grusdt, Percolation as a confinement order parameter in $\mathbb{Z}_2$ lattice gauge theories, Phys. Rev. B **110**, L241101 (2024).

[42] G. Dünnweber, S. M. Linsel, A. Bohrdt, and F. Grusdt, Percolation renormalization group analysis of confinement in $\mathbb{Z}_2$ lattice gauge theories, Phys. Rev. B **111**, 024314 (2025).

[43] K. Fredenhagen and M. Marcu, Charged states in z_2 gauge theories, Commun. Math. Phys. **92**, 81 (1983).

[44] K. Fredenhagen and M. Marcu, Confinement criterion for QCD with dynamical quarks, Phys. Rev. Lett. **56**, 223 (1986).

[45] K. Fredenhagen and M. Marcu, Dual interpretation of order parameters for lattice gauge theories with matter fields, Nucl. Phys. B—Proc. Suppl. **4**, 352 (1988).

[46] S. Sachdev, Topological order, emergent gauge fields, and Fermi surface reconstruction, Rep. Prog. Phys. **82**, 014001 (2019).

[47] W.-T. Xu, F. Pollmann, and M. Knap, Critical behavior of Fredenhagen-Marcu string order parameters at topological phase transitions with emergent higher-form symmetries, npj Quantum Inf. **11**, 74 (2025).

[48] I. Cong, N. Maskara, M. C. Tran, H. Pichler, G. Semeghini, S. F. Yelin, S. Choi, and M. D. Lukin, Enhancing detection of topological order by local error correction, Nat. Commun. **15**, 1527 (2024).

[49] It is vital that in the QMC the SIT is *not* averaged over the whole lattice before evaluating the Binder cumulant, otherwise it shows crossover behavior for physical phase transitions and the Binder cumulant does not feature crossing points!

[50] A. Patel, A flux tube model of the finite temperature deconfining transition in QCD, Nucl. Phys. B **243**, 411 (1984).

[51] H. Satz, Deconfinement and percolation, Nucl. Phys. A **642**, c130 (1998).

[52] M. Ghanbarpour and L. von Smekal, Quarks and triality in a finite volume, Phys. Rev. D **106**, 054513 (2022).

[53] D. N. Politis and J. P. Romano, The stationary bootstrap, J. Am. Stat. Assoc. **89**, 1303 (1994).

[54] D. N. Politis and H. White, Automatic block-length selection for the dependent bootstrap, Econom. Rev. **23**, 53 (2004).

[55] A. Patton, D. N. Politis, and H. White, Correction to "Automatic block-length selection for the dependent bootstrap" by D. Politis and H. White, Econom. Rev. **28**, 372 (2009).

[56] H. W. J. Blöte and Y. Deng, Cluster Monte Carlo simulation of the transverse Ising model, Phys. Rev. E **66**, 066110 (2002).

[57] M. F. Sykes and J. W. Essam, Critical percolation probabilities by series methods, Phys. Rev. **133**, A310 (1964).

[58] J. C. Wierman, Bond percolation on honeycomb and triangular lattices, Adv. Appl. Probab. **13**, 298 (1981).

[59] R. Balian, J. M. Drouffe, and C. Itzykson, Gauge fields on a lattice. III. Strong-coupling expansions and transition points, Phys. Rev. D **11**, 2104 (1975).

[60] M. Creutz, L. Jacobs, and C. Rebbi, Experiments with a gauge-invariant Ising system, Phys. Rev. Lett. **42**, 1390 (1979).

[61] M. H. Zarei, Strong-weak coupling duality between two perturbed quantum many-body systems: Calderbank-Shor-Steane codes and Ising-like systems, Phys. Rev. B **96**, 165146 (2017).

[62] K. Jansen, I. Montvay, G. Münster, T. Trappenberg, and U. Wolff, Broken phase of the 4-dimensional Ising model in a finite volume, Nucl. Phys. B **322**, 698 (1989).

[63] R. Verresen, M. D. Lukin, and A. Vishwanath, Prediction of toric code topological order from Rydberg blockade, Phys. Rev. X **11**, 031005 (2021).

[64] Z. Wang and L. Pollet, Renormalized classical spin liquid on the ruby lattice, Phys. Rev. Lett. **134**, 086601 (2025).

[65] S. M. Linsel and L. Pollet, Paratoric 1.0-beta: Continuous-time quantum Monte Carlo for the toric code in a parallel field, arXiv:2510.14781 [quant-ph].

[66] M. E. Fisher, The theory of equilibrium critical phenomena, Rep. Prog. Phys. **30**, 615 (1967).

[67] L. Hahn, A. Bohrdt, and F. Grusdt, Dynamical signatures of thermal spin-charge deconfinement in the doped Ising model, Phys. Rev. B **105**, L241113 (2022).

[68] M. B. Hastings, G. H. Watson, and R. G. Melko, Self-correcting quantum memories beyond the percolation threshold, Phys. Rev. Lett. **112**, 070501 (2014).

[69] H. Kesten, The critical probability of bond percolation on the square lattice equals 1/2, Commun. Math. Phys. **74**, 41 (1980).

2.11 Publication 5: Approximately Symmetric Neural Networks for Quantum Spin Liquids

In this section, the following publication is reprinted:

P5 *Approximately Symmetric Neural Networks for Quantum Spin Liquids*,
Dominik S. Kufel, Jack Kemp, DinhDuy Vu, Simon M. Linsel, Chris R. Laumann, Norman Y. Yao,
Physical Review Letters **135**, 056702 (2025), ©2025 American Physical Society,
doi: 10.1103/pgnx-11ph.
Reprinted on pages 101–124.

PHYSICAL REVIEW LETTERS **135,** 056702 (2025)

Editors' Suggestion

Approximately Symmetric Neural Networks for Quantum Spin Liquids

Dominik S. Kufel,[1,2,*] Jack Kemp,[1,2,*] DinhDuy Vu,[1,2] Simon M. Linsel,[1,3,4]
Chris R. Laumann,[5] and Norman Y. Yao[1,2]
[1]*Department of Physics, Harvard University, 17 Oxford Street, Cambridge, Massachusetts 02138, USA*
[2]*Harvard Quantum Initiative, 60 Oxford Street, Cambridge, Massachusetts 02138, USA*
[3]*Faculty of Physics, Arnold Sommerfeld Centre for Theoretical Physics (ASC), Ludwig-Maximilians-Universität München,*
Theresienstraße 37, 80333 München, Germany
[4]*Munich Center for Quantum Science and Technology (MCQST), Schellingstraße 4, 80799 München, Germany*
[5]*Department of Physics, Boston University, 590 Commonwealth Avenue, Boston, Massachusetts 02215, USA*

(Received 4 June 2024; accepted 27 June 2025; published 29 July 2025)

We propose and analyze a family of *approximately symmetric* neural networks for quantum spin liquid problems. These tailored architectures are parameter efficient, scalable, and significantly outperform existing symmetry-unaware neural network architectures. Utilizing the mixed-field toric code and PXP Rydberg Hamiltonian models, we demonstrate that our approach is competitive with state-of-the-art tensor network and quantum Monte Carlo methods. Moreover, at the largest system sizes ($N = 480$ for toric code, $N = 1584$ for Rydberg PXP), our method allows us to explore Hamiltonians with sign problems beyond the reach of both quantum Monte Carlo and finite-size matrix-product states. The network comprises an exactly symmetric block following a nonsymmetric block, which we argue learns a transformation of the ground state analogous to quasiadiabatic continuation. Our Letter paves the way toward investigating quantum spin liquid problems within interpretable neural network architectures.

DOI: 10.1103/pgnx-11ph

Quantum spin liquids represent exotic phases of strongly correlated matter exhibiting long-range entanglement and fractionalization [1–4]. Their detection and characterization remain the subject of intense experimental interest in both quantum materials and simulators [5–12]. On the numerical front, the exploration of spin-liquid phases inevitably runs into the wall of an exponential Hilbert space. Quantum Monte Carlo (QMC) methods can efficiently explore this space, but suffer from the sign problem which limits their applicability.

Alternatively, variational methods, such as tensor networks [13–15] or variational Monte Carlo methods [16–19], avoid the sign problem but instead restrict themselves to a small subspace, parametrized by physically motivated variational *Ansätze*.

A tremendous amount of recent attention has focused on a new approach, which utilizes neural networks as the variational *Ansätze* (Fig. 1) [20]. The interest in such neural quantum states (NQS) owes in part to theoretical guarantees of their expressivity [21], which is strictly greater than that of efficiently contractible tensor networks [22]. Moreover, from a more pragmatic perspective, NQS have achieved state-of-the-art ground state energies in certain archetypal models [23,24], such as the two-dimensional transverse-field Ising model [23].

The simulation of more exotic and delicate quantum phases, such as spin liquids, remains challenging for both NQS and more traditional methods [4,27–29]. Indeed, for neural quantum states, despite recent progress on the J_1-J_2 Heisenberg model [30–34], the long-range entangled nature of quantum spin liquids leads to inherently complicated optimization landscapes [35,36]. This causes the training of generic network architectures to become trapped in local minima [Fig. 2(b)].

One strategy for simplifying the optimization landscape is to make use of symmetries. Indeed, by imposing symmetries on the neural network via group equivariant methods [31,37], one can significantly reduce the number of optimization parameters without sacrificing expressivity. This strategy has been extensively employed for both lattice translation and point group symmetries [35,38]. In the context of quantum spin liquids, exploiting symmetry ought to yield even greater dividends as the ground states are invariant under an exponentially large emergent "gauge" group [26]. For certain models, for which these emergent symmetries are exactly known, group-equivariant neural networks have been shown to yield significant improvements over more conventional methods such as restricted Boltzmann machines or multilayered perceptrons [39–41].

Unfortunately, for generic spin liquids, it is only possible to specify the exact form of the emergent symmetry operators at particular points in phase space [42]. Away from these special regions, applying such operators will

---

[*] These authors contributed equally to this work.

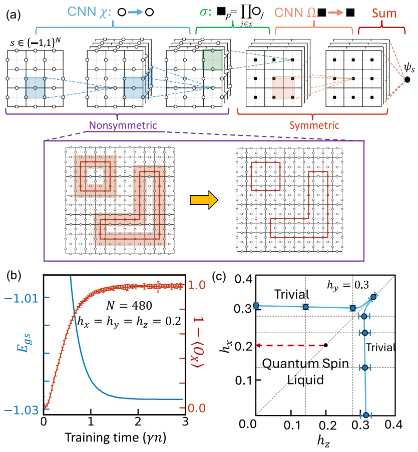

FIG. 1. (a) The approximately symmetric NQS architecture for a mixed-field toric code model. The network computes the ground-state amplitude, $\psi_s = \Omega\{\sigma[\chi(s)]\}$, given an input bit string s. The circles (squares) represent edge (plaquette) variables. The convolutional neural networks χ and Ω consist of between 1–16 layers and 2–16 channels (only 1 layer and 4 channels shown for each) and use normalized $\mathbb{C}$-sigmoid and $\mathbb{C}$-ELU nonlinearities, respectively [25]. The nonlinear map σ imposes invariance on all the following layers. For training, χ is initialized to the identity, while Ω is randomly initialized. The nonsymmetric layers "unfatten" the loop symmetry operators of the quantum spin liquid (purple box) in the spirit of quasiadiabatic continuation [26]. These symmetries are then enforced exactly in the following layers. (b) The convergence of the energy density (blue) and the nonlocal Bricmont-Frölich-Fredenhagen-Marcu string order parameter (red) as a function of training time (step size times iteration number), in a regime of the mixed-field toric code model which suffers from the sign problem. (c) Phase diagram of the toric code [Eq. (1)] as a function of magnetic field strength with $h_y = 0.2$ imposing a sign problem. The phase-transition locations are extracted from finite-size extrapolation of the string order parameter [25]. The red arrow indicates the approximate-to-exact mapping carried out by the nonsymmetric block of the network depicted in panel (a).

only leave the ground state approximately invariant. This precludes their strict imposition on the neural network.

In this Letter, we demonstrate that *approximately* invariant neural networks can impose a soft inductive bias on the ground-state search while maintaining the flexibility to capture complex quantum states (e.g., spin liquids) that are not exactly symmetric [Fig. 1(a)].

Our main results are threefold. First, to impose approximate symmetries on neural quantum states, we leverage techniques from the field of approximately group-equivariant networks [43,44]. We modify these constructions for quantum many-body problems, incorporating physical insights into the structure of the neural network. Next, we demonstrate the accuracy of our approach on a paradigmatic quantum spin liquid model: the $\mathbb{Z}_2$ toric code perturbed by a magnetic field. We show that the variational energies obtained (i) outperform conventional NQS methods; (ii) converge to exact diagonalization results for small system sizes [Fig. 2(b)]; (iii) match state-of-the-art tensor network and quantum Monte Carlo results for larger system sizes [Fig. 2(c)]; and (iv) enable access to large system sizes ($N = 480$) even when the Hamiltonian has a significant sign problem, beyond the reach of both QMC and finite-size matrix product state methods [Fig. 1(c)]. Finally, we discuss how the approximate-symmetries framework facilitates NQS interpretability. In particular, we argue that the neural network discovers a representation of the emergent ground-state symmetries of spin liquids in the spirit of the quasiadiabatic continuation of Hastings and Wen [26] [Fig. 1(a)].

Emergent symmetries and the toric code—Consider an $L \times L$ square lattice with open boundary conditions and $N = 2L^2 - 2L$ qubits placed on its edges [Fig. 1(a)]. The mixed-field, $\mathbb{Z}_2$ toric-code model is given by the following Hamiltonian:

$$H = -\sum_v A_v - \sum_p B_p - \sum_i (h_x X_i + h_y Y_i + h_z Z_i), \quad (1)$$

where X_i, Y_i, and Z_i are Pauli operators, the vertex operator $A_v = \prod_{j\in v} X_j$ acts on qubits neighboring a lattice vertex v, and the plaquette operator $B_p = \prod_{j\in p} Z_j$ acts on qubits around a square plaquette p. Let us begin by considering the case where $h_y = 0$. In this regime, it is well understood that the phase diagram hosts a gapped quantum spin liquid up to finite values of h_x and h_z [45–47]. Along the $h_z = 0$ line, there is an exact local $\mathbb{Z}_2$ symmetry group, $G_{\mathrm{TC}} = \mathbb{Z}_2^{\times N/2}$, generated by the A_v operators. To wit, the ground state $|\psi\rangle$ is invariant under G_{TC}, $A_v|\psi\rangle = |\psi\rangle$. We refer to elements of G_{TC} as loop operators W_c, since they have support on closed loops c on the dual lattice.

For $|h_z| > 0$, exact symmetry under G_{TC} no longer holds. Nonetheless, as long as the system remains in the gapped spin liquid phase, it is possible to quasiadiabatically continue the ground state back to the $h_z = 0$ line, where G_{TC} is again exact [26]. Crucially, the continuation is accomplished by a *local* unitary U, which implies that for $h_z \neq 0$ there are a set of "fattened" loop operators $\tilde{W}_c = U W_c U^\dagger$, which remain symmetries of the ground state. The fattened loop operators are supported on ribbons of finite width about the unperturbed contours c, up to exponentially small errors [Fig. 1(a)].

Approximate symmetries in neural networks—In order to exploit the emergent symmetries to improve the NQS *Ansatz*, we must first construct an approximately invariant

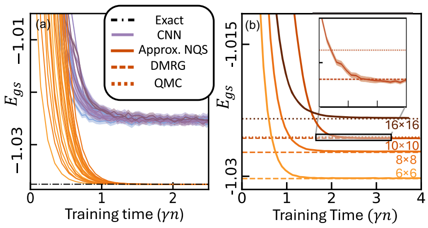

FIG. 2. Benchmarking the approximately symmetric NQS applied to the sign-problem-free toric code with $(h_x, h_y, h_z) = (0.2, 0.0, 0.2)$. (a) The convergence of the energy density as a function of training time (step size times iteration number) for a 4×4 ($N = 24$) lattice. Convolutional neural networks (CNNs) (solid purple) become stuck in local minima, while the approximately symmetric NQS (solid brown) converges to the exact diagonalization result (dashed black). Different shades correspond to different random initializations and network hyperparameters [25]. (b) At larger system sizes, where exact diagonalization is unavailable, we compare our approximately symmetric NQS to state-of-the-art DMRG (dashed brown) and QMC (dotted brown) calculations. Because of memory constraints, we were unable to obtain converged DMRG results for the 16×16 lattice. Inset: enlargement comparing the NQS, DMRG, and QMC energy densities for $L = 10$. For further analysis under different perturbations and with different network hyperparameters, see [25]. NQS error bars are shown as shading. QMC uncertainty (not shown) is of order $\sim 10^{-4}$ in units of energy density.

neural network. For a system composed of N qubits, each with state-space $\{|\pm 1\rangle\}$, a many-body quantum state vector $|\psi\rangle$ can be decomposed into a complete basis labeled by 2^N bit strings s: $|\psi\rangle = \sum_s \psi_s |s\rangle$, where $\psi_s \in \mathbb{C}$ is a complex amplitude and $|s\rangle$ is the quantum state associated with the bit string (e.g. $|s\rangle = |-1, 1, 1, -1, \cdots\rangle$).

The key idea underlying NQS is to represent ψ_s as a neural network that gives a complex scalar output for a particular bit string input, s. To compute the ground state of a Hamiltonian, H, one solves a variational energy-minimization problem with respect to the parameters, θ, of the neural network: $\min_\theta \langle H\rangle = \min_\theta (\langle\psi(\theta)|H|\psi(\theta)\rangle / \langle\psi(\theta)|\psi(\theta)\rangle)$. The energy $\langle H\rangle$ is typically evaluated via Monte Carlo Markov chain sampling [20], while the network parameters θ are optimized via either gradient descent or more complicated second order methods (e.g., stochastic reconfiguration [48–50]).

Let us now consider the problem of incorporating approximate symmetries into an NQS *Ansatz*. Suppose that the ground state $|\psi\rangle$ exhibits a particular group of symmetries G, such that $g|\psi\rangle = |\psi\rangle$ for all $g \in G$. We will assume that the basis $\{|s\rangle\}$ is chosen such that the group G acts as a permutation on bit-string basis elements. In such a basis, the invariance of the state $|\psi\rangle$ under G is ensured if two inputs of the network connected by symmetry yield the same output (i.e., complex amplitude): $\psi_{gs} = \psi_s$ for all $g \in G$ [31,37].

For approximate symmetries, the strict invariance condition above is relaxed to $\mathbb{E}_{g\in G}\mathbb{E}_s |\psi_{gs} - \psi_s| < \epsilon$, where the expectation value $\mathbb{E}$ is taken over all group elements and input bit strings [51]. Given a fully invariant neural network with $\epsilon = 0$, one can lift the strict constraints by adding an extra noninvariant layer to the network or by using a noninvariant skip connection [43,44]. In principle, for sufficiently large breaking ϵ of the fixed point symmetries, a neural network constructed in such a fashion can target any vector in the Hilbert space. In practice, the appropriate value of ϵ is learned by the network itself, and is independent of network hyperparameters [25].

Approximately invariant neural quantum states for the toric code—We propose a family of approximately symmetric neural networks utilizing the so-called "combo" architecture [25,44]. While we focus on the mixed field toric code model [Eq. (1)], our approach is applicable to a broad class of quantum spin liquid problems.

Our proposed architecture is schematically depicted in Fig. 2(a) and structured as follows: we first impose the constraints $A_v|\psi\rangle = |\psi\rangle$ on the neural network and then weakly break these constraints by transforming the input with a non-invariant layer. More specifically, the neural network is defined by $\psi_s = \Omega(\sigma(\chi(s)))$. Here, s is the bit string input, χ is a noninvariant convolutional layer acting on the qubits and σ is a G_{TC}-invariant nonlinearity that maps qubits to plaquettes. Finally, Ω is a further convolutional layer (consisting of square-shaped kernels) acting on the plaquettes themselves followed by a summation and exponentiation to calculate ψ_s [Fig. 2(a)]. The noninvariant convolutional layer χ has a kernel centered at each link of the lattice, and explicitly breaks the G_{TC} symmetry. Meanwhile, the nonlinear layer σ is constructed using the G_{TC}-invariant operators, $B_p = \prod_{j\in p} Z_j$ (since $[B_p, A_v] = 0$) and ensures the G_{TC} invariance of any further layers [39,52]. We describe a number of other choices for approximately symmetric architectures, along with their implementation details, in the Supplemental Material [25] (see also references [53–98] therein).

Let us begin benchmarking the accuracy of the approximately symmetric NQS architecture for the mixed-field toric-code Hamiltonian in the sign-problem-free case (with $h_x = h_z = 0.2$ and $h_y = 0$). Starting with small 4×4 lattices ($N = 24$ spins), we compute the ground state energy density E_{gs} using (i) our architecture—(ii) a conventional convolutional neural network (CNN) and (iii) exact diagonalization. The energy as a function of training time (measured in units of stochastic reconfiguration stepsize γ times iteration number n) is depicted in Fig. 2(b). While the CNN becomes stuck in local minima for all runs (with different initializations and hyperparameters) [20,66], the approximately symmetric architecture converges to the exact diagonalization energy up to a relative error, $\delta E = |E_{\mathrm{gs}}^{\mathrm{NQS}} - E_{\mathrm{gs}}^{\mathrm{ED}}|/E_{\mathrm{gs}}^{\mathrm{ED}} \sim 10^{-8}$ (see also Fig. S2 in the Supplemental Material [25] for further comparisons with full-lattice-symmetrized restricted Boltzmann machines and additional validation of the results).

We further find that the performance of the approximately symmetric NQS is not limited to small values of the symmetry-violating h_z field. Indeed, it is accurate to a relative error of $\sim 10^{-5}$ even outside of the topological phase at $h_z = 0.7$ [25]. This suggests that the *Ansatz* is more widely applicable than naively expected and, due to the inclusion of a noninvariant block in the architecture, enables us to identify the phases and phase transitions out of the spin-liquid state using a single *approximately* symmetric NQS architecture.

To demonstrate the scalability of the architecture, we perform an extensive set of numerical simulations on lattices up to 16×16 ($N = 480$ spins) using three methods: state-of-the-art density matrix renormalization group (DMRG) [13,99–101], continuous-time QMC [45,102,103], and the approximately symmetric NQS architecture. As illustrated in Fig. 2(c), the approximately symmetric NQS yields competitive energies at all system sizes [inset, Fig. 2(c)].

Crucially, this scalability extends to spin liquid models beyond the mixed-field toric code. As an example setting, which has received widespread recent attention, we utilize our approximately symmetric NQS to explore the so-called PXP model (on the ruby lattice), which describes the physics associated with Rydberg atom arrays in the blockade regime [4,5,104–106]. Similar to the toric code setting, we find that our approximately symmetric neural network significantly outperforms non-gauge-symmetry aware NQS and yields competitive ground state energies compared to finite DMRG methods (see Fig. 5 in the Appendix). Moreover, we are able to reach significantly larger system sizes (up to $N = 1584$ Rydberg atoms), which will be crucial for benchmarking the next generation of Rydberg atom array experiments [107]. Further application settings natural for our approximately symmetric NQS are discussed in Table I in the Supplemental Material [25].

Toric code with a sign problem—Many physical perturbations naturally lead to sign problems, including magnetic fields, frustrated long-range couplings, and antiferromagnetic Heisenberg interactions [3,108,109]. In principle, variational methods such as DMRG can be used to study such models, even as QMC hits an exponential sampling barrier. However, as we have just seen in the sign-problem-free case, the memory requirements for DMRG on finite-size two-dimensional clusters can quickly become prohibitive. Accordingly, this is a regime in which the NQS approach should be uniquely well suited.

We introduce a sign problem in the toric code by turning on $h_y = 0.3$. We compute the ground state phase diagram as a function of h_x and h_z [Fig. 1(c)]. We utilize two diagnostics to identify the transition out of the spin liquid phase: (i) the string order parameter due to Bricmont and Frölich [110], Fredenhagen, and Marcu [111] and (ii) the entanglement entropy.

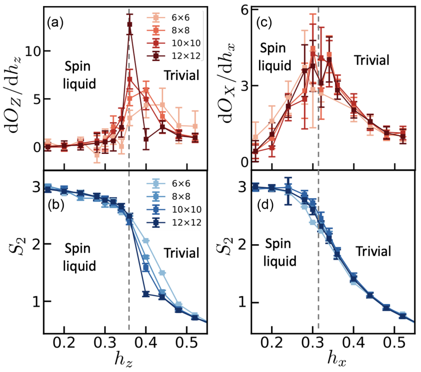

FIG. 3. Detecting phase transitions in the toric code with a sign problem at $h_y = 0.3$ [Fig. 1(c)]. (a),(c) The derivative of the BFFM string order parameter O_Z (O_X) with respect to the magnetic field, calculated for a square loop around the center of the lattice with perimeter $\ell = 8$ ($\ell = 4$). We use finite-size extrapolation of the position of the peaks in order to estimate the location of the phase transition (dashed gray line, extrapolation in [25]). (b),(d) The second Renyi entropy for a square, 4-qubit subsystem in the center of the lattice. Panels (a) and (c) illustrate the horizontal cut (at $h_x = 0$) through the phase diagram, while panels (b) and (d) illustrate the vertical cut (at $h_z = 0$) through the phase diagram.

The string order parameter, $\mathcal{O}_Z$, diagnoses the confinement of the e-type excitations of the toric code. Consider a closed square loop C of side length ℓ on the primal lattice. The order parameter is defined in the limit $\ell \to \infty$,

$$\mathcal{O}_Z = \lim_{\ell\to\infty} \sqrt{|O_Z|}; \qquad O_Z = \frac{\langle\psi|\prod_{j\in\tilde{C}} Z_j|\psi\rangle}{\sqrt{\langle\psi|\prod_{j\in C} Z_j|\psi\rangle}},$$

where $\tilde{C}$ is the open string corresponding to half of the square C. One expects $\mathcal{O}_Z$ to be finite in the trivial confining phase, while it vanishes in the spin liquid phase because each end of the open string creates a deconfined excitation [110–112]. An analogous order parameter $\mathcal{O}_X$, diagnosing the confinement of m-type excitations, can be defined with strings on the dual lattice and Pauli X operators. Our second diagnostic is the entanglement entropy, $S_2(\rho) = -\log \mathrm{Tr}(\rho_A^2)$, where A represents a particular subsystem. One expects the entanglement entropy to be larger deep in the spin liquid phase, since the trivial phase is smoothly connected to an unentangled product state.

As shown in Fig. 3, both of these expectations are borne out by the NQS simulations (at $h_y = 0.3$). In particular, fixing $h_x = 0$ and sweeping h_z, we observe a pronounced peak in the derivative of the string order parameter, $\mathrm{d}O_z/\mathrm{d}h_z$ [Fig. 3(a)], as well as a sharp change in the entanglement entropy at the same field strength [Fig. 3(b)]. Analogous results fixing $h_z = 0$ and sweeping h_x are depicted in Figs. 3(c) and 3(d). To estimate the location of the thermodynamic critical point [Fig. 1(c)], we perform a power-law extrapolation in $1/L$ of the location of the observed finite-size crossover [25]. After this finite-size extrapolation, the phase boundaries in [Fig. 1(c)] match those obtained by "infinite system-size" infinite projected-entangled pair states (iPEPS) and perturbative continuous unitary transformation (pCUT) computations to about 5% (Fig. 2 of [113,114]).

Interpretability—The approximately symmetric NQS architecture facilitates partial interpretation of which physical features are learned by different sections of the network. In particular, the noninvariant χ block maps the model from an approximately symmetric regime to an exactly symmetric one, which the G_{TC}-invariant Ω block of the architecture can then learn efficiently. This mapping is analogous to the quasiadiabatic continuation of Hastings and Wen [26], in which the exact "emergent" symmetries of the model (i.e., the fattened loops) are constructed by applying a finite-depth unitary circuit to the unperturbed toric code. We hypothesize that the dominant effect of the noninvariant block of the network is to reverse this finite-depth unitary dressing.

To test this hypothesis, we investigate the following two-step training scheme [Fig. 4(a)]: First, we train the network in the fully symmetric regime at $(h_x, h_y, h_z) = (0.2, 0.0, 0.0)$, by optimizing only the parameters of the invariant Ω layer and keeping the noninvariant χ layer fixed to the identity. Second, we fix the invariant Ω layer at these optimized parameters and turn on a field ($h_z = 0.2$), which breaks the exact invariance of the state under the group, G_{TC}; then, we find the ground state by only optimizing the parameters of the χ layer. Despite this restricted training procedure, we still obtain an excellent ground state energy [Fig. 4(b)], strongly suggesting that the network is indeed effectively learning the fattened loops [Fig. 1(a), red arrow] [25].

Outlook—Our work opens the door to a number of intriguing directions. First, straightforward extensions of the approximately symmetric architecture may be used to study increasingly exotic Abelian spin liquid models, ranging from experimentally motivated microscopic models of $\mathbb{Z}_2$ liquids [5], to more general chiral and nonchiral $\mathbb{Z}_p$ and U(1) liquids. By further adapting techniques from [73,115], models with non-Abelian anyons and/or non-Abelian continuous symmetries may also be accessible (see [25] for more discussion).

Second, on the numerical front, there are multiple avenues for further improvement, including: (i) tuning the depth of the architecture, (ii) exploring alternative representations for the complex amplitudes required for models with sign problems, (iii) increasing parameter efficiency with pooling layers, or (iv) replacing the CNNs with more elaborate backbone architectures (e.g., transformers) [24]. Finally, although our focus here has been on finding ground states, the approximately symmetric architecture can also be applied to simulate real-time dynamics in such systems. The source code supporting this Letter is publicly available [116].

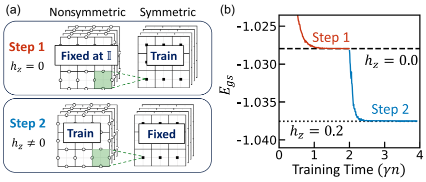

FIG. 4. (a) The training scheme used to demonstrate interpretability of the approximately symmetric network. In step 1, we find the ground state of the model at the exactly symmetric point $(h_x, h_y, h_z) = (0.2, 0.0, 0.0)$ by training only the symmetric part of the network. In step 2, we turn to $(h_x, h_y, h_z) = (0.2, 0.0, 0.2)$, fix the symmetric weights within the network, and train the nonsymmetric block. (b) Energy convergence curve for this training scheme for a 4×4 ($N = 24$) lattice, compared with exact diagonalization (dashed lines).

Acknowledgments—We gratefully thank Andrea Pizzi, Johannes Feldmeier, Lode Pollet, Quynh Nguyen, Rui Wang, Wen-Tao Xu, Marc Machaczek, Di Luo, Phil Crowley, Yichen Huang, Marc Finzi, Max Welling, Shivaji Sondhi, Saumya Shivam, Ruben Verresen, Robert Huang, Leo Lo, Joaquin Rodriguez-Nieva, and Arthur Pesah for interesting discussions. We also thank Curtis McMullen for an inspiring group theory class. We acknowledge support from the NSF via the STAQ program and the QLCI program (Grant No. OMA-2016245), and from the Wellcome Leap under the Q4Bio program. D. K. acknowledges support from a Generation-Q AWS and HQI fellowship. S. M. L. acknowledges support from the European Research Council (ERC) under the European Union's Horizon 2020 research and innovation program (Grant Agreement No. 948141) from ERC Starting Grant SimUcQuam. N. Y. Y. acknowledges support from a Simons Investigator Award. C. R. L. acknowledges the Gutzwiller Fellowship at Max Planck Institute for the Physics of Complex Systems and the partial support of SFB 1143 and ct.qmat.

Data availability—The data are not publicly available. The data are available from the authors upon reasonable request.

[1] Philip W. Anderson, Resonating valence bonds: A new kind of insulator?, Mater. Res. Bull. **8**, 153 (1973).

[2] Alexei Kitaev, Anyons in an exactly solved model and beyond, Ann. Phys. (Amsterdam) **321**, 2 (2006).

[3] Lucile Savary and Leon Balents, Quantum spin liquids: A review, Rep. Prog. Phys. **80**, 016502 (2016).

[4] Ruben Verresen, Mikhail D. Lukin, and Ashvin Vishwanath, Prediction of toric code topological order from Rydberg blockade, Phys. Rev. X **11**, 031005 (2021).

[5] Giulia Semeghini, Harry Levine, Alexander Keesling, Sepehr Ebadi, Tout T. Wang, Dolev Bluvstein, Ruben Verresen, Hannes Pichler, Marcin Kalinowski, Rhine Samajdar *et al.*, Probing topological spin liquids on a programmable quantum simulator, Science **374**, 1242 (2021).

[6] K. J. Satzinger, Y-J. Liu, A. Smith, C. Knapp, M. Newman, C. Jones, Z. Chen, C. Quintana, X. Mi, A. Dunsworth *et al.*, Realizing topologically ordered states on a quantum processor, Science **374**, 1237 (2021).

[7] Mohsin Iqbal, Nathanan Tantivasadakarn, Ruben Verresen, Sara L. Campbell, Joan M. Dreiling, Caroline Figgatt, John P. Gaebler, Jacob Johansen, Michael Mills, Steven A. Moses *et al.*, Non-Abelian topological order and anyons on a trapped-ion processor, Nature (London) **626**, 505 (2024).

[8] Google Quantum AI and Collaborators, Non-Abelian braiding of graph vertices in a superconducting processor, Nature (London) **618**, 264 (2023).

[9] C. Broholm, R. J. Cava, S. A. Kivelson, D. G. Nocera, M. R. Norman, and T. Senthil, Quantum spin liquids, Science **367**, eaay0668 (2020).

[10] Sijie Xu, Rabindranath Bag, Nicholas E. Sherman, Lalit Yadav, Alexander I. Kolesnikov, Andrey A. Podlesnyak, Joel E. Moore, and Sara Haravifard, Realization of U(1) Dirac quantum spin liquid in $\mathrm{YbZn_2GaO_5}$, Phys. Rev. Lett. **133**, 266703 (2024).

[11] A. O. Scheie, E. A. Ghioldi, J. Xing, J. A. M. Paddison, N. E. Sherman, M. Dupont, L. D. Sanjeewa, Sangyun Lee, A. J. Woods, D. Abernathy *et al.*, Proximate spin liquid and fractionalization in the triangular antiferromagnet $\mathrm{KYbSe_2}$, Nat. Phys. **20**, 74 (2024).

[12] Quanzhen Zhang, Wen-Yu He, Yu Zhang, Yaoyao Chen, Liangguang Jia, Yanhui Hou, Hongyan Ji, Huixia Yang, Teng Zhang, Liwei Liu, Hong-Jun Gao, Thomas A. Jung, and Yeliang Wang, Quantum spin liquid signatures in monolayer $\mathrm{1T-NbSe_2}$, Nat. Commun. **15**, 2336 (2024).

[13] Ulrich Schollwöck, The density-matrix renormalization group in the age of matrix product states, Ann. Phys. (Amsterdam) **326**, 96 (2011).

[14] Jutho Haegeman, J. Ignacio Cirac, Tobias J. Osborne, Iztok Pižorn, Henri Verschelde, and Frank Verstraete, Time-dependent variational principle for quantum lattices, Phys. Rev. Lett. **107**, 070601 (2011).

[15] Mari Carmen Bañuls, Tensor network algorithms: A route map, Annu. Rev. Condens. Matter Phys. **14**, 173 (2023).

[16] W. L. McMillan, Ground state of liquid He^4, Phys. Rev. **138**, A442 (1965).

[17] D. Ceperley, G. V. Chester, and M. H. Kalos, Monte Carlo simulation of a many-fermion study, Phys. Rev. B **16**, 3081 (1977).

[18] P. R. C. Kent, R. J. Needs, and G. Rajagopal, Monte Carlo energy and variance-minimization techniques for optimizing many-body wave functions, Phys. Rev. B **59**, 12344 (1999).

[19] W. M. C. Foulkes, L. Mitas, R. J. Needs, and G. Rajagopal, Quantum Monte Carlo simulations of solids, Rev. Mod. Phys. **73**, 33 (2001).

[20] Giuseppe Carleo and Matthias Troyer, Solving the quantum many-body problem with artificial neural networks, Science **355**, 602 (2017).

[21] Kurt Hornik, Maxwell Stinchcombe, and Halbert White, Multilayer feedforward networks are universal approximators, Neural Netw. **2**, 359 (1989).

[22] Or Sharir, Amnon Shashua, and Giuseppe Carleo, Neural tensor contractions and the expressive power of deep neural quantum states, Phys. Rev. B **106**, 205136 (2022).

[23] Or Sharir, Yoav Levine, Noam Wies, Giuseppe Carleo, and Amnon Shashua, Deep autoregressive models for the efficient variational simulation of many-body quantum systems, Phys. Rev. Lett. **124**, 020503 (2020).

[24] Kyle Sprague and Stefanie Czischek, Variational Monte Carlo with large patched transformers, Commun. Phys. **7**, 90 (2024).

[25] See Supplemental Material at http://link.aps.org/supplemental/10.1103/pgnx-11ph for implementation details of the network architectures, additional benchmarking data and ablation results.

[26] Matthew B. Hastings and Xiao-Gang Wen, Quasiadiabatic continuation of quantum states: The stability of topological ground-state degeneracy and emergent gauge invariance, Phys. Rev. B **72**, 045141 (2005).

[27] Pranay Patil, Quantum Monte Carlo simulations in the restricted Hilbert space of Rydberg atom arrays, arXiv:2309.00482.

[28] Luciano Loris Viteritti, Francesco Ferrari, and Federico Becca, Accuracy of restricted Boltzmann machines for the one-dimensional $j_1 - j_2$ Heisenberg model, SciPost Phys. **12**, 166 (2022).

[29] Agnes Valenti, Eliska Greplova, Netanel H. Lindner, and Sebastian D. Huber, Correlation-enhanced neural networks as interpretable variational quantum states, Phys. Rev. Res. **4**, L012010 (2022).

[30] Kenny Choo, Titus Neupert, and Giuseppe Carleo, Two-dimensional frustrated $j_1 - j_2$ model studied with neural network quantum states, Phys. Rev. B **100**, 125124 (2019).

[31] Christopher Roth, Attila Szabó, and Allan H. MacDonald, High-accuracy variational Monte Carlo for frustrated magnets with deep neural networks, Phys. Rev. B **108**, 054410 (2023).

[32] Zhuo Chen, Laker Newhouse, Eddie Chen, Di Luo, and Marin Soljačić, Autoregressive neural tensornet: Bridging neural networks and tensor networks for quantum many-body simulation, arXiv:2304.01996.

[33] Jonas Beck, Jonathan Bodky, Johannes Motruk, Tobias Müller, Ronny Thomale, and Pratyay Ghosh, Phase diagram of the J-J_d Heisenberg model on the maple leaf lattice: Neural networks and density matrix renormalization group, Phys. Rev. B **109**, 184422 (2024).

[34] Christopher Roth and Allan H. MacDonald, Group convolutional neural networks improve quantum state accuracy, arXiv:2104.05085.

[35] Kevin Zhang, Samuel Lederer, Kenny Choo, Titus Neupert, Giuseppe Carleo, and Eun-Ah Kim, Hamiltonian reconstruction as metric for variational studies, SciPost Phys. **13**, 063 (2022).

[36] Tanja Duric, Jia Hui Chung, Bo Yang, and Pinaki Sengupta, Spin-$1/2$ kagome Heisenberg antiferromagnet: Machine learning discovery of the spinon pair density wave ground state, Phys. Rev. X **15**, 011047 (2025).

[37] Taco Cohen and Max Welling, Group equivariant convolutional networks, in *International Conference on Machine Learning* (PMLR, New York City, NY, 2016), pp. 2990–2999.

[38] Moritz Reh, Markus Schmitt, and Martin Gärttner, Optimizing design choices for neural quantum states, Phys. Rev. B **107**, 195115 (2023).

[39] Di Luo, Giuseppe Carleo, Bryan K. Clark, and James Stokes, Gauge equivariant neural networks for quantum lattice gauge theories, Phys. Rev. Lett. **127**, 276402 (2021).

[40] Di Luo, Shunyue Yuan, James Stokes, and Bryan Clark, Gauge equivariant neural networks for $2+1$D U(1) gauge theory simulations in Hamiltonian formulation, in *Advances in Neural Information Processing systems, NeurIPS 2022 – AI for Science: Progress and Promises, New Orleans (LA), USA* (2022).

[41] Di Luo, Zhuo Chen, Kaiwen Hu, Zhizhen Zhao, Vera Mikyoung Hur, and Bryan K. Clark, Gauge-invariant and anyonic-symmetric autoregressive neural network for quantum lattice models, Phys. Rev. Res. **5**, 013216 (2023).

[42] Of course, for some spin liquids, there may not even be exactly solvable lattice models for which the exact symmetry operators are known.

[43] Marc Finzi, Gregory Benton, and Andrew G. Wilson, Residual pathway priors for soft equivariance constraints, in *Advances in Neural Information Processing Systems, NeurIPS 2021, Vancouver* (2021), Vol. 34, pp. 30037–30049.

[44] Rui Wang, Robin Walters, and Rose Yu, Approximately equivariant networks for imperfectly symmetric dynamics, in *International Conference on Machine Learning* (PMLR, Baltimore, MD, 2022), pp. 23078–23091.

[45] Fengcheng Wu, Youjin Deng, and Nikolay Prokof'ev, Phase diagram of the toric code model in a parallel magnetic field, Phys. Rev. B **85**, 195104 (2012).

[46] Simon Trebst, Philipp Werner, Matthias Troyer, Kirill Shtengel, and Chetan Nayak, Breakdown of a topological phase: Quantum phase transition in a loop gas model with tension, Phys. Rev. Lett. **98**, 070602 (2007).

[47] Eduardo Fradkin and Stephen H. Shenker, Phase diagrams of lattice gauge theories with Higgs fields, Phys. Rev. D **19**, 3682 (1979).

[48] Sandro Sorella, Green function Monte Carlo with stochastic reconfiguration, Phys. Rev. Lett. **80**, 4558 (1998).

[49] Shun-Ichi Amari, Natural gradient works efficiently in learning, Neural Comput. **10**, 251 (1998).

[50] James Stokes, Josh Izaac, Nathan Killoran, and Giuseppe Carleo, Quantum natural gradient, Quantum **4**, 269 (2020).

[51] Here the expectation $\mathbb{E}_s$ is calculated with respect to the probability $p(s) = |\psi(s)|^2$.

[52] Matteo Favoni, Andreas Ipp, David I. Müller, and Daniel Schuh, Lattice gauge equivariant convolutional neural networks, Phys. Rev. Lett. **128**, 032003 (2022).

[53] S. Unnikrishna Pillai, Torsten Suel, and Seunghun Cha, The Perron-Frobenius theorem: Some of its applications, IEEE Signal Process. Mag. **22**, 62 (2005).

[54] Marc Machaczek, Neural quantum states for fracton models, https://zenodo.org/records/10728168 (2024).

[55] Ao Chen and Markus Heyl, Efficient optimization of deep neural quantum states toward machine precision, Nat. Phys. **20**, 1476 (2024).

[56] Sékou-Oumar Kaba, Arnab Kumar Mondal, Yan Zhang, Yoshua Bengio, and Siamak Ravanbakhsh, Equivariance with learned canonicalization functions, in *International Conference on Machine Learning* (PMLR, Honolulu, HI, 2023), pp. 15546–15566.

[57] Sékou-Oumar Kaba and Siamak Ravanbakhsh, Symmetry breaking and equivariant neural networks, arXiv:2312.09016.

[58] Djork-Arné Clevert, Thomas Unterthiner, and Sepp Hochreiter, Fast and accurate deep network learning by exponential linear units (ELUs), arXiv:1511.07289.

[59] Matthew Fishman, Steven R. White, and E. Miles Stoudenmire, The ITensor software library for tensor network calculations, SciPost Phys. Codebases **4**, 004 (2022).

[60] Matthew Fishman, Steven R. White, and E. Miles Stoudenmire, Codebase release 0.3 for ITensor, SciPost Phys. Codebases **4**, 005 (2022).

[61] Risi Kondor, Zhen Lin, and Shubhendu Trivedi, Clebsch–Gordan nets: A fully fourier space spherical convolutional neural network, in *Advances in Neural Information Processing Systems Neurips 2018, Montreal (QC), Canada* (2018), Vol. 31.

[62] Sergey Bravyi, Giuseppe Carleo, David Gosset, and Yinchen Liu, A rapidly mixing Markov Chain from any gapped quantum many-body system, Quantum **7**, 1173 (2023).

[63] Sergey Bravyi, David Gosset, and Yinchen Liu, How to simulate quantum measurement without computing marginals, Phys. Rev. Lett. **128**, 220503 (2022).

[64] Aki Vehtari, Andrew Gelman, Daniel Simpson, Bob Carpenter, and Paul-Christian Bürkner, Rank-normalization, folding, and localization: An improved $\hat{R}$ for assessing convergence of MCMC (with discussion), Bayesian Anal. **16**, 667 (2021).

[65] Gregory D. Kahanamoku-Meyer and Julia Wei, GregDMeyer/dynamite: V0.4.0 (2024).

[66] Filippo Vicentini, Damian Hofmann, Attila Szabó, Dian Wu, Christopher Roth, Clemens Giuliani, Gabriel Pescia, Jannes Nys, Vladimir Vargas-Calderón, Nikita Astrakhantsev *et al.*, NetKet 3: Machine learning toolbox for many-body quantum systems, SciPost Phys. Codebases **4**, 007 (2022).

[67] James Bradbury, Roy Frostig, Peter Hawkins, Matthew James Johnson, Chris Leary, Dougal Maclaurin, George Necula, Adam Paszke, Jake VanderPlas, Skye Wanderman-Milne, and Qiao Zhang, JAX: Composable

transformations of Python+NumPy programs, GitHub repository version 0.4.25 (2018), https://github.com/google/jax.

[68] Remmy Zen, Long My, Ryan Tan, Frédéric Hébert, Mario Gattobigio, Christian Miniatura, Dario Poletti, and Stéphane Bressan, Transfer learning for scalability of neural-network quantum states, Phys. Rev. E **101**, 053301 (2020).

[69] Jonathan Heek, Anselm Levskaya, Avital Oliver, Marvin Ritter, Bertrand Rondepierre, Andreas Steiner, and Marc van Zee, Flax: A neural network library and ecosystem for JAX, Zenodo (2023), 10.5281/zenodo.7865805.

[70] Attila Szabó and Claudio Castelnovo, Neural network wave functions and the sign problem, Phys. Rev. Res. **2**, 033075 (2020).

[71] Nikita Astrakhantsev, Tom Westerhout, Apoorv Tiwari, Kenny Choo, Ao Chen, Mark H. Fischer, Giuseppe Carleo, and Titus Neupert, Broken-symmetry ground states of the Heisenberg model on the pyrochlore lattice, Phys. Rev. X **11**, 041021 (2021).

[72] Marc Finzi, Understanding and incorporating mathematical inductive biases in neural networks, Ph.D. thesis, New York University, 2023.

[73] Tom Vieijra and Jannes Nys, Many-body quantum states with exact conservation of non-Abelian and lattice symmetries through variational Monte Carlo, Phys. Rev. B **104**, 045123 (2021).

[74] Maurice Weiler, Mario Geiger, Max Welling, Wouter Boomsma, and Taco S. Cohen, 3d steerable CNNs: Learning rotationally equivariant features in volumetric data, in *Advances in Neural information processing systems, Neurips 2018, Montreal (QC), Canada* (2018), Vol. 31.

[75] M. Hibat-Allah, M. Ganahl, L. E. Hayward, R. G. Melko, and Juan Carrasquilla, Recurrent neural network wave functions, Phys. Rev. Res. **2**, 023358 (2020).

[76] Kaiming He, Xiangyu Zhang, Shaoqing Ren, and Jian Sun, Deep residual learning for image recognition, in *Proceedings of the IEEE Conference on Computer Vision and Pattern Recognition, Las Vegas (NV), USA* (2016), pp. 770–778.

[77] Ian Goodfellow, Yoshua Bengio, and Aaron Courville, *Deep Learning* (MIT Press, Cambridge, England, 2016).

[78] Li Jing, Yichen Shen, Tena Dubcek, John Peurifoy, Scott Skirlo, Yann LeCun, Max Tegmark, and Marin Soljačić, Self-supervised equivariant graph neural networks, in *International Conference on Machine Learning* (PMLR, Sydney, NSW, 2017), pp. 1733–1741.

[79] Kenny Choo, Giuseppe Carleo, Nicolas Regnault, and Titus Neupert, Symmetries and many-body excitations with neural-network quantum states, Phys. Rev. Lett. **121**, 167204 (2018).

[80] John Jumper, Richard Evans, Alexander Pritzel, Tim Green, Michael Figurnov, Olaf Ronneberger, Kathryn Tunyasuvunakool, Russ Bates, Augustin Žídek, Anna Potapenko *et al.*, Highly accurate protein structure prediction with alphafold, Nature (London) **596**, 583 (2021).

[81] Maurice Weiler and Gabriele Cesa, General E(2)-equivariant steerable ENNs, in *Advances in Neural Information Processing Systems NIPS, Vancouver (QC), Canada* (2019), Vol 32.

[82] Manzil Zaheer, Satwik Kottur, Siamak Ravanbakhsh, Barnabas Poczos, Russ R. Salakhutdinov, and Alexander J. Smola, Deep sets, in *Advances in Neural Information Processing Systems, NIPS, Long Beach, CA, USA* (2017), Vol. 30.

[83] Taco S. Cohen and Max Welling, Steerable CNNs, arXiv:1612.08498.

[84] Tom Vieijra, Corneel Casert, Jannes Nys, Wesley De Neve, Jutho Haegeman, Jan Ryckebusch, and Frank Verstraete, Restricted Boltzmann machines for quantum states with non-Abelian or anyonic symmetries, Phys. Rev. Lett. **124**, 097201 (2020).

[85] Matthew B. Hastings, Iván González, Ann B. Kallin, and Roger G. Melko, Measuring Renyi entanglement entropy in quantum Monte Carlo simulations, Phys. Rev. Lett. **104**, 157201 (2010).

[86] Johannes Feldmeier, Nishad Maskara, Nazlı Uğur Köylüoğlu, and Mikhail D. Lukin, Quantum simulation of dynamical gauge theories in periodically driven Rydberg atom arrays, arXiv:2408.02733.

[87] Uwe-Jens Wiese, Towards quantum simulating QCD, Nucl. Phys. **A931**, 246 (2014).

[88] Reinhard Alkofer and Jeff Greensite, Quark confinement: The hard problem of hadron physics, J. Phys. G **34**, S3 (2007).

[89] Julian Bender, Patrick Emonts, Erez Zohar, and J. Ignacio Cirac, Real-time dynamics in $2+1$D compact QED using complex periodic Gaussian states, Phys. Rev. Res. **2**, 043145 (2020).

[90] Marc Daniel Schulz, Sébastien Dusuel, Roman Orus, Julien Vidal, and Kai Phillip Schmidt, Breakdown of a perturbed topological phase, New J. Phys. **14**, 025005 (2012).

[91] Julian Boesl, Rohit Dilip, Frank Pollmann, and Michael Knap, Characterizing fractional topological phases of lattice bosons near the first Mott lobe, Phys. Rev. B **105**, 075135 (2022).

[92] Michael A. Levin and Xiao-Gang Wen, String-net condensation: A physical mechanism for topological phases, Phys. Rev. B **71**, 045110 (2005).

[93] Keitaro Nagata, Finite-density lattice QCD and sign problem: Current status and open problems, Prog. Part. Nucl. Phys. **127**, 103991 (2022).

[94] Nathanan Tantivasadakarn, Ruben Verresen, and Ashvin Vishwanath, Shortest route to non-Abelian topological order on a quantum processor, Phys. Rev. Lett. **131**, 060405 (2023).

[95] Nathanan Tantivasadakarn, Ashvin Vishwanath, and Ruben Verresen, Hierarchy of topological order from finite-depth unitaries, measurement, and feedforward, PRX Quantum **4**, 020339 (2023).

[96] Erik Lennart Weerda and Matteo Rizzi, Fractional quantum Hall states with variational projected entangled-pair states: A study of the bosonic Harper-Hofstadter model, Phys. Rev. B **109**, L241117 (2024).

[97] Matthew B. Hastings, How quantum are non-negative wavefunctions?, J. Math. Phys. (N.Y.) **57** (2016).

[98] Dian Wu, Riccardo Rossi, Filippo Vicentini, Nikita Astrakhantsev, Federico Becca, Xiaodong Cao, Juan Carrasquilla, Francesco Ferrari, Antoine Georges, Mohamed Hibat-Allah *et al.*, Variational benchmarks for quantum many-body problems, Science **386**, 296 (2024).

[99] Steven R. White, Density matrix formulation for quantum renormalization groups, Phys. Rev. Lett. **69**, 2863 (1992).

[100] Steven R. White, Density-matrix algorithms for quantum renormalization groups, Phys. Rev. B **48**, 10345 (1993).

[101] U. Schollwöck, The density-matrix renormalization group, Rev. Mod. Phys. **77**, 259 (2005).

[102] Simon M. Linsel, Annabelle Bohrdt, Lukas Homeier, Lode Pollet, and Fabian Grusdt, Percolation as a confinement order parameter in $\mathbb{Z}_2$ lattice gauge theories, Phys. Rev. B **110**, L241101 (2024).

[103] Jonas Greitemann and Lode Pollet, Lecture notes on diagrammatic Monte Carlo for the Fröhlich polaron, SciPost Phys. Lect. Notes **2** (2018).

[104] Rahul Sahay, Ashvin Vishwanath, and Ruben Verresen, Quantum spin puddles and lakes: NISQ-era spin liquids from non-equilibrium dynamics, arXiv:2211.01381.

[105] Giuliano Giudici, Mikhail D. Lukin, and Hannes Pichler, Dynamical preparation of quantum spin liquids in Rydberg atom arrays, Phys. Rev. Lett. **129**, 090401 (2022).

[106] Zhenjiu Wang and Lode Pollet, Renormalized classical spin liquid on the ruby lattice, Phys. Rev. Lett. **134**, 086601 (2025).

[107] Hannah J. Manetsch, Gyohei Nomura, Elie Bataille, Kon H. Leung, Xudong Lv, and Manuel Endres, A tweezer array with 6100 highly coherent atomic qubits, arXiv:2403.12021.

[108] Jiří Chaloupka, George Jackeli, and Giniyat Khaliullin, Kitaev-Heisenberg model on a honeycomb lattice: Possible exotic phases in iridium oxides A_2Iro$_3$, Phys. Rev. Lett. **105**, 027204 (2010).

[109] Hong-Chen Jiang, Hong Yao, and Leon Balents, Spin liquid ground state of the spin-$\frac{1}{2}$ square J_1-J_2 Heisenberg model, Phys. Rev. B **86**, 024424 (2012).

[110] Jean Bricmont and Jürg Frölich, An order parameter distinguishing between different phases of lattice gauge theories with matter fields, Phys. Lett. **122B**, 73 (1983).

[111] Klaus Fredenhagen and Mihail Marcu, Charged states in $\mathbb{Z}2$ gauge theories, Commun. Math. Phys. **92**, 81 (1983).

[112] K. Gregor, David A. Huse, R. M. oessner, and S. L. Sondhi, Diagnosing deconfinement and topological order, New J. Phys. **13**, 025009 (2011).

[113] Sébastien Dusuel, Michael Kamfor, Román Orús, Kai Phillip Schmidt, and Julien Vidal, Robustness of a perturbed topological phase, Phys. Rev. Lett. **106**, 107203 (2011).

[114] Note the factor of $1/2$ rescaling in the definition of magnetic fields between our Letter and [113].

[115] Nichita Diaconu and Daniel Worrall, Learning to convolve: A generalized weight-tying approach, in *International Conference on Machine Learning* (PMLR, Long Beach, CA, 2019), pp. 1586–1595.

[116] https://github.com/dom-kufel/Approximate-Symmetries-TC

End Matter

Appendix: Spin liquid of the PXP model on the ruby lattice—This appendix presents details associated with our Letter on utilizing approximately symmetric neural quantum states to simulate the PXP model. We begin by introducing the setting. Consider a system of N Rydberg atoms placed on an $L \times (2L+1)$ ruby lattice $[N = 3L(2L+1)]$ with open boundary conditions [25] and described by the following Hamiltonian:

$$H = -\frac{\Omega}{2}\sum_i (b_i + b_i^\dagger) + \sum_{ij} V_{ij} n_i n_j - \delta \sum_i n_i, \qquad \text{(A1)}$$

where on-site Hilbert space is $\{|g_i\rangle, |e_i\rangle\}$, $n_i = |e_i\rangle\langle e_i|$ measures the ith site atom occupation number, and $|e_i\rangle = b_i^\dagger |g_i\rangle$, $|g_i\rangle = b_i|e_i\rangle$. In the so-called PXP limit of this Hamiltonian, the interaction strength is assumed to be infinite for atoms within the blockade radius R_b (i.e., $r_{ij} \leq R_b = 2a$ with a being the shortest distance between two atoms), and zero elsewhere; this strictly prohibits the presence of two excited atoms within a Rydberg blockade radius.

For this PXP model, iDMRG numerics on cylinders have shown that the ground state phase diagram consists of three phases [4]: a trivial phase connected to $|g\rangle^{\otimes N}$ for $\delta/\Omega \lesssim 1.4$, a $\mathbb{Z}_2$ quantum spin liquid phase (QSL) for $1.4 \lesssim \delta/\Omega \lesssim 2.0$, and a symmetry-broken valence-bond solid (VBS) phase for $\delta/\Omega \gtrsim 2.0$. The QSL and VBS phases arise from a local constraint permitting exactly one excited atom per lattice vertex when $\delta/\Omega \gtrsim 1/4$. There are exponentially many configurations that fulfill these local (Gauss's law) constraints. In the QSL phase, the ground state is approximately an equal superposition of all fully packed configurations, while in the VBS phase, the state

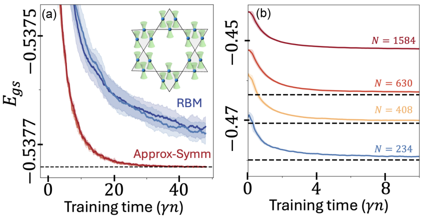

FIG. 5. (a) Convergence of the energy density $E_{\mathrm{GS}} = \langle H\rangle/N$ for approximately symmetric neural networks (red curves), compared to symmetrized RBMs (blue curves) and exact diagonalization (dashed black) on a system of $N = 30$ Rydberg atoms. Inset: schematic depiction of Rydberg atoms trapped in optical tweezers on a ruby lattice [5]. (b) Energy density convergence for larger system sizes $N = 234$, 408, 630, 1584 using approximately symmetric neural quantum states (solid curves), compared to finite-cluster DMRG (dashed black curves) with bond dimension $\chi = 1024$ and 100 sweeps.

spontaneously collapses into one such particular configuration.

To explore the PXP model using approximately symmetric NQS, we tailor the Wilson loop operators (which act around each hexagon of the ruby lattice) such that they map one Gauss's-law-satisfying configuration to another [4]. Since this symmetry is only *approximate* for generic values of δ (even within the PXP limit), our architecture includes a gauge-invariant block alongside a nonsymmetric block. Additional details of the implementation are provided in the Supplemental Material [25]. We compare the performance of this architecture to both RBMs and finite-cluster DMRG. In all cases, we focus on $\delta = 1.6$, which corresponds to a point within the QSL phase.

As depicted in Fig. 5(a), we find that, much as in the mixed-field toric code case, our approximately symmetric NQS yields a nearly 3 order of magnitude improvement in terms of relative energies (dashed line obtained from exact diagonalization) as compared to an RBM architecture. In Fig. 5(b), we present a comparison of the ground-state energy densities obtained via our approximately symmetric NQS with finite DMRG results. For those system sizes accessible to DMRG ($L = 6$, 8, 10), we observe excellent agreement between NQS and DMRG, with a relative energy difference within $\epsilon_{\mathrm{rel}} = 10^{-3} - 10^{-4}$. In the same figure, we also show the NQS numerics for $L = 16$ (equivalent to $N = 1584$ Rydberg atoms) which goes beyond the system sizes that have been investigated using either finite DMRG or QMC [106]. Finally, we note that our approach for studying the PXP limit of the Rydberg Hamiltonian can also be directly applied to the full long-range $1/r^6$ interacting model [5], where the existence of a spin liquid ground state remains under debate [4,106].

Supplementary Information:
Approximately-symmetric neural networks for quantum spin liquids

Dominik S. Kufel*,[1,2] Jack Kemp*,[1,2] DinhDuy Vu,[1,2] Simon
M. Linsel,[1,3,4] Chris R. Laumann,[5] and Norman Y. Yao[1,2]

[1]*Department of Physics, Harvard University, 17 Oxford St., MA 02138, USA*
[2]*Harvard Quantum Initiative, 60 Oxford St., MA 02138, USA*
[3]*Faculty of Physics, Arnold Sommerfeld Centre for Theoretical Physics (ASC),*
Ludwig-Maximilians-Universität München, Theresienstr. 37, 80333 München, Germany
[4]*Munich Center for Quantum Science and Technology (MCQST), Schellingstr. 4, 80799 München, Germany*
[5]*Department of Physics, Boston University, 590 Commonwealth Avenue, Boston, Massachusetts 02215, USA*

CONTENTS

I. NEURAL QUANTUM STATES AND SYMMETRIES OF MANY-BODY SYSTEMS

In the main text, we discussed the concept of approximately-symmetric networks and illustrated an explicit example of an approximately-symmetric NQS. Here we discuss the general methodology for constructing approximately-invariant NQS architectures. We start by discussing different ways of imposing many-body system symmetries on neural networks, followed by highlighting connections between our approach and group-equivariant neural network research in the ML community. We detail an explicit example of a different approximately-invariant architecture from the "combo" architecture in the main text, based on an alternate approach in the ML literature known as "residual pathway priors" (RPP).

A. Overview of different ways of imposing NQS symmetries

Symmetries of many body states ($g|\psi\rangle = |\psi\rangle \; \forall g \in G$) might be imposed on a neural network in multiple ways. If the symmetries of the states are also symmetries of the Hamiltonian, then the approach perhaps most familiar to a physicist is that of mimicking imposing symmetries in the exact diagonalization (ED). As discussed in the main text, in NQS one decomposes an arbitrary state in a certain basis $|\psi\rangle = \sum_s \psi_s |s\rangle$ where $\{|s\rangle\}$ is typically chosen to be an eigenbasis of the Z_j operators. Then a simple way of imposing Hamiltonian symmetries is to turn to the shared eigenbasis of the Hamiltonian and symmetry group G. This approach works for an *arbitrary* group G and has been demonstrated in NQS for e.g., Heisenberg $SU(2)$ symmetric model by [1]. Within such approach one rotates the basis while recalculating matrix elements of the Hamiltonian (in a new basis) and picks a symmetry sector (particular representation of the symmetry group) e.g., $J = 0$ for $SU(2)$ by selecting a *subset* of input bit strings. This approach plays well together with the standard Monte Carlo Markov Chain (MCMC) sampling of bit string configurations in NQS: one initializes the MCMC chain in the symmetry-consistent configuration and then applies a symmetry-preserving update rule. For instance for a $U(1)$ symmetry (e.g., of a quantum XY model) one would only sample configurations with a total spin 0 by initializing the chain accordingly and later using total spin conserving rule for its updates (e.g., one which only exchanges individual spins within the configuration). It should be noted that within this approach the architecture of the neural network does not need to be constrained in any way, yet requires many less parameters to achieve the same relative error in ground state energy (see Fig. 2 in Ref. [1]).

Alternatively, another commonly used approach to imposing symmetries is "post-symmetrization" [2, 3] where one averages the output of the unconstrained NQS over the symmetry group i.e. in the simplest form $\tilde{\psi}_s = \frac{1}{|G|}\sum_{g\in G}\psi_{gs}\chi_g$ where χ_g are characters of a chosen representation of the symmetry group G (where G is abelian). This approach suffers from an extra computational overhead proportional to the size of the group, and thus becomes infeasible for gauge groups or continuous symmetry groups. Its success also heavily depends on the specific choice of the post-symmetrization method: see Ref. [3] for details.

Finally in the autoregressive NQS, another method is instead to simply enforce that the probability of sampling configurations violating the state symmetry constraints vanishes [4–6].

We note that, for all the above methods, it is not immediately clear how to generalize them to the *approximate* symmetries context. We therefore turn to a class of methods which put constraints on the neural-network architecture itself, and allow flexible inclusion of approximate symmetries: group-equivariant neural networks.

B. (Approximately) group-equivariant neural networks

a. Group-equivariance and group-invariance Group-equivariant networks [7] are neural network architectures which by construction are *equivariant* under the action of a particular symmetry group. Group equivariance is one of the essential building blocks for the success of the accurate protein structure prediction with AlphaFold 2 architecture [8]. So far, in the NQS context, group-equivariant networks have mostly been applied within the context of imposing lattice symmetries [9]. Within this approach, one restricts the NQS to (by construction) fulfill a certain constraint: in our case $\psi_{gs} = \psi_s$ i.e. that of group-invariance of the output. Here we assume that the group action maps bit strings to bit strings [10].

The usual way of imposing group-invariance on a neural network is to ensure *group-equivariance* of each of its layers, $\Xi : V \to W$, and non-linearities. Group-equivariance of each layer means that $\Xi(\rho_{in}(g)x) = \rho_{out}(g)\Xi(x)\ \ \forall x \in V, g \in G$ where V is an N-dimensional input vector space, W is an n-dimensional output space, and $\rho_{in} : G \to GL(N, \mathbb{C})$ and $\rho_{out} : G \to GL(n, \mathbb{C})$ are the input and output representations of the symmetry group G. In other words, for a G-equivariant neural network, transforming the input by a certain group element corresponds to transforming features by the same group element (though perhaps expressed in a different representation). The difference between "equivariance" and "invariance" is intuitively illustrated in the animation [11]. As one transforms (rotates) an input (image in the left panel) to the G-*equivariant* neural network, features extracted by the neural network transform accordingly (i.e. rotate; see middle panel). In a G-*invariant* neural network (see right panel), as one transforms the input (left panel), feature fields remain unchanged. In other words, rotational *equivariance* might be thought of as an *invariance* in a co-transforming (co-rotating) frame. The fact that generic neural network architectures are not G-equivariant might be illustrated on the case of the convolutional neural networks (CNNs) for the case of e.g., $SO(2)$ rotation group symmetries. CNNs are by construction translationally equivariant but are not rotationally equivariant. For any equivariant network, a final layer with a scalar output can be used to promote the equivarance to invariance, because it can be chosen to transform under the trivial representation of the symmetry group.

b. Approximate invariance Critically, generalizing the above approach to approximate symmetries is straightforward: instead of demanding $\psi_{gs} = \psi_s\ \ \forall g \in G,\ s \in V$ we demand $\mathbb{E}_{g\in G}\ \mathbb{E}_{s\sim|\psi(s)|^2}||\psi_{gs} - \psi_s|| < \epsilon$ for some $\epsilon > 0$ as discussed in the main text (and where we average over group elements in G and bit strings $s \in V$). We emphasize that ϵ is learnt by the network itself, perhaps with a help of initialization at the fully symmetric point $\epsilon = 0$.

For completeness, we mention that our approach to imposing approximate symmetries within NQS might be perhaps also extended to the framework of Ref. [12]. Therein one evaluates NQS only on "canonical" bit strings which ensures equivariance of the output (for any Abelian group). A "canonical" bit string is a fixed representative of each equivalence class under the group action. Although it is unclear how efficient evaluation of such cannonicalization would be for general Abelian (gauge) groups, we point out an interesting connection to the recent ML literature: [13]. Therein a related cannonicalization function is learnt efficiently by an equivariant neural network. It is thus potentially feasible that the above approximate-symmetries framework might be carried on to this context as well (akin to [14]) - we leave this direction for future work.

C. General construction for approximately-symmetric NQS

a. Exactly-symmetric architecture Here we present a general approach for imposing group equivariance in quantum many-body physics problems, provided that group action maps bit strings to bit strings i.e. $gs \in V \; \forall g \in G, \; s \in V$. Following [15], we construct group-equivariant / group-invariant layers of the network by using equivariant multi-layered perceptrons (EMLP). There, equivariance is achieved by appropriately restricting weights of the multi-layered perceptron architecture. In special cases, this approach reduces to other group-equivariant frameworks such as G-convolutional [7], G-steerable [16] or deep set [17] architectures. We note that G-convolutional networks cannot be directly applied to problems possessing gauge symmetry since their evaluation cost scales with the size of the group. G-steerable convolutions, on the other hand, require decomposition of the group of symmetries G onto semidirect product of group of translations and some other group [18] - which does not seem to be feasible in our case and would require recomputation of irreducible representations for every new group.

Within the EMLP framework, we consider linear layers with dimensions $O(N)$, which are constructed by appropriately restricting weights of the otherwise fully-connected layer. Weight restriction is obtained from an efficient algorithm [15], which is feasible since the cost of imposing equivariance couples only to the size of the generating set of the group—at worst $O(\text{poly}(N))$ for the groups we consider.

Due to the non-regular hidden-layer representations, one needs to ensure that the activation functions $\sigma(x)$ are also equivariant (i.e. that $\sigma(\rho_{in}(g)x) = \rho_{out}(g)\sigma(x)$. Instead of traditionally used gated/norm [19] non-linearities, we utilize other gauge-equivariant non-linearities derived from a physical model in mind i.e. we construct the non-linearity as $\sigma(x) = xh(x)$ where $h(x)$ is a gauge-invariant function of the input to a layer (an example of $h(x)$ for a $\mathbb{Z}_2$ lattice gauge theory is described in the main text). Finally, in the last layer one applies a gauge-invariant non-linearity constructed in a similar fashion by $\tilde{\sigma}(x) = h(x)$. Note that for large symmetry groups (such as gauge groups discussed in the main text), most general linear equivariant layers fulfilling the gauge constraint might be trivial, e.g., for the $\mathbb{Z}_2$ gauge group from the main text, if one considers N-dimensional hidden layer vector space, a linear equivariant layer would simply be proportional to the identity.

Finally, we remark that gauge-invariant architectures discussed above might also in principle be used to find selected excited states of the fully symmetric model. For example, for a purely h_x-perturbed toric code, the lowest lying excitations would correspond to the lowest energy states within the e-anyon excitation sectors. In practice, this might be achieved by applying a local basis transformation for the Hamiltonian $H \mapsto UHU^\dagger$ where e.g., $U = Z_l$ would introduce e-anyon excitation to vertices v, v' belonging to the boundary of the link l. This method of finding an excited state might be further combined with the orthogonalization-based approach used in Refs. [12, 20].

b. Approximately-symmetric architecture Let us now discuss how to generalize to the case when the symmetries are only approximate. The basic idea behind any such generalization is to add non-invariant blocks to an otherwise symmetric architecture. We demonstrate this approach with two examples: the "Combo" architecture in the spirit of [21], discussed in the main text, and the residual pathway prior "RPP" architecture in the spirit of [22]. The RPP architecture is constructed to mimic the ResNet [23] skip-connection architecture. Apart from a gauge-invariant pathway, it also contains a non-invariant skip-connection which allows incorporation of non-symmetric features. In practice, for $G = \mathbb{Z}_2^{\times N/2}$, we construct the skip connection with a non-G-equivariant convolutional layer $\Omega : E \to P$ which maps set of edges to plaquettes. Finally the two pathways (equivariant and non-equivariant) are summed together and post-processed with another convolutional layer acting on plaquettes (as for the "Combo" architecture) – see Fig. 1(b) for "RPP" as compared with "Combo" in Fig. 1(a).

We have implemented and tested both architectures, and find both yield comparable performance (see details below). However, the "Combo" architecture has the advantage that we have some physical intuition about the action the non-invariant layer (see the interpretability sections of the main text and also below for more details), which is why we chose to focus on that architecture.

D. Potential use cases for approximately-symmetric models

We emphasize that there exists many target systems with multiple open physics questions where our approximately-symmetric neural network may be applied. These can be addressed using our approximately symmetric architecture, with minor extensions, for both ground state and real-time evolution studies. For clarity we summarize them in the Table I.

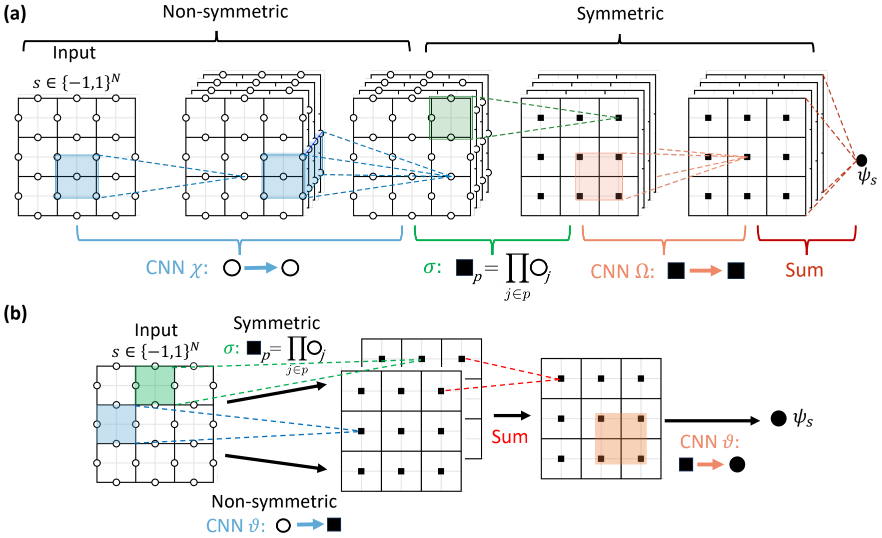

FIG. 1. (a) Replotted "Combo" approximately-symmetric architecture from the main text. (b) For comparison, a sketch of an alternative "RPP" approximately-symmetric architecture. In practice each layer and "branch" (symmetric/non-symmetric) of the network will have multiple channels, but only one has been depicted for simplicity. Initialization of all layers is according to a random Gaussian distribution.

II. APPROXIMATELY-SYMMETRIC NQS TORIC CODE PERFORMANCE STUDY

In this section, we first detail the specific hyperparameters used within our simulations, as well as the Monte Carlo Markov chain update rule we use. Second, we discuss the performance and characteristics of the model for a toric code in h_x and h_z fields. We claim that increasing the depth of the network allows us to systematically improve the accuracy of the simulations. Third, we then discuss the performance of the model under a variety of perturbations, both with and without a sign problem, and identify its key architectural components. Fourth, we track the main issues for further improving the accuracy of the network predictions in different regimes, culminating in suggestions for future architecture improvements with increased parameter-efficiency and enhanced performance. Finally, we provide more details on observable evaluations and extracting phase transitions with NQS.

A. Simulation parameters

For the simulations in the main text, we consider neural networks with real bit string $s \in \{-1,1\}^N$ inputs, (i) complex parameters and outputs if the Hamiltonian has a sign problem ($h_y \neq 0$) and (ii) real parameters, and scalar positive outputs if the Hamiltonian is sign-problem-free ($h_y = 0$) (as then underlying Hamiltonian is stoquastic so by Perron-Frobenius theorem the coefficients of the eigenvector can be chosen real and non-negative in the chosen basis [34]).

We evaluate the energy $\langle H\rangle$ through MCMC sampling. It is performed by noting that $\langle H\rangle = \langle\psi|H|\psi\rangle/\langle\psi|\psi\rangle = \sum_s p(s)E_{loc,s}$ where $p(s) = |\psi(s)|^2$ and $E_{loc,s} = \sum_{\mathbf{s}'} \frac{H_{ss'}}{\psi_s}\psi'_s$ where the latter is evaluated exactly for each bit string s (due to only $\mathcal{O}(poly(N))$ non-zero matrix elements of the Hamiltonian). Then for N_{samples} samples one approximates $\langle H\rangle \approx \frac{1}{N_{\text{samples}}}\sum_{i=1}^{N_{\text{samples}}} E_{loc,s_i}$ where samples $\{s_i\}$ are found by applying a Metropolis-Hastings algorithm.

Extension	Motivation	Framework modification
$\mathbb{Z}_2$ **Spin Liquids**	Realizable in quantum simulators via engineering [24, 25]; resulting ground states (and their dynamical preparation) away from exactly symmetric fixed point.	No modification
Chiral $\mathbb{Z}_d$ **toric code**	$\mathbb{Z}_d$ has an exact symmetry limit and for $d > 2$ permits chiral (exact local symmetry-breaking) perturbations; allows study of fractional quantum Hall physics [26].	Increase onsite dimension d, modify group nonlinearity [27]: $x_1x_2x_3x_4 \to x_1x_2x_3^*x_4^*$ (around each plaquette)
$U(1)$ **lattice gauge theory**	Approximately realizable in quantum simulators via engineering [28]; study fractionalization and confinement dynamics in $U(1)$ gauge theories	Similar to $\mathbb{Z}_d$; promote input variables from binary to continuous [5].
Kitaev double	Study phases and dynamics of models with discrete non-abelian symmetries and non-abelian anyons [29].	Similar to $\mathbb{Z}_d$ with special care taken for multiplication ordering [27].
Double semion	Study of sign-problem-full [30] twisted gauge theories featuring semionic excitations [31].	Modify product non-linearity from group invariance to group equivariance [12, 13].
Non-abelian local continuous symmetries	Study of realizations of non-Abelian lattice gauge theories such as QCD in quantum simulators [32].	Generalizing framework to non-Abelian continuous symmetries [33].
Approximate global symmetries	Study of weakly positionally disordered systems e.g., with approximate translation symmetry.	Using group equivariant neural networks with relaxed group convolutions [21].

TABLE I. Partial list of models where approximately symmetric neural networks may be helpful and the extensions that they would require.

We use a custom sampling rule, closely related to the one used in [35], which involves flipping either a single spin per update step, or all the spins surrounding a single vertex. The intution for this update rules stems from the fact that in the ground state of the toric code, a single spin-flip creates (two) excitations, whereas a vertex-flip does not. Thus close to the toric code fixed point, a single-spin flip update would generically be expected to take a high-amplitude state to a low amplitude state, in contrast to a vertex-flip. Nevertheless, single-spin flips are still required for ergodicity. Given N_v vertices and N spins, on each update we choose to flip a vertex with probability $p = N_v/N$ or else flip a spin. For open boundary conditions, we neglect any verticies with spins on the boundary in this procedure (for periodic boundary conditions, a more complicated procedure is required, see [35]). We find that this vertex-spin update rule empirically yields a significant improvement in MCMC sample acceptance probabilities compared to only using single spin updates.

In order to benefit from GPU parallelization, as well as improving the ergodicity of exploring possibly multi-modal probability landscapes, we draw samples from $\mathcal{O}(10^3)$ independent MCMC chains processed in parallel. We apply $N_{\text{subsample}}$ updates between each collected sample in order to reduce the autocorrelations within each chain. Furthermore, we discard the first $N_{\text{burn-in}}$ samples while the chain thermalizes passed its initial transient. We evaluate $\langle H \rangle$ using C_L samples per chain, so that the total number of samples is $N_{\text{samples}} = C_L N_{\text{chains}}$. The total number of updates which must be applied is thus $(N_{\text{burn-in}} + C_L)\, N_{\text{subsample}} N_{\text{chains}}$.

We initialize the neural network parameters such that the neural network is fully-symmetric before training. This is achieved by initializing the weights of the non-invariant kernels to $\mathbb{1}$ and utilizing the sigmoid non-linearity in the non-invariant layers, given for real inputs as $\phi_{\text{sigmoid}}(x) = \frac{\tanh(x/2)}{\tanh(1/2)} = \frac{2+2e}{e-1}\,(\text{sigmoid}(x) - 1/2)$ and $\text{sigmoid}(x) = \frac{1}{1+e^{-x}}$ (shift and rescaling of the sigmoid to ensure that $\phi_{\text{sigmoid}}(x = \pm 1) = \pm 1$ for identity initialization of the non-invariant block). For invariant layers we use ELU non-linearity [36]. For complex neural network parameters, we separately pass real and imaginary parts of the input to the non-linearity $\mathbb{C} -$ sigmoid (non-invariant layer) and $\mathbb{C} -$ ELU (invariant layer) e.g., $\phi_{\mathbb{C}}(x) = \phi(Re[x]) + i\phi(Im[x])$ for either non-linearity ϕ.

We optimize the network parameters using stochastic reconfiguration [37] with diagonal shift regularization. This might be thought as an imaginary time evolution for the states [38] and amounts to 1st order time evolution on a TDVP manifold, yielding linear equations of motion for the vectorized parameters $\boldsymbol{\theta}_t$: $\mathbf{S}\dot{\boldsymbol{\theta}}_t = -\gamma \mathbf{F}$ where $\mathbf{F}$ is a force vector, γ is a learning rate, and $\mathbf{S}$ is a quantum geometric tensor (see e.g., [39] for details). We solve this equation by performing a singular value decomposition on the $\mathbf{S}$ matrix, which has complexity of $\mathcal{O}(N_{\text{parameters}}^3 + N_{\text{parameters}}^2 N_{\text{samples}})$ [40]. We choose it over the conjugate gradients solver with complexity $\mathcal{O}(N_{\text{parameters}} \kappa N_{\text{samples}})$ (where κ is a condition number of the matrix $\mathbf{S}$), because we empirically observed that for the family of ground states of the system and architecture under consideration κ is very large ($\mathbf{S}$ eigenvalues span 15 to 30 orders of magnitude) which in practice yields rather unpredictable and slower runtimes. Furthermore, in order to stabilize the simulations we add a small shift to the diagonal of the $\mathbf{S}$ matrix i.e., $\mathbf{S} \mapsto \mathbf{S} + d\mathbb{1}$.

Parameters used for running simulations with the architecture presented in Fig. (1a) of the main text for 16×16 are listed in the Table II below. All simulations are run in *NetKet* [41] that benefits from *JAX* [42] auto-differentiation and just-in-time compilation. We follow the convention in *NetKet 3.11* such that in code neural network outputs represent a *logarithm* of an amplitude ψ_s to facilitate calculations. All neural networks are coded in *FLAX* [43]. Density Matrix Renormalization Group (DMRG) simulations were performed in *iTensor* [44, 45] and exact diagonalization in *Dynamite* [46]. Energy densities as used in the figures are defined as $E_{gs} = \frac{\langle H \rangle}{N+1}$ i.e. energy per stabilizer. Training time in all figures refers to the γn (where n is iteration number, and γ, as above, is a learning rate).

Parameter Type	Parameter	Value
Optimization parameters	Learning rate	7e-3
	Diagonal shift d	5e-5
Architecture parameters	NIB: Channels & Depth	$[1, 2, 4]$
	NIB: Initialization	Identity $\mathbb{1}$
	NIB: Kernel Size	3
	NIB: Non-linearity	$\mathbb{C}$ − sigmoid
	IB: Channels & Depth	$[4, 4, 4]$
	IB: Initialization	Random Gaussian $\mu = 0, \sigma = 0.02$
	IB: Kernel Size	15
	IB: Non-linearity	$\mathbb{C}$ − ELU
	Total $N_{\text{parameters}}$	11324
Sampling characteristics	N_{chains}	1024
	$N_{\text{burn-in}}$ (per chain)	8
	$N_{\text{subsample}}$	480
	N_{samples}	8192

TABLE II. Summary of neural network parameters for 16×16 runs. NIB=Non-invariant block, IB=Invariant-block; channels & depth specifies the number of channels in each layer within a block.

B. Comparisons with baseline neural networks for a 4×4 system

We provide more details on comparing our approach with baseline neural network architectures which incorporate lattice symmetries but no local gauge symmetries. In the main text this was performed for CNNs, which by construction incorporate translation symmetries and contain $4 - 10$ layers with multiple filters per layer. We note that the main difference between CNNs and our architecture is the presence of the group-invariant block and both networks have a comparable runtime. As mentioned in the main text (cf. Fig. 2(a) therein), we found that unlike our approximately-symmetric network approach, CNNs are trapped in local minima, thus conclusively showing the importance of imposing approximate gauge symmetries. Additionally, in Fig. 2, we show that symmetric restricted Boltzmann machines (RBMs), which incorporate *all* lattice symmetries rather than only translations [39], perform better than CNNs. However, they still get trapped in local minima with errors several orders of magnitude larger than those achieved by our architecture. Furthermore, we expect the performance gap between symmetric RBMs (or their deeper variants, such as GCNNs) and approximate symmetry-based approaches to grow with system size, as the local symmetry space scales exponentially ($\mathcal{O}(2^{N/2})$) compared to the linear scaling of lattice symmetries ($\mathcal{O}(N)$).

C. Performance in h_x and h_z fields for a 4×4 system

For a 4×4 system and the "Combo" and "RPP" architectures, we plot the best relative error for different values of fields (h_x, h_z), optimized over hyperparameters after multiple simulation runs on a cluster (Fig. 3).

As expected from the built-in inductive bias, the neural network has the best performance for the small h_z fields (where the approximate symmetries of the model are close to being exact). Although the network's performance drops slightly as the value of the h_x field is increased (owing to the increasing complexity of the wavefunction associated with the higher correlation length), the drop along the h_z field is much more pronounced. As mentioned in the main text, the accuracy does not sharply diminish at the edge of the topological phase, but instead slowly decreases with the h_z field, making the ansatz applicable even when h_z is roughly comparable to the strength of the toric-code Hamiltonian coupling. Further, the energies obtained from our architecture (although not directly comparable due to

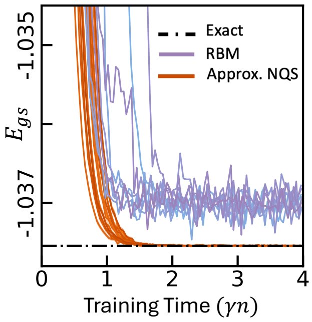

FIG. 2. Energy convergence curve for approximately-symmetric networks and RBMs as compared with exact diagonalization on $N = 24$ system in $(h_x, h_y, h_z) = (0.2, 0.0, 0.2)$ fields.

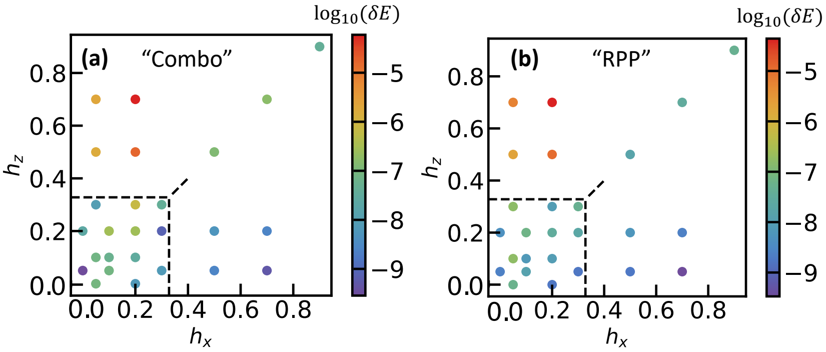

FIG. 3. Performance of (a) "Combo" and (b) "RPP" neural network architectures at different magnetic field strengths for system size 4×4 and $h_y = 0$.

different boundary conditions and system sizes) are much lower than these obtained in Ref. [20] when studied on the perturbed toric code model. Finally, we do not observe any significant differences in performance between the "RPP" and "Combo" architectures. We note that for 4×4 systems, having a kernel size for the invariant part of the network covering the entire system ($O(N)$) is crucial for achieving the reported accuracies (in contrast to the non-invariant network kernel size which can be $O(1)$ without any significant loss in accuracy).

D. Performance under different perturbations for 4×4

We demonstrate that our ansatz is stable against a variety of different Hamiltonian perturbations: including ones introducing a sign problem. We broadly divide perturbations of the toric code Hamiltonian into different classes (see Table III). For sign-problem-full perturbations, the Hamiltonian will not be stoquastic, and therefore the Frobenius theorem does not apply, permitting a non-trivial ground-state sign structure. For sign-problem-full perturbations we therefore allow for complex network outputs by using complex parameters.

We note that the performance of our ansatz has accuracy below 10^{-3} for all perturbations tested. As generically

Perturbation type	**Perturbation**	ϵ_{rel}
Sign-problem-free, invariant	XX	1e-9
Sign-problem-free, non-invariant	ZZ	6e-8
	XX+YY+ZZ	2e-5
	XX+YY	1e-5
Sign-problem-full, invariant	YYYY on plaquettes	1e-5
Sign-problem-full, non-invariant	Y	1e-4
	YY	1e-3
	YYYY on vertices	4e-6

TABLE III. Relative energies obtained within Combo architecture for different perturbations on N=24 toric code. All perturbations are fixed to value 0.2 in magnitude and in addition we add a small $h_x = 0.05$ field to all of them.

expected [47], perturbations introducing sign-problem are more difficult for the NQS. This is most likely due to difficulty in propagation of complex phases through the network [48]. We notice that achieving the performance we have reached for the *sign-problem-full* case hinges upon including correlations between different channels of the non-invariant architecture as depicted in Fig. (1 a) of the main text. For instance, architecture with a "bottleneck" where one sums over all channels before passing the output to the Wilson loop non-linearity, performs one to two orders of magnitude worse in accuracy as compared with the presented results.

Although we have not further tailored our ansatz for the sign-problem-full case, there are several ways of doing this e.g., by (i) experimenting with different complex phase representation e.g., by two decoupled networks with real parameters (one representing amplitude and the other the phase) [47, 49] and performing their sequential training [47, 49], (ii) modifying form of complex non-linearities within the complex parameters architectures [48].

E. Performance in (h_x, h_y, h_z) magnetic fields for a 10×10 system

a. Approximately-symmetric neural network analysis and improvement We proceed to investigating what limits the performance of the approximately-symmetric neural network. We first study the performance of the purely gauge-invariant architecture (constructed by omitting non-invariant block in the architecture in Fig. (2a) in the main text). We performed additional validations to characterize the converged ground states—such as evaluating order parameters for the topological phase—and found that the V-score [50] was of the same order of magnitude as the relative error compared to state-of-the-art DMRG/QMC results, consistent with expectations. Additionally, we note that the relative energies achieved for $(h_x, h_y, h_z) = (0.2, 0.0, 0.0)$ fields with a fully gauge-invariant architecture are comparable to these for $(h_x, h_y, h_z) = (0.2, 0.0, 0.2)$ with an approximately-symmetric one. We further observe a systematic scaling with the number of parameters and particularly depth of the network. We suggest therefore that the accuracy of the approximately-symmetric network behavior is not limited by the non-invariant block of the network but the invariant one. We investigate this hypothesis by investigating scaling of the relative energy error with the number of channels and depth of the symmetric and non-symmetric block of the network. In agreement with the purely gauge-invariant network results, we observe that by increasing the depth of the invariant part of the network, one can systematically improve the achievable energies (Fig. 4(a)). No similar scaling was observed with the depth of the non-invariant block (Fig. 4(b)) or the number of channels in the non-invariant or invariant part blocks (not shown). This conclusion holds for a range of other values of magnetic fields and system sizes.

We therefore suggest that the accuracy of our approximately-symmetric architecture might be improved by increasing the depth of the invariant part of the architecture. This might be potentially achieved by trying to further stabilize the training of deep neural network architectures (e.g., by introducing batch or layer normalization, see also [51]) and by increasing the efficiency of utilizing neural network parameters e.g., through pooling layers and decreasing invariant kernel sizes (simulations were run for $O(N)$-sized invariant kernels, but we did not observe any noticeable drop of accuracy in network performance with the reduction of the kernel size). Finally, one could try applying some of the transfer learning techniques [52] and optimizing ansatz with minSR for shorter runtimes [40]. We leave these suggested improvements for future work.

b. Sampling statistics We provide more data on MCMC statistics for simulations on a 10×10 system under an h_y field to demonstrate that, for the system under consideration and architecture chosen, one does not run into any significant sampling issues. Sampling for the sign-problem full toric code with an $h_y \neq 0$ field should be the most difficult: e.g., for stoquastic Hamiltonians it can be proven [53, 54] that MCMC mixing time for sampling their ground states scales polynomially with the number of qubits. To demonstrate that there are no issues with sampling, we show that (Fig. 4(c)): (i) the acceptance probabilities of the MCMC chain remain large ($> 25\%$) throughout the optimization; (ii) the energy autocorrelation time τ is small (where $\tau = 0$ is ideal and one would like to avoid $\tau \gg 1$).

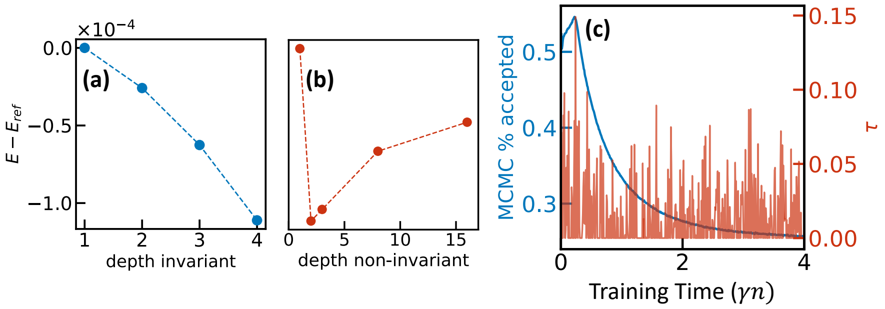

FIG. 4. Scaling of the relative variational energies with the number of layers (depth) of the neural network architecture on a 10×10 model for (a) the invariant and (b) the non-invariant block under $(h_x, h_y, h_z) = (0.2, 0.0, 0.2)$ field. The accuracy of the ansatz can be systematically improved with the depth of the invariant block (but not the non-invariant one). Reference energy corresponds to the depth= 1 value. (c) Sampling statistics for a $(h_x, h_y, h_z) = (0.2, 0.2, 0.2)$ on 10×10 system. τ refers to an energy autocorrelation time. We see that the acceptance rate remains high throughout, while the autocorrelation time does not significantly increase.

Furthermore, we verified that the split-$\hat{R}$ characteristics [55] remains < 1.01 throughout the simulation (where $\hat{R}$ is ideally 1 and $\hat{R} < 1.01$ tolerance is heuristically recommended [55]).

F. Extracting phase transitions for a mixed field toric code

We provide more details about evaluating observables and extracting the phase diagram of the mixed field toric code under $h_y = 0.3$ field (Fig. 1(c) main text). As mentioned in the main text, to find the phase transition we evaluate BFFM X and Z observables (O_X and O_Z) and second Renyi entropy. Assuming that observables of interests have only a polynomial number of non-zero matrix elements in each column of the matrix, they can be efficiently evaluated in the NQS by MCMC sampling [41]. This is indeed the case for the O_Z (O_X) order parameters (defined in the main text). Formally these observables become order parameters ($\mathcal{O}_Z$ and $\mathcal{O}_X$) only as the loop perimeter $m \to \infty$. In practice however, relatively small value of m allows one to observe phase transitions. The intuition behind the $\mathcal{O}_Z$ ($\mathcal{O}_X$) order parameters is the following: close to $h_x = h_y = h_z = 0$ (unperturbed toric code limit) one would expect that the numerator is vanishing (open half-loop string creates two excitations at its ends which have a vanishing expectation value in a ground state) and denominator finite (closed Wilson loops are near exact symmetries of the ground state); away from $h_x = h_y = h_z = 0$ point, closed Wilson loop decay exponentially with the loop perimeter m, but this decay is compensated by a similar decay of the half-loops, leaving only the contributions from the endpoints yielding vanishing expectation value of the string order parameter [56].

On the other hand, the second Renyi entropy can be efficiently evaluated using Monte Carlo method as the expectation value of a SWAP operator on two copies of the state [57].

For a fixed h_z cut through the phase diagram we find no significant shift of the peak in the derivative of both BFFM and second Renyi entropy with increasing L which we associate with the location of the phase transition. For a fixed h_x cut, on the other hand, we find stronger finite-size effects [58]. To obtain a more accurate estimate of the thermodynamic critical points along these cuts, we perform a simple finite-size extrapolation of the position of extracted $\frac{\mathrm{d}O_Z}{\mathrm{d}h_z}$ and $\frac{\mathrm{d}S_{\mathrm{Renyi}}}{\mathrm{d}h_z}$ peaks (see Fig. 5). In particular, we fit the peak location to a power law in inverse system size, $h_{\mathrm{peak}} = h_{\mathrm{crit}} + b(\frac{1}{L})^x$ and extrapolate $1/L \to 0$. Uncertainty in the extrapolation determines the uncertainty in critical point extraction (errorbars in Fig. 1(c) in the main text).

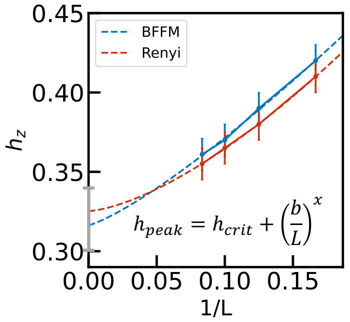

FIG. 5. Finite-size extrapolation of BFFM and Renyi observables for an $h_x = 0$ cut through the phase diagram. b and x are fit parameters. Uncertainty in the $1/L \to 0$ intercept corresponds to the gray errorbar.

III. INTERPRETABILITY

We proceed to discussing interpretability of the approximately-symmetric neural network. We first discuss some caveats on the approximate-to-exact symmetries mapping proposed as the operational principle of the neural network. We second proceed to discuss the network invariance error (a quantity well-known in the machine-learning community [59]) and demonstrate that its derivative appears to exhibit divergent behavior at the same location as the phase transition from the quantum spin liquid to a trivial phase.

A. Approximate to exact symmetries mapping

In the main text we have argued that our approximately symmetric architecture operates mainly by mapping "fattened" Wilson loops to their known form at the fixed point within the non-symmetric block, and later solves the fully symmetric problem in the symmetric block. We have shown this strictly for an independent neural network training procedure (see main text). We expect this conclusion to largely hold for training both blocks together. One subtlety of the joint training is that the non-symmetric block is capable of learning some symmetric features of the state as well. One of the consequences of this is that after such training on $h_z \neq 0$ (and $h_y = 0$) simply setting weights of the non-invariant layer to an identity does not produce the $h_z = 0$ ground state. We leave it for future investigations how to fully decouple features learnt by two blocks of the network during the joint training.

B. Invariance error

In the definition of the approximate group invariance $\mathbb{E}_{s\sim p(s)}\mathbb{E}_{g\in G}|\psi_{gs} - \psi_s| < \epsilon$, we defined a measure of the magnitude of the symmetry breaking, ϵ. Here we discuss the dynamics and asymptotic values of the closely related quantity $\tilde{\epsilon} = \mathbb{E}_{s\sim p(s)}\mathbb{E}_{g\in G}\|\log\psi_{gs} - \log\psi_s\|$ as learnt by the neural network. We note that: (i) value of $\tilde{\epsilon}$ approaches the same value irrespective of the network hyperparameters over the course of optimization, (ii) $\tilde{\epsilon}$ appears to have a divergent derivative as one tunes the *symmetry-violating* field in a point closely matching the more conventional observables of the toric code phase transitions such as BFFM order parameters (see main text).

a. Invariance error universality In the "Combo" approximately-symmetric architecture discussed in the main text, one increases the (maximum) degree of non-invariance implicitly by increasing the number of channels in the non-invariant layer. We note, however, that $\tilde{\epsilon}$ (and correspondingly ϵ) converges to the same value towards the end of optimization (see Fig. 6b), regardless of the number of channel configuration (assuming that optimization has succeeded; this might require a certain minimum number of non-invariant channels).

b. Invariance error divergence Furthermore, we found that the invariance error $\tilde{\epsilon}$ significantly increases with the increasing values of the h_z field. To investigate this behaviour further we plot the $\log\tilde{\epsilon}$ as a function of h_z field in

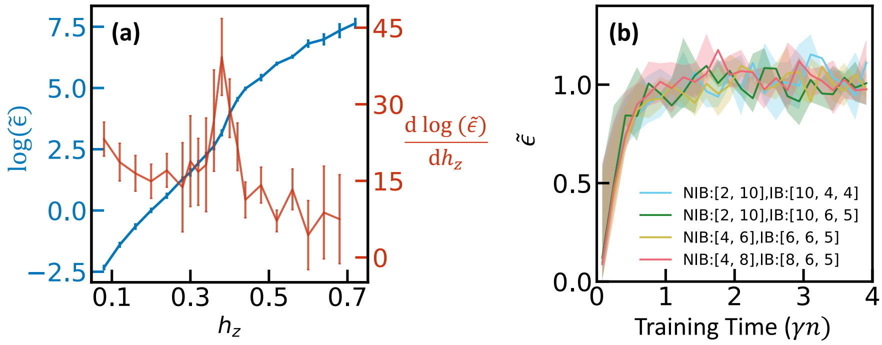

FIG. 6. (a) Logarithm of an invariance error $\tilde{\epsilon}$ (blue line) and its derivative (red line) for $L = 8$ for $h_x = 0.14, h_y = 0$ as a function of the group symmetry breaking field (h_z), displaying a peak at a point consistent at the phase transition point identified by more conventional observables at the same system size (see Fig. 3(a) and 3(c) in the main text). (b) Invariance error $\tilde{\epsilon}$ as a function of time for ($h_x = 0.14, h_y = 0.0, h_z = 0.2$) for $L = 8$. Up to sampling errors, for any (successful) optimization, it converges to the fixed value, dependent only on the value of the h_z field. NIB denotes non-invariant block, IB denotes invariant-block and numbers specify the channel configuration in every layer.

the Fig. 6a. First, as expected, at $h_z = 0$ the approximately-symmetric architecture learns to stay fully invariant (despite of extra flexibility). Second, we observe that $\mathrm{d}\log\tilde{\epsilon}/\mathrm{d}h_z$ reveals a peak matching the critical point found by more conventional observables (as in Fig. 3 main text). Such behavior is most likely comes from the connection of ϵ invariance error to the extent by which X-Wilson loops act non-trivially on a system's ground state: $\epsilon \sim ||A_v|\psi\rangle - |\psi\rangle||$. It should be noted that, as expected, $\tilde{\epsilon}$ exhibits no such divergent behaviour when tuning *symmetry-preserving* terms (e.g., h_x magnetic field) – under which the network stays fully invariant.

IV. APPROXIMATELY-SYMMETRIC NQS FOR RYDBERG SPIN LIQUIDS

Here we provide more information about approximately-symmetric neural network applied to a PXP limit of the Rydberg Hamiltonian on a ruby lattice. First, we efficiently incorporate the Rydberg blockade within each triangle by reducing the local Hilbert space to that of a spin-3/2, since double-occupancy configurations cost infinite energy in the PXP limit. The resulting local basis over a triangle is $\{|ggg\rangle, |egg\rangle, |geg\rangle, |gge\rangle\}$, effectively defining a spin-3/2 system on a honeycomb lattice. Second, we use an approximately-symmetric neural network consisting of a gauge invariant block, non-gauge-symmetric CNN added together with the non-gauge-symmetric mean-field ansatz (thus forming the "RPP" architecture discussed before). Relevant gauge invariant Wilson operators – with respect to which gauge-invariant product non-linearities are constructed – are shown in Fig. 7(a) and Fig. 7(b) - see also Ref. [60]. The mean-field ansatz $\mathrm{MF} = \sum_i c_i n_i$ is added for numerical stability. We symmetrize the input to the neural network with lattice symmetries (horizontal and vertical parity). We use, single layer, $4 - 20$ features in the non-symmetric part (in addition to the mean-field features), GELU activation functions and stochastic reconfiguration with the SVD-based solution to the set of linear equations. Finally, on small system sizes we benchmark our architecture against RBMs enhanced with spin-3/2 blockade constraints and a mean-field ansatz respecting all lattice symmetries (including inversion around the x and y axes).

We find evidence of the quantum spin liquid phase by inspecting Wilson loop operators for large system sizes ($L \geq 6$) and finite size versions of BFFM order parameters (on $L = 6$ they evaluate to $\langle X_{BFFM}\rangle \sim 0.01$ for equal-superposition probing loop passing through 12 spins-1/2 and $\langle Z_{BFFM}\rangle \sim 0.07$ for Gauss' law probing loop passing through 18 spins-1/2), in agreement with the predictions from iDMRG [60]. Loops used to calculate BFFM order parameters are defined in Fig. 7(c).

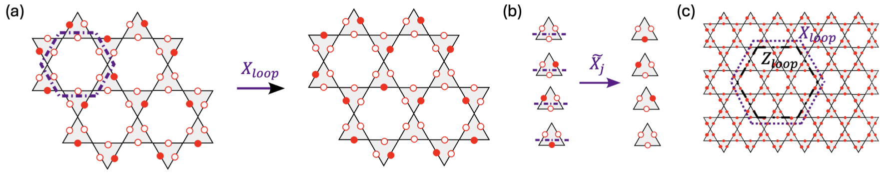

FIG. 7. (a) $X_{loop} = \prod_{j\in\text{hexagon}} \tilde{X}_j$ operators used to construct gauge invariant non-linearites for the ruby model. Red filled/empty circles denote Rydberg atoms in an excited/ground state (b) Action of $\tilde{X}_j$ within each triangle (c) Loop operators used to calculate BFFM order parameters on $L = 6$.

[1] Tom Vieijra, Corneel Casert, Jannes Nys, Wesley De Neve, Jutho Haegeman, Jan Ryckebusch, and Frank Verstraete, "Restricted boltzmann machines for quantum states with non-abelian or anyonic symmetries," Physical review letters **124**, 097201 (2020).

[2] Kenny Choo, Titus Neupert, and Giuseppe Carleo, "Two-dimensional frustrated j 1- j 2 model studied with neural network quantum states," Physical Review B **100**, 125124 (2019).

[3] Moritz Reh, Markus Schmitt, and Martin Gärttner, "Optimizing design choices for neural quantum states," Physical Review B **107**, 195115 (2023).

[4] Zhuo Chen, Laker Newhouse, Eddie Chen, Di Luo, and Marin Soljacic, "Antn: Bridging autoregressive neural networks and tensor networks for quantum many-body simulation," Advances in Neural Information Processing Systems **36**, 450–476 (2023).

[5] Di Luo, Shunyue Yuan, James Stokes, and Bryan Clark, "Gauge equivariant neural networks for 2+ 1d u (1) gauge theory simulations in hamiltonian formulation," in *NeurIPS 2022 AI for Science: Progress and Promises* (2022).

[6] Mohamed Hibat-Allah, Martin Ganahl, Lauren E Hayward, Roger G Melko, and Juan Carrasquilla, "Recurrent neural network wave functions," Physical Review Research **2**, 023358 (2020).

[7] Taco Cohen and Max Welling, "Group equivariant convolutional networks," in *International conference on machine learning* (PMLR, 2016) pp. 2990–2999.

[8] John Jumper, Richard Evans, Alexander Pritzel, Tim Green, Michael Figurnov, Olaf Ronneberger, Kathryn Tunyasuvunakool, Russ Bates, Augustin Žídek, Anna Potapenko, *et al.*, "Highly accurate protein structure prediction with alphafold," Nature **596**, 583–589 (2021).

[9] Christopher Roth, Attila Szabó, and Allan H MacDonald, "High-accuracy variational monte carlo for frustrated magnets with deep neural networks," Physical Review B **108**, 054410 (2023).

[10] Extending the applicability of the method beyond bit string to bit string mapping is perhaps possible by proceeding along lines of Ref. [61] where one imposes $SU(2)$ + lattice symmetries within the constrained neural network architecture utilizing idea of an equivariant Clebsch-Gordan nets [62].

[11] University of Amsterdam QUVA lab, "Group-equivariant neural network demonstration," `https://github.com/dom-kufel/g_equiv_networks/blob/main/conventional_cnn.gif`.

[12] Kenny Choo, Giuseppe Carleo, Nicolas Regnault, and Titus Neupert, "Symmetries and many-body excitations with neural-network quantum states," Physical review letters **121**, 167204 (2018).

[13] Sékou-Oumar Kaba, Arnab Kumar Mondal, Yan Zhang, Yoshua Bengio, and Siamak Ravanbakhsh, "Equivariance with learned canonicalization functions," in *International Conference on Machine Learning* (PMLR, 2023) pp. 15546–15566.

[14] Sékou-Oumar Kaba and Siamak Ravanbakhsh, "Symmetry breaking and equivariant neural networks," arXiv preprint arXiv:2312.09016 (2023).

[15] Marc Finzi, Max Welling, and Andrew Gordon Wilson, "A practical method for constructing equivariant multilayer perceptrons for arbitrary matrix groups," in *International conference on machine learning* (PMLR, 2021) pp. 3318–3328.

[16] Taco S Cohen and Max Welling, "Steerable cnns," arXiv preprint arXiv:1612.08498 (2016).

[17] Manzil Zaheer, Satwik Kottur, Siamak Ravanbakhsh, Barnabas Poczos, Russ R Salakhutdinov, and Alexander J Smola, "Deep sets," Advances in neural information processing systems **30** (2017).

[18] Maurice Weiler and Gabriele Cesa, "General e (2)-equivariant steerable cnns," Advances in neural information processing systems **32** (2019).

[19] Maurice Weiler, Mario Geiger, Max Welling, Wouter Boomsma, and Taco S Cohen, "3d steerable cnns: Learning rotationally equivariant features in volumetric data," Advances in Neural Information Processing Systems **31** (2018).

[20] Agnes Valenti, Eliska Greplova, Netanel H Lindner, and Sebastian D Huber, "Correlation-enhanced neural networks as interpretable variational quantum states," Physical Review Research **4**, L012010 (2022).

[21] Rui Wang, Robin Walters, and Rose Yu, "Approximately equivariant networks for imperfectly symmetric dynamics," in

International Conference on Machine Learning (PMLR, 2022) pp. 23078–23091.

[22] Marc Finzi, Gregory Benton, and Andrew G Wilson, "Residual pathway priors for soft equivariance constraints," Advances in Neural Information Processing Systems **34**, 30037–30049 (2021).

[23] Kaiming He, Xiangyu Zhang, Shaoqing Ren, and Jian Sun, "Deep residual learning for image recognition," in *Proceedings of the IEEE conference on computer vision and pattern recognition* (2016) pp. 770–778.

[24] Giulia Semeghini, Harry Levine, Alexander Keesling, Sepehr Ebadi, Tout T Wang, Dolev Bluvstein, Ruben Verresen, Hannes Pichler, Marcin Kalinowski, Rhine Samajdar, *et al.*, "Probing topological spin liquids on a programmable quantum simulator," Science **374**, 1242–1247 (2021).

[25] Ruben Verresen, Mikhail D Lukin, and Ashvin Vishwanath, "Prediction of toric code topological order from rydberg blockade," Physical Review X **11**, 031005 (2021).

[26] Erik Lennart Weerda and Matteo Rizzi, "Fractional quantum hall states with variational projected entangled-pair states: A study of the bosonic harper-hofstadter model," Physical Review B **109**, L241117 (2024).

[27] Di Luo, Giuseppe Carleo, Bryan K Clark, and James Stokes, "Gauge equivariant neural networks for quantum lattice gauge theories," Physical review letters **127**, 276402 (2021).

[28] Johannes Feldmeier, Nishad Maskara, Nazlı Uğur Köylüoğlu, and Mikhail D Lukin, "Quantum simulation of dynamical gauge theories in periodically driven rydberg atom arrays," arXiv preprint arXiv:2408.02733 (2024).

[29] Mohsin Iqbal, Nathanan Tantivasadakarn, Ruben Verresen, Sara L Campbell, Joan M Dreiling, Caroline Figgatt, John P Gaebler, Jacob Johansen, Michael Mills, Steven A Moses, *et al.*, "Non-abelian topological order and anyons on a trapped-ion processor," Nature **626**, 505–511 (2024).

[30] Matthew B Hastings, "How quantum are non-negative wavefunctions?" Journal of Mathematical Physics **57** (2016).

[31] Michael A Levin and Xiao-Gang Wen, "String-net condensation: A physical mechanism for topological phases," Physical Review B—Condensed Matter and Materials Physics **71**, 045110 (2005).

[32] Uwe-Jens Wiese, "Towards quantum simulating qcd," Nuclear Physics A **931**, 246–256 (2014).

[33] Nichita Diaconu and Daniel Worrall, "Learning to convolve: A generalized weight-tying approach," in *International Conference on Machine Learning* (PMLR, 2019) pp. 1586–1595.

[34] S Unnikrishna Pillai, Torsten Suel, and Seunghun Cha, "The perron-frobenius theorem: some of its applications," IEEE Signal Processing Magazine **22**, 62–75 (2005).

[35] Marc Machaczek, "Neural quantum states for fracton models," `https://zenodo.org/records/10728168` (2024).

[36] Djork-Arné Clevert, Thomas Unterthiner, and Sepp Hochreiter, "Fast and accurate deep network learning by exponential linear units (elus)," arXiv preprint arXiv:1511.07289 (2015).

[37] Sandro Sorella, "Green function monte carlo with stochastic reconfiguration," Physical review letters **80**, 4558 (1998).

[38] James Stokes, Josh Izaac, Nathan Killoran, and Giuseppe Carleo, "Quantum natural gradient," Quantum **4**, 269 (2020).

[39] Giuseppe Carleo and Matthias Troyer, "Solving the quantum many-body problem with artificial neural networks," Science **355**, 602–606 (2017).

[40] Ao Chen and Markus Heyl, "Efficient optimization of deep neural quantum states toward machine precision," arXiv preprint arXiv:2302.01941 (2023).

[41] Filippo Vicentini, Damian Hofmann, Attila Szabó, Dian Wu, Christopher Roth, Clemens Giuliani, Gabriel Pescia, Jannes Nys, Vladimir Vargas-Calderón, Nikita Astrakhantsev, *et al.*, "Netket 3: Machine learning toolbox for many-body quantum systems," SciPost Physics Codebases , 007 (2022).

[42] James Bradbury, Roy Frostig, Peter Hawkins, Matthew James Johnson, Chris Leary, Dougal Maclaurin, George Necula, Adam Paszke, Jake VanderPlas, Skye Wanderman-Milne, and Qiao Zhang, "JAX: composable transformations of Python+NumPy programs," (2018).

[43] Jonathan Heek, Anselm Levskaya, Avital Oliver, Marvin Ritter, Bertrand Rondepierre, Andreas Steiner, and Marc van Zee, "Flax: A neural network library and ecosystem for JAX," (2023).

[44] Matthew Fishman, Steven R. White, and E. Miles Stoudenmire, "The ITensor Software Library for Tensor Network Calculations," SciPost Phys. Codebases , 4 (2022).

[45] Matthew Fishman, Steven R. White, and E. Miles Stoudenmire, "Codebase release 0.3 for ITensor," SciPost Phys. Codebases , 4–r0.3 (2022).

[46] Gregory D. Kahanamoku-Meyer and Julia Wei, "GregDMeyer/dynamite: v0.4.0," (2024).

[47] Attila Szabó and Claudio Castelnovo, "Neural network wave functions and the sign problem," Physical Review Research **2**, 033075 (2020).

[48] Li Jing, Yichen Shen, Tena Dubcek, John Peurifoy, Scott Skirlo, Yann LeCun, Max Tegmark, and Marin Soljačić, "Tunable efficient unitary neural networks (eunn) and their application to rnns," in *International Conference on Machine Learning* (PMLR, 2017) pp. 1733–1741.

[49] Nikita Astrakhantsev, Tom Westerhout, Apoorv Tiwari, Kenny Choo, Ao Chen, Mark H Fischer, Giuseppe Carleo, and Titus Neupert, "Broken-symmetry ground states of the heisenberg model on the pyrochlore lattice," Physical Review X **11**, 041021 (2021).

[50] Dian Wu, Riccardo Rossi, Filippo Vicentini, Nikita Astrakhantsev, Federico Becca, Xiaodong Cao, Juan Carrasquilla, Francesco Ferrari, Antoine Georges, Mohamed Hibat-Allah, *et al.*, "Variational benchmarks for quantum many-body problems," Science **386**, 296–301 (2024).

[51] Ian Goodfellow, Yoshua Bengio, and Aaron Courville, *Deep learning* (MIT press, 2016).

[52] Remmy Zen, Long My, Ryan Tan, Frédéric Hébert, Mario Gattobigio, Christian Miniatura, Dario Poletti, and Stéphane Bressan, "Transfer learning for scalability of neural-network quantum states," Physical Review E **101**, 053301 (2020).

[53] Sergey Bravyi, David Gosset, and Yinchen Liu, "How to simulate quantum measurement without computing marginals,"

Physical Review Letters **128**, 220503 (2022).
[54] Sergey Bravyi, Giuseppe Carleo, David Gosset, and Yinchen Liu, "A rapidly mixing markov chain from any gapped quantum many-body system," Quantum **7**, 1173 (2023).
[55] Aki Vehtari, Andrew Gelman, Daniel Simpson, Bob Carpenter, and Paul-Christian Bürkner, "Rank-normalization, folding, and localization: An improved r for assessing convergence of mcmc (with discussion)," Bayesian analysis **16**, 667–718 (2021).
[56] Wen-Tao Xu, Frank Pollmann, and Michael Knap, "Critical behavior of the fredenhagen-marcu order parameter at topological phase transitions," arXiv preprint arXiv:2402.00127 (2024).
[57] Matthew B Hastings, Iván González, Ann B Kallin, and Roger G Melko, "Measuring renyi entanglement entropy in quantum monte carlo simulations," Physical review letters **104**, 157201 (2010).
[58] Lack of symmetry between X and Z perturbations comes from the open boundary conditions: it might be seen in perturbation theory that X and Z magnetic field excitations at the boundary give contributions to energy in different orders of perturbation theory.
[59] Marc Finzi, *Understanding and Incorporating Mathematical Inductive Biases in Neural Networks*, Ph.D. thesis, New York University (2023).
[60] Ruben Verresen, Mikhail D Lukin, and Ashvin Vishwanath, "Prediction of toric code topological order from rydberg blockade," Physical Review X **11**, 031005 (2021).
[61] Tom Vieijra and Jannes Nys, "Many-body quantum states with exact conservation of non-abelian and lattice symmetries through variational monte carlo," Physical Review B **104**, 045123 (2021).
[62] Risi Kondor, Zhen Lin, and Shubhendu Trivedi, "Clebsch–gordan nets: a fully fourier space spherical convolutional neural network," Advances in Neural Information Processing Systems **31** (2018).

2.12 Publication 6: Topology meets symmetry breaking: Hidden order, intrinsically gapless topological states and finite-temperature topological transitions

In this section, the following publication is reprinted:

P6 *Topology meets symmetry breaking: Hidden order, intrinsically gapless topological states and finite-temperature topological transitions*,
Reja H. Wilke, Henning Schlömer, Simon M. Linsel, Annabelle Bohrdt, Fabian Grusdt,
submitted to Physical Review B,
doi: 0.48550/arXiv.2506.03146.
Reprinted on pages 126–141.

Topology meets symmetry breaking: Hidden order, intrinsically gapless topological states and finite-temperature topological transitions

Reja H. Wilke,[1, 2, 3] Henning Schlömer,[1, 2] Simon M. Linsel,[1, 2] Annabelle Bohrdt,[1, 2] and Fabian Grusdt[1, 2]
[1] *Department of Physics and Arnold Sommerfeld Center for Theoretical Physics (ASC),*
Ludwig-Maximilians-Universität München, Theresienstr. 37, München D-80333, Germany
[2] *Munich Center for Quantum Science and Technology (MCQST), Schellingstr. 4, München D-80799, Germany*
[3] *Institute for Theoretical Physics, ETH Zürich, CH-8093 Zurich, Switzerland*
(Dated: October 17, 2025)

Since the discovery of phase transitions driven by topological defects, the classification of phases of matter has been significantly extended beyond Ginzburg and Landau's paradigm of spontaneous symmetry breaking (SSB). In particular, intrinsic and symmetry-protected topological (SPT) orders have been discovered in (mostly gapped) quantum many-body ground states. However, these are commonly viewed as zero-temperature phenomena, and their robustness in a gapless ground state or against thermal fluctuations remains challenging to tackle. Here we introduce an explicit construction for SPT-type states with hidden order associated with SSB: They feature (quasi) long-range correlations along appropriate edges, but short-range order in the bulk; ground state degeneracy associated with SSB; and non-local string order in the bulk. We apply our construction to predict two types of finite-temperature SPT transitions protected by 1-form symmetries, in the Ising and BKT class respectively, where the usual signs of criticality appear despite the absence of a diverging correlation length in the bulk. While the state featuring hidden Ising order is gapped, the other SPT state associated with the BKT-SPT transition has hidden $U(1)$, or XY-order and constitutes an intrinsically gapless SPT state, associated with a gapless Goldstone mode. Specifically, in this work we discuss spins with global $\mathbb{Z}_2$ or $U(1)$ symmetry coupled to link variables constituting a loop gas model with a 1-form symmetry. By mapping this system to an Ising-gauge theory, we demonstrate that one of the SPT phases we construct corresponds to the Higgs-SPT phase at $T = 0$ – which we show here to remain stable at finite temperature. Our work paves the way for a more systematic search for hidden order SPT phases, including in gapless systems, and raises the question if a natural (finite-T) spin liquid candidate exists that realizes hidden order in the Higgs-SPT class.

The Ginzburg-Landau paradigm connects long-range order (LRO) to the spontaneous breaking of an underlying symmetry. Together with the subsequently discovered notion of topological phase transitions, driven by the proliferation of topological defects [1–3], this forms the backbone of today's classification of the phases of matter. While spontaneously symmetry-broken (SSB) orders are thoroughly understood [4], both at temperatures $T = 0$ and $T > 0$, the complete characterization of topological orders, including symmetry-protected topological (SPT) states, remains an ongoing task. Although topology in gapped one-dimensional systems is well classified [5, 6], higher-dimensional settings [7, 8], gapless topological phases [9–11] as well as interacting systems [12, 13] remain subject of ongoing research, to name a few.

Another avenue of active research concerns the fate of topological states of matter at finite temperatures, $T > 0$. While intrinsic topological order is not robust to thermal fluctuations in two spatial dimensions, it can survive e.g. in the form of a passively protected quantum memory in four dimensions [14, 15]. Since two-point correlations in the bulk decay exponentially in topological phases, most characterizations of topological order, intrinsic or SPT, rely on the analysis of the non-local structure of the entanglement [16–18], which becomes cumbersome at finite temperatures [19]. Nevertheless, generalizations of topological invariants to mixed states [20–30] and finite temperatures [31–34] have been proposed. While a no-go theorem rules out the existence of entangled SPT states protected by a global 0-form symmetry [34] at $T > 0$, a general understanding when and which features of SPT states can remain stable at finite temperatures remains lacking.

In this article, we construct a class of SPT states featuring hidden order (HO), or hidden SSB (hSSB). While the connection of SSB and SPT [35] as well as hidden order and SPT [10, 36–38] have been previously studied at $T = 0$, here we show that such HO-SPT states in general remain robust at finite temperatures in $d \geq 2$ dimensions, and constitute intrinsically gapless SPT phases when the underlying protecting, global symmetry is continuous. The basic strategy is related to the construction of SPT phases from decorated domain walls [12, 39], which naturally leads us to the Higgs-SPT phase recently discovered in the $\mathbb{Z}_2$ Ising gauge theory (IGT) [40–42]. Similarly, antiferromagnetic (AFM) order hidden by fluctuating stripes was recently proposed as a description of the pseudogap phase of the cuprate superconductors [43], see also [44, 45]. In this article we clarify how all these scenarios can be viewed as forms of HO-SPT phases, which remain robust at finite temperature and naturally extend to intrinsically gapless SPT states.

Our starting point is a model of spins, locally coupled to fluctuating link variables, which has a global symmetry $\hat{\mathcal{S}}$ associated with the spins, i.e. $[\hat{H}, \hat{\mathcal{S}}] = 0$ where $\hat{H}$ is

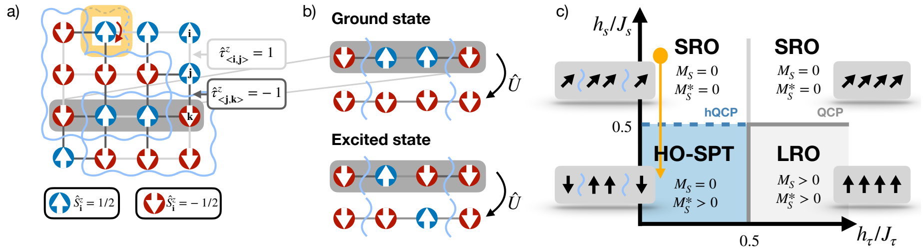

FIG. 1: We predict a class of HO-SPT phases featuring SSB without a local bulk order parameter, in systems where domain walls of a spin order parameter couple to a loop gas of fluctuating link variables. a) In the hidden-Ising order (HIO) model, the sign of Ising interactions $\propto \hat{S}^z_{\mathbf{i}}\hat{S}^z_{\mathbf{j}}$ between spins is flipped across strings defined by link variables $\tau^z_{\langle \mathbf{i},\mathbf{j}\rangle} = -1$ (blue, wiggly lines). Fluctuations of the strings around sites (highlighted in yellow) are accompanied by flips of the central spin. In addition, spin-flips driven by a transverse field can be included. The 1D HIO model can be understood as an excerpt of the 2D model (dark gray box). b) Deep in the HO-SPT phase, the ground state satisfies the hidden order rule, illustrated in the top panel: spins flip sign only across a flipped link. The bottom panel shows an excitation, corresponding to a spin-flip without a link-flip. Spins and link variables in the HIO model at $\lambda = 0$ can be exactly decoupled by the non-local unitary transformation $\hat{U}$ illustrated in both panels, which flips all spins between two strings with $\tau^z = -1$. c) The phase diagrams of the HIO model in 1D, Eq. (1) for $\lambda = 0$, and in 2D, Eq. (4), have the same structure [only the critical values in 2D, $(h_\tau/J_\tau)_{\mathrm{c,2D}}$ and $(h_S/J_S)_{\mathrm{c,2D}}$, differ from their shown value 0.5 in 1D]. The conventional SSB phase with bulk long-range order (LRO) and non-zero magnetization $M_S > 0$ is located next to a symmetric phase with short-range order (SRO) and the SPT phase with hidden order (HO-SPT), which features hSSB. As explained in the text, the HO can be detected by the magnetization of Ising spins in squeezed space, M^*_S. A hidden quantum critical point (hQCP), or HO-SPT transition, separates the HO-SPT from the SRO phase. The orange arrow in c) indicates the corresponding scan in our numerics shown in Fig. 2 a).

the Hamiltonian. We further assume that the link variables form a loop gas model [3], constituted by closed string configurations on the dual lattice, see Fig. 1 a) for an illustration. When the underlying spin-link interactions lead to binding of domain walls of the local spin-order parameter to the strings of the loop gas, sufficiently strong fluctuations of the latter can lead to short-range correlations between spins in the bulk. Nevertheless, the underlying global symmetry $\hat{\mathcal{S}}$ of the spins can remain spontaneously broken, turning the expected long-range correlations associated with this SSB into non-local string order in the bulk. By this construction, an SPT phase protected by $\hat{\mathcal{S}}$ is obtained. Crucially, this construction does not rely on the topological ground-state of the loop gas model.

To describe HO-SPT phases featuring such hSSB, we provide explicit solutions of different microscopic models in this class. To this end, we construct an exact, non-local unitary transformation $\hat{U}$ that allows to decouple the original Hamiltonian into two independent parts: a conventional spin model, symmetric under $\hat{\mathcal{S}}$, and a fluctuating loop gas model realized as a perturbed toric code in a field [46–48]. The motivation for this transformation derives from the concept of squeezed space originally introduced to describe doped AFMs [43, 49, 50] and applied for the construction of intrinsically gapless, one-dimensional (1D) SPT states [10]. As a consequence of the strong correlations between spins and links, the unitary $\hat{U}$ basically unwinds the domain walls of the spin order parameter and turns the hidden order into conventional long-range order of the spins in the newly constructed basis, see Fig. 1 b) for an illustration.

This construction will lead us to the generic HO phase diagram shown in Fig. 1 c), where the HO-SPT phase is located next to a conventional, ordered phase and a trivial, symmetric phase. The first transition (HO-SPT to LRO) appears to be conventional symmetry-breaking in the bulk, although it is driven by the confinement of the loop gas and hence in a different universality class in general. The second transition (HO-SPT to SRO) is of SPT type and constitutes a hidden quantum critical point (hQCP): Since both sides of the transition have short-range correlations in the bulk, it cannot be characterized by a diverging correlation length. However, the correlation length associated with the hidden, non-local string order diverges, and likewise other characteristics of quantum criticality, such as critical transport or collective mode softening, remain present.

In principle, our construction can be adapted to any symmetry $\hat{\mathcal{S}}$. In this paper, we explicitly consider the discrete $\mathbb{Z}_2$ and the continuous $U(1)$ symmetries. One of the most striking consequences of the hSSB in the HO-

SPT phase is its robustness at finite temperatures, $T > 0$ in two or more dimensions: Since the hidden order can be described by a conventional spin system decoupled from the loop gas, it inherits the usual Ginzburg-Landau classification of SSB. Indeed, the underlying symmetry $\hat{\mathcal{S}}$ is broken globally, rather than locally, while LRO is hidden, rather than destroyed, by the fluctuating loop gas. In this paper we explicitly discuss hidden Ising and BKT orders, associated with $\mathbb{Z}_2$ and $U(1)$ symmetries.

Our paper is organized as follows: In the first section, we illustrate the connection between SSB, SPT and HO for the example of two coupled 1D transverse-field Ising models (TFIMs). An almost identical model was recently discussed [40], and our results completely agree with their conclusions derived from considering the spontaneous breaking of higher-form symmetries [51]. We provide a new perspective by explicitly constructing the HO unitary transformation $\hat{U}$, see Fig. 1 b), which decouples the *entire* spectrum of the Hamiltonian. This paves the way for our subsequent extensions to higher dimensions, continuous symmetries and finite temperature.

In the second section, we discuss hidden order associated with a discrete $\mathbb{Z}_2$ symmetry in 2D, where we consider a transverse-field Ising model (TFIM) of spins coupled to a perturbed toric code. By a mapping to the double-Higgs IGT, we argue that the HO-SPT phase we identify coincides with the Higgs-SPT phase of the $\mathbb{Z}_2$ IGT [40, 52]. As a central new result, we demonstrate that the HO-SPT phase is robust to thermal fluctuations and gives rise to a finite-T SPT transition.

In the third section, we extend our results to hidden order associated with a continuous $U(1)$ symmetry in 2D. In the ground state, we find an intrinsically gapless HO-SPT phase with hidden $U(1)$ or XY order and a gapless Goldstone mode. This phase essentially survives at finite temperatures, although with hidden quasi-long range order and power-law correlations at the edge, before it disappears in a finite-T SPT transition of BKT type. We predict these physics in an IGT coupled to a $U(1)$ matter field, closely related to the classical 3D XY model [53].

Our paper closes with an outlook and a discussion how HO-SPT phases may be experimentally observed, in real materials and synthetic quantum matter.

HIDDEN ORDER IN 1D: SPT = HIDDEN SSB

We start by explaining the fundamental idea how hSSB and HO can be realized in an exactly solvable model in one dimension (1D). We provide an explicit construction of a (HO-) SPT phase in 1D, which by itself is well understood [40, 54]. However, as we show below, the construction we make can be straightforwardly generalized to higher dimensions, finite temperature or continuous symmetries and provides valuable insights into the relation of SPT and SSB orders.

We consider a 1D lattice with spin-1/2 degrees of freedom residing both on the lattice sites j and on the links $\langle j, j+1\rangle$, see Fig. 1 a) and b). We define the following Hamiltonian, which we refer to as the 1D hidden-Ising order (HIO) Hamiltonian,

$$\begin{aligned}\hat{H} = &-J_S \sum_j \hat{S}^z_{j+1}\hat{S}^z_j[\hat{\tau}^z_{\langle j,j+1\rangle}(1-\lambda)+\lambda] + h_S \sum_j \hat{S}^x_j \\ &- h_\tau \sum_j \hat{\tau}^z_{\langle j,j+1\rangle} + J_\tau \sum_j \hat{\tau}^x_{\langle j-1,j\rangle}\hat{\tau}^x_{\langle j,j+1\rangle}\hat{S}^x_j \; .\end{aligned} \tag{1}$$

Here, $\hat{S}^\alpha_j$ denotes the α-component of the spin on site j with $\alpha = x, y, z$, and $\hat{\tau}^\alpha_{\langle j,j+1\rangle}$ refers to Pauli matrices on the links between neighboring sites. The model exhibits a NN Ising-like interaction $\propto J_S$ and a transverse field h_S. The real parameter $\lambda \in [0,1]$ interpolates between a conventional NN Ising interaction (for $\lambda = 1$) and one with a sign-flip controlled by the $\hat{\tau}^z$-field on the link connecting both sites (for $\lambda = 0$). A very similar model was constructed starting from the cluster model ($h_S = h_\tau = \lambda = 0$) to construct the same SPT phase [40] that we will discuss now.

In the following we focus on the ordered and disordered phases of the spins $\hat{\mathbf{S}}_j$, associated with the global $\mathbb{Z}_2$ symmetry $\hat{S}^z_j \to -\hat{S}^z_j$ of the HIO model, Eq. (1). The model has an additional, global $\mathbb{Z}_2$ symmetry, $\hat{\tau}^x_j \to -\hat{\tau}^x_j$, which is not important for the following discussion and can be broken by a weak longitudinal field term, $b_\tau \sum_j \hat{\tau}^x_{\langle j,j+1\rangle}$, without changing the nature of the observed phase transitions of the spins $\hat{\mathbf{S}}_j$. Moreover, the HIO model at $b_\tau = \lambda = 0$ has a self-duality $\tau^z \leftrightarrow \hat{S}^x$ and a local $\mathbb{Z}_2$ gauge symmetry [55, 56], neither of which will be essential for the physics that we describe now.

When the link field $\hat{\tau}^z = 1$ is fully polarized, for large $h_\tau \gg J_\tau \geq 0$, the 1D HIO Hamiltonian reduces to a TFIM. In this limit, it exhibits a well-known quantum critical point (QCP) describing a transition from a SSB ferromagnet (FM) to a paramagnet (PM) [4, 57], assuming $J_S > 0$ and tuning h_S. The situation becomes more interesting when quantum fluctuations of the link variables, introduced by the last term $\propto J_\tau$ in Eq. (1), dominate, $J_\tau \gg h_\tau \geq 0$: On one hand, this tends to depolarize the links $\hat{\tau}^z$; on the other hand, the operator $\hat{S}^x_j$ appearing in this term introduces spin flips in the FM. By construction of the HIO Hamiltonian, the latter lead to no additional energy cost $\propto J_S$ for $\lambda = 0$ since the values of $\hat{\tau}^z_{\langle j,j\pm 1\rangle}$ are also flipped by the term $\propto J_\tau$. I.e., by adding J_τ processes, we introduce fluctuating domain walls in the FM which are bound to $\hat{\tau}^z$ excitations – as we show next, these can hide the FM order when they proliferate for small values of h_τ, see Fig. 1 c).

Now we construct an exact, non-local unitary transformation to demonstrate that the fluctuating domain walls destroy the long-range FM order of the spins $\hat{S}^z_j$ when J_τ and J_S are sufficiently large. Moreover, this transformation allows for an exact solution of Eq. (1) in the case $\lambda = 0$, and reveals that SSB still takes place even in the absence of long-range FM spin correlations. Our construction is similar to the idea of squeezed space [50, 58], introduced to solve the 1D $t-J$ model [49], and leads to a non-local string order parameter characterizing the hSSB phase of the 1D HIO model. Notably, the same construction will allow us to derive a similar solution of the HIO model in 2D, which we discuss in the next section.

The unitary transformation $\hat{U}$ we construct disentangles the spin configurations $\hat{S}^z_j = \pm 1/2$ from the fluctuating link variables $\hat{\tau}^z_{\langle j,j+1\rangle} = \pm 1$. We define $\hat{U}$ by its action on basis states $|\{S^z_j, \tau^z_{\langle j,j+1\rangle}\}\rangle$ as follows,

$$\hat{U}\,|\{S^z_j, \tau^z_{\langle j,j+1\rangle}\}\rangle = |\{\tilde{S}^z_j = (-1)^{p_j} S^z_j, \tau^z_{\langle j,j+1\rangle}\}\rangle \ , \tag{2}$$

where p_j denotes the number of negative links for $i < j$, i.e. $(-1)^{\hat{p}_j} = \prod_{i<j} \hat{\tau}^z_{\langle i,i+1\rangle}$. The action of the unitary $\hat{U}$ is illustrated in Fig. 1 b): A spin on site j is flipped if and only if the number of negative links on sites $i < j$ is odd. Our transformation $\hat{U}$ can be viewed as a generalization of the unitary proposed in Ref. [40] in the limit $J_\tau \to \infty$ for the ground state.

Applying the unitary on the Hamiltonian we obtain a representation of the 1D HIO model in the new basis, which we refer to as the *squeezed space*, in analogy with doped 1D quantum magnets. The result are two decoupled TFIMs for spin (S) and link (τ) degrees of freedom,

$$\hat{U}^\dagger \hat{H}(\lambda = 0)\hat{U} = \hat{H}^S_{\mathrm{TFIM}} + \hat{H}^\tau_{\mathrm{TFIM}} \ , \tag{3}$$

see Appendix A for details. Hence, in squeezed space, the eigenstates of Eq. (3) at $\lambda = 0$ factorize, $|\psi\rangle = |\psi\rangle_S \otimes |\psi\rangle_\tau$; here $|\psi\rangle_{S/\tau}$ denote eigenstates of the TFIM on sites/links. Since the latter can be expressed analytically by a combination of a Jordan-Wigner transformation and a Bogoliubov transformation [59], the 1D HIO model is integrable at $\lambda = 0$.

From Eq. (3), we directly obtain the phase diagram of the HIO model at $\lambda = 0$, shown in Fig. 1 c). It consists of two independent Ising-type phase transitions, of links and spins respectively, manifesting in crossing, straight lines in Fig. 1 c). In squeezed space, the usual order parameters of the TFIM can be used to characterize the SSB Ising transition of the spins $\hat{S}^z$, such as magnetization $M^*_S = \langle|\frac{1}{L}\sum_j \hat{S}^z_j|\rangle_{\mathrm{sq}}$ or long-range spin-spin correlations $C^*(d) = \langle \hat{S}^z_0 \hat{S}^z_d\rangle_{\mathrm{sq}}$. Here $\langle\cdot\rangle_{\mathrm{sq}} = \langle \hat{U}\cdot\hat{U}^\dagger\rangle$ is the expectation value in the new basis after applying $\hat{U}$, which turns the squeezed space order parameters into non-local string operators in the original model Eq. (1), e.g. $C^*(d) = \langle \hat{S}^z_0 \left(\prod_{0\leq j<d} \hat{\tau}^z_{\langle j,j+1\rangle}\right) \hat{S}^z_d\rangle$. In particular, the string order parameter $C^*(d)$ can retain long-range correlations when $\hat{\tau}^z$ fluctuates strongly, while the two-point spin-correlations $C(d) = \langle \hat{S}^z_0 \hat{S}^z_d\rangle \simeq e^{-d/\xi}$ decay exponentially in this regime, with ξ the correlation length of the link variables: This leads to a hidden order, or SPT, phase which exhibits SSB without long-range correlations.

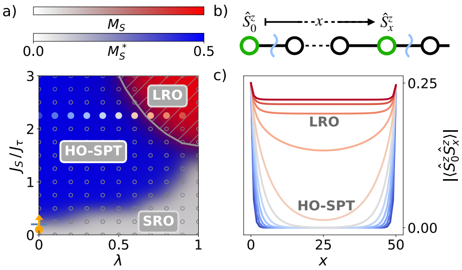

FIG. 2: Numerical study of the HO-SPT phase in the 1D HIO model. a) We perform DMRG simulations using the SyTen toolkit and take snapshots of the many-body wavefunction via the perfect sampling approach [60, 61], allowing us to evaluate magnetizations M_S and M^*_S in real and squeezed space; the latter are indicated by two overlaid color maps. For the exactly solvable case $\lambda = 0$, the hQCP found in Fig. 1 c) is located at a critical value $(J_S/J_\tau)_c = 0.2$, indicated by a short blue line. The orange arrow corresponds to the same scan in Fig. 1 c). We find that for non-zero values of λ, the HO phase persists until eventually it transitions to the LRO phase (with $M_S > 0$, for large J_S/J_τ) or the disordered phase (with $M_S = M^*_S = 0$, for small J_S/J_τ). Areas with $\frac{1}{(L-1)}\langle|\sum_j \hat{\tau}^z_{\langle j,j+1\rangle}|\rangle > 0.3$ are indicated by hatched, grey lines. b) We define standard spin-spin correlations $\langle|\hat{S}^z_0 \hat{S}^z_x|\rangle$ as a function of distance x, computed along the transition from HO to LRO at $J_S/J_\tau = 2.25$ in c). Colors in c) correspond to different values of λ, as highlighted by data points of the same color in a). We find that the bulk order disappears around $\lambda = 0.7$, whereas long-range edge-to-edge correlations continue to indicate the presence of SSB in the HO phase for smaller values of λ. In a) and c) we considered a chain of $L = 51$ spins and 50 links in between, and set $h_\tau/J_\tau = h_S/J_\tau = 0.1$; gray circles indicate the underlying data points. See Appendix B for more details on our numerical simulations.

The unitary $\hat{U}$ also affects the link variables $\hat{\tau}^x_{\langle j,j+1\rangle}$, by attaching a string of $\hat{S}^x$ operators, see Appendix A. Since our focus is on the physics of the spins $\hat{\mathbf{S}}_j$, in the following we will only consider order parameters for $\hat{\tau}$ variables in squeezed space, e.g. the link magnetization $M^*_\tau = \langle|\frac{1}{L}\sum_j \hat{\tau}^x_{\langle j,j+1\rangle}|\rangle_{\mathrm{sq}}$. Combining all order parameters, for spins and links, we arrive at the following groundstate phase diagram of the 1D HIO model at $\lambda = 0$ which depends only on the ratios h_τ/J_τ and h_s/J_s, cf. Fig. 1 c):

(i) Hidden order HO-SPT phase: $M^*_\tau, M^*_S > 0$, for $h_\tau/J_\tau < 1/2$ and $h_S/J_S < 1/2$. In this phase the link variables $\hat{\tau}^z$ fluctuate strongly, while the spins $\hat{S}^z$ exhibit SSB and the associated long-range order in squeezed space. In the original basis (referred to as real space in the following) spin-correlations are hidden, with $M_S = \langle|\frac{1}{L}\sum_j \hat{S}^z_j|\rangle = 0$ due to the proliferation of domain walls tied to negative links,

$\hat{\tau}^z = -1$. Since $[\prod_{j=0}^{L-2} \hat{\tau}^z_{\langle j,j+1\rangle}, \hat{H}] = 0$ is conserved, with L the system size, edge-to-edge correlations $\langle \hat{S}^z_0 \hat{S}^z_{L-1}\rangle \equiv \pm\langle \hat{S}^z_0 \left(\prod_{j=0}^{L-2} \hat{\tau}^z_{\langle j,j+1\rangle}\right) \hat{S}^z_{L-1}\rangle$ correspond to non-local string correlations and become long-ranged, as a direct manifestation in real space of the hidden order in squeezed space. When $h_S = 0$, the ground state exactly satisfies the *hidden-order rule*, i.e. $\hat{S}^z_j = \left(\prod_{0\leq i<j} \hat{\tau}^z_{\langle i,i+1\rangle}\right) \hat{S}^z_0$, and the HIO model exhibits Hilbert space fragmentation [62]. Excitations correspond to spin flips not accompanied by changes in the link variables, see Fig. 1 b).

(ii) Link-ordered phase (SRO): $M^*_\tau > 0, M^*_S = 0$, for $h_\tau/J_\tau < 1/2$ and $h_S/J_S > 1/2$. This phase has no SSB and lacks long-range order in the spin variables, both in real and squeezed space; the link variables $\hat{\tau}^x$ feature long-range correlations. As in the HO phase, $M_S = 0$, and this phase is separated from the HO phase by a hQCP or SPT transition [blue dashed line in Fig. 1 c)]: across the hQCP, no local bulk order parameter of the spins $\hat{\mathbf{S}}_j$ can detect the transition in real space.

(iii) Fully disordered phase (SRO): $M^*_\tau = M^*_S = 0$, for $h_\tau/J_\tau > 1/2$ and $h_S/J_S > 1/2$. This completely symmetric phase breaks none of the two $\mathbb{Z}_2$ symmetries ($\hat{\tau}^x/\hat{S}^z \to -\hat{\tau}^x/\hat{S}^z$), implying $M_S = M_\tau = 0$. It is separated from the link-ordered phase via a QCP associated with the breaking of the link-$\mathbb{Z}_2$ symmetry [light gray line in Fig. 1 c)]. This QCP disappears when the link-$\mathbb{Z}_2$ symmetry is explicitly broken in the Hamiltonian, e.g. by $b_\tau \neq 0$, in which case the link-ordered and fully disordered phases combine into one.

(iv) Long-range ordered (LRO) phase: $M^*_\tau = 0, M^*_S > 0$, for $h_\tau/J_\tau > 1/2$ and $h_S/J_S < 1/2$. This phase spontaneously breaks the spin-$\mathbb{Z}_2$ symmetry, but remains link-$\mathbb{Z}_2$ symmetric. Since flipped $\hat{\tau}^z$ links remain confined [63], the non-zero magnetization in squeezed space, $M^*_S > 0$, also manifests in long-range correlations and $M_S > 0$ in real space. Transitions into the LRO phase, both from the HO and fully disordered phases, constitute QCPs of Ising type.

The HO phase we find in the 1D HIO model can be understood as an SPT phase, protected by the global $\mathbb{Z}_2$ symmetry $\hat{S}^z_j \to -\hat{S}^z_j$ that is spontaneously broken in squeezed space. This demonstrates that the exact unitary transformation $\hat{U}$, decoupling spins and link variables in squeezed space for $\lambda = 0$, is not necessary (though helpful) to observe the HO phase. Indeed, for $\lambda \neq 0$, the unitary $\hat{U}$ does not lead to an exact decoupling, but the HO phase still exists even for values of λ close to unity, as we demonstrate in Fig. 2.

Similarly, the hQCP between the fully symmetric and the HO phases remains robust when $\lambda \neq 0$. In the 1D HIO model, the hQCP is accompanied by the emergence of link order of the $\hat{\tau}^x$ field, with $M_\tau > 0$ for $h_S/J_S > 1/2$. However this is an artifact of the additional global $\mathbb{Z}_2$ symmetry of the link variables. It is absent if the latter is explicitly broken, or, as we will show next, when generalizing the HIO model to 2D.

HIDDEN ORDER IN 2D: DISCRETE SSB AND FINITE-T SPT

Now we extend the construction of HO and hSSB to higher dimensions. Since SSB at temperatures $T > 0$ can only take place in 2D and higher, this opens up the possibility of a finite-temperature hidden critical point (hCP). Indeed, by considering a generalization of the 2D TFIM, we will now explicitly construct a 2D Ising-type hCP, realizing a finite-T SPT transition protected by a 1-form symmetry [34]. The central idea is to decorate domain walls of the Ising spins $\hat{S}^z_{\mathbf{j}}$ with flipped links $\hat{\tau}^z_{\langle \mathbf{i},\mathbf{j}\rangle} = -1$, as in 1D. To guarantee that no frustrated links appear, we further ensure that the flipped link variables $\hat{\tau}^z_{\langle \mathbf{i},\mathbf{j}\rangle} = -1$ form closed loops without ends, realizing the required 1-form symmetry. I.e., the link fields $\hat{\tau}$ need to be described by a loop gas model, the simplest instance of which is Kitaev's toric code [7, 47].

Squeezed space and HIO model in 2D.– This leads us to the 2D HIO Hamiltonian,

$$\begin{aligned}\hat{H} = &-J_S \sum_{\langle \mathbf{i},\mathbf{j}\rangle} \hat{S}^z_{\mathbf{i}} \hat{S}^z_{\mathbf{j}} \hat{\tau}^z_{\langle \mathbf{i},\mathbf{j}\rangle} + h_S \sum_{\mathbf{j}} \hat{S}^x_{\mathbf{j}} \\ &- h_\tau \sum_{l} \hat{\tau}^z_l - \mu_\tau \sum_{\square} \prod_{l\in\square} \hat{\tau}^z_l + J_\tau \sum_{\mathbf{j}} \hat{S}^x_{\mathbf{j}} \prod_{l\in+_{\mathbf{j}}} \hat{\tau}^x_l \,. \end{aligned} \quad (4)$$

The first line describes a TFIM with sign-flipped Ising interactions on bonds where $\hat{\tau}^z_{\langle \mathbf{i},\mathbf{j}\rangle} = -1$. The second line starts with the string tension h_τ, followed by a plaquette term $\propto \mu_\tau$ defined on plaquettes $\square$ which penalizes open strings. Finally a correlated fluctuation of spins and links $\propto J_\tau$ is added, involving a product over links l forming a star $+_{\mathbf{j}}$ around site $\mathbf{j}$. This last term guarantees flipped spins $\hat{S}^z_{\mathbf{j}}$ to be accompanied by a flip of all links $\hat{\tau}^z_l$ surrounding site $\mathbf{j}$. The model is illustrated on the square lattice in Fig. 1 a).

The 2D HIO model features a global $\mathbb{Z}_2$ symmetry, $\hat{S}^z \to -\hat{S}^z$ that can be spontaneously broken. Restricted to a 1D chain, the 2D HIO model reduces to the 1D HIO model Eq. (1) (for $\lambda = \mu_\tau = 0$) if the four-link operators are reduced to two-link terms; this is illustrated in Fig. 1 a) and b). For simplicity we only consider the case $\lambda = 0$ here, but a generalization of the Ising interactions to $\lambda \in [0, 1]$ as in 1D, Eq. (1), is also possible. Like the 1D HIO model, the 2D HIO model features a second global $\mathbb{Z}_2$ symmetry, $\hat{\tau}^x \to -\hat{\tau}^x$, but this symmetry cannot be broken spontaneously because it turns into a local $\mathbb{Z}_2$ gauge symmetry of the loop gas model in Eq. (4) that will be discussed further below.

To derive the phase diagram and solve the 2D HIO model, Eq. (4), we apply a similar strategy as in 1D and construct a unitary $\hat{U}$ that disentangles spins and link variables. This only works, however, when the strings defined by $\hat{\tau}^z_l = -1$ form *closed* loops, i.e. for

$$\prod_{l\in\square} \hat{\tau}^z_l \left|\psi\right\rangle \equiv \hat{B}_\square \left|\psi\right\rangle = \left|\psi\right\rangle, \quad \forall\ \square. \quad (5)$$

Since $[\hat{B}_\square, \hat{H}] = 0$ this defines a sector of the HIO Hilbert space, realized by $\mu_\tau \to \infty$, to which we will restrict ourselves in the following. In the $T = 0$ ground state it is sufficient to assume $\mu_\tau > 0$, which leads to a ground state of Eq. (4) in the closed-loop sector.

The unitary transformation $\hat{U}$ defining squeezed space in 2D, is the same as in 1D, see Eq. (2). It is only in the definition of $\hat{p}_\mathbf{j}$ that care has to be taken: We define

$$(-1)^{\hat{p}_\mathbf{j}} = \prod_{l \in \mathcal{L}_\mathbf{j}} \hat{\tau}^z_l \tag{6}$$

as a product of link variables along a path $\mathcal{L}_\mathbf{j}$ from some fixed reference site to $\mathbf{j}$. For the different sites $\mathbf{j}$ we choose a path $\mathcal{L}_\mathbf{j}$ following a one-dimensional snake-like covering of all lattice sites, as described in Appendix A. Since this parity $\hat{p}_\mathbf{j}$ is independent of the path $\mathcal{L}_\mathbf{j}$ in the subspace of closed loops, Eq. (5), the above expression for $(-1)^{\hat{p}_\mathbf{j}}$ is well-defined. Intuitively, the parity $\pi_\mathbf{j} = (-1)^{p_\mathbf{j}}$ distinguishes sites $\mathbf{j}$ inside ($\pi_\mathbf{j} = -1$) and outside ($\pi_\mathbf{j} = +1$) of the closed loops of strings $\tau^z = -1$. By applying the unitary $\hat{U}$ in Eq. (2), spins inside closed loops are flipped: This is the defining property of squeezed space in 2D.

Now we apply $\hat{U}$ to the 2D HIO Hamiltonian in the closed-loop subspace, which decouples the system into a TFIM of spins $\hat{\mathbf{S}}$ and a toric code in a field (TC-F), see Appendix A for a derivation,

$$\hat{U}^\dagger \hat{H} \hat{U} = \underbrace{-J_S \sum_{\langle \mathbf{i},\mathbf{j} \rangle} \hat{S}^z_\mathbf{i} \hat{S}^z_\mathbf{j} + h_S \sum_\mathbf{j} \hat{S}^x_\mathbf{j}}_{\hat{H}_\mathrm{TFIM}} + \underbrace{\frac{J_\tau}{2} \sum_\mathbf{j} \prod_{l \in +_\mathbf{j}} \hat{\tau}^x_l - h_\tau \sum_l \hat{\tau}^z_l}_{\hat{H}_\mathrm{TC-F}} . \tag{7}$$

Note that we dropped the term $\propto \mu_\tau$ from Eq. (4), since we work in the sector $\hat{B}_\square = 1$ where it becomes a constant. Similar transformations have recently been discussed by Ref. [42].

Zero-temperature phase diagram.– As in the 1D HIO model, the decoupling of the spin and link degrees of freedom results in a factorization of eigenstates in squeezed space. The zero-temperature phase diagram is similar to the 1D case, shown in Fig. 1 c), with independent, straight phase boundaries. For $h_S/J_S < (h_S/J_S)_\mathrm{c,2D}$ the global $\mathbb{Z}_2$ symmetry is spontaneously broken, $M^*_S > 0$, manifesting in hidden and long-range order, respectively, depending on the loop gas configuration. For larger values of h_S/J_S, the spins realize a $\mathbb{Z}_2$ symmetric paramagnet with $M_S = M^*_S = 0$.

The most interesting phase is the HO phase, in which long-range order in squeezed space, $M^*_S > 0$, is hidden in real space by fluctuating strings, $M_S = 0$. This happens for $h_\tau/J_\tau < (h_\tau/J_\tau)_\mathrm{c,2D}$ when the loop gas is deconfined (topologically non-trivial) and strings $\hat{\tau}^z = -1$ percolate through the entire system [64–66]. The most direct way to understand this SPT phase comes from the limit $h_S = 0$: In this case, spins $\hat{S}^z$ are fully polarized in squeezed space; in real space, the hidden-order rule relates spins to links through

$$\hat{S}^z_\mathbf{j} = \hat{S}^z_\mathbf{r} \prod_{l \in \mathcal{L}_\mathbf{j}} \hat{\tau}^z_l, \qquad \text{for } h_S = 0, \tag{8}$$

where $\mathbf{r}$ is the reference site to which $\mathcal{L}_\mathbf{j}$ connects site $\mathbf{j}$. I.e., the spins $\hat{S}^z$ realize the dual variables of the loop gas [67, 68]. The latter undergo an Ising transition as h_τ/J_τ is increased beyond $(h_\tau/J_\tau)_\mathrm{c,2D}$, restoring long-range order in real space, $M_S > 0$, in the confined (topologically trivial) phase of the loop gas where strings form finite-size loops and do not percolate.

The transition from the HO phase to the disordered phase realizes a hQCP, or a 2D SPT transition. It is invisible to local order parameters in real space, since $M_S = 0$ remains zero; i.e., both sides of the transition appear symmetric in their bulks. The hQCP can be detected directly in squeezed space or, equivalently, via a string order parameter

$$C^*(\mathbf{j}) = \left\langle \hat{S}^z_\mathbf{r} \Big(\prod_{l \in \mathcal{L}_\mathbf{j}} \hat{\tau}^z_l \Big) \hat{S}^z_\mathbf{j} \right\rangle. \tag{9}$$

Along edges of the system without open strings (dangling bonds) and still considering the closed-loop subspace $\mu_\tau \to \infty$, the correlator $C^*(\mathbf{j})$ develops long-range edge correlations $C_\mathrm{e}(d_\mathrm{e}) = \langle \hat{S}^z_{\mathbf{r}_\mathrm{e}} \hat{S}^z_{\mathbf{r}_\mathrm{e}+\mathbf{d}_\mathrm{e}} \rangle$ in the HO phase, demonstrating the SPT nature of the latter. These long-range edge correlations require the 1-form symmetry underlying the closed-loop condition to remain stable.

Finally, within the $\mathbb{Z}_2$ symmetric, disordered phase for $h_S/J_S > (h_S/J_S)_\mathrm{c,2D}$, another topological phase transition takes place at $(h_\tau/J_\tau)_\mathrm{c,2D}$: This is the confining transition of the loop gas, which can be detected through a Wilson loop [46] or a percolation analysis of link snapshots [64], but has no influence on the spins $\hat{\mathbf{S}}$.

Finite-temperature phase diagram.– Next, we turn to the finite-temperature phase diagram of the 2D HIO model, which is a lot more interesting than in 1D since the discrete $\mathbb{Z}_2$ symmetry $\hat{S}^z \to -\hat{S}^z$ can be broken at $T > 0$. In the following we assume $\mu_\tau \to \infty$, restricting our entire model to the closed loop subspace[1], Eq. (5). Hence, the decoupled Hamiltonian in squeezed space, Eq. (7), remains valid, allowing us to derive the phases of spin and link variables independently. We start with the spins in the 2D TFIM, which spontaneously break the discrete $\mathbb{Z}_2$ symmetry, and form an ordered state in 2D squeezed space signified by $M^*_S(T) > 0$, below a critical temperature $T < T_c(J_S, h_S)$ depending on J_S and h_S.

---

[1] Note that in an experimentally relevant, finite-size setup it is sufficient to choose μ_τ large enough to suppress the total number of open-loop defects to below one on average. This requires $\mu_\tau \to \infty$ as the linear system size $L \to \infty$.

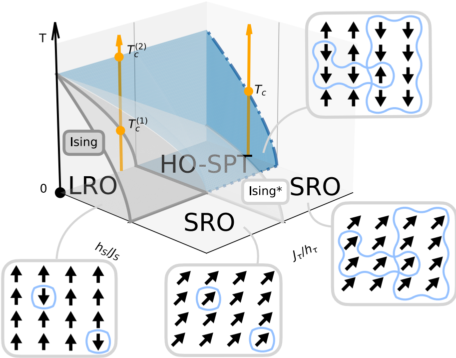

FIG. 3: Schematic phase diagram of the 2D HIO model, Eq. (4), at finite temperature and in the closed-loop limit, $\mu_\tau \to \infty$. The decoupling of spin and link degrees of freedom in squeezed space, after applying the unitary transformation in Eq. (2), leads to a factorization of the phase diagram. The insets illustrate the respective system configurations. The TFIM of spins $\hat{\mathbf{S}}$ features a finite-T Ising transition, describing where SSB takes place. The toric code in a field describing links $\hat{\tau}$ is dual to a TFIM, with an associated Ising* transition characterizing the deconfinement of the loop gas. In regimes where the loop gas is deconfined (percolating), through quantum or thermal fluctuations, spin order is hidden (blue region) in real space. For large J_τ/h_τ, a finite-T SPT transition at T_c is obtained. In the confined (non-percolating) region of the loop gas, for small J_τ/h_τ, and when h_S/J_S is small, low-T LRO gives way to a HO phase at $T_c^{(1)}$ where the loop gas thermally deconfines, before entering the fully symmetric, disordered phase at $T_c^{(2)}$. In this regime, the critical temperature separating the ordered and disordered phase is $T/J_S \approx 2.27$ at elevated temperatures.

The phase diagram of the closed-loop gas model at $T > 0$ in squeezed space is similar. Through the help of a duality mapping, the toric code in a field is equivalent to a 2D TFIM, with Ising interactions h_τ and a transverse field J_τ [68]. Below $T_c(J_\tau, h_\tau)$, in the ordered phase of the dual variables, the loop gas forms non-percolating, finite-size clusters of strings. In contrast, above $T_c(h_\tau, J_\tau)$, in the disordered phase of the dual variables, the loop gas forms a percolating net of strings extending across the entire system [64]. The respective configurations are indicated in the insets of Fig. 3. Notably, SSB of the dual variables in their ordered phase has no equivalent in the original string basis – in contrast to SSB of the spins $\hat{\mathbf{S}}$, which leads to e.g. a doubly-degenerate ground state. For both models in squeezed space, the respective $T_c = 0$ vanishes at the zero-temperature quantum phase transitions at $(J_S/h_S)_{\mathrm{c,2D}}$ and $(J_\tau/h_\tau)_{\mathrm{c,2D}}$.

The resulting finite-temperature phase diagram of the closed-loop 2D HIO model is shown in Fig. 3. One of its most interesting features is the extension of the HO, SPT-type phase above $T > 0$. For small h_S/J_S, ensuring $M_S^* > 0$, and provided the loop gas is in its percolating phase, i.e. for large J_τ/h_τ and ensuring that $M_S = 0$, we find that the $T = 0$ HO phase extends to some $T_c > 0$. At this T_c, it turns into the fully symmetric, disordered phase, realizing a *finite-T SPT transition.*

For smaller values of J_τ/h_τ, where the loop gas is in its non-percolating, confined phase at low T, the spontaneous breaking of the spin's $\mathbb{Z}_2$ symmetry manifests in long-range order, $M_S > 0$. This is stable up to a critical temperature $T_c^{(1)}$, above which $M_S = 0$. When simultaneously h_S/J_S is sufficiently small, we obtain a second critical $T_c^{(2)}$: In between, for $T_c^{(1)} < T < T_c^{(2)}$, the $\mathbb{Z}_2$ symmetry remains broken but the system is in the HO-SPT phase. Here, thermal fluctuations induce fluctuations of the link variables which gives rise to a thermally restored SPT phase [69]. Only beyond $T > T_c^{(2)}$ the $\mathbb{Z}_2$ symmetry is restored. Thereby we establish an interesting new scenario how long-range order can be destroyed in a step-like manner as temperature is increased, from LRO to HO and finally to the disordered phase in an SPT transition. The two scenarios are illustrated in Fig. 3 along exemplary scans through the phase diagram (orange arrows).

Open strings & relation to Ising gauge theory.– So far we restricted our discussion of the 2D HIO model to the subspace of closed $\hat{\tau}^z$ loops. Next, we consider finite $\mu_\tau < \infty$ and include an additional term in the Hamiltonian introducing $\hat{\tau}^z$ strings with open ends:

$$\hat{H} \to \hat{H} + h_X \sum_l \hat{\tau}_l^x. \tag{10}$$

With this term included, we can no longer use the unitary $\hat{U}$ to decouple spin and link variables, since the inside and outside of the $\hat{\tau}^z$ loops become ill-defined in the presence of open strings.

We will argue next that the HO phase remains stable even when $h_X \neq 0$ and open $\hat{\tau}^z$ strings are included. By relating the HIO model to a double-Higgs Ising gauge theory (IGT) [40, 42], we will show that the HO phase coincides with the Higgs phase of the IGT. Indeed, it was recently shown at zero temperature that the Higgs phase realizes an SPT phase [40]: We conjecture that the HO-SPT phase we constructed above is identical to the Higgs-SPT phase found by Verresen et al., see Fig. 4 a), and extends to $T > 0$.

Before going into details, we provide intuition why the HO phase remains stable upon including open strings, for $h_X > 0$. To this end, we consider the limit $h_S = 0$, where the hidden-order rule, Eq. (8), applies when $h_X = 0$. I.e., any string segment $\tau^z_{\langle \mathbf{i},\mathbf{j}\rangle} = -1$ is bound to a domain wall of the Ising spins, $S^z_{\mathbf{i}} = -S^z_{\mathbf{j}}$. Adding small $|h_X| \ll \mu_\tau$ can perturbatively open the string, but keeps the spin-domain wall unchanged, as we illustrate in Fig. 4 b). This costs energy $\propto J_s$ per open string segment, and realizes a force linear in the distance between the two charges, $B_\square = -1$, at the open ends of the strings. As long as these charges remain confined, the inside and outside of the loop gas can still be meaningfully defined and HO is stabilized. When h_X/μ_τ becomes too large, open ends with $B_\square = -1$ proliferate and deconfine, destroying the HO phase in an SPT transition at $h_{X,c} > 0$.

Now we proceed by describing the 2D HIO model in the framework of an IGT. When the string tension associated with the links vanishes, $h_\tau = 0$, the Hamiltonian Eq. (4) features a further local Gauss law, $[\hat{H}, \hat{G}_\mathbf{j}] = 0$ with $\hat{G}_\mathbf{j} = \prod_{l \in +_\mathbf{j}} \hat{\tau}^x_l \hat{S}^x_\mathbf{j}$, in addition to the closed-loop constraint, Eq. (5). By introducing a second Higgs field $\hat{\sigma}^x$, in addition to $\hat{S}^z$, to describe the open ends of the $\hat{\tau}^x$ strings, we can elevate the entire HIO model, for any h_τ, to an IGT:

$$\begin{aligned}\hat{H}_\mathrm{IGT} = &-J_S \sum_{\langle \mathbf{i},\mathbf{j} \rangle} \hat{S}^z_\mathbf{i} \hat{S}^z_\mathbf{j} \hat{\tau}^z_{\langle \mathbf{i},\mathbf{j} \rangle} + h_S \sum_\mathbf{j} \hat{S}^x_\mathbf{j} + h_X \sum_l \hat{\tau}^x_l \\ &- h_\tau \sum_{\langle \mathbf{i},\mathbf{j} \rangle} \hat{\sigma}^z_\mathbf{i} \hat{\sigma}^z_\mathbf{j} \hat{\tau}^z_{\langle \mathbf{i},\mathbf{j} \rangle} + J_\tau \sum_\mathbf{j} \hat{\sigma}^x_\mathbf{j} - \mu_\tau \sum_\square \prod_{l \in \square} \hat{\tau}^z_l \, . \end{aligned} \tag{11}$$

This Hamiltonian acts in a Hilbert space satisfying the following Gauss law,

$$2 \hat{S}^x_\mathbf{j} \hat{\sigma}^x_\mathbf{j} \prod_{l \in +_\mathbf{j}} \hat{\tau}^x_l \left| \psi \right\rangle \equiv \hat{G}_\mathbf{j} \left| \psi \right\rangle = \left| \psi \right\rangle , \quad \forall \, \mathbf{j}. \tag{12}$$

The $T = 0$ phase diagram of the double-Higgs IGT, Eq. (11), is shown in Fig. 4 a). We construct it starting from the phase diagram of the 2D HIO, see Fig. 4 a), at $h_X/\mu_\tau = 0$. Next, we set $h_\tau = 0$ ($J_\tau \gg 0$) in Eq. (11) and eliminate $\hat{S}^x$ making use of the Gauss law, Eq. (12): $\hat{S}^x_\mathbf{j} = \frac{1}{2} \hat{\sigma}^x_\mathbf{j} \prod_{l \in +_\mathbf{j}} \hat{\tau}^x_l$. The resulting Hamiltonian commutes with $\hat{\sigma}^x_\mathbf{j}$, which takes the value $\sigma^x_\mathbf{j} = -1$ in the ground state of the link variables. This finally leads to the identification $\hat{S}^x_\mathbf{j} = -\frac{1}{2} \prod_{l \in +_\mathbf{j}} \hat{\tau}^x_l$ and

$$\begin{aligned}\hat{H}({}^{h_\tau}/_{J_\tau} = 0) = &-J_S \sum_l \hat{\tau}^z_l - \frac{h_S}{2} \sum_\mathbf{j} \prod_{l \in +_\mathbf{j}} \hat{\tau}^x_l \\ &+ h_X \sum_l \hat{\tau}^x_l - \mu_\tau \sum_\square \prod_{l \in \square} \hat{\tau}^z_l , \end{aligned} \tag{13}$$

which is the well-known perturbed toric code Hamiltonian with two fields, J_S and h_X [46, 47]. Its phase diagram is sketched in the $h_\tau = 0$ plane in Fig. 4 a), demonstrating that the HO phase is directly connected to the Higgs-SPT phase.

Further insights into the phase diagram of the double-Higgs IGT can be obtained by using the symmetry between the two Higgs fields. Exchanging $2\hat{\mathbf{S}} \leftrightarrow \hat{\sigma}$, as well as $J_S \leftrightarrow h_\tau$ and $h_S \leftrightarrow J_\tau$, the Hamiltonian $\hat{H}_\mathrm{IGT}$ is invariant. This establishes the relation between the σ-HO phase and the σ-Higgs-SPT phases on the vertical planes in Fig. 4 a). The ordered phase at large h_τ/J_τ and small h_S/J_S features LRO of both Higgs fields, σ^z and S^z. Finally, for large h_X/μ_τ both Higgs fields are in a fully symmetric, paramagnetic (PM) phase.

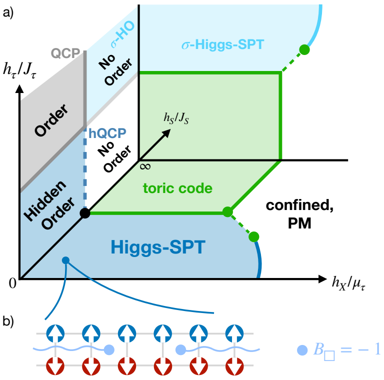

FIG. 4: Zero-temperature phase diagram of the double-Higgs $\mathbb{Z}_2$ gauge theory, Eq. (11). a) On the left vertical plane, for $h_X = 0$, the exactly solvable phases of the 2D HIO model are obtained, including HO of both Higgs fields. The latter regimes connect directly to the respective Higgs-SPT phases of S (σ) on the bottom horizontal (back vertical) plane. The phase boundaries of these SPT phases - which we conjecture to coincide with our HO-SPT phases - are taken from Ref. [40]. The topological toric code phase (green) corresponds to the disordered, PM phases of the Higgs fields. b) The HO phase remains stable upon including open τ^z strings, by $h_X \neq 0$, because domain walls of $\hat{S}^z$ spins lead to a linear confining force between open ends of the strings, $B_\square = -1$.

In combination with our earlier results, we conclude that the HO / Higgs-SPT phase protected by the global $\mathbb{Z}_2$ symmetry of spins, $\hat{S}^z \to -\hat{S}^z$, remains stable at finite temperatures, $T > 0$. We conjecture that it features hSSB of the global $\mathbb{Z}_2$ symmetry, and thus constitutes an extension of the SSB $\hat{S}^z$-ordered phase to a regime with hidden order. This stability to thermal fluctuations is in stark contrast to the topological toric code phase, which is *not* robust at any $T > 0$ due to the emergence of a non-zero density of thermal excitations.

HIDDEN ORDER IN 2D: CONTINUOUS SSB AND HIDDEN BKT

Next we extend our construction of phases with hidden order to systems with continuous symmetries. To this end we replace the TFIM of the spins $\hat{\mathbf{S}}$ by the XY or XXZ model featuring a continuous $U(1)$ symmetry. At $T = 0$ the latter can be spontaneously broken, and in this regime we will construct a HO / SPT phase featuring a (hidden) gapless Goldstone mode associated with the broken continuous symmetry. This constitutes an intrinsically gapless SPT phase [10] in two dimensions. At $T > 0$, by the Mermin-Wagner-Hohenberg theorem, the $U(1)$ symmetry cannot be spontaneously broken. Instead, the XY model features a topological BKT transition from which we will construct a hidden BKT (or BKT-class SPT) transition at finite T. The latter can be characterized by edge correlations, protected by a 1-form symmetry realized through the closed-loop condition, that turn from quasi-long ranged power-law to short-ranged exponential.

Squeezed space and HXYO model.– Our starting point is the following Hamiltonian, which we will refer to as the hidden-XY order (HXYO) model,

$$\begin{aligned}\hat{H} = &-\frac{J_S}{2}\sum_{\langle\mathbf{i},\mathbf{j}\rangle}\left(\hat{S}^+_{\mathbf{i}}\hat{S}^-_{\mathbf{j}}\hat{\tau}^z_{\langle\mathbf{i},\mathbf{j}\rangle} + \text{H.c.}\right) + \Delta\sum_{\langle\mathbf{i},\mathbf{j}\rangle}\hat{S}^z_{\mathbf{i}}\hat{S}^z_{\mathbf{j}} \\ &- h_\tau\sum_l \hat{\tau}^z_l - \mu_\tau\sum_{\square}\prod_{l\in\square}\hat{\tau}^z_l + J_\tau\sum_{\mathbf{j}}\hat{S}^z_{\mathbf{j}}\prod_{l\in+_{\mathbf{j}}}\hat{\tau}^x_l \ . \end{aligned} \tag{14}$$

It describes spin-1/2 $\hat{\mathbf{S}}$ with XY interactions $\propto J_S$ coupled to a loop gas model, where links $\tau^z_{\langle\mathbf{i},\mathbf{j}\rangle} = -1$ introduce flipped signs. Here $\hat{S}^\pm_{\mathbf{j}} = \hat{S}^x_{\mathbf{j}} \pm i\hat{S}^y_{\mathbf{j}}$ denotes the spin raising and lowering operators on site $\mathbf{j}$. We added Ising interactions $\propto \Delta$ among the spins, which are not affected by the link variables. The second line describes a perturbed toric code, where the last term is a correlated fluctuation of strings $\tau^z = -1$ and spins; note that $\hat{S}^z_{\mathbf{j}}$ in the last term flips the sign of both $\hat{S}^\pm_{\mathbf{j}}$.

The HXYO model has a global continuous $U(1)$ symmetry of the spins, $\hat{S}^\pm \to e^{\pm i\varphi}\hat{S}^\pm$, corresponding to rotations around $\hat{S}^z$. This symmetry will protect the hidden order that we describe next. Moreover, it implies that $[\hat{H}, \hat{S}^z_{\text{tot}}] = 0$, i.e. $\hat{H}$ can be solved for every value of $S^z_{\text{tot}} = \sum_{\mathbf{j}} S^z_{\mathbf{j}}$ separately. Alternatively, a chemical potential term $\mu_S \sum_{\mathbf{j}} \hat{S}^z_{\mathbf{j}}$ can be added to the Hamiltonian and μ_S can be tuned instead of S^z_{tot}.

As before, in order to solve the HXYO model we work in the closed-loop subspace obtained in the limit $\mu_\tau \to \infty$. We apply the same unitary transformation $\hat{U}$ as in the HIO model, Eqs. (2), (6) with $\hat{S}^x$ replaced by $\hat{S}^z$, see Appendix A, which decouples the HXYO Hamiltonian:

$$\begin{aligned}\hat{U}^\dagger\hat{H}\hat{U} = &\underbrace{-\frac{J_S}{2}\sum_{\langle\mathbf{i},\mathbf{j}\rangle}\left(\hat{S}^+_{\mathbf{i}}\hat{S}^-_{\mathbf{j}} + \text{H.c.}\right) + \Delta\sum_{\langle\mathbf{i},\mathbf{j}\rangle}\hat{S}^z_{\mathbf{i}}\hat{S}^z_{\mathbf{j}}}_{=\hat{H}_{\text{XXZ}}} \\ &\underbrace{-h_\tau\sum_l\hat{\tau}^z_l + \frac{J_\tau}{2}\sum_{\mathbf{j}}\prod_{l\in+_{\mathbf{j}}}\hat{\tau}^x_l}_{=\hat{H}_{\text{TC}-\text{F}}} \ . \end{aligned} \tag{15}$$

The toric code model in the second line is defined in the sector with $B_\square = 1$.

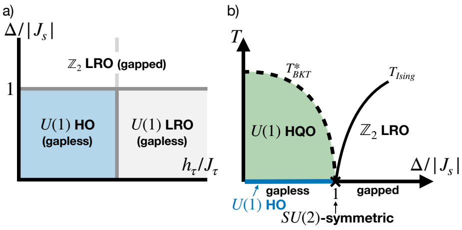

FIG. 5: Phase diagram of the HXYO model, Eq. (14), in the closed-loop limit $\mu_\tau \to \infty$. a) At zero temperature, long-range $U(1)$ (or XY) order associated with a spontaneously broken $U(1)$ symmetry develops in squeezed space when $|\Delta| < |J_S|$. This manifests in a gapless SPT phase with $U(1)$ hidden order (HO) for small h_τ/J_τ, and turns into a conventional $U(1)$-ordered phase when τ^z strings confine at large h_τ. For $|\Delta| > |J_S|$, a $\mathbb{Z}_2$ ordered phase in the original basis is obtained, independent of the loop gas. b) At finite temperature, the hidden $U(1)$ order turns into hidden quasi-long range order, with power-law correlations in squeezed space. At higher temperatures T^*_{BKT} a hCP / finite-T SPT transition into a symmetric, paramagnetic phase is found. The $\mathbb{Z}_2$ order remains stable up to T_{Ising} where it disappears in a finite-T symmetry-breaking transition of Ginzburg-Landau type, in the Ising universality class. At $|\Delta| = |J_S|$, a hidden $SU(2)$ symmetry precludes any finite-T phase transitions.

Zero-temperature phase diagram.– From the exact decoupling of spins and links in Eq. (15) we obtain again a typical hidden-order phase diagram as in Fig. 1 c), with two orthogonal phase boundaries, see Fig. 5 a). For small $|\Delta| < |J_S|$, an XY-phase with a spontaneously broken continuous $U(1)$ symmetry is formed in squeezed space. When $h_\tau < J_\tau$ is small, strings formed by links l with $\tau^z_l = -1$ percolate through the system, suppressing the long-range XY correlations in squeezed space in the original basis: this leads to a hidden-XY, or $U(1)$, ordered phase. It can be characterized by a non-zero string order parameter of the form $C^*(\mathbf{j}) = \langle \hat{S}^+_{\mathbf{r}} (\prod_{l\in\mathcal{L}_{\mathbf{j}}} \hat{\tau}^z_l) \hat{S}^-_{\mathbf{j}} \rangle$, similar to the one in Eq. (9).

When h_τ/J_τ increases and reaches a critical value $(h_\tau/J_\tau)_{\text{c,2D}}$, the τ^z strings confine and stop to percolate through the entire system. In this regime, the long-range XY order associated with the spontaneously broken $U(1)$ symmetry also manifests as long-range order, $\langle \hat{S}^+_{\mathbf{i}} \hat{S}^-_{\mathbf{j}} \rangle \to$ const. as $|\mathbf{i} - \mathbf{j}| \to \infty$, in the original basis. This corresponds to the $U(1)$-ordered phase in Fig. 5 a).

For $|\Delta| > |J_S|$, the spins in the XXZ model transition to a gapped, $U(1)$ symmetric phase. For $\mu_S = 0$ this phase is not entirely trivial, because it spontaneously breaks an additional, discrete $\mathbb{Z}_2$ symmetry associated with the reversal of S^z spins, leading to an Ising (anti-)

ferromagnet for $\Delta < 0 (> 0)$. Since S^z interactions $\propto \Delta$ decouple from the link degrees of freedom in the HXYO model, the $\mathbb{Z}_2$ order associated with this phase can be detected in real and squeezed space alike. Moreover, it is unaffected by the confinement transition of the loop gas model which only depends on the ratio h_τ / J_τ.

Next, we discuss the excitation spectrum of the HXYO model. Because excitation energies are invariant under the unitary $\hat{U}$, we immediately conclude that the loop gas sector is always gapped, except at the transition point $(h_\tau/J_\tau)_{\mathrm{c,2D}}$. In contrast, the XY phase of the XXZ model features a gapless Goldstone mode, for $|\Delta| < |J_S|$, demonstrating that the hidden $U(1)$ ordered phase represents a class of intrinsically gapless SPT states.

Understanding the spectral weight of the low-energy Goldstone boson requires more care, because the unitary transformation $\hat{U}$ entangles spin and link variables. Since the Goldstone mode can be viewed as a combination of $S^\pm$ operators, $\hat{\gamma} \sim u\hat{S}^- + v\hat{S}^+$, it turns into a non-local string operator in the original basis,

$$\hat{U}\ \hat{\gamma}\ \hat{U}^\dagger \sim \left(\prod_{l \in \mathcal{L}} \hat{\tau}^z_l \right) \hat{\gamma}. \tag{16}$$

Thus, in general, local operators in the original basis couple to collective excitations of both the link and the spin sectors, complicating the direct detection of the gapless SPT Goldstone boson we predict. A detailed discussion will be devoted to future work.

Finite-temperature phase diagram.– The 2D HXYO model also has a rich finite-temperature phase diagram, see Fig. 5 b). We still consider the closed-loop subspace, $\mu_\tau \to \infty$, and begin our discussion in the regime where $|\Delta| < |J_S|$. Although the long-range $U(1)$ order in squeezed space is immediately destroyed by thermal fluctuations at any $T > 0$, below a critical T^*_{BKT} the spins feature quasi-long range order with power-law correlations in squeezed space, $C^*(\mathbf{i}-\mathbf{j}) = \langle \hat{S}^+_\mathbf{i} \hat{S}^-_\mathbf{j} \rangle_{\mathrm{sq}} \simeq |\mathbf{i}-\mathbf{j}|^{-\alpha}$. These correspond to power-law, non-local string correlations in the original basis, where the bare two-point correlator $C(\mathbf{i}-\mathbf{j}) = \langle \hat{S}^+_\mathbf{i} \hat{S}^-_\mathbf{j} \rangle \simeq \exp(|\mathbf{i}-\mathbf{j}|/\xi)$ decays exponentially. I.e., as in the 2D HIO model we obtain a finite-temperature SPT phase, which we refer to as the hidden quasi-XY ordered phase, with hidden quasi-long range order.

Thermodynamically, the finite-T SPT transition out of the hidden-XY ordered phase is in the BKT universality class. At high T a phase with exponential correlations $C^*(\mathbf{i}-\mathbf{j}) \simeq \exp(|\mathbf{i}-\mathbf{j}|/\xi^*(T))$ in squeezed space is realized, and similar but with a different correlation length $\xi(T)$ in the original basis. Probing this SPT transition in the BKT class directly in the bulk is likely challenging, due to the infinite order of non-analyticities in thermodynamic properties and the non-local nature of the nontrivial bulk correlations. Hence the most robust probe of the BKT-SPT transition, we believe, is through edge correlations in a system without strings exiting the bulk. As in the 2D HIO phase, in the closed-loop subspace the latter provide direct access to long-range correlations in squeezed space, see discussion around Eq. (9). In the 2D HXYO model we obtain a sequence from long-range, at $T = 0$, to power-law, between $0 < T < T^*_{\mathrm{BKT}}$, to exponential, for $T > T^*_{\mathrm{BKT}}$, edge correlations.

At $|\Delta| = |J_S|$, the XXZ model in squeezed space becomes $SU(2)$ invariant. From the point of view of the original model, Eq. (14), this is a hidden $SU(2)$ symmetry: constructing it requires the highly non-local unitary $\hat{U}$ to obtain the decoupled XXZ model in squeezed space from which this symmetry is apparent. As a direct consequence of this hidden $SU(2)$ symmetry, the BKT transition disappears at $|\Delta| = |J_S|$. For antiferromagnetic (AFM) interactions, $\Delta = |J_S| > 0$, any non-zero $T > 0$ leads to a symmetric phase characterized by a non-linear sigma model in squeezed space.

For $\Delta > |J_S|$, i.e. an for easy-axis AFM, the gapped phase retains $\mathbb{Z}_2$, or Ising, long-range order up to a critical temperature T_{Ising} when $S^z_{\mathrm{tot}} = 0$. For other values of S^z_{tot}, the $\mathbb{Z}_2$ symmetry is explicitly broken, the transition disappears and one symmetric, PM phase is formed. The situation for ferromagnetic coupling $\Delta < 0$ is similar. As in the ground state, this phase is independent of the loop gas properties.

Open strings & Ising gauge theory.– Finally, we discuss the effects of open $\hat{\tau}^z$ strings, introduced by adding a term $\propto h_X$ as in Eq. (10) to the Hamiltonian Eq. (14). Again we find it useful to discuss this case in the language of IGT. To this end, we express spins as hard-core bosons via $\hat{S}^+_\mathbf{j} = \hat{a}^\dagger_\mathbf{j}$ ($\hat{S}^-_\mathbf{j} = \hat{a}_\mathbf{j}$) and $\hat{S}^z_\mathbf{j} = \hat{n}^a_\mathbf{j} - 1/2$, where $\hat{n}^a_\mathbf{j} = \hat{a}^\dagger_\mathbf{j} \hat{a}_\mathbf{j}$; these bosons $\hat{a}_\mathbf{j}$ correspond to a $U(1)$ matter field. Moreover, we introduce a Higgs field $\hat{\sigma}^x_\mathbf{j}$ on the sites $\mathbf{j}$ in order to impose the $\mathbb{Z}_2$ Gauss law

$$(-1)^{\hat{n}^a_\mathbf{j}} \hat{\sigma}^x_\mathbf{j} \prod_{l \in +_\mathbf{j}} \hat{\tau}^x_l \left|\psi\right\rangle \equiv \hat{G}_\mathbf{j} \left|\psi\right\rangle = \left|\psi\right\rangle, \quad \forall\, \mathbf{j}. \tag{17}$$

This leads to the $U(1)$-plus-IGT Hamiltonian

$$\begin{aligned} \hat{H} = &-\frac{J_S}{2} \sum_{\langle \mathbf{i},\mathbf{j} \rangle} \left(\hat{a}^\dagger_\mathbf{i} \hat{\tau}^z_{\langle \mathbf{i},\mathbf{j} \rangle} \hat{a}_\mathbf{j} + \mathrm{H.c.} \right) + \mu_S \sum_\mathbf{j} \hat{n}^a_\mathbf{j} \\ &- h_\tau \sum_{\langle \mathbf{i},\mathbf{j} \rangle} \hat{\sigma}^z_\mathbf{i} \hat{\tau}^z_{\langle \mathbf{i},\mathbf{j} \rangle} \hat{\sigma}^z_\mathbf{j} - \mu_\tau \sum_\square \prod_{l \in \square} \hat{\tau}^z_l - \frac{J_\tau}{2} \sum_\mathbf{j} \hat{\sigma}^x_\mathbf{j} \\ &+ h_X \sum_{\langle \mathbf{i},\mathbf{j} \rangle} \hat{\tau}^x_{\langle \mathbf{i},\mathbf{j} \rangle} + \Delta \sum_{\langle \mathbf{i},\mathbf{j} \rangle} (\hat{n}^a_\mathbf{i} - 1/2)(\hat{n}^a_\mathbf{j} - 1/2)\,, \end{aligned} \tag{18}$$

which commutes with $\hat{G}_\mathbf{j}$.

In Fig. 6 a) we show the phase diagram of Eq. (18) at $\mu_S = 0$ and assuming ferromagnetic $\Delta < 0$. The vertical plane with $h_X = 0$ corresponds to the $T = 0$ phase diagram of the HXYO model discussed above. For large $|\Delta|/|J_S| \to \infty$, spins and links factorize in the original basis and the topological toric code phase is known to extend to non-zero values of h_X/μ_τ. In the horizontal plane, for $h_\tau = 0$, the ferromagnetic state turns into a trivial PM because the term $\propto J_\tau$, through the Gauss

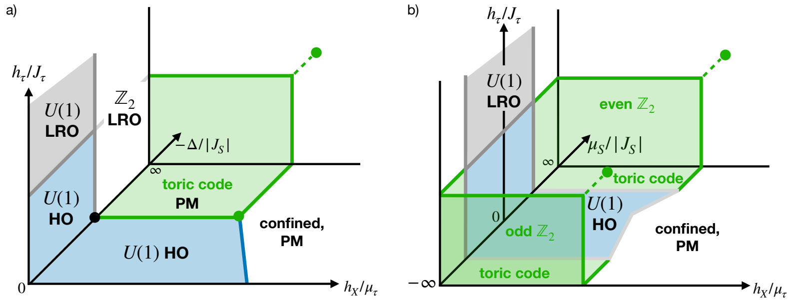

FIG. 6: Schematic phase diagram of the IGT with a $U(1)$ matter field and a $\mathbb{Z}_2$ Higgs field, Eq. (18). a) In the S^z_{tot} sector corresponding to chemical potential $\mu_S = 0$, the HXYO model with $h_X = 0$ corresponds to the left vertical plane. Both, the $U(1)$ HO / SPT phase (blue) and the topological $U(1)$ symmetric paramagnet (PM, green), remain stable when open τ^z strings are introduced by $h_X \neq 0$. For large enough h_X/μ_τ the topologically trivial, confined PM is obtained. b) As a function of the chemical potential μ_S the HXYO model is realized at $h_X = 0$ for variable S^z_{tot}, with $S^z_{\text{tot}} = \pm L^2/2$ for $\mu_S = \mp\infty$ for $\Delta < 0$, where $L^2 = \sum_{\mathbf{j}}$ is the number of lattice sites.

law, favors a definite orientation of spins $\hat{S}^z$. Since the state is gapped, this phase survives upon introducing h_X and the topologically ordered regime extends into the plane. Likewise, the application of h_X-terms creates a gapped excitation, with energy $\propto \mu_\tau$, when starting from the hidden-XY ordered SPT phase. Hence we expect the latter to remain stable upon increasing h_X. Eventually, for large enough values of h_X/μ_τ, open strings with $B_\square = -1$ proliferate and a confined, PM phase is realized. The phase diagram in the $h_\tau = 0$ plane resembles that of the $\mathbb{Z}_2$ IGT coupled to soft-core bosons at unit-filling [53].

In Fig. 6 b) we tune the chemical potential μ_S and keep $\Delta < 0$ fixed (ferromagnetic coupling). When $\mu_S \to \pm\infty$, trivial polarized states are realized with $S^z_{\text{tot}} = \mp\text{max}$. Comparison to Eq. (14) shows that these states lead to even and odd $\mathbb{Z}_2$ toric codes, respectively, for $J_\tau > 0$. In squeezed space, both topological phases are described by the same toric-code Hamiltonian. For intermediate values of μ_S, the gapped, topologically ordered states are connected through the gapless, $U(1)$ HO-SPT phase when $h_X = 0$. As in Fig 6 a), we conjecture that the HO phase initially remains stable upon increasing h_X. For large h_X, the trivial, confined PM is realized, which adiabatically connects the trivially polarized spin states.

Finally, we note that the fate of the gapless $U(1)$ HO-SPT phase at intermediate h_X remains to be analyzed more carefully. In particular, it has been proposed that non-zero h_X can act as a confining force for $\hat{a}$ particles, leading to the formation of $\mathbb{Z}_2$ neutral bosonic pairs whose number $N_{\text{pair}} = N_a/2$ is conserved [70]. If the latter condense, a topologically ordered loop gas may remain stable. Whether such a state exists, and how it connects to the $U(1)$ HO phase proposed here for small h_X remains to be worked out.

DISCUSSION

In this article we discussed a class of hidden-order symmetry-protected topological (HO-SPT) phases, in which a global symmetry is spontaneously broken but long-range correlations, or any other local order parameter, are hidden by the proliferation of domain walls of the order parameter bound to the strings constituting a loop gas model. Some of the phenomenology we propose has previously been explored, mostly in the context of (emergent) higher-form symmetries [40, 52] and at $T = 0$. We went beyond existing studies in three key ways. (i) We demonstrate that the HO-SPT phases protected by the closed loop property of the loop-gas model (corresponding to a 1-form symmetry) are stable to thermal fluctuations, in two or more spatial dimensions, leading to rich finite-T phase diagrams. (ii) We construct an exact unitary transformation, which allows to exactly decouple and solve the full spectrum of an entire class of quantum spin models coupled to a loop gas / perturbed toric code. Specifically, we apply this approach to an XY model of spins featuring a continuous $U(1)$ symmetry, which leads to an intrinsically gapless HO-SPT phase with finite-T power-law correlations along appropriate edges and a HO-SPT phase transition in the hidden-BKT universality class. (iii) While the non-trivial edge correlations are expected to disappear immediately when open strings of the loop gas are introduced (i.e. when the 1-form symmetry is broken), we put forward a characterization of the $T = 0$ and $T > 0$ SPT phases in terms of a spontaneously broken global symmetry acting on the spins (which correspond to the matter sector of the equivalent bulk gauge-theory description). Since the mechanism we propose, where SSB of the global spin symmetry is hidden by the fluctuating loop gas, does not require higher-form or local gauge symmetries to protect the SPT phase, we argue that the HO-SPT phases are stable against general perturbations of the loop gas model. Currently we are not aware of an order parameter which is able to detect the hidden SSB without the 1-form symmetry in place, and finding one remains a interesting topic of future research.

Our work has important implications for material sciences: we suggest to search for quantum spin liquids in the HO-SPT class. These states of matter are distinct from the deconfinded, topological toric code phase that underlies several gapped, $\mathbb{Z}_2$ topological quantum spin liquids [71–76], but also feature short-range correlations without local order parameters in the bulk. Such HO-SPT phases might most easily be identified through their unconventional effect on edge correlations, and they are robust at finite temperatures. Another system in which hidden order has recently been proposed to play a role by some of us is the pseudogap (PG) phase of hole-doped cuprate superconductors [43]. Specifically, we suggested that a fluctuating string net of AFM stripes may hide an underlying broken $SU(2)$ symmetry, leading to a fractionalized orthogonal metal. Building upon this picture, we speculate that the finite-temperature transition into the PG phase, at a characteristic temperature T^* that depends on the hole doping, might realize a finite-T HO-SPT transition protected by the global $SU(2)$ symmetry [77] ending in a hQCP around optimal doping, where the $SU(2)$ symmetry is fully restored. Exploring the physics of $SU(2)$ HO-SPT phases will be an important future task enabled by our work.

While we laid out the basic physics of HO-SPT phases, understanding further signatures of HO-SPT phases constitutes an important future research direction [78]. For example, for systems with hidden continuous symmetry breaking we predict gapless Goldstone modes in the spectrum. Since the latter involve strong entanglement between links and spins, their spectral signatures in the HO-SPT phase remain to be clarified. It will also be interesting to study the relation between HO-SPT phases and nematic states of matter, which can also be described in the framework of lattice gauge theories [45].

Finally, we propose to search for HO-SPT phases directly in quantum simulators. One avenue is to start from digital schemes, where the perturbed toric code has already been successfully implemented [79]. The stability of the HO-SPT phase to thermal fluctuations also suggests some intrinsic robustness to noise, and the study of edge-correlations in mixed quantum states constitutes a promising route to demonstrate this effect. On the other hand, Rydberg tweezer arrays [80] constitute a promising alternative platform for directly realizing HO-SPT phases. Specifically, by using so-called local pseudogenerators [81], it is possible to implement $\mathbb{Z}_2$ lattice gauge theories on the honeycomb lattice with couplings to $\mathbb{Z}_2$ or $U(1)$ matter fields [70], and implement the toy models introduced in this work: the HIO model in 1D or 2D, and the HXYO model.

ACKNOWLEDGMENTS

The authors acknowledge inspiring discussions with G. De Paciani, G. Dünnweber, L. Homeier, T. Rakovszky, R. Verresen, M. Kebric, S. Paeckel, S. Gazit, E. Demler and L. Pollet. This project has received funding from the European Research Council (ERC) under the European Union's Horizon 2020 research and innovation programm (Grant Agreement no 948141) — ERC Starting Grant SimUcQuam, and by the Deutsche Forschungsgemeinschaft (DFG, German Research Foundation) under Germany's Excellence Strategy – EXC-2111 – 390814868.

Appendix A: Hidden order transformation

1D HIO model.– We explicitly construct the unitary transformation $\hat{U}$ disentangling link and spin degrees of freedom at $\lambda = 0$. In the main text we defined $\hat{U}$ by its action on the basis states, see Eq. (2). The explicit operator form of the unitary is given by

$$\hat{U} = \prod_j \hat{U}_j = \prod_j (2\hat{S}^x_j)^{\hat{\gamma}_j}, \quad \hat{\gamma}_j = \frac{1}{2}(1 - \hat{\pi}_j) \, , \tag{A1}$$

with the parity $\hat{\pi}_j = (-1)^{\hat{p}_j} = \prod_{i<j} \hat{\tau}^z_{\langle i,i+1\rangle}$. Furthermore, it holds that $\hat{U}^\dagger = \hat{U}$ and $\hat{U}^2 = \mathbb{1}$. As a consequence, a given spin on site j is flipped if the number of links $\tau^z_{\langle i,i+1\rangle} = -1$ with $i < j$ is odd.

Let us consider the action of $\hat{U}$ on (1), in particular the terms $\propto J_S, J_\tau$ in Eq. 1 on which it acts non-trivially. The term $\propto J_S$ transforms as

$$\hat{U}^\dagger \hat{S}^z_j \hat{S}^z_{j+1} \hat{\tau}^z_{\langle j,j+1\rangle} \hat{U} = \hat{S}^z_j \hat{S}^z_{j+1} (\hat{\tau}^z_{\langle j,j+1\rangle})^2 = \hat{S}^z_j \hat{S}^z_{j+1} \, , \tag{A2}$$

where we made use of the anti-commutation relation of spins $\{\hat{S}^\alpha, \hat{S}^\beta\} = \frac{1}{2}\delta_{\alpha\beta}$ and $\hat{\gamma}_{j+1} = \hat{\gamma}_j + 1 \mod 2$ ($\hat{\gamma}_{j+1} = \hat{\gamma}_j \mod 2$) if $\tau^z_{\langle j,j+1\rangle} = -1$ ($\tau^z_{\langle j,j+1\rangle} = 1$). From $\hat{\tau}^x_{\langle j,j+1\rangle} (2\hat{S}^x_i)^{\hat{\gamma}_i} = (2\hat{S}^x_i)^{\hat{\gamma}_i + 1} \hat{\tau}^x_{\langle j,j+1\rangle}$ for $i \geq j+1$, it follows

$$\hat{U}^\dagger \hat{\tau}^x_{\langle j,j+1\rangle} \hat{U} = \prod_{i \geq j+1} (2\hat{S}^x_i) \hat{\tau}^x_{\langle j,j+1\rangle} \, , \tag{A3}$$

i.e. the unitary attaches a string of $\hat{S}^x_i$ to $\hat{\tau}^x_{\langle j,j+1\rangle}$. As a result, the term $\propto J_\tau$ transforms as

$$\begin{aligned} \hat{U}^\dagger \hat{\tau}^x_{\langle j-1,j\rangle} \hat{\tau}^x_{\langle j,j+1\rangle} \hat{S}^x_j \hat{U} &= (2\hat{S}^x_j) \hat{S}^x_j \hat{\tau}^x_{\langle j-1,j\rangle} \hat{\tau}^x_{\langle j,j+1\rangle} \\ &= \frac{1}{2} \hat{\tau}^x_{\langle j-1,j\rangle} \hat{\tau}^x_{\langle j,j+1\rangle} \, . \end{aligned} \tag{A4}$$

The final decoupled Hamiltonian is given by

$$\begin{aligned} \hat{U}^\dagger \hat{H} \hat{U} = -J_S \sum_j \hat{S}^z_{j+1} \hat{S}^z_j + h_S \sum_j \hat{S}^x_j \\ - h_\tau \sum_j \hat{\tau}^z_{\langle j,j+1\rangle} + \frac{J_\tau}{2} \sum_j \hat{\tau}^x_{\langle j-1,j\rangle} \hat{\tau}^x_{\langle j,j+1\rangle} \\ = \hat{H}^S_{\mathrm{TFIM}} + \hat{H}^\tau_{\mathrm{TFIM}} \, . \end{aligned} \tag{A5}$$

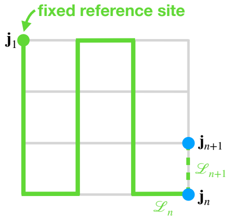

FIG. 7: Hidden order transformation $\hat{U}$ for the 2D HIO and 2D HXYO models. We choose a particular set of paths $\mathcal{L}_{\mathbf{j}_n}$, such that for a consecutive set of nearest-neighbor sites $\langle \mathbf{j}_{n+1}, \mathbf{j}_n \rangle$, the trajectory $\mathcal{L}_{\mathbf{j}_{n+1}}$ is obtained from $\mathcal{L}_{\mathbf{j}_n}$ by adding the nearest-neighbor link $\langle \mathbf{j}_{n+1}, \mathbf{j}_n \rangle$. Site $\mathbf{j}_1$ where all $\mathcal{L}_{\mathbf{j}_n}$ start defines a fixed reference site.

2D HIO model.– In a similar manner, we demonstrate the action of the unitary transformation $\hat{U}$ in the $2D$ HIO model:

$$\hat{U} = \prod \hat{U}_{\mathbf{j}} = \prod_{\mathbf{j}} (2\hat{S}^x_{\mathbf{j}})^{\hat{\gamma}_{\mathbf{j}}}, \quad \hat{\gamma}_{\mathbf{j}} = \frac{1}{2}(1 - \hat{\pi}_{\mathbf{j}}) \ . \tag{A6}$$

In 2D, the parity is defined as $(-1)^{\hat{p}_{\mathbf{j}}} = \prod_{l \in \mathcal{L}_{\mathbf{j}}} \hat{\tau}^z_l$, where $\mathcal{L}_{\mathbf{j}}$ denotes a path on the links starting at a fixed reference site and leading to $\mathbf{j}$. While there is only one choice of trajectory $\mathcal{L}_{\mathbf{j}}$ in the 1D model, care has to be taken in the 2D model.

For the first term in Eq. (4) that transform non-trivially under $\hat{U}$, the one $\propto J_S$, any choice of $\mathcal{L}_{\mathbf{j}}$ starting at the same, fixed reference site for all $\mathbf{j}$ leads to the following transformation:

$$\begin{aligned} &\hat{U}^\dagger \hat{S}^z_{\mathbf{i}} \hat{S}^z_{\mathbf{j}} \hat{\tau}^z_{\langle \mathbf{i},\mathbf{j} \rangle} \hat{U} \\ &= \begin{cases} (\pm 1)^2 \hat{\tau}^z_{\langle \mathbf{i},\mathbf{j} \rangle} \hat{S}^z_{\mathbf{i}} \hat{S}^z_{\mathbf{j}} \ , & \tau^z_{\langle \mathbf{i},\mathbf{j} \rangle} = 1 \\ -\hat{\tau}^z_{\langle \mathbf{i},\mathbf{j} \rangle} \hat{S}^z_{\mathbf{i}} \hat{S}^z_{\mathbf{j}} \ , & \tau^z_{\langle \mathbf{i},\mathbf{j} \rangle} = -1 \end{cases} \\ &= (\hat{\tau}^z_{\langle \mathbf{i},\mathbf{j} \rangle})^2 \hat{S}^z_{\mathbf{i}} \hat{S}^z_{\mathbf{j}} = \hat{S}^z_{\mathbf{i}} \hat{S}^z_{\mathbf{j}} \ , \end{aligned} \tag{A7}$$

since we work in the closed loop subspace.

To decouple spins from links in the second term, $\propto J_\tau$, a particular choice of trajectories $\mathcal{L}_{\mathbf{j}}$ is required. As illustrated in Fig. 7, we consider a recursive construction of $\mathcal{L}_{\mathbf{j}}$: it starts by labeling all sites by a one-dimensional snake $\mathbf{j}_n$, with $n = 1 \ldots N_s$ where N_s is the total number of sites of the lattice; $\mathbf{j}_1$ is the reference sites common to all $\mathcal{L}_n \equiv \mathcal{L}_{\mathbf{j}_n}$. The snake is chosen such that any set of consecutive sites constitutes a nearest-neighbor pair, $\langle \mathbf{j}_{n+1}, \mathbf{j}_n \rangle$ for all n. The trajectory $\mathcal{L}_1$ is trivial and contains only the reference site $\mathbf{j}_1$. In every step of the recursion, $\mathcal{L}_{n+1}$ is obtained from $\mathcal{L}_n$ by starting from $\mathcal{L}_n$ and extending it by the link $\langle \mathbf{j}_{n+1}, \mathbf{j} \rangle$. Thereby, every trajectory $\mathcal{L}_m \supset \mathcal{L}_n$ for $m > n$ contains all previous trajectories.

Now we apply the unitary transformation $\hat{U}$ to the term $\propto J_\tau$ in Eq. (4). Since $\hat{\tau}^z_{\langle \mathbf{i},\mathbf{j} \rangle}$ on bonds $\langle \mathbf{i}, \mathbf{j} \rangle$ which are not part of the snake do not appear in any $\mathcal{L}_{\mathbf{r}}$, these variables commute with $\hat{U}$ and can be viewed as c-numbers in the following. Hence, $\hat{\tau}^z_{\langle \mathbf{j}_{n+1}, \mathbf{j}_n \rangle}$ on bonds $\langle \mathbf{j}_{n+1}, \mathbf{j}_n \rangle$ which are part of the snake form an effective 1D HIO model, along the snake, and we obtain the same transformation law as above, see Eq. (A4). Making use of $(2\hat{S}^x_j)^{\hat{\gamma}_j} \hat{\tau}^x_{\langle j-1,j \rangle} (2\hat{S}^x_j)^{\hat{\gamma}_j} = (2\hat{S}^x_j)^{\hat{\gamma}_j} (2\hat{S}^x_j)^{\hat{\gamma}_j+1} \hat{\tau}^x_{\langle j-1,j \rangle} = 2\hat{S}^x_j \hat{\tau}^x_{\langle j-1,j \rangle}$, the term $\propto J_\tau$ transforms as

$$\begin{aligned} \hat{U}^\dagger \left(\prod_{l \in +_{\mathbf{j}}} \hat{\tau}^x_l \right) \hat{S}^x_{\mathbf{j}} \hat{U} &= (2\hat{S}^x_{\mathbf{j}})^{\hat{\gamma}_{\mathbf{j}}} \left[\left(\prod_{l \in +_{\mathbf{j}}} \hat{\tau}^x_l \right) \hat{S}^x_{\mathbf{j}} \right] (2\hat{S}^x_{\mathbf{j}})^{\hat{\gamma}_{\mathbf{j}}} \\ &= (2\hat{S}^x_{\mathbf{j}}) \hat{S}^x_{\mathbf{j}} \prod_{l \in +_{\mathbf{j}}} \hat{\tau}^x_l = \frac{1}{2} \prod_{l \in +_{\mathbf{j}}} \hat{\tau}^x_l \ . \end{aligned} \tag{A8}$$

Hence, the unitary transformation allows us to decouple the Ising and toric code model,

$$\hat{U}^\dagger \hat{H} \hat{U} = \hat{H}_{\mathrm{TC-F}} + \hat{H}_{\mathrm{TFIM}} \ . \tag{A9}$$

2D HXYO model.– In this case, the unitary transformation is defined as

$$\hat{U} = \prod \hat{U}_{\mathbf{j}} = \prod_{\mathbf{j}} (2\hat{S}^z_{\mathbf{j}})^{\hat{\gamma}_{\mathbf{j}}}, \quad \hat{\gamma}_{\mathbf{j}} = \frac{1}{2}(1 - \hat{\pi}_{\mathbf{j}}) \ , \tag{A10}$$

with the path defined in the same way as for the 2D HIO model. The calculation can be performed in a similar manner, making use of the anti-commutation of spins and

$$\begin{aligned} &\hat{U}^\dagger \hat{S}^\mu_{\mathbf{i}} \hat{S}^\mu_{\mathbf{j}} \hat{\tau}^z_{\langle \mathbf{i},\mathbf{j} \rangle} \hat{U} \\ &= \begin{cases} (\pm 1)^2 \hat{\tau}^z_{\langle \mathbf{i},\mathbf{j} \rangle} \hat{S}^\mu_{\mathbf{i}} \hat{S}^\mu_{\mathbf{j}} \ , & \tau^z_{\langle \mathbf{i},\mathbf{j} \rangle} = 1 \\ -\hat{\tau}^z_{\langle \mathbf{i},\mathbf{j} \rangle} \hat{S}^\mu_{\mathbf{i}} \hat{S}^\mu_{\mathbf{j}} \ , & \tau^z_{\langle \mathbf{i},\mathbf{j} \rangle} = -1 \end{cases} \\ &= (\tau^z_{\langle \mathbf{i},\mathbf{j} \rangle})^2 \hat{S}^\mu_{\mathbf{i}} \hat{S}^\mu_{\mathbf{j}} = \hat{S}^\mu_{\mathbf{i}} \hat{S}^\mu_{\mathbf{j}} \ . \end{aligned} \tag{A11}$$

with $\mu = x, y$.

Appendix B: Numerical DMRG simulations: 1D HIO model

We perform DMRG simulations using the SyTen toolkit to evaluate magnetization M_S (M_S^*) in real (squeezed) space, as well as the correlator $|\langle \hat{S}^z_0 \hat{S}^z_x \rangle|$. The former are computed from snapshots of the many-body wavefunction via the perfect sampling approach [60, 61]. The sample-averaged magnetization of the state of a system of L sites is computed as

$$M = \frac{1}{N} \sum_i |M_i|, \quad M_i = \frac{1}{L} \sum_j S^z_j|_i \ . \tag{B1}$$

Here, $S^z_j|_i$ denotes the spin-z value on site j in snapshot i and $N = 10^4$ denotes the total number of sampled snapshots. In analogy, the sample-averaged squeezed space magnetization is computed with respect to the squeezed space value $S^z_j|_{\mathrm{sq},i}$, i.e. the unitary (2) is applied to the Fock basis state prior to the evaluation of S^z_j.

[1] V. L. Berezinskii, "Destruction of long-range order in one-dimensional and two-dimensional systems possessing a continuous symmetry group. ii. quantum systems." Sov. Phys. JETP **34**, 610–616 (1972).

[2] J. M. Kosterlitz and D. J. Thouless, "Ordering, metastability and phase transitions in two-dimensional systems," Journal of Physics C: Solid State Physics **6**, 1181– (1973).

[3] M. A. Levin and X.-G. Wen, "String-net condensation: A physical mechanism for topological phases," Phys. Rev. B **71**, 045110 (2005).

[4] S. Sachdev, *Quantum Phase Transitions*, 2nd ed. (Cambridge University Press, 2011).

[5] X. Chen, Z.-C. Gu, and X.-G. Wen, "Complete classification of one-dimensional gapped quantum phases in interacting spin systems," Phys. Rev. B **84**, 235128 (2011).

[6] F. Pollmann and A. M. Turner, "Detection of symmetry-protected topological phases in one dimension," Phys. Rev. B **86**, 125441 (2012).

[7] A. Kitaev, "Fault-tolerant quantum computation by anyons," Annals of Physics **303**, 2–30 (2003).

[8] A. Kitaev, "Anyons in an exactly solved model and beyond," Annals of Physics **321**, 2–111 (2006).

[9] T. Scaffidi, D. E. Parker, and R. Vasseur, "Gapless symmetry-protected topological order," Phys. Rev. X **7**, 041048 (2017).

[10] R. Thorngren, A. Vishwanath, and R. Verresen, "Intrinsically gapless topological phases," Phys. Rev. B **104**, 075132 (2021).

[11] R. Verresen, R. Thorngren, N. G. Jones, and F. Pollmann, "Gapless topological phases and symmetry-enriched quantum criticality," Phys. Rev. X **11**, 041059 (2021).

[12] X. Chen, Y.-M. Lu, and A. Vishwanath, "Symmetry-protected topological phases from decorated domain walls," Nature Communications **5**, 3507 (2014).

[13] P. Mai, J. Zhao, B. E. Feldman, and P. W. Phillips, "1/4 is the new 1/2 when topology is intertwined with mottness," Nature Communications (2023), doi.org/10.1038/s41467-023-41465-6.

[14] E. Dennis, A. Kitaev, A. Landahl, and J. Preskill, "Topological quantum memory," Journal of Mathematical Physics **43**, 4452–4505 (2002), https://pubs.aip.org/aip/jmp/article-pdf/43/9/4452/19183135/4452_1_online.pdf.

[15] R. Alicki, M. Horodecki, P. Horodecki, and R. Horodecki, "On thermal stability of topological qubit in kitaev's 4d model," Open Systems & Information Dynamics **17**, 1–20 (2010), https://doi.org/10.1142/S1230161210000023.

[16] A. Kitaev and J. Preskill, "Topological entanglement entropy," Physical Review Letters **96**, 110404 (2006).

[17] H. Li and F. D. M. Haldane, "Entanglement spectrum as a generalization of entanglement entropy: Identification of topological order in non-abelian fractional quantum hall effect states," Phys. Rev. Lett. **101**, 010504 (2008).

[18] X. Chen, Z.-C. Gu, and X.-G. Wen, "Local unitary transformation, long-range quantum entanglement, wave function renormalization, and topological order," Physical Review B **82**, 155138 (2010).

[19] F. Grusdt, "Topological order of mixed states in correlated quantum many-body systems," Phys. Rev. B **95**, 075106 (2017).

[20] S. Diehl, E. Rico, M. A. Baranov, and P. Zoller, "Topology by dissipation in atomic quantum wires," Nature Physics **7**, 971–977 (2011).

[21] A. Uhlmann, "Parallel transport and "quantum holonomy" along density operators," Reports on Mathematical Physics **24**, 229–240 (1986).

[22] A. Rivas, O. Viyuela, and M. A. Martin-Delgado, "Density-matrix chern insulators: Finite-temperature generalization of topological insulators," Physical Review B **88**, 155141 (2013).

[23] J. C. Budich and S. Diehl, "Topology of density matrices," Phys. Rev. B **91**, 165140 (2015).

[24] C.-E. Bardyn, L. Wawer, A. Altland, M. Fleischhauer, and S. Diehl, "Probing the topology of density matrices," Phys. Rev. X **8**, 011035 (2018).

[25] Z.-M. Huang and S. Diehl, "Mixed state topological order parameters for symmetry protected fermion matter," (2024), arXiv:2401.10993 [cond-mat.quant-gas].

[26] Z.-M. Huang, S. Diehl, and X.-Q. Sun, "Topological response in open quantum systems with weak symmetries," (2025), arXiv:2504.02941 [quant-ph].

[27] Z.-M. Huang, L. Colmenarez, M. Müller, and S. Diehl, "Coherent information as a mixed-state topological order parameter of fermions," (2024), arXiv:2412.12279 [quant-ph].

[28] R. Ma and C. Wang, "Average symmetry-protected topological phases," Physical Review X **13** (2023), 10.1103/physrevx.13.031016.

[29] R. Ma, J.-H. Zhang, Z. Bi, M. Cheng, and C. Wang, "Topological phases with average symmetries: The decohered, the disordered, and the intrinsic," Phys. Rev. X **15**, 021062 (2025).

[30] Z. Zhang, U. Agrawal, and S. Vijay, "Quantum communication and mixed-state order in decohered symmetry-protected topological states," (2024), arXiv:2405.05965 [quant-ph].

[31] Z. Huang and D. P. Arovas, "Topological indices for open and thermal systems via uhlmann's phase," Phys. Rev. Lett. **113**, 076407 (2014).

[32] P. Molignini and N. R. Cooper, "Topological phase transitions at finite temperature," Phys. Rev. Res. **5**, 023004 (2023).

[33] Z.-M. Huang and S. Diehl, "Interaction-induced topological phase transition at finite temperature," Phys. Rev. Lett. **134**, 053002 (2025).

[34] S. Roberts, B. Yoshida, A. Kubica, and S. D. Bartlett, "Symmetry-protected topological order at nonzero temperature," Phys. Rev. A **96**, 022306 (2017).

[35] T. Kennedy and H. Tasaki, "Hidden $z_2\times z_2$ symmetry breaking in haldane-gap antiferromagnets," Phys. Rev. B **45**, 304–307 (1992).

[36] D. V. Else, S. D. Bartlett, and A. C. Doherty, "Hidden symmetry-breaking picture of symmetry-protected topological order," Phys. Rev. B **88**, 085114 (2013).

[37] M. Levin and Z.-C. Gu, "Braiding statistics approach to symmetry-protected topological phases," Phys. Rev. B **86**, 115109 (2012).

[38] L.-Y. Hung and X.-G. Wen, "Quantized topological terms in weakly coupled gauge theories and their connection to symmetry protected topological phases," (2012), arXiv:1211.2767 [cond-mat.str-el].

[39] D. E. Parker, T. Scaffidi, and R. Vasseur, "Topological luttinger liquids from decorated domain walls," Phys. Rev. B **97**, 165114 (2018).

[40] R. Verresen, U. Borla, A. Vishwanath, S. Moroz, and R. Thorngren, "Higgs condensates are symmetry-protected topological phases: I. discrete symmetries," (2024), arXiv:2211.01376 [cond-mat.str-el].

[41] H. Sukeno, K. Ikeda, and T.-C. Wei, "Bulk and boundary entanglement transitions in the projective gauge-higgs model," Phys. Rev. B **110**, 245102 (2024).

[42] T. Rakovszky and V. Khemani, "The physics of (good) ldpc codes i. gauging and dualities," (2023), arXiv:2310.16032 [quant-ph].

[43] H. Schlömer, A. Bohrdt, and F. Grusdt, "Geometric fractionalized fermi liquids: Hidden antiferromagnetism and pseudogap from fluctuating stripes," (2024), arXiv:2411.03419 [cond-mat.str-el].

[44] Y. Zhang, E. Demler, and S. Sachdev, "Competing orders in a magnetic field: Spin and charge order in the cuprate superconductors," Phys. Rev. B **66**, 094501 (2002).

[45] D. Podolsky and E. Demler, "Properties and detection of spin nematic order in strongly correlated electron systems," New Journal of Physics **7**, 59– (2005).

[46] E. Fradkin and S. H. Shenker, "Phase diagrams of lattice gauge theories with higgs fields," Phys. Rev. D **19**, 3682–3697 (1979).

[47] S. Trebst, P. Werner, M. Troyer, K. Shtengel, and C. Nayak, "Breakdown of a topological phase: Quantum phase transition in a loop gas model with tension," Phys. Rev. Lett. **98**, 070602 (2007).

[48] F. Wu, Y. Deng, and N. Prokof'ev, "Phase diagram of the toric code model in a parallel magnetic field," Phys. Rev. B **85**, 195104 (2012).

[49] M. Ogata and H. Shiba, "Bethe-ansatz wave function, momentum distribution, and spin correlation in the one-dimensional strongly correlated hubbard model," Phys. Rev. B **41**, 2326–2338 (1990).

[50] H. V. Kruis, I. P. McCulloch, Z. Nussinov, and J. Zaanen, "Geometry and the hidden order of luttinger liquids: The universality of squeezed space," Phys. Rev. B **70**, 075109 (2004).

[51] X.-G. Wen, "Emergent anomalous higher symmetries from topological order and from dynamical electromagnetic field in condensed matter systems," Phys. Rev. B **99**, 205139 (2019).

[52] W.-T. Xu, T. Rakovszky, M. Knap, and F. Pollmann, "Entanglement properties of gauge theories from higher-form symmetries," Phys. Rev. X **15**, 011001 (2025).

[53] S. Sachdev, "Topological order, emergent gauge fields, and fermi surface reconstruction," Reports on Progress in Physics **82**, 014001 (2018).

[54] H. J. Briegel and R. Raussendorf, "Persistent entanglement in arrays of interacting particles," Phys. Rev. Lett. **86**, 910–913 (2001).

[55] U. Borla, R. Verresen, J. Shah, and S. Moroz, "Gauging the Kitaev chain," SciPost Phys. **10**, 148 (2021).

[56] M. Kebrič, U. Schollwöck, and F. Grusdt, "Mean-field theory of 1+1d $\mathbb{Z}_2$ lattice gauge theory with matter," arXiv:2404.02890 (2024), arXiv:2404.02890 [cond-mat.quant-gas].

[57] J. Simon, W. S. Bakr, R. Ma, M. E. Tai, P. M. Preiss, and M. Greiner, "Quantum simulation of antiferromagnetic spin chains in an optical lattice," Nature **472**, 307–312 (2011).

[58] T. A. Hilker, G. Salomon, F. Grusdt, A. Omran, M. Boll, E. Demler, I. Bloch, and C. Gross, "Revealing hidden antiferromagnetic correlations in doped hubbard chains via string correlators," Science **357**, 484–487 (2017), https://www.science.org/doi/pdf/10.1126/science.aam8990.

[59] P. Coleman, *Introduction to Many-Body Physics* (Cambridge University Press, 2015).

[60] A. J. Ferris and G. Vidal, "Perfect sampling with unitary tensor networks," Phys. Rev. B **85**, 165146 (2012).

[61] M. Buser, U. Schollwöck, and F. Grusdt, "Snapshot-based characterization of particle currents and the hall response in synthetic flux lattices," Phys. Rev. A **105**, 033303 (2022).

[62] T. Rakovszky, P. Sala, R. Verresen, M. Knap, and F. Pollmann, "Statistical localization: From strong fragmentation to strong edge modes," Phys. Rev. B **101**, 125126 (2020).

[63] M. Endres, M. Cheneau, T. Fukuhara, C. Weitenberg, P. Schauss, C. Gross, L. Mazza, M. C. Banuls, L. Pollet, I. Bloch, and S. Kuhr, "Observation of correlated particle-hole pairs and string order in low-dimensional mott insulators," Science **334**, 200–203 (2011).

[64] S. M. Linsel, A. Bohrdt, L. Homeier, L. Pollet, and F. Grusdt, "Percolation as a confinement order parameter in z_2 lattice gauge theories," Phys. Rev. B **110**, L241101 (2024).

[65] G. Dünnweber, S. M. Linsel, A. Bohrdt, and F. Grusdt, "Percolation renormalization group analysis of confinement in z_2 lattice gauge theories," Phys. Rev. B **111**, 024314 (2025).

[66] S. M. Linsel, L. Pollet, and F. Grusdt, "Independent e- and m-anyon confinement in the parallel field toric code on non-square lattices," (2025), arXiv:2504.03512 [quant-ph].

[67] R. Peierls, "On ising's model of ferromagnetism," Mathematical Proceedings of the Cambridge Philosophical Society **32**, 477–481 (1936).

[68] F. J. Wegner, "Duality in Generalized Ising Models and Phase Transitions without Local Order Parameters," Journal of Mathematical Physics **12**, 2259–2272 (1971), https://pubs.aip.org/aip/jmp/article-pdf/12/10/2259/19106483/2259_1_online.pdf.

[69] D. Tiwari, S. Bollmann, S. Paeckel, and E. J. König, "Quantum restored symmetry protected topological phases," (2024), arXiv:2410.02689 [cond-mat.str-el].

[70] L. Homeier, A. Bohrdt, S. Linsel, E. Demler, J. C. Halimeh, and F. Grusdt, "Realistic scheme for quantum simulation of z2 lattice gauge theories with dynamical matter in (2 + 1)d," Communications Physics **6**, 127 (2023).

[71] L. Savary and L. Balents, "Quantum spin liquids: a review," Reports on Progress in Physics **80**, 016502– (2017).

[72] D. S. Rokhsar and S. A. Kivelson, "Superconductivity and the quantum hard-core dimer gas," Phys. Rev. Lett. **61**, 2376–2379 (1988).

[73] R. Verresen, M. D. Lukin, and A. Vishwanath, "Prediction of toric code topological order from rydberg blockade," Phys. Rev. X **11**, 031005 (2021).

[74] R. Samajdar, W. W. Ho, H. Pichler, M. D. Lukin, and S. Sachdev, "Quantum phases of rydberg atoms on a kagome lattice," Proceedings of the National Academy of Sciences **118**, e2015785118 (2021), https://www.pnas.org/doi/pdf/10.1073/pnas.2015785118.

[75] G. Semeghini, H. Levine, A. Keesling, S. Ebadi, T. T. Wang, D. Bluvstein, R. Verresen, H. Pichler, M. Kalinowski, R. Samajdar, A. Omran, S. Sachdev, A. Vishwanath, M. Greiner, V. Vuletić, and M. D. Lukin, "Probing topological spin liquids on a programmable quantum simulator," Science **374**, 1242–1247 (2021).

[76] Z. Wang and L. Pollet, "Renormalized classical spin liquid on the ruby lattice," Phys. Rev. Lett. **134**, 086601 (2025).

[77] G. D. Paciani, G. Dünnweber, H. Schlömer, S. Linsel, and F. Grusdt, "In preparation," (2025).

[78] R. Wilke, H. Schlömer, A. Bohrdt, and F. Grusdt, "In preparation," (2025).

[79] T. A. Cochran, B. Jobst, E. Rosenberg, Y. D. Lensky, G. Gyawali, N. Eassa, M. Will, D. Abanin, R. Acharya, L. A. Beni, T. I. Andersen, M. Ansmann, F. Arute, K. Arya, A. Asfaw, J. Atalaya, R. Babbush, B. Ballard, J. C. Bardin, A. Bengtsson, A. Bilmes, A. Bourassa, J. Bovaird, M. Broughton, D. A. Browne, B. Buchea, B. B. Buckley, T. Burger, B. Burkett, N. Bushnell, A. Cabrera, J. Campero, H.-S. Chang, Z. Chen, B. Chiaro, J. Claes, A. Y. Cleland, J. Cogan, R. Collins, P. Conner, W. Courtney, A. L. Crook, B. Curtin, S. Das, S. Demura, L. D. Lorenzo, A. D. Paolo, P. Donohoe, I. Drozdov, A. Dunsworth, A. Eickbusch, A. M. Elbag, M. Elzouka, C. Erickson, V. S. Ferreira, L. F. Burgos, E. Forati, A. G. Fowler, B. Foxen, S. Ganjam, R. Gasca, Élie Genois, W. Giang, D. Gilboa, R. Gosula, A. G. Dau, D. Graumann, A. Greene, J. A. Gross, S. Habegger, M. Hansen, M. P. Harrigan, S. D. Harrington, P. Heu, O. Higgott, J. Hilton, H.-Y. Huang, A. Huff, W. J. Huggins, E. Jeffrey, Z. Jiang, C. Jones, C. Joshi, P. Juhas, D. Kafri, H. Kang, A. H. Karamlou, K. Kechedzhi, T. Khaire, T. Khattar, M. Khezri, S. Kim, P. V. Klimov, B. Kobrin, A. N. Korotkov, F. Kostritsa, J. M. Kreikebaum, V. D. Kurilovich, D. Landhuis, T. Lange-Dei, B. W. Langley, K.-M. Lau, J. Ledford, K. Lee, B. J. Lester, L. L. Guevel, W. Y. Li, A. T. Lill, W. P. Livingston, A. Locharla, D. Lundahl, A. Lunt, S. Madhuk, A. Maloney, S. Mandrà, L. S. Martin, O. Martin, C. Maxfield, J. R. McClean, M. McEwen, S. Meeks, A. Megrant, K. C. Miao, R. Molavi, S. Molina, S. Montazeri, R. Movassagh, C. Neill, M. Newman, A. Nguyen, M. Nguyen, C.-H. Ni, M. Y. Niu, W. D. Oliver, K. Ottosson, A. Pizzuto, R. Potter, O. Pritchard, C. Quintana, G. Ramachandran, M. J. Reagor, D. M. Rhodes, G. Roberts, K. Sankaragomathi, K. J. Satzinger, H. F. Schurkus, M. J. Shearn, A. Shorter, N. Shutty, V. Shvarts, V. Sivak, S. Small, W. C. Smith, S. Springer, G. Sterling, J. Suchard, A. Szasz, A. Sztein, D. Thor, M. M. Torunbalci, A. Vaishnav, J. Vargas, S. Vdovichev, G. Vidal, C. V. Heidweiller, S. Waltman, S. X. Wang, B. Ware, T. White, K. Wong, B. W. K. Woo, C. Xing, Z. J. Yao, P. Yeh, B. Ying, J. Yoo, N. Yosri, G. Young, A. Zalcman, Y. Zhang, N. Zhu, N. Zobris, S. Boixo, J. Kelly, E. Lucero, Y. Chen, V. Smelyanskiy, H. Neven, A. Gammon-Smith, F. Pollmann, M. Knap, and P. Roushan, "Visualizing dynamics of charges and strings in (2+1)d lattice gauge theories," (2024), arXiv:2409.17142 [quant-ph].

[80] H. Bernien, S. Schwartz, A. Keesling, H. Levine, A. Omran, H. Pichler, S. Choi, A. S. Zibrov, M. Endres, M. Greiner, V. Vuletić, and M. D. Lukin, "Probing many-body dynamics on a 51-atom quantum simulator," Nature **551**, 579–584 (2017).

[81] J. C. Halimeh, L. Homeier, C. Schweizer, M. Aidelsburger, P. Hauke, and F. Grusdt, "Stabilizing lattice gauge theories through simplified local pseudogenerators," Phys. Rev. Res. **4**, 033120 (2022).

Chapter Three

Feshbach resonances as a pairing mechanism for partons in frustrated quantum magnets

3.1 High-temperature superconductivity

Superconductivity was discovered in 1911 by Onnes [93, 94] when he reported that the resistance of mercury vanishes below temperatures of 4.2 K. Another characteristic feature of superconductors is the expulsion of magnetic fields within the superconducting material up to a critical temperature T_c and a critical magnetic field h_c, the so-called *Meissner effect*, which was discovered in 1933 by Meissner and Ochsenfeld [95].

The first theoretical description of superconductivity were the *London equations* by Fritz and Heinz London [96], which explained the Meissner effect. An important milestone was the introduction of a complex order parameter for superconductivity by Ginzburg and Landau [97]. Based on this work, Abrikosov theoretically explained type-II superconductors [98]. Compared to type-I superconductors, they have an additional intermediate phase between the superconducting and non-superconducting phase, where the magnetic flux penetrates the material through quantized vortices while the material remains superconducting.

The first microscopic theory of superconductivity was the famous Bardeen-Cooper-Schrieffer (BCS) theory [99]:

$$\mathcal{H}_{\mathrm{BCS}} = \sum_{\mathbf{k},\sigma} \xi_{\mathbf{k}}\, c^{\dagger}_{\mathbf{k}\sigma} c_{\mathbf{k}\sigma} - \sum_{\mathbf{k},\mathbf{k}'} V_{\mathbf{k}\mathbf{k}'}\, c^{\dagger}_{\mathbf{k}\uparrow} c^{\dagger}_{-\mathbf{k}\downarrow} c_{-\mathbf{k}'\downarrow} c_{\mathbf{k}'\uparrow}, \qquad \xi_{\mathbf{k}} = \varepsilon_{\mathbf{k}} - \mu. \tag{3.1}$$

Here, $c_{\mathbf{k}\sigma}$ is a fermionic annihilation operator with spin σ and momentum k, $\varepsilon_{\mathbf{k}}$ is the single-particle energy, μ is the chemical potential, and $V_{\mathbf{k}\mathbf{k}'}$ is an effective attractive interaction mediated by phonons. In the superconducting phase below the critical temperature T_c, *Cooper pairs* [100] form a coherent condensate in the superconducting phase and open up a gap. Bardeen, Cooper, and Schrieffer got the 1972 Nobel prize in physics *for their jointly developed theory of superconductivity, usually called the BCS-theory.*[1]

In *conventional superconductors*, the pairing of electrons is mediated by phonons and can be described within the BCS theory. Superconductors with other pairing mechanisms are called *unconventional* superconductors. Most conventional superconductors have an isotropic complex order parameter, which is called s-wave superconductivity in analogy to the labels of atomic orbitals. Other common symmetries for unconventional superconductors are p-wave and d-wave superconductors [101].

In 1986, a critical temperature of $T_\mathrm{c} \approx 35\,\mathrm{K}$ was measured in the cuprate composition $\mathrm{Ba}_x\mathrm{La}_{5-x}\mathrm{Cu}_5\mathrm{O}_{5(3-y)}$ [18]. Ever since, cuprates have been the focal point of theoretical and experimental studies, reaching critical temperatures up to $T_\mathrm{c} \approx 134\,\mathrm{K}$ at ambient pressure [102], well above the boiling temperature of nitrogen at $T \approx 77\,\mathrm{K}$.[2] Understanding the microscopic pairing mechanism of the Cooper pairs in high-T_c materials is essential for designing materials with higher T_c.

Cuprates feature a complex phase diagram that has yet to be described by a unifying theory [22]. Theoretical physicists have worked to qualitatively describe cuprates using simplified models, which are analytically and numerically tractable, but crucially still capture the essential physics, including the pairing mechanism. A paradigmatic model is the Fermi-Hubbard model and its variants, which describes the CuO_2-layers of cuprates as quasi two-dimensional systems.

3.2 Effective models for cuprates – Fermi-Hubbard and $t - J$ models

The Fermi-Hubbard model [13–17] describes spinful fermions on a lattice in the tight-binding limit and, in its simplest form, approximates the Coulomb interactions as purely on-site:

$$\hat{H}_{\mathrm{Hub.}} = -t \sum_{\langle i,j\rangle,\sigma} \left[\hat{c}^\dagger_{i,\sigma}\hat{c}_{j,\sigma} + \mathrm{H.c.}\right] + U \sum_j \hat{n}_{j\uparrow}\hat{n}_{j\downarrow}. \tag{3.2}$$

Here, $\hat{c}_{j,\sigma}$ is a fermionic annihilation operator on site j with spin $\sigma \in \{\uparrow, \downarrow\}$; $\hat{n}_{j,\sigma} = \hat{c}^\dagger_{j,\sigma}\hat{c}_{j,\sigma}$ is the number operator.[3] The hopping term $\propto t$ lets fermions tunnel between nearest neighbors $\langle i, j\rangle$ and favors delocalization and metal-type behavior; the interaction $U > 0$[4] is a penalty for two fermions of opposite spins on the same lattice site and favors insulating states. This competition leads to a rich phase diagram when hole-doping (i.e., removing fermions) the two-dimensional Fermi-Hubbard model away from half-filling (i.e., on average one fermion per lattice site), see Fig. 3.1.[5] Importantly, it features a d-wave superconducting phase at low temperatures and intermediate doping. For a detailed discussion of all phases, see [104].

---

[1] https://www.nobelprize.org/prizes/physics/1972/press-release/

[2] In this thesis, we focus on cuprates but other materials classes also host high T_c. These include iron-based superconductors, hydrides, nickelates, and bismuthates.

[3] Here we restrict ourselves to one energy band and spin-1/2 particles, but versions with more bands and higher symmetries are common, see e.g. [103].

[4] U is typically positive for fermions but can also be attractive [26].

[5] The particle-doped phase diagram [26] is equally rich but is not discussed here.

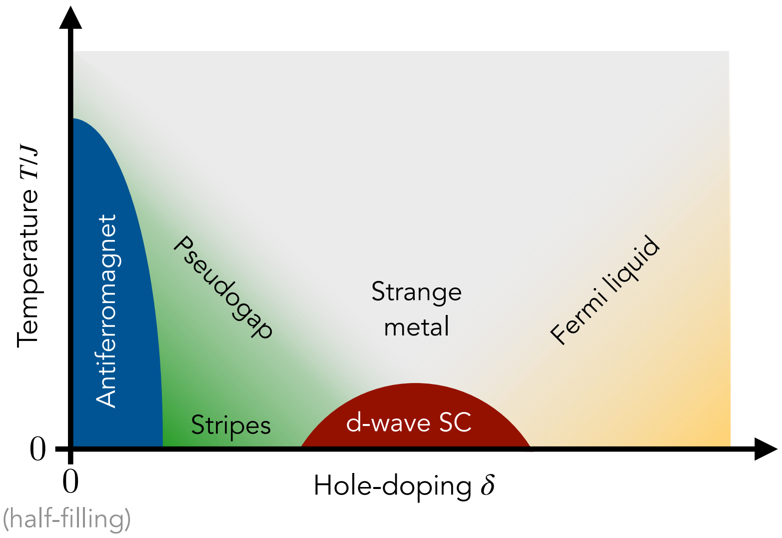

Figure 3.1: **Schematic phase diagram of the hole-doped Fermi-Hubbard model**. The individual phases are discussed in detail in [104]. Most notably, the Fermi-Hubbard model hosts a d-wave superconducting phase at low temperatures and intermediate doping. It has been argued that the nearest-neighbor Fermi-Hubbard model does not have a superconducting phase due to the competing stripe phase [105]. However, numerical data suggests that adding a next-nearest neighbor coupling could restore the superconducting phase [106]. Figure adapted from [26].

In recent decades, experimental advances have enabled the construction of analog quantum simulators which implement the microscopic interactions of the Hubbard model using ultracold atoms in optical lattices (quantum gas microscopes) [107]. Another successful platform are semiconductor quantum dot arrays [108]. These experimental advances have revolutionized the field and are fundamentally improving the testability of theories. Due to new cooling techniques [109, 110], the experimental temperatures are approaching the predicted d-wave phase, but it has not been measured so far.

In the strong-coupling limit $U \gg t$[6], a Schrieffer-Wolff transformation [112] can be applied to project out double-occupancies (i.e., two fermions with opposite spin on the same lattice site), thus reducing the local Hilbert space dimension. The result is the $t - J$ model [113]:

$$\hat{H}_{t-J} = \hat{\mathcal{P}}_{\mathrm{GW}} \left[-t \sum_{\langle i,j,\rangle,\sigma} (\hat{c}^{\dagger}_{i,\sigma} \hat{c}_{j,\sigma} + \mathrm{H.c.}) + J \sum_{\langle i,j,\rangle} \left(\hat{\boldsymbol{S}}_i \cdot \hat{\boldsymbol{S}}_j - \frac{\hat{n}_i \hat{n}_j}{4} \right) \right] \hat{\mathcal{P}}_{\mathrm{GW}}, \tag{3.3}$$

---

[6] Typical hole-doped cuprate parameters lie in the intermediate–strong regime $U/t \approx 6 - 10$ [111].

$\hat{\boldsymbol{S}}_i$ is the spin on site i; $\hat{n}_i = \sum_\sigma \hat{n}_{i,\sigma}$.[7] The first term describes the hopping of fermions; the Gutzwiller projector $\hat{\mathcal{P}}_{\mathrm{GW}}$ projects onto the subspace of no double-occupancy on any lattice site. The second term is the *superexchange coupling* $J = \frac{4t^2}{U}$, an effective antiferromagnetic interaction[8] as a consequence of a virtual second order process in perturbation theory where a fermion tunnels to a nearest neighbor (t), interacts with another fermion (U) and tunnels back (t).

At zero doping and large couplings $U \gg t$, both the $t - J$ model (reduces to the Heisenberg antiferromagnet) and the Hubbard model enter a *Mott* phase, which has a charge gap and, at low temperatures $T \lesssim J$, antiferromagnetic (AFM) spin order, see Fig. 3.1.[9] The breakdown of the AFM order in the vicinity of dopants and its relation to the emergence of superconductivity are central in revealing the underlying electron pairing mechanism [22]. Fractionalized Fermi liquids (FL*) were originally introduced to describe Kondo lattices [23, 24] and were adapted to doped Mott insulators. In FL* phases, electrons fractionalize: the fermionic annihilation operator $\hat{c}_{i\sigma} \sim \hat{f}_{i\sigma}\hat{b}_i^\dagger$ is composed of the spinon $\hat{f}_{i\sigma}$ with spin σ and zero charge, and the holon (or chargon) $\hat{b}_i$ has zero spin and charge $+e$. This is consistent with microscopic studies of hole pairs in Hubbard models [114] and doped holes in $t - J$ models [115]. The spinons form a (topological) quantum spin liquid with emergent gauge symmetries (compare to 2.1) and bound spinon-holon states form a small Fermi surface with volume $\propto \delta$, where δ is the hole-doping.[10] These quantum spin liquids with emergent gauge symmetries can be numerically exploited using our approximately-symmetric NQS architecture [P5], highlighting another connection between our work on the toric code and doped Mott insulators.

In [P7], we study an extension of the 1D $t - J$ model, the Majumdar-Ghosh model [47, 48], which serves as a paradigmatic doped quantum magnet to investigate the pairing mechanism of partons. Using matrix product states, we calculate the one-hole ARPES spectrum and show that the unbinding of a spinon-holon bound state is associated with a Feshbach resonance [116], a two-body resonantly-enhanced interaction of spinons and holons. We further establish doped quantum magnets as a platform for studying few-body physics.

3.3 Matrix product states

In this section, we give a concise introduction to matrix product states (MPS), which are indispensable for simulating frustrated quantum magnets. We closely follow the reviews by Schollwöck [117–119]. We only review the most basic versions of the algorithms; in practice, there are many optimizations and variants.

Any finite lattice quantum state can be written as

$$|\psi\rangle = \sum_{\sigma_1,\ldots,\sigma_L} c_{\sigma_1,\ldots,\sigma_L} |\sigma_1,\ldots,\sigma_L\rangle\,, \tag{3.4}$$

---

[7] Higher order three-body terms were omitted here.

[8] The antiferromagnetic interaction is in fact identical to the quantum Heisenberg model discussed in Sec. 2.2.

[9] In purely two-dimensional models, the AFM order is only long-range at zero temperature due to the Mermin-Wagner theorem. Real cuprates have weak interlayer couplings, which can stabilize long-range order.

[10] This is consistent with a modified version of Luttinger's theorem [23] that accounts for the topology.

where σ_j is a local basis on lattice site j with local Hilbert space dimension d and $c_{\sigma_1,\ldots,\sigma_L}$ are generally complex coefficients (compare to Sec. 2.6). By iteratively applying singular value decompositions (SVDs) or QR decompositions (QRs), we can, in principle, rewrite any quantum state into an MPS

$$|\psi\rangle = \sum_{\sigma_1,\ldots,\sigma_L} M^{\sigma_1} \ldots M^{\sigma_N} \, |\sigma_1, \ldots, \sigma_L\rangle \,, \tag{3.5}$$

where M is a $D \times D$ ($1 \times D/D \times 1$ at the boundaries) matrix on site j. The MPS representation is exact for an arbitrary quantum state $|\psi\rangle$ when $D \sim d^{L/2}$. A significant advantage of MPS compared to other numerical techniques is that their expressivity is controlled by a single parameter, which considerably simplifies convergence diagnostics.

MPS are numerically useful if they fit into the memory of a computer, i.e., if they can represent the quantum state with sufficient precision at a bond dimension that grows polynomially with the system size. The maximum entanglement that can be represented by an MPS scales with

$$S \sim \log_2(D) \tag{3.6}$$

1D area-law entangled gapped states have $S \sim \alpha$ can be represented with $D > 2^{\alpha}$; critical 1D states have $S \sim \alpha \log_2(L)$ need $D > L^{\alpha}$ which is usually still numerically tractable.

Two-dimensional area-law entangled states have $S \sim L$, which requires $D \sim 2^L$, which quickly becomes intractable for large L. Thus, MPS are typically not practically applicable to large, true two-dimensional systems; though they can be applied to "1.5D" cylinder geometries where $L_x \gg L_y$ [120] and the boundaries in y-direction are periodic. In 1D, however, MPS have been extremely successful and are the method of choice to simulate quantum magnets due to their efficient encoding of the entanglement.

MPS representations of $|\psi\rangle$ are not unique. We define left-normalized matrices A and right-normalized matrices B:

$$\mathbf{1} = \sum_{\sigma_j} A^{\sigma_j \dagger} A^{\sigma_j} = \sum_{\sigma_j} B^{\sigma_j} B^{\sigma_j \dagger}. \tag{3.7}$$

MPS that are made up entirely of As (Bs) are called *left-canonical* (*right-canonical*). MPS containing both A and B in the form $A \ldots AMB \ldots B$ are called *mixed-canonical*. We can transform an MPS between these so-called gauges by iteratively applying SVDs or QRs through the system.

Matrix product operators (MPOs) are used for applying operators to MPS and are defined as

$$\hat{O} = \sum_{\sigma_1,\ldots,\sigma_L} \sum_{\sigma'_1,\ldots,\sigma'_L} W^{\sigma_1,\sigma'_1} \ldots W^{\sigma_L,\sigma'_L} \, |\sigma_1, \ldots, \sigma_L\rangle \langle \sigma'_1, \ldots, \sigma'_L| \,. \tag{3.8}$$

Both MPS and MPO can be represented graphically for clarity:

$M^{\sigma_1} \ldots M^{\sigma_N} =$

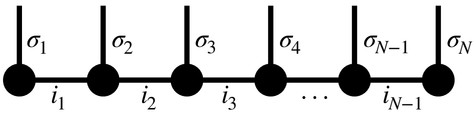

(3.9)

$$W^{\sigma_1,\sigma_1'}...W^{\sigma_L,\sigma_L'} = \qquad (3.10)$$

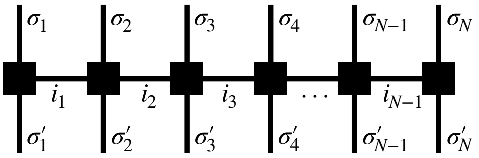

The circles (squares) represent MPS (MPO). The σ_j are called physical indices in contrast to dummy indices i_j that get *contracted* when performing the matrix multiplications. The matrices $W^{\sigma_j,\sigma_j'}$ have two physical indices, while M^{σ_j} have one physical index. Applying MPOs to MPS and calculating expectation values is graphically represented as:

$$\langle\psi_1|\psi_2\rangle = \qquad (3.11)$$

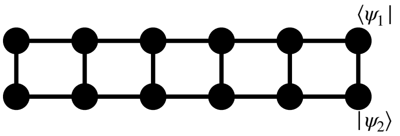

$$\hat{O}|\psi_2\rangle = \qquad (3.12)$$

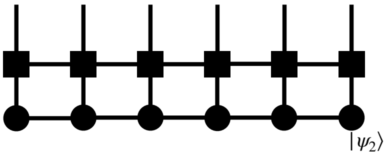

$$\langle\psi_1|\hat{O}|\psi_2\rangle = \qquad (3.13)$$

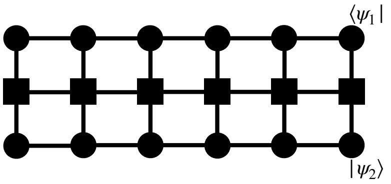

Lines connecting two tensors represent contracted indices, while lines with an open end represent open indices.

In the following, we will present two key algorithms for MPS, which we use in [P7]: the density matrix renormalization group and the time-dependent variational principle.

3.3.1 Density matrix renormalization group

The density matrix renormalization group (DMRG) is a numerical technique for finding the ground state of an MPS. It approximates the ground state by locally minimizing the variational energy

$$E = \frac{\langle\psi|\,\hat{H}\,|\psi\rangle}{\langle\psi|\psi\rangle}. \qquad (3.14)$$

Using a Lagrange multiplier λ, we can rewrite this into

$$\langle\psi|\,\hat{H}\,|\psi\rangle - \lambda\,\langle\psi|\psi\rangle\,. \qquad (3.15)$$

For a mixed-canonical MPS, we can rewrite Eq. (3.15) as

$$\langle\psi|\psi\rangle = \sum_{\sigma_j}\sum_{a_{j-1},a_j} M^{\sigma_j *}_{a_{j-1},a_j} M^{\sigma_j}_{a_{j-1},a_j} \qquad (3.16)$$

and

$$\langle\psi|\,\hat{H}\,|\psi\rangle = \sum_{\sigma_j,\sigma'_j}\sum_{a_{j-1},a_j}\sum_{a'_{j-1},a'_j}\sum_{b_{j-1},b_j} L^{a_{j-1},a'_{j-1}}_{b_{j-1}} W^{\sigma_j,\sigma'_j}_{b_{j-1},b_j} R^{a_j,a'_j}_{b_j} M^{\sigma_j *}_{a_{j-1},a_j} M^{\sigma'_j}_{a'_{j-1},a'_j}, \tag{3.17}$$

with

$$\begin{aligned} L^{a_{j-1},a'_{j-1}}_{b_{j-1}} = \sum_{\{a_i,a'_i,b_i;i<j-1\}} & \left(\sum_{\sigma_1,\sigma'_1} A^{\sigma_1 *}_{1,a_1} W^{\sigma_1,\sigma'_1}_{1,b_1} A^{\sigma'_1}_{1,a'_1}\right)\dots \\ & \dots\left(\sum_{\sigma_{j-1},\sigma'_{j-1}} A^{\sigma_{j-1}*}_{a_{j-2},a_{j-1}} W^{\sigma_{j-1},\sigma'_{j-1}}_{b_{j-2},b_{j-1}} A^{\sigma'_{j-1}}_{a'_{j-2},a'_{j-1}}\right) \end{aligned} \tag{3.18}$$

and

$$\begin{aligned} R^{a_j,a'_j}_{b_j} = \sum_{\{a_i,a'_i,b_i;i>j\}} & \left(\sum_{\sigma_{j+1},\sigma'_{j+1}} B^{\sigma_{j+1}*}_{a_j,a_{j+1}} W^{\sigma_{j+1},\sigma'_{j+1}}_{b_j,b_{j+1}} B^{\sigma'_{j+1}}_{a'_j,a'_{j+1}}\right)\dots \\ & \dots\left(\sum_{\sigma_L,\sigma'_L} B^{\sigma_L *}_{a_{L-1},1} W^{\sigma_L,\sigma'_L}_{b_{L-1},1} B^{\sigma'_L}_{a'_{L-1},1}\right). \end{aligned} \tag{3.19}$$

We optimize the local matrices M, the optimization reads

$$\frac{\partial}{\partial M^{\sigma_j *}_{a_{j-1},a_j}}\left(\langle\psi|\,\hat{H}\,|\psi\rangle - \lambda\,\langle\psi|\psi\rangle\right) \overset{!}{=} 0, \tag{3.20}$$

or equally

$$\sum_{\sigma_j,\sigma'_j}\sum_{a'_{j-1},a'_j}\sum_{b_{j-1},b_j} L^{a_{j-1},a'_{j-1}}_{b_{j-1}} W^{\sigma_j,\sigma'_j}_{b_{j-1},b_j} R^{a_j,a'_j}_{b_j} M^{\sigma'_j}_{a'_{j-1},a'_j} - \lambda M^{\sigma_j}_{a_{j-1},a_j} = 0. \tag{3.21}$$

This is an eigenvalue equation for M, and the ground state energy is given by the smallest eigenvalue. To solve it, we apply *large sparse eigensolvers*, such as the Lanczos method or Jacobi-Davidson methods.

The DMRG algorithm starts from an initial state, which is often chosen randomly. The algorithm then optimizes local matrices one at a time, as in the pictorial representation of Eq. (3.21)

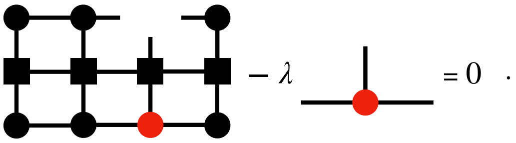

(3.22)

After updating a local matrix, an SVD/QR is applied, after which the next matrix is updated. This procedure is repeated until the user-defined convergence criteria are reached for all observables of interest.

3.3.2 Time-Dependent Variational Principle

The time-dependent variational principle (TDVP) [121, 122] is one of the most successful time-evolution algorithms for MPS. In this section, we follow the review on MPS time evolution algorithms by Paeckel *et al.* [123].

We define a projector, which projects onto the tangent space (spanned by the variations of single MPS tensors):

$$\hat{\mathcal{P}}_{T_{|\psi\rangle}} = \sum_{j=1}^{L} \hat{\mathcal{P}}^{\mathrm{L},|\psi\rangle}_{j-1} \otimes \mathbf{1}_j \otimes \hat{\mathcal{P}}^{\mathrm{R},|\psi\rangle}_{j+1} - \sum_{j=1}^{L-1} \hat{\mathcal{P}}^{\mathrm{L},|\psi\rangle}_{j} \otimes \hat{\mathcal{P}}^{\mathrm{R},|\psi\rangle}_{j+1}, \tag{3.23}$$

and define left/right projectors

$$\hat{\mathcal{P}}^{\mathrm{L},|\psi\rangle}_{j;\overline{\sigma}_1,\ldots,\overline{\sigma}_j,\sigma_1,\ldots,\sigma_j} = \sum_{m_j} \overline{\psi}^{\mathrm{L};\overline{\sigma}_1,\ldots,\overline{\sigma}_j}_{j;m_j} \otimes \psi^{\mathrm{L};\sigma_1,\ldots,\sigma_j}_{j;m_j} \tag{3.24}$$

$$\hat{\mathcal{P}}^{\mathrm{R},|\psi\rangle}_{j;\overline{\sigma}_j,\ldots,\overline{\sigma}_L,\sigma_j,\ldots,\sigma_L} = \sum_{m_{j-1}} \overline{\psi}^{\mathrm{R};\overline{\sigma}_j,\ldots,\overline{\sigma}_L}_{j;m_{j-1}} \otimes \psi^{\mathrm{R};\sigma_j,\ldots,\sigma_L}_{j;m_{j-1}}. \tag{3.25}$$

We further use the notation

$$|\psi\rangle = \sum_{\sigma_1,\ldots,\sigma_L,m_{j-1},m_j} \underbrace{A_1^{\sigma_1}\ldots A_{j-1}^{\sigma_{j-1}}}_{\equiv\psi^{\mathrm{L},\sigma_1,\ldots,\sigma_{j-1}}_{j-1;m_{j-1}}} M_{j;m_{j-1},m_j} \underbrace{B_{j+1}^{\sigma_{j+1}}\ldots B_L^{\sigma_L}}_{\equiv\psi^{\mathrm{R},\sigma_{j+1},\ldots,\sigma_L}_{j+1;m_j}} |\sigma_1,\ldots,\sigma_L\rangle \tag{3.26}$$

for the left- and right-normalized parts of the MPS.

We now solve the time-dependent Schrödinger equation in the tangent space:

$$\begin{aligned}\frac{\partial}{\partial t}|\psi\rangle &= -i\hat{\mathcal{P}}_{T_{|\psi\rangle}}\hat{H}|\psi\rangle \\ &= -i\sum_{j=1}^{L} \hat{\mathcal{P}}^{\mathrm{L},|\psi\rangle}_{j-1} \otimes \mathbf{1}_j \otimes \hat{\mathcal{P}}^{\mathrm{R},|\psi\rangle}_{j+1}\hat{H}|\psi\rangle + i\sum_{j=1}^{L-1} \hat{\mathcal{P}}^{\mathrm{L},|\psi\rangle}_{j} \otimes \hat{\mathcal{P}}^{\mathrm{R},|\psi\rangle}_{j+1}\hat{H}|\psi\rangle.\end{aligned} \tag{3.27}$$

We can approximately solve Eq. (3.27) by sequentially solving each term individually, resulting in L forward-evolving equations

$$\frac{\partial}{\partial t}|\psi\rangle = -i\hat{\mathcal{P}}^{\mathrm{L},|\psi\rangle}_{j-1} \otimes \mathbf{1}_j \otimes \hat{\mathcal{P}}^{\mathrm{R},|\psi\rangle}_{j+1}\hat{H}|\psi\rangle \tag{3.28}$$

and in $L-1$ backward-evolving equations

$$\frac{\partial}{\partial t}|\psi\rangle = +i\hat{\mathcal{P}}^{\mathrm{L},|\psi\rangle}_{j} \otimes \hat{\mathcal{P}}^{\mathrm{R},|\psi\rangle}_{j+1}\hat{H}|\psi\rangle. \tag{3.29}$$

Applying the single-site map $\overline{\psi}^{\mathrm{L}}_{j-1}\otimes\overline{\psi}^{\mathrm{R}}_{j+1}$ or the center-bond map $\overline{\psi}^{\mathrm{L}}_{j}\otimes\overline{\psi}^{\mathrm{R}}_{j+1}$ gives local Schrödinger equations of the form

$$\frac{\partial}{\partial t}M_j = -i\hat{H}^{\mathrm{eff}}_j M_j, \tag{3.30}$$

$$\frac{\partial}{\partial t} C_{j'} = +i \hat{H}^{\text{eff}}_{j'} C_{j'}. \tag{3.31}$$

We can use a Krylov time evolution to solve them.

3.4 Publication 7: Emergent spinon-holon Feshbach resonance in a doped Majumdar-Ghosh model

In this section, the following publication is reprinted:

P7 *Emergent spinon-holon Feshbach resonance in a doped Majumdar-Ghosh model*,
Simon M. Linsel, Ulrich Schollwöck, Annabelle Bohrdt, and Fabian Grusdt,
Physical Review B **111**, 054430 (2025), ©2025 American Physical Society,
doi: 10.1103/PhysRevB.111.054430.
Reprinted on pages 153–160.

PHYSICAL REVIEW B **111**, 054430 (2025)

Emergent spinon-holon Feshbach resonance in a doped Majumdar-Ghosh model

Simon M. Linsel,[1,2,3,*] Ulrich Schollwöck,[1,2] Annabelle Bohrdt,[2,4] and Fabian Grusdt[1,2,†]
[1]*Department of Physics and Arnold Sommerfeld Center for Theoretical Physics (ASC), Ludwig-Maximilians-Universität München, Theresienstr. 37, D-80333 München, Germany*
[2]*Munich Center for Quantum Science and Technology (MCQST), Schellingstr. 4, D-80799 München, Germany*
[3]*Department of Physics, Harvard University, Cambridge, Massachusetts 02138, USA*
[4]*Institute of Theoretical Physics, University of Regensburg, D-93053, Germany*

(Received 21 June 2024; revised 12 August 2024; accepted 11 February 2025; published 19 February 2025)

Experimental and numerical spectroscopy have revealed rich physics in antiferromagnets, in particular in frustrated and doped systems. The Majumdar-Ghosh (MG) model has an analytically known spin-disordered ground state of dimerized singlets as a result of magnetic frustration. Here we study the single-hole angle-resolved photoemission spectrum (ARPES) of a doped MG model, where we introduce a spin-hole interaction that is experimentally accessible with ultracold molecules. We report a bound spinon-holon ground state and clear signatures of a spinon-holon molecule state and polarons in the ARPES spectrum at different magnetizations. Moreover, we find signatures of an emergent Feshbach resonance with tunable interactions associated with the unbinding of the spinon and the holon. Our results provide new insights into the physics of dopants in frustrated t-J models and establish the latter as a new platform for studies of emergent few-body phenomena.

DOI: 10.1103/PhysRevB.111.054430

I. INTRODUCTION

The resonating valence bond theory (RVB), developed by Anderson and Fazekas [1,2], describes a quantum spin liquid (QSL) on a triangular lattice with featureless constituents: holons and spinons. Historically, RVB was proposed to describe high-temperature superconductivity in the 2D Hubbard model [3–5]. While the RVB paradigm is still widely applied for describing spin liquids, in the context of doped antiferromagnets theories with confined phases or nontrivial constituents have emerged in recent years. A prominent example are fractionalized Fermi liquids (FL*) [6,7], often studied in the context of doped quantum dimer models [8]. This parton picture is in line with microscopic studies of doped holes [9] and hole pairs [10] in t-J and Hubbard models.

Feshbach resonances have originally been introduced in the context of particle physics, where slow-moving colliding particles undergo resonant scattering [11]. Since then, Feshbach resonances have been widely used to realize tunable interactions in cold-atom experiments [12–15] and 2D semiconductors [16,17]. Recently, Feshbach resonances have further been proposed as a possible pairing mechanism for high-temperature superconductivity in cuprates [18–20].

In this paper, we report Feshbach-like resonant interactions upon tuning across the spinon/holon unbinding in a paradigmatic doped frustrated quantum magnet. We study the doped Majumdar-Ghosh model [21,22] extended by spin-hole interactions that can be realized, e.g., by ultracold polar molecules [23,24], serving as a toy model relevant for other settings featuring spinon-holon bound states. The resonant spinon-holon interactions we reveal are directly probed by varying the density of unpaired spinons. Using matrix product states (MPS), we study the ground state properties and calculate the single-hole ARPES spectrum. In addition to the Feshbach-like resonance, we find a rich set of emergent few-body states realized in the doped MG model. Our results have possible implications for the physics of cuprates in the pseudogap regime.

II. DOPED MAJUMDAR-GHOSH MODEL

We study the frustrated Hamiltonian

$$\hat{\mathcal{H}} = -t\sum_{\langle i,j\rangle,\sigma}\hat{\mathcal{P}}_{\mathrm{GW}}[\hat{c}^{\dagger}_{i,\sigma}\hat{c}_{j,\sigma}+\mathrm{H.c.}]\hat{\mathcal{P}}_{\mathrm{GW}} + J\sum_{j=1}^{N}\hat{\boldsymbol{S}}_j\cdot\hat{\boldsymbol{S}}_{j+1} + \frac{J}{2}\sum_{j=1}^{N}\hat{\boldsymbol{S}}_j\cdot\hat{\boldsymbol{S}}_{j+2} - g\sum_{\langle i,j\rangle}[\hat{n}^{\mathrm{h}}_i\hat{S}^z_j+\mathrm{H.c.}] \tag{1}$$

on the triangular ladder, see Fig. 1, where $\hat{c}_{j,\sigma}$ is a fermionic annihilation operator on site j with spin $\sigma \in \{\uparrow,\downarrow\}$, $\hat{\boldsymbol{S}}_j$ is the spin operator and $\hat{n}^{\mathrm{h}}_j = \prod_\sigma(1-\hat{c}^{\dagger}_{j,\sigma}\hat{c}_{j,\sigma})$ is the hole density. It includes the bare Majumdar-Ghosh model featuring Heisenberg interactions between nearest neighbors (NN) and next-nearest neighbors (NNN) $\propto J$. We allow NN hopping of

---

[*] Contact author: simon.linsel@lmu.de

[†] Contact author: fabian.grusdt@lmu.de

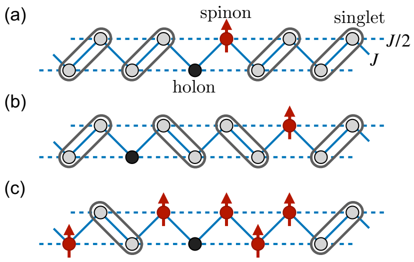

FIG. 1. Spinon-holon bound state in the doped Majumdar-Ghosh model. The bare Majumdar-Ghosh model features a ground state of dimerized spin singlets. We illustrate (a) a bound and (b) an unbound spinon-holon state in the Majumdar-Ghosh model with one hole. (c) We show a Majumdar-Ghosh model with one hole and high magnetization. The unpaired spinons form a Luttinger liquid.

fermions $\propto t$; here $\hat{\mathcal{P}}_{\text{GW}}$ denotes the Gutzwiller projector on states with no more than one fermion per site. In addition, we add a spin-hole interaction $\propto g$ that can be experimentally realized using, e.g., ultracold polar molecules [23,24], ultracold atoms [25], or in Rydberg tweezer arrays [26]. We set $t = J$; this choice is not particularly special.

We microscopically simulate the system using MPS and apply the density-matrix renormalization group (DMRG) [27] to calculate the ground state (GS). Time evolutions of the MPS are obtained using generalized subspace expansion (GSE) [28] for the first few time steps and then using the two-site time-dependent variational principle (TDVP2) [29]. In addition, we use linear extrapolation to improve the quality of the ARPES spectrum [30]. We enforce a global $U(1)\otimes U(1)$ symmetry of the hole number and the magnetization $m = 2\langle\sum_j \hat{S}^z_j\rangle/L$. The magnetization is always positive in this paper. We use the SYTEN toolkit [31].

A. Spinon-holon Feshbach resonance

The undoped Majumdar-Ghosh model, i.e., Hamiltonian (1) at $\hat{n}^{\text{h}}_j = 0$, features a GS of dimerized singlets, see Fig. 1. We dope one hole into the system and set the magnetization to a small but nonzero value, i.e., we have some unpaired spinons in the system that are not bound in a singlet. Consequently, the GS of this doped and magnetized system is translationally invariant. By tuning the microscopic spin-hole interaction $\propto g$, we can realize both an unbound and a bound regime, in which a spinon-holon bound state forms. The existence of the bound state itself is very natural and we will study the microscopic details later; for now, it is only important that its existence can be controlled via g.

This brings us to the central idea put forward in this paper. We propose that the *unbinding transition* of the spinon-holon bound state is associated with a *Feshbach-type resonance* with resonantly enhanced scattering.

To reveal signatures of such resonantly enhanced spinon-holon interactions, we consider a system at finite magnetization. For the moment, let us *assume* a Feshbach-like resonance, in which the spinon and the holon undergo two-body scattering: the interaction energy near the transition is given by

$$\hat{\mathcal{H}}_{\text{int}} \sim -g_{\text{eff}}(g)\,\hat{n}^{\text{h}}\langle\hat{n}^S\rangle, \tag{2}$$

where $g_{\text{eff}}(g)$ is the resonantly enhanced effective interaction that depends on the bare coupling g and $\hat{n}^S$ is the unpaired spinon density. Here we employed a mean-field ansatz, replacing the unpaired spinon density by its average, i.e., $\hat{n}^S \to \langle\hat{n}^S\rangle = m$. Thus increasing m leads to a stronger interaction energy shift in the system. This situation resembles a 1D Fermi polaron problem [32], where the holon corresponds to an impurity. The unpaired spinons around the holon form a Luttinger liquid and "dress" the holon in the following sense: The attractive (repulsive) polaron is a holon that is surrounded by ↑ spinons (singlets). Since the unpaired spinons are mutually hard-core, we expect the polarons to resemble 1D Fermi polarons.

In order to extract $g_{\text{eff}}(g)$, we start by tuning g, m and searching for Fermi polaron signatures in the one-hole ARPES spectrum

$$A_\sigma(k,\omega) = \frac{1}{2\pi}\text{Re}\int_{-\infty}^{\infty} \text{d}t\, e^{i\omega t}\langle\psi_0|e^{i\hat{\mathcal{H}}t}\hat{c}^\dagger_{k,\sigma}e^{-i\hat{\mathcal{H}}t}\hat{c}_{k,\sigma}|\psi_0\rangle, \tag{3}$$

where $|\psi_0\rangle$ is the GS without holes. We calculate the full one-hole ARPES spectrum, thus going beyond mean-field theory. In addition to Fermi polaron-like branches, whose energy we will model by Eq. (2) to extract $g_{\text{eff}}(g)$, the spectrum reveals a rich set of few-body states, e.g., molecular spinon-holon states. First, we will focus on the polaron branches as they are immediately relevant to establish proof of the Feshbach resonance; however, we will discuss the other branches later.

We fix $ka = 1.0$ (corresponding approximately to the GS of the one-hole dispersion; a is the lattice constant) and plot the majority ($\sigma = \uparrow$) ARPES spectrum with respect to g for different magnetizations m; our result for $m = 37/81$ is shown in Fig. 2(a). Indeed, we identify two branches with attractive and repulsive Fermi polaron characters, respectively. The attractive Fermi polaron has a negative energy compared to the zero-hole GS energy $E_0 \equiv 0$. It has a particularly large spectral weight in the *repulsive* region ($g < 0$) of the bare coupling g. This is in line with the Feshbach picture: A repulsive bare interaction corresponds to a strong resonantly enhanced effective attractive interaction and vice versa, giving rise to the existence of the two polaron branches.

As a side note, the attractive polaron might still exist deep in the attractive region $g > 0$ while the repulsive polaron will typically decay because of its high energy compared to the GS. The repulsive Fermi polaron has a positive energy and a large spectral weight for attractive bare interactions ($g > 0$). In Fig. 2(a), we only fit the peak positions (blue lines) in the parts of the two polaron branches with high spectral weight.

We repeat these calculations for different magnetizations and show the fitted peak positions of the polaron branches in Fig. 2(b). We clearly observe a *repulsion* of the attractive/repulsive branches with increasing m, as expected from Eq. (2), thus strongly suggesting a resonantly enhanced

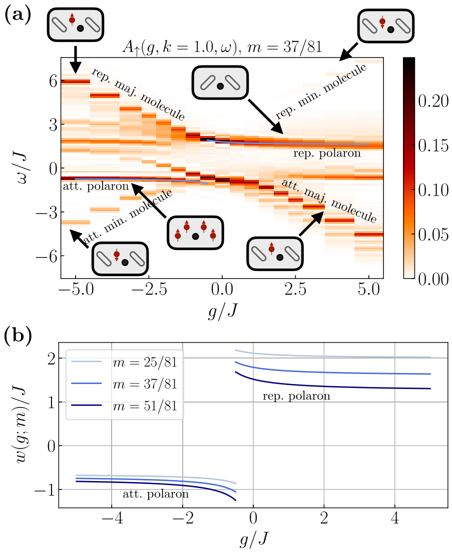

FIG. 2. Emergent Feshbach-like interaction. We perform microscopic MPS simulations of the single-hole ARPES spectrum Eq. (3) of Hamiltonian (1). Details of the MPS calculations can be found in Appendix A. (a) We show the one-hole majority ARPES spectrum $A_\uparrow$ (i.e., we remove an ↑-spinon and probe the time evolution of the resulting hole) at fixed momentum $ka = 1.0$ (corresponding approximately to the GS of the one-hole dispersion; a is the lattice constant) for $L = 81$ and magnetization $m = 37/81$. We find signatures of attractive/repulsive Fermi polarons. We probe the Feshbach resonance by tuning the density of unpaired spinons (m) and extracting the peak positions $\omega(g; m)$ of the polaron branches, see (b). The polaron branches repel each other for increasing m, signaling a resonantly enhanced interaction.

Feshbach interaction at $g_c \approx -0.5$ ($J \equiv 1$). We find that the fitted peak positions of the polaron branches indeed satisfy Eq. (2) with $g_{\text{eff}}(g) \sim g_{\text{bg}} - 1/g$ and $g_{\text{eff}}(g_c) = 2.7 \times |g_c|$, i.e., a *weak*, *repulsive* microscopic g corresponds to a *strong*, *attractive* $g_{\text{eff}}(g)$, see Appendix B.

We will discuss the microscopic details of the spinon-holon bound state next, after making one more remark: the Feshbach resonance is connected to the unbinding of a spinon-holon pair, our ARPES calculation is just a way to *probe* it. In fact, we argue that Feshbach resonances might be more generally prevalent in scenarios where partons form bound states, e.g., in the context of FL-FL* transitions [6,7]: in the FL* phase, deconfined spinons and holons exist but the relevant charge carriers at low energies are constituted by bound pairs of spinons and holons, yielding electron-like quantum numbers.

B. Free molecule limit

We study the microscopic structure of the bound spinon-holon state at minimal magnetization, i.e., with only one hole and one unpaired spinon in the system. To study the effect of tuning the spin-hole interaction $\propto g$, we calculate the QP weight

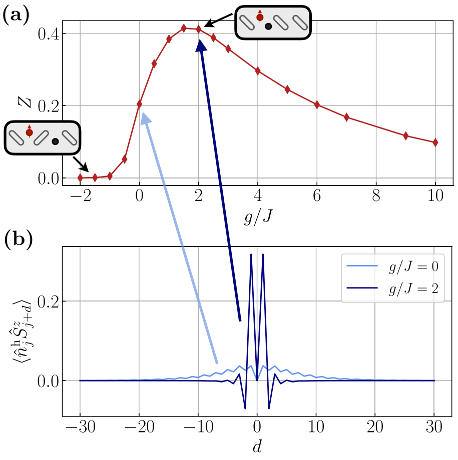

FIG. 3. Spinon-holon bound state signatures. We show the effect of tuning the interaction g in the DMRG ground state of Hamiltonian (1). (a) We show the quasiparticle weight $Z(g)$. We observe a maximum around $g/J = 2$, where sizable values $Z \sim 0.4$ are realized. (b) We show the spin-hole correlator $\langle \hat n^h_j \hat S^z_{j+d}\rangle$ averaged over the system. For $g = 0(2)$, we observe a bound spinon-holon state which extends over approximately 20 (a few) sites, i.e., the size of the bound state decreases with increasing Z.

$$Z = \sum_j \left|\langle \psi_0^{1\text{h}}|\hat c_{j,\downarrow}|\psi_0^{0\text{h}}\rangle\right|^2, \tag{4}$$

where $|\psi_0^{0(1)\text{h}}\rangle$ is the DMRG GS with zero (one) holes at $m = 0(1/2)$. It includes the MPS overlap between the one-hole DMRG GS and the undoped GS in which we put a spinon directly next to a holon (by removing one spin from a singlet). Thus Z probes the existence of a spinon-holon bound state. Note that in contrast to the ARPES simulations, here we use an even system size of $L = 80$. We perform a scan over $-2 \leqslant g/J \leqslant 10$ and plot Z in Fig. 3(a). Z is zero for $g/J \ll -1$ and features a maximum around $g/J = 2$, where sizable values $Z \sim 0.4$ are realized. This confirms the formation of a spinon-holon bound state for $g > 0$. Interestingly, the bare interaction g at the approximate location of the resonance coincides with the transition from the unbound to the bound regime in the free molecule limit, see Fig. 3(a), which is consistent with the bare interaction g driving the transition.

To study the microscopic structure of the bound state further, we calculate the spin-hole correlator $\langle \hat n^h_j \hat S^z_{j+d}\rangle$ for $g/J = 0$ and 2. For $g/J = 0$, we observe a large bound state that extends over approximately 20 lattice sites, still well below the system size $L = 80$. The size of the bound state decreases significantly down to a few lattice sites for $g/J = 2$. Thus

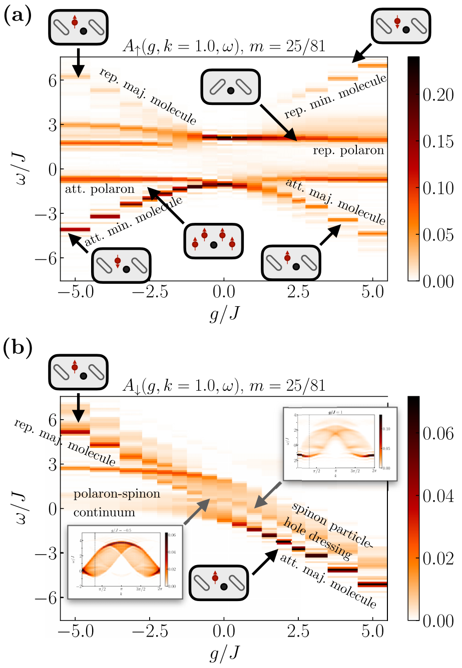

FIG. 4. Majority and minority ARPES spectrum. We perform microscopic MPS simulations of the single-hole ARPES spectrum Eq. (3) of Hamiltonian (1) at fixed momentum $k = 1.0$ for $L = 81$ and magnetization $m = 25/81$. We tune the spin-hole interaction $\propto g$ and show the ARPES spectrum at different interactions. ARPES spectra for other m can be found in Appendix B. (a) We show the majority spectrum $A_\uparrow$. The linear branches represent the majority/minority spinon-holon molecule states, which can be attractively/repulsively bound, respectively. (b) We show the minority spectrum $A_\downarrow$. The minority molecule is not visible due to vanishing spectral weight. In addition to the molecule branches, we observe a polaron-spinon continuum signaled by a cosine dispersion of the momentum-dependent ARPES (see lower left inset), and spinon-particle hole dressing signaled by a continuum of states above the attractive majority molecule ground state (see upper right inset).

the existence and the size of a bound spinon-holon state are directly tunable by g/J.

C. Emergent few-body physics

The calculated ARPES spectra feature not only Fermi polarons but also a rich set of further branches, some of which we will identify here. We show the majority ($\sigma = \uparrow$) ARPES spectrum for different spin-hole interactions $\propto g$ at $m = 25/81$ in Fig. 4(a). In addition to the Fermi polarons, we identify four branches where a spinon and the holon form a molecular state, signaled by a linear dependence of the energy $E \sim \pm|g|$. We call the state where the holon binds to a ↑ spinon (↓ spinon) a majority (minority) molecule. Both molecule types can be either attractively (negative energy) or repulsively (positive energy) bound. A repulsively bound molecule is an excited state that can be long-lived due to a lack of low-order resonant decay processes.

We show the minority ($\sigma = \downarrow$) ARPES spectrum for different spin-hole interactions $\propto g$ at $m = 25/81$ in Fig. 4(b). In addition to the attractive and repulsive majority molecule, we observe a polaron-spinon continuum enclosed by a cosine dispersion in the momentum-dependent ARPES spectrum at fixed g/J, see inset of Fig. 4(b). Further, we observe spinon particle-hole dressing as a continuum of excited states above the attractive majority molecule, where the interaction between the impurity (i.e., the holon) with the Luttinger liquid results in particle-hole excitations (i.e., collective excitations of spinons). Attentive readers may have noticed that the minority molecule and the Fermi polarons are not visible in the minority spectrum. This is due to their low spectral weight as a result of vanishing wave function overlaps in the ARPES spectrum, as we discuss further in Appendix B. More detailed studies of the molecular branches and the other few-body excitations not discussed here are tasks left for future research.

III. CONCLUSION

We have investigated a doped Majumdar-Ghosh model as a paradigmatic frustrated quantum magnet. The model can be experimentally implemented using, e.g., ultracold dipolar molecules [23,24], and for $g = 0$ using ultracold fermions in quantum gas microscopes [33–38]. Using ARPES based on MPS, we have found signatures of a spinon-holon Feshbach-like resonance which can be probed by tuning the density of unpaired spinons (i.e., magnetization). We have also found emergent few-body physics in the ARPES spectra, including different (partly repulsively bound) molecular branches of a spinon and a holon.

Our results suggest wider applicability of this emergent Feshbach-like resonance to study the physics of superconducting phases or parton unbinding. It is potentially relevant to clarify the physics of doped quantum spin liquids and has potential applications in the context of heavy electrons [39,40] and cuprates.

ACKNOWLEDGMENTS

We thank T. Blatz, M. Grundner, L. Homeier, M. Kebrič, N. Mostaan, S. Paeckel, F. Palm, H. Schlömer, and Y. Tan for fruitful discussions. This research was funded by the European Research Council (ERC) under the European Union's Horizon 2020 research and innovation program (Grant Agreement No. 948141) — ERC Starting Grant SimUcQuam, and by the Deutsche Forschungsgemeinschaft (DFG, German Research Foundation) under Germany's Excellence Strategy – EXC-2111 – 390814868.

APPENDIX A: CALCULATING THE ARPES SPECTRUM & MPS CONVERGENCE

We perform microscopic MPS simulations of Hamiltonian (1) for magnetization $m = 13/81, 25/81, 37/81, 51/81$

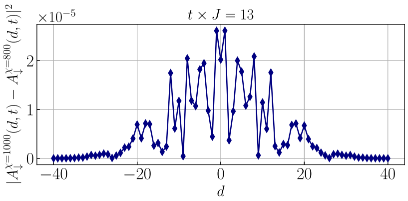

FIG. 5. MPS time evolution convergence. We show the difference of the minority Green's function $A_\downarrow(d,t) = \langle e^{i\hat{\mathcal{H}}t}\, \hat{c}^\dagger_{L/2+d}\, e^{-i\hat{\mathcal{H}}t}\, \hat{c}_{L/2}\rangle$ evaluated at bond dimensions $\chi = 800$ and 1000, at time $t = 13/J$. We exponentially suppress times after $t = 40/3J$ with a Gaussian $w(t) = \exp(-2(t/t_0)^2)$ where $t_0 = 20/3J$. The difference is $\sim 10^{-5}$, thus the time evolution is well converged.

and spin-hole interaction $-5 \leqslant g/J \leqslant 5$. Note that in our convention $m = 2\langle \sum_j \hat{S}^z_j\rangle/L > 0$, i.e., each spin contributes $\pm 1/L$ to m. Our procedure is similar to [41] but here we use the SYTEN toolkit [31]. To probe signatures of Feshbach-like resonances, we calculate the majority ($\sigma = \uparrow$) and minority ($\sigma = \downarrow$) ARPES spectrum Eq. (3):

$$A_\sigma(k,\omega) = \frac{1}{2\pi}\mathrm{Re}\int_{-\infty}^{\infty} dt\, e^{i\omega t} A_\sigma(k,t),$$

where

$$A_\sigma(k,t) = \frac{1}{L}\sum_{i,j} e^{-ik(i-j)}\langle\psi_0|e^{i\hat{\mathcal{H}}t}\hat{c}^\dagger_{j,\sigma}e^{-i\hat{\mathcal{H}}t}\hat{c}_{i,\sigma}|\psi_0\rangle.$$

First, we calculate the MPS groundstate (GS) $|\psi_0\rangle$ without holes using DMRG with bond dimension $\chi = 1000$. The GS is well converged with variance $\langle\hat{\mathcal{H}}^2\rangle - \langle\hat{\mathcal{H}}\rangle^2 < 10^{-11}$.

Then, we dope a hole into the system and calculate the time evolution up to times $t = 20/J$ using generalized subspace expansion (GSE) [28] for the first few time steps and then using the two-site time-dependent variational principle (TDVP2) [29] for later times. We choose the time step $\Delta t = 0.02/J$. In Fig. 5, we compare the minority Green's function $\langle e^{i\hat{\mathcal{H}}t}\, \hat{c}^\dagger_{L/2+d}\, e^{-i\hat{\mathcal{H}}t}\, \hat{c}_{L/2}\rangle$ for bond dimensions $\chi = 800$ and 1000, at time $t = 13/J$. The difference is $\sim 10^{-5}$, thus the time evolution is well converged. We calculate the MPS overlap with the original GS $|\psi_0\rangle$.

Next, we perform a Fourier transform into momentum space to obtain $A_\sigma(k,t)$. To prevent unphysical oscillations in the time Fourier transform resulting from a cutoff at $t = 20/J$, we apply linear extrapolation [30]. As a tradeoff between the error of the TDVP2 time evolution and the error of extrapolating the signal, we choose to suppress parts of our original signal and the complete extrapolated signal. We exponentially suppress times after $t = 40/3J$ with a Gaussian $w(t) = \exp(-2(t/t_0)^2)$ where $t_0 = 20/3J$.

Finally, we perform a time Fourier transform into energy space which grants us access to the full ARPES spectrum $A_\sigma(k,\omega)$.

APPENDIX B: ARPES SPECTRA

In Fig. 6, we show the interaction-dependent majority [$\sigma = \uparrow$, Figs. 6(a)–6(d)] and minority [$\sigma = \downarrow$, Figs. 6(e)–6(h)] ARPES spectra at fixed momentum $k = 1.0$ at different magnetizations. We label branches according to their qualitative behavior and illustrate the fitting of the polaron branches (see below). Here we also briefly discuss the spectral weights of the polaron and the molecular branches.

The minority molecule is not visible in the minority spectrum because of its vanishing spectral weight. We remove a ↓ spinon from a GS where practically all ↓ spinons are bound in singlets, see Figs. 6(e)–6(h). Conversely, the majority molecule ARPES weight increases for increasing m since we have more free ↑-spinons in the GS. This is especially relevant for the majority spectrum where the entire majority molecule spectral weight originates from free ↑ spinons in the GS, see Figs. 6(a)–6(d).

The polaron branches are very dominant in the highly magnetized majority spectrum because of a high chance to remove a free ↑ spinon. Vice versa, in a highly magnetized minority spectrum, the removal of a down spin will break a singlet; the holon and the adjacent ↑ spinon form a molecule, resulting in a vanishing polaron spectral weight.

We set $J = 1$ for convenience and fit the attractive/repulsive polaron branches using the ansatz

$$E_{\mathrm{a/r}}(g,m) = \frac{A_{\mathrm{a/r}}}{g - g_{\mathrm{c,a/r}}} \times m + B_{\mathrm{a/r}}(m), \tag{B1}$$

where crucially $A_{\mathrm{a/r}}$ and $g_{\mathrm{c,a/r}}$ are independent of the magnetization. We find good agreement with $g_{\mathrm{c,a}} = 0.2$, $g_{\mathrm{c,r}} = -1.3$, and $A_{\mathrm{a}} = A_{\mathrm{r}} = 0.56$, the fits are the blue curves in Figs. 6(a)–6(c).

We can estimate the location of the Feshbach resonance as

$$g_c = \frac{g_{\mathrm{c,a}} + g_{\mathrm{c,r}}}{2} = -0.55, \tag{B2}$$

which is in good agreement with Fig. 2(b). $g_{\mathrm{eff}}(g_c)$ can be estimated from Eq. (2) as

$$\begin{aligned} g_{\mathrm{eff}}(g_c) &= \frac{\langle\hat{\mathcal{H}}_{\mathrm{int}}\rangle}{m \times \langle\hat{n}^{\mathrm{h}}\rangle} \\ &= \frac{E_{\mathrm{r}}(g_{\mathrm{c}},m) - E_{\mathrm{r}}(g \to \infty, m)}{m \times \langle\hat{n}^{\mathrm{h}}\rangle} \\ &\quad - \frac{E_{\mathrm{a}}(g_{\mathrm{c}},m) - E_{\mathrm{a}}(g \to -\infty, m)}{m \times \langle\hat{n}^{\mathrm{h}}\rangle} \\ &= \frac{4A_{\mathrm{a}}}{[g_{\mathrm{c,a}} - g_{\mathrm{c,r}}] \times \langle\hat{n}^{\mathrm{h}}\rangle} \\ &\approx 1.5 \approx 2.7 \times |g_{\mathrm{c}}|, \end{aligned} \tag{B3}$$

thus confirming that the effective interaction we find is Feshbach-like, i.e., resonantly enhanced! Intuitively, the interaction energy corresponds to the bending of the polaron branches which is a direct consequence of the resonantly enhanced interaction.

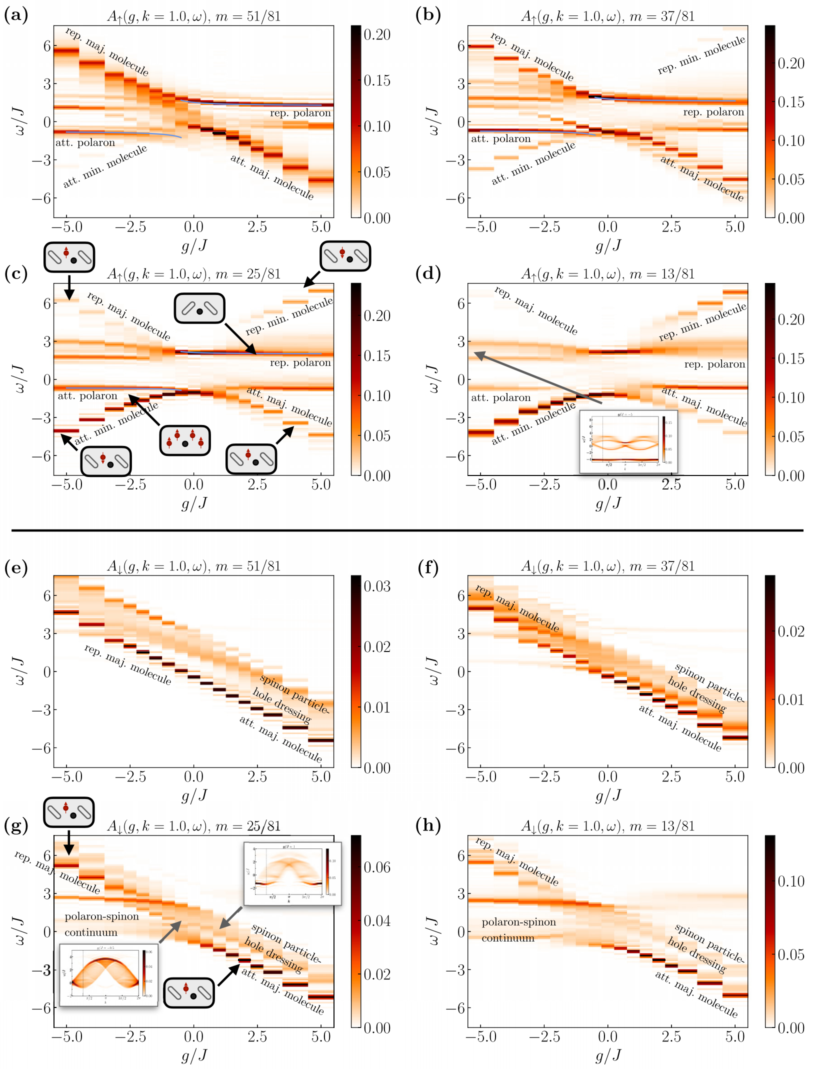

FIG. 6. ARPES spectra. We plot the majority [$\sigma = \uparrow$, (a)–(d)] and minority [$\sigma = \downarrow$, (e)–(h)] ARPES spectrum Eq. (3) of Hamiltonian (1) at fixed GS momentum $k = 1.0$ for $L = 81$ and at different magnetizations m. We label the branches according to their qualitative behavior. We fit the polaron branches using the ansatz Eq. (B1) and plot the fits in blue. We find an almost flat band for the attractive minority molecule in the inset of (d).

[1] P. Anderson, Resonating valence bonds: A new kind of insulator? Mater. Res. Bull. **8**, 153 (1973).

[2] P. Fazekas and P. W. Anderson, On the ground state properties of the anisotropic triangular antiferromagnet, Philos. Mag. **30**, 423 (1974).

[3] P. W. Anderson, The resonating valence bond state in La_2CuO_4 and superconductivity, Science **235**, 1196 (1987).

[4] G. Baskaran, Z. Zou, and P. Anderson, The resonating valence bond state and high-T_c superconductivity — a mean field theory, Solid State Commun. **63**, 973 (1987).

[5] G. Baskaran and P. W. Anderson, Gauge theory of high-temperature superconductors and strongly correlated Fermi systems, Phys. Rev. B **37**, 580 (1988).

[6] T. Senthil, S. Sachdev, and M. Vojta, Fractionalized Fermi liquids, Phys. Rev. Lett. **90**, 216403 (2003).

[7] T. Senthil, M. Vojta, and S. Sachdev, Weak magnetism and non-Fermi liquids near heavy-fermion critical points, Phys. Rev. B **69**, 035111 (2004).

[8] M. Punk, A. Allais, and S. Sachdev, Quantum dimer model for the pseudogap metal, Proc. Natl. Acad. Sci. USA **112**, 9552 (2015).

[9] A. Bohrdt, E. Demler, and F. Grusdt, Rotational resonances and regge-like trajectories in lightly doped antiferromagnets, Phys. Rev. Lett. **127**, 197004 (2021).

[10] A. Bohrdt, E. Demler, and F. Grusdt, Dichotomy of heavy and light pairs of holes in the $t-J$ model, Nat. Commun. **14**, 8017 (2023).

[11] H. Feshbach, A unified theory of nuclear reactions. II, Ann. Phys. **19**, 287 (1962).

[12] P. Courteille, R. S. Freeland, D. J. Heinzen, F. A. van Abeelen, and B. J. Verhaar, Observation of a Feshbach resonance in cold atom scattering, Phys. Rev. Lett. **81**, 69 (1998).

[13] S. Inouye, M. R. Andrews, J. Stenger, H. J. Miesner, D. M. Stamper-Kurn, and W. Ketterle, Observation of Feshbach resonances in a Bose–Einstein condensate, Nature (London) **392**, 151 (1998).

[14] I. Bloch, J. Dalibard, and W. Zwerger, Many-body physics with ultracold gases, Rev. Mod. Phys. **80**, 885 (2008).

[15] C. Chin, R. Grimm, P. Julienne, and E. Tiesinga, Feshbach resonances in ultracold gases, Rev. Mod. Phys. **82**, 1225 (2010).

[16] M. Sidler, P. Back, O. Cotlet, A. Srivastava, T. Fink, M. Kroner, E. Demler, and A. Imamoglu, Fermi polaron-polaritons in charge-tunable atomically thin semiconductors, Nat. Phys. **13**, 255 (2017).

[17] I. Schwartz, Y. Shimazaki, C. Kuhlenkamp, K. Watanabe, T. Taniguchi, M. Kroner, and A. Imamoğlu, Electrically tunable Feshbach resonances in twisted bilayer semiconductors, Science **374**, 336 (2021).

[18] R. H. Squire and N. H. March, Microscopic model of cuprate superconductivity, Int. J. Quantum Chem. **110**, 2808 (2010).

[19] L. Homeier, H. Lange, E. Demler, A. Bohrdt, and F. Grusdt, Feshbach hypothesis of high-Tc superconductivity in cuprates, Nat. Commun. **16**, 314 (2025).

[20] L. Homeier, P. Bermes, and F. Grusdt, Scattering theory of mesons in doped antiferromagnetic Mott insulators: Multichannel perspective and Feshbach resonance, Phys. Rev. B **109**, 125135 (2024).

[21] C. K. Majumdar and D. K. Ghosh, On next-nearest-neighbor interaction in linear chain. I, J. Math. Phys. **10**, 1388 (1969).

[22] C. K. Majumdar and D. K. Ghosh, On next-nearest-neighbor interaction in linear chain. II, J. Math. Phys. **10**, 1399 (1969).

[23] A. V. Gorshkov, S. R. Manmana, G. Chen, E. Demler, M. D. Lukin, and A. M. Rey, Quantum magnetism with polar alkali-metal dimers, Phys. Rev. A **84**, 033619 (2011).

[24] A. N. Carroll, H. Hirzler, C. Miller, D. Wellnitz, S. R. Muleady, J. Lin, K. P. Zamarski, R. R. W. Wang, J. L. Bohn, A. M. Rey, and J. Ye, Observation of generalized $t-J$ spin dynamics with tunable dipolar interactions, arXiv:2404.18916.

[25] P. N. Jepsen, W. W. Ho, J. Amato-Grill, I. Dimitrova, E. Demler, and W. Ketterle, Transverse spin dynamics in the anisotropic Heisenberg model realized with ultracold atoms, Phys. Rev. X **11**, 041054 (2021).

[26] L. Homeier, T. J. Harris, T. Blatz, S. Geier, S. Hollerith, U. Schollwöck, F. Grusdt, and A. Bohrdt, Antiferromagnetic bosonic $t-J$ models and their quantum simulation in tweezer arrays, Phys. Rev. Lett. **132**, 230401 (2024).

[27] U. Schollwöck, The density-matrix renormalization group in the age of matrix product states, Ann. Phys. **326**, 96 (2011).

[28] M. Yang and S. R. White, Time-dependent variational principle with ancillary Krylov subspace, Phys. Rev. B **102**, 094315 (2020).

[29] S. Paeckel, T. Köhler, A. Swoboda, S. R. Manmana, U. Schollwöck, and C. Hubig, Time-evolution methods for matrix-product states, Ann. Phys. **411**, 167998 (2019).

[30] T. Barthel, U. Schollwöck, and S. R. White, Spectral functions in one-dimensional quantum systems at finite temperature using the density matrix renormalization group, Phys. Rev. B **79**, 245101 (2009).

[31] C. Hubig, F. Lachenmaier, N.-O. Linden, T. Reinhard, L. Stenzel, A. Swoboda, M. Grundner, and S. Mardazad, The SyTen Toolkit (2024).

[32] P. Massignan, M. Zaccanti, and G. M. Bruun, Polarons, dressed molecules and itinerant ferromagnetism in ultracold Fermi gases, Rep. Prog. Phys. **77**, 034401 (2014).

[33] A. Bohrdt, L. Homeier, C. Reinmoser, E. Demler, and F. Grusdt, Exploration of doped quantum magnets with ultracold atoms, Ann. Phys. **435**, 168651 (2021).

[34] L. Tarruell and L. Sanchez-Palencia, Quantum simulation of the Hubbard model with ultracold fermions in optical lattices, C. R. Phys. **19**, 365 (2018).

[35] T. Esslinger, Fermi-Hubbard physics with atoms in an optical lattice, Annu. Rev. Condens. Matter Phys. **1**, 129 (2010).

[36] M. L. Prichard, B. M. Spar, I. Morera, E. Demler, Z. Z. Yan, and W. S. Bakr, Directly imaging spin polarons in a kinetically frustrated Hubbard system, Nature (London) **629**, 323 (2024).

[37] M. Xu, L. H. Kendrick, A. Kale, Y. Gang, G. Ji, R. T. Scalettar, M. Lebrat, and M. Greiner, Frustration- and doping-induced magnetism in a Fermi–Hubbard simulator, Nature (London) **620**, 971 (2023).

[38] J. Yang, L. Liu, J. Mongkolkiattichai, and P. Schauss, Site-resolved imaging of ultracold fermions in a triangular-lattice quantum gas microscope, PRX Quantum **2**, 020344 (2021).

[39] H. v. Löhneysen, T. Pietrus, G. Portisch, H. G. Schlager, A. Schröder, M. Sieck, and T. Trappmann, Non-Fermi-liquid behavior in a heavy-fermion alloy at a magnetic instability, Phys. Rev. Lett. **72**, 3262 (1994).

[40] H. von Löhneysen, Non-Fermi-liquid behaviour in the heavy-fermion system, J. Phys.: Condens. Matter **8**, 9689 (1996).

[41] A. Bohrdt, E. Demler, F. Pollmann, M. Knap, and F. Grusdt, Parton theory of angle-resolved photoemission spectroscopy spectra in antiferromagnetic Mott insulators, Phys. Rev. B **102**, 035139 (2020).

Chapter Four

Conclusion and outlook

In this dissertation, we numerically explored three closely connected subclasses of strongly correlated quantum systems: Frustrated quantum magnets, toric codes, and $\mathbb{Z}_2$ lattice gauge theories.

With the package ParaToric [P1], we provide the community with a state-of-the-art continuous-time QMC package for the toric code, which is relevant not only to lattice gauge theories and topology but also to quantum error correction and quantum information. The number of interfaces (C, C++, Python) and the extensive documentation in [P1] make ParaToric easy to use for non-experts. The practically achievable system sizes are unprecedented. Earlier versions of ParaToric were used in [P2, P3, P4, P5], making it the backbone of this dissertation and a strong foundation for future projects from the ParaToric user base.

In the future, we plan to extend ParaToric with more lattices like the experimentally relevant ruby lattice [124], more boundary conditions, including dangling edge bonds used to probe long-range edge correlation in SPT phases [65], and more observables such as fidelity susceptibilities and entanglement entropies, providing users with more flexibility. We also want to extend the implemented Hamiltonian with (long-range) Ising-type interactions that typically arise in the context of emergent topological order. Adding these terms would at the same time implement the (long-range) TFIM. A long-term goal is to include even more Hamiltonians in the package, especially $t-J$-type models with hopping terms. It would also be insightful to simulate toric code with higher symmetries, such as $\mathbb{Z}_n$ toric codes. This generalization is pretty straightforward, as already mentioned by [81].

In [P2, P3, P4], we have proposed a new geometric confinement order parameter for $\mathbb{Z}_2$ LGTs based on percolation theory, which is accessible to snapshot measurements from state-of-the-art quantum simulators. It outperforms competing order parameters, which either cannot be extracted from snapshots or exhibit extreme noise. In the extended toric code on the triangular, honeycomb, and cubic lattices, we have found topological phases where one anyon type is confined while the other type is deconfined. This is remarkable, given that in the literature the terms "topological" and "deconfined" are often used interchangeably at zero temperature. We have also mapped out the topological diagrams of the toric code on the aforementioned lattice for the first time with a numerically exact method, substantially improving previous approximations of the phase diagram. The percolation order parameter admits a natural extension to $\mathbb{Z}_n$ strings, consistent with the planned roadmap for ParaToric. For even higher symmetries such as $U(1)$, we speculate that defining thresholds to define whether a link contributes to percolation or not could capture confinement.

We have defined an innovative architecture for NQS in [P5], exploiting approximate symmetries that are ubiquitous in quantum spin liquids and related phases. We have demonstrated the broad applicability of the architecture by mapping out the phase diagram of a variant of the toric code with a sign-problem, and by applying it to the PXP Rydberg Hamiltonian, which hosts emergent symmetries. Since symmetries are fundamental to physics and present in practically every Hamiltonian, we expect that upgrades and variations of our architecture will be broadly applicable and help to uncover new physics, especially for Hamiltonians with sign-problems that are fundamentally inaccessible to QMC.

We have proposed a new type of SPT phase that remains stable against thermal fluctuations in [P6]. In the literature, SPT was previously widely believed to exist only at zero temperature. Our results have broad implications, particularly for finding materials that host QSL phases at finite temperature. A further significant connection concerns the pseudogap phase of the Fermi–Hubbard model: we speculate that the transition from the stripe phase to the pseudogap phase might realize a finite-temperature SPT transition protected by an $SU(2)$ symmetry. Further analytical and numerical studies are required to test this theory.

In the publication [P7], we have found signatures of magnetic polarons and a resonantly-enhanced Feshbach resonance in the one-hole ARPES spectrum obtained using MPS. This is a timely result in the context of other studies, which propose Feshbach resonances as a microscopic pairing mechanism in cuprates [125] by considering holon-holon pairs. An obvious next step is therefore to include a second hole and study not only spinon-holon bound states but also holon-holon bound states. A long-term goal is to simulate a finite hole-density; for large systems, this is numerically very challenging, even in one dimension. Another important step would be an experimental realization of the Feshbach resonance[1], see here for an experimental protocol to calculate the ARPES spectrum of one-dimensional models in quantum gas microscopes [126]. We also showed that the Feshbach resonance in the Majumdar-Ghosh model does not rely on a fine-tuned parameter point, which may simplify its experimental realization.

---

[1] Feshbach resonance are used to realize tunable interactions for cold atoms, thus a Feshbach resonance could be used to probe an emergent Feshbach resonance, which is an amusing thought.

Bibliography

[P1] S. M. Linsel and L. Pollet, “Paratoric 1.0: continuous-time quantum monte carlo for the toric code in a parallel field”, 2026, arXiv:2510.14781 [quant-ph].

[P2] S. M. Linsel, A. Bohrdt, L. Homeier, L. Pollet, and F. Grusdt, “Percolation as a confinement order parameter in $Z2$ lattice gauge theories”, Phys. Rev. B **110**, L241101 (2024).

[P3] G. Dünnweber, S. M. Linsel, A. Bohrdt, and F. Grusdt, “Percolation renormalization group analysis of confinement in $Z2$ lattice gauge theories”, Phys. Rev. B **111**, 024314 (2025).

[P4] S. M. Linsel, L. Pollet, and F. Grusdt, “Independent e- and m-anyon confinement in the parallel field toric code on non-square lattices”, PRX Quantum **7**, 010332 (2026).

[P5] D. S. Kufel, J. Kemp, D. Vu, S. M. Linsel, C. R. Laumann, and N. Y. Yao, “Approximately symmetric neural networks for quantum spin liquids”, Phys. Rev. Lett. **135**, 056702 (2025).

[P6] R. H. Wilke, H. Schlömer, S. M. Linsel, A. Bohrdt, and F. Grusdt, “Topology meets symmetry breaking: hidden order, intrinsically gapless topological states and finite-temperature topological transitions”, 2025, arXiv:2506.03146 [cond-mat.str-el].

[P7] S. M. Linsel, U. Schollwöck, A. Bohrdt, and F. Grusdt, “Emergent spinon-holon feshbach resonance in a doped majumdar-ghosh model”, Phys. Rev. B **111**, 054430 (2025).

[P8] L. Homeier, A. Bohrdt, S. Linsel, E. Demler, J. C. Halimeh, and F. Grusdt, “Realistic scheme for quantum simulation of $\mathbb{Z}_2$ lattice gauge theories with dynamical matter in (2 + 1)d”, Communications Physics **6**, 127 (2023).

[1] W. C. Wimsatt, “Reductionism and its heuristics: making methodological reductionism honest”, Synthese **151**, 445 (2006).

[2] F. C. Fang and A. Casadevall, “Reductionistic and holistic science”, Infection and Immunity **79**, 1401 (2011), eprint: https://journals.asm.org/doi/pdf/10.1128/iai.01343-10.

[3] P. W. Anderson, “More is different”, Science **177**, 393 (1972), eprint: https://www.science.org/doi/pdf/10.1126/science.177.4047.393.

[4] L. Boltzmann, “Further studies on the thermal equilibrium of gas molecules”, *The kinetic theory of gases* (), pp. 262–349, eprint: https://www.worldscientific.com/doi/pdf/10.1142/9781848161337_0015.

[5] C. R. Doering, “The 3d navier-stokes problem”, Annual Review of Fluid Mechanics **41**, 109 (2009).

[6] D. A. Bandurin, A. V. Shytov, L. S. Levitov, R. K. Kumar, A. I. Berdyugin, M. Ben Shalom, I. V. Grigorieva, A. K. Geim, and G. Falkovich, “Fluidity onset in graphene”, Nature Communications **9**, 4533 (2018).

[7] J. L. Ville, R. Saint-Jalm, É. Le Cerf, M. Aidelsburger, S. Nascimbène, J. Dalibard, and J. Beugnon, “Sound propagation in a uniform superfluid two-dimensional bose gas”, Phys. Rev. Lett. **121**, 145301 (2018).

[8] M. C. Marchetti, J. F. Joanny, S. Ramaswamy, T. B. Liverpool, J. Prost, M. Rao, and R. A. Simha, “Hydrodynamics of soft active matter”, Rev. Mod. Phys. **85**, 1143 (2013).

[9] I. Carusotto and C. Ciuti, “Quantum fluids of light”, Rev. Mod. Phys. **85**, 299 (2013).

[10] E. Shuryak, “Strongly coupled quark-gluon plasma in heavy ion collisions”, Rev. Mod. Phys. **89**, 035001 (2017).

[11] K. G. Wilson, “The renormalization group and critical phenomena”, Rev. Mod. Phys. **55**, 583 (1983).

[12] H. Georgi, “Effective field theory”, Annual Review of Nuclear and Particle Science **43**, 209 (1993).

[13] M. C. Gutzwiller, “Effect of correlation on the ferromagnetism of transition metals”, Phys. Rev. Lett. **10**, 159 (1963).

[14] J. Hubbard, “Electron correlations in narrow energy bands”, Proceedings of the Royal Society of London. A. Mathematical and Physical Sciences **276**, 238 (1963), eprint: https://royalsocietypublishing.org/rspa/article-pdf/276/1365/238/54456/rspa.1963.0204.pdf.

[15] J. Hubbard, “Electron correlations in narrow energy bands iii. an improved solution”, Proceedings of the Royal Society of London. A. Mathematical and Physical Sciences **281**, 401 (1964), eprint: https://royalsocietypublishing.org/rspa/article-pdf/281/1386/401/55044/rspa.1964.0190.pdf.

[16] J. Hubbard, “Electron correlations in narrow energy bands. ii. the degenerate band case”, Proceedings of the Royal Society of London. A. Mathematical and Physical Sciences **277**, 237 (1964), eprint: https://royalsocietypublishing.org/rspa/article-pdf/277/1369/237/54540/rspa.1964.0019.pdf.

[17] J. Kanamori, “Electron Correlation and Ferromagnetism of Transition Metals”, Progress of Theoretical Physics **30**, 275 (1963), eprint: https://academic.oup.com/ptp/article-pdf/30/3/275/5278869/30-3-275.pdf.

[18] J. G. Bednorz and K. A. Müller, “Possible high T_c superconductivity in the ba-la-cu-o system”, Zeitschrift für Physik B Condensed Matter **64**, 189 (1986).

[19] L. Rossi, “The lhc main dipoles and quadrupoles toward series production”, IEEE Transactions on Applied Superconductivity **13**, 1221 (2003).

[20] M. Manso Jimeno, J. T. Vaughan, and S. Geethanath, “Superconducting magnet designs and mri accessibility: a review”, NMR in Biomedicine **36**, e4921 (2023), eprint: https://analyticalsciencejournals.onlinelibrary.wiley.com/doi/pdf/10.1002/nbm.4921.

[21] M. Kjaergaard, M. E. Schwartz, J. Braumüller, P. Krantz, J. I.-J. Wang, S. Gustavsson, and W. D. Oliver, “Superconducting qubits: current state of play”, Annual Review of Condensed Matter Physics **11**, 369 (2020).

[22] B. Keimer, S. A. Kivelson, M. R. Norman, S. Uchida, and J. Zaanen, “From quantum matter to high-temperature superconductivity in copper oxides”, Nature **518**, 179 (2015).

[23] T. Senthil, S. Sachdev, and M. Vojta, “Fractionalized fermi liquids”, Phys. Rev. Lett. **90**, 216403 (2003).

[24] T. Senthil, M. Vojta, and S. Sachdev, “Weak magnetism and non-fermi liquids near heavy-fermion critical points”, Phys. Rev. B **69**, 035111 (2004).

[25] R. Mondaini, S. Tarat, and R. T. Scalettar, “Quantum critical points and the sign problem”, Science **375**, 418 (2022), eprint: https://www.science.org/doi/pdf/10.1126/science.abg9299.

[26] M. Qin, T. Schäfer, S. Andergassen, P. Corboz, and E. Gull, “The hubbard model: a computational perspective”, Annual Review of Condensed Matter Physics **13**, 275 (2022).

[27] P. Corboz, “Variational optimization with infinite projected entangled-pair states”, Phys. Rev. B **94**, 035133 (2016).

[28] M. Scheb and R. M. Noack, “Finite projected entangled pair states for the hubbard model”, Phys. Rev. B **107**, 165112 (2023).

[29] P. Coleman, *Introduction to many-body physics* (Cambridge University Press, 2015).

[30] L. Onsager, “Crystal statistics. i. a two-dimensional model with an order-disorder transition”, Phys. Rev. **65**, 117 (1944).

[31] H. A. Kramers and G. H. Wannier, “Statistics of the two-dimensional ferromagnet. part i”, Phys. Rev. **60**, 252 (1941).

[32] R. J. Baxter, *Exactly solved models in statistical mechanics* (ACADEMIC PRESS LIMITED, 2024/01/11 1982).

[33] A. M. Ferrenberg and D. P. Landau, “Critical behavior of the three-dimensional ising model: a high-resolution monte carlo study”, Phys. Rev. B **44**, 5081 (1991).

[34] A. M. Ferrenberg, J. Xu, and D. P. Landau, “Pushing the limits of monte carlo simulations for the three-dimensional ising model”, Phys. Rev. E **97**, 043301 (2018).

[35] M. Hasenbusch, “Finite size scaling study of lattice models in the three-dimensional ising universality class”, Phys. Rev. B **82**, 174433 (2010).

[36] A. L. Talapov and H. W. J. Blöte, “The magnetization of the 3d ising model”, Journal of Physics A: Mathematical and General **29**, 5727 (1996).

[37] R. H. Swendsen and J.-S. Wang, “Nonuniversal critical dynamics in monte carlo simulations”, Phys. Rev. Lett. **58**, 86 (1987).

[38] U. Wolff, “Collective monte carlo updating for spin systems”, Phys. Rev. Lett. **62**, 361 (1989).

[39] N. D. Mermin and H. Wagner, “Absence of ferromagnetism or antiferromagnetism in one- or two-dimensional isotropic heisenberg models”, Phys. Rev. Lett. **17**, 1133 (1966).

[40] J. M. Kosterlitz and D. J. Thouless, “Ordering, metastability and phase transitions in two-dimensional systems”, Journal of Physics C: Solid State Physics **6**, 1181 (1973).

[41] V. L. Berezinskii, “Destruction of Long-range Order in One-dimensional and Two-dimensional Systems having a Continuous Symmetry Group I. Classical Systems”, Sov. Phys. JETP **32**, 493 (1971).

[42] V. L. Berezinskii, “Destruction of Long-range Order in One-dimensional and Two-dimensional Systems Possessing a Continuous Symmetry Group. II. Quantum Systems”, Sov. Phys. JETP **34**, 610 (1972).

[43] F. D. M. Haldane, “Continuum dynamics of the 1-d heisenberg antiferromagnet: identification with the o(3) nonlinear sigma model”, Physics Letters A **93**, 464 (1983).

[44] F. D. M. Haldane, “Nonlinear field theory of large-spin heisenberg antiferromagnets: semiclassically quantized solitons of the one-dimensional easy-axis néel state”, Phys. Rev. Lett. **50**, 1153 (1983).

[45] J. Richter, J. Schulenburg, and A. Honecker, “Quantum magnetism in two dimensions: from semi-classical néel order to magnetic disorder”, *Quantum magnetism*, edited by U. Schollwöck, J. Richter, D. J. J. Farnell, and R. F. Bishop (Springer Berlin Heidelberg, Berlin, Heidelberg, 2004), pp. 85–153.

[46] I. Affleck, T. Kennedy, E. H. Lieb, and H. Tasaki, “Rigorous results on valence-bond ground states in antiferromagnets”, Phys. Rev. Lett. **59**, 799 (1987).

[47] C. K. Majumdar, “Antiferromagnetic model with known ground state”, Journal of Physics C: Solid State Physics **3**, 911 (1970).

[48] C. K. Majumdar and D. K. Ghosh, “On next-nearest-neighbor interaction in linear chain. i”, Journal of Mathematical Physics **10**, 1388 (1969), eprint: https://doi.org/10.1063/1.1664978.

[49] K. C. Smith, E. Crane, N. Wiebe, and S. Girvin, “Deterministic constant-depth preparation of the aklt state on a quantum processor using fusion measurements”, PRX Quantum **4**, 020315 (2023).

[50] R. Thorngren, A. Vishwanath, and R. Verresen, “Intrinsically gapless topological phases”, Phys. Rev. B **104**, 075132 (2021).

[51] D. Gaiotto, A. Kapustin, N. Seiberg, and B. Willett, “Generalized global symmetries”, Journal of High Energy Physics **2015**, 172 (2015).

[52] F. J. Wegner, “Duality in generalized ising models and phase transitions without local order parameters”, Journal of Mathematical Physics **12**, 2259 (1971).

[53] H. W. J. Blöte and Y. Deng, “Cluster monte carlo simulation of the transverse ising model”, Phys. Rev. E **66**, 066110 (2002).

[54] S. Hesselmann and S. Wessel, “Thermal ising transitions in the vicinity of two-dimensional quantum critical points”, Phys. Rev. B **93**, 155157 (2016).

[55] A. W. Sandvik, “Stochastic series expansion method for quantum ising models with arbitrary interactions”, Phys. Rev. E **68**, 056701 (2003).

[56] J. Jordan, R. Orús, G. Vidal, F. Verstraete, and J. I. Cirac, “Classical simulation of infinite-size quantum lattice systems in two spatial dimensions”, Phys. Rev. Lett. **101**, 250602 (2008).

[57] R. Orús and G. Vidal, “Simulation of two-dimensional quantum systems on an infinite lattice revisited: corner transfer matrix for tensor contraction”, Phys. Rev. B **80**, 094403 (2009).

[58] J. Oitmaa, C. Hamer, and W. Zheng, *Series expansion methods for strongly interacting lattice models* (Cambridge University Press, 2006).

[59] C.-W. Liu, A. Polkovnikov, and A. W. Sandvik, “Quasi-adiabatic quantum monte carlo algorithm for quantum evolution in imaginary time”, Phys. Rev. B **87**, 174302 (2013).

[60] S. Sachdev, “Topological order, emergent gauge fields, and fermi surface reconstruction”, Reports on Progress in Physics **82**, 014001 (2018).

[61] S. Elitzur, “Impossibility of spontaneously breaking local symmetries”, Phys. Rev. D **12**, 3978 (1975).

[62] G. ’t Hooft, “On the phase transition towards permanent quark confinement”, Nuclear Physics B **138**, 1 (1978).

[63] E. Fradkin and S. H. Shenker, “Phase diagrams of lattice gauge theories with higgs fields”, Phys. Rev. D **19**, 3682 (1979).

[64] R. Thorngren, T. Rakovszky, R. Verresen, and A. Vishwanath, “Higgs condensates are symmetry-protected topological phases: ii. $U(1)$ gauge theory and superconductors”, 2023, arXiv:2303.08136 [cond-mat.str-el].

[65] R. Verresen, U. Borla, A. Vishwanath, S. Moroz, and R. Thorngren, “Higgs condensates are symmetry-protected topological phases: i. discrete symmetries”, 2024, arXiv:2211.01376 [cond-mat.str-el].

[66] K. G. Wilson, “Confinement of quarks”, Phys. Rev. D **10**, 2445 (1974).

[67] W.-T. Xu, F. Pollmann, and M. Knap, “Critical behavior of fredenhagen-marcu string order parameters at topological phase transitions with emergent higher-form symmetries”, npj Quantum Information **11**, 74 (2025).

[68] L. Barbiero, C. Schweizer, M. Aidelsburger, E. Demler, N. Goldman, and F. Grusdt, "Coupling ultracold matter to dynamical gauge fields in optical lattices: from flux attachment to $\mathbb{Z}_2$ lattice gauge theories", Science Advances **5**, eaav7444 (2019).

[69] J. C. Halimeh, M. Aidelsburger, F. Grusdt, P. Hauke, and B. Yang, "Cold-atom quantum simulators of gauge theories", Nature Physics **21**, 25 (2025).

[70] L. Homeier, C. Schweizer, M. Aidelsburger, A. Fedorov, and F. Grusdt, "$\mathbb{Z}_2$ lattice gauge theories and kitaev's toric code: a scheme for analog quantum simulation", Phys. Rev. B **104**, 085138 (2021).

[71] C. Schweizer, F. Grusdt, M. Berngruber, L. Barbiero, E. Demler, N. Goldman, I. Bloch, and M. Aidelsburger, "Floquet approach to $\mathbb{Z}_2$ lattice gauge theories with ultracold atoms in optical lattices", Nature Physics **15**, 1168 (2019).

[72] E. Zohar, A. Farace, B. Reznik, and J. I. Cirac, "Digital quantum simulation of $\mathbb{Z}_2$ lattice gauge theories with dynamical fermionic matter", Phys. Rev. Lett. **118**, 070501 (2017).

[73] J. W. Essam, "Percolation theory", Reports on Progress in Physics **43**, 833 (1980).

[74] L. P. Kadanoff, "Scaling laws for ising models near T_c", Physics Physique Fizika **2**, 263 (1966).

[75] A. Kitaev and J. Preskill, "Topological entanglement entropy", Phys. Rev. Lett. **96**, 110404 (2006).

[76] C. Castelnovo and C. Chamon, "Entanglement and topological entropy of the toric code at finite temperature", Phys. Rev. B **76**, 184442 (2007).

[77] J. R. Norris, *Markov chains*, Cambridge Series in Statistical and Probabilistic Mathematics (Cambridge University Press, 1997).

[78] C. Robert and G. Casella, *Monte carlo statistical methods* (Springer, 2004).

[79] N. Metropolis, A. W. Rosenbluth, M. N. Rosenbluth, A. H. Teller, and E. Teller, "Equation of state calculations by fast computing machines", The Journal of Chemical Physics **21**, 1087 (1953), eprint: https://doi.org/10.1063/1.1699114.

[80] W. K. Hastings, "Monte Carlo sampling methods using Markov chains and their applications", Biometrika **57**, 97 (1970), eprint: https://academic.oup.com/biomet/article-pdf/57/1/97/23940249/57-1-97.pdf.

[81] F. Wu, Y. Deng, and N. Prokof'ev, "Phase diagram of the toric code model in a parallel magnetic field", Phys. Rev. B **85**, 195104 (2012).

[82] E. Y. Loh, J. E. Gubernatis, R. T. Scalettar, S. R. White, D. J. Scalapino, and R. L. Sugar, "Sign problem in the numerical simulation of many-electron systems", Phys. Rev. B **41**, 9301 (1990).

[83] M. Troyer and U.-J. Wiese, "Computational complexity and fundamental limitations to fermionic quantum monte carlo simulations", Phys. Rev. Lett. **94**, 170201 (2005).

[84] S. Bravyi, D. P. Divincenzo, R. Oliveira, and B. M. Terhal, “The complexity of stoquastic local hamiltonian problems”, Quantum Info. Comput. **8**, 361 (2008).

[85] G. Carleo and M. Troyer, “Solving the quantum many-body problem with artificial neural networks”, Science **355**, 602 (2017), eprint: https://www.science.org/doi/pdf/10.1126/science.aag2302.

[86] O. Sharir, A. Shashua, and G. Carleo, “Neural tensor contractions and the expressive power of deep neural quantum states”, Phys. Rev. B **106**, 205136 (2022).

[87] H. Lange, A. Van de Walle, A. Abedinnia, and A. Bohrdt, “From architectures to applications: a review of neural quantum states”, Quantum Science and Technology **9**, 040501 (2024).

[88] D. Luo, G. Carleo, B. K. Clark, and J. Stokes, “Gauge equivariant neural networks for quantum lattice gauge theories”, Phys. Rev. Lett. **127**, 276402 (2021).

[89] Y. Nomura, “Helping restricted boltzmann machines with quantum-state representation by restoring symmetry”, Journal of Physics: Condensed Matter **33**, 174003 (2021).

[90] M. Reh, M. Schmitt, and M. Gärttner, “Optimizing design choices for neural quantum states”, Phys. Rev. B **107**, 195115 (2023).

[91] C. Roth, A. Szabó, and A. H. MacDonald, “High-accuracy variational monte carlo for frustrated magnets with deep neural networks”, Phys. Rev. B **108**, 054410 (2023).

[92] R. Verresen, M. D. Lukin, and A. Vishwanath, “Prediction of toric code topological order from rydberg blockade”, Phys. Rev. X **11**, 031005 (2021).

[93] H. K. Onnes, *Further experiments with liquid helium. v. the disappearance of the resistance of mercury*, Communications from the Physical Laboratory of the University of Leiden 122b, Original report; no DOI assigned (Physical Laboratory of the University of Leiden, Leiden, The Netherlands, May 1911).

[94] H. K. Onnes, “Further experiments with liquid helium. d. on the change of the electrical resistance of pure metals at very low temperatures, etc. v. the disappearance of the resistance of mercury”, *Through measurement to knowledge: the selected papers of heike kamerlingh onnes 1853–1926*, edited by K. Gavroglu and Y. Goudaroulis (Springer Netherlands, Dordrecht, 1991), pp. 264–266.

[95] W. Meissner and R. Ochsenfeld, “Ein neuer effekt bei eintritt der supraleitfähigkeit”, Naturwissenschaften **21**, 787 (1933).

[96] F. London and H. London, “The electromagnetic equations of the supraconductor”, Proceedings of the Royal Society of London. Series A - Mathematical and Physical Sciences **149**, 71 (1935), eprint: https://royalsocietypublishing.org/doi/pdf/10.1098/rspa.1935.0048.

[97] V. L. Ginzburg and L. D. Landau, “On the theory of superconductivity”, Russian, Zh. Eksp. Teor. Fiz. **20**, 1064 (1950).

[98] A. A. Abrikosov, “On the Magnetic Properties of Superconductors of the Second Group”, Sov. Phys. JETP **5**, 1174 (1957).

[99] J. Bardeen, L. N. Cooper, and J. R. Schrieffer, “Theory of superconductivity”, Phys. Rev. **108**, 1175 (1957).

[100] L. N. Cooper, “Bound electron pairs in a degenerate fermi gas”, Phys. Rev. **104**, 1189 (1956).

[101] M. Sigrist and K. Ueda, “Phenomenological theory of unconventional superconductivity”, Reviews of Modern Physics **63**, 239 (1991).

[102] A. Schilling, M. Cantoni, J. D. Guo, and H. R. Ott, “Superconductivity above 130 k in the hg–ba–ca–cu–o system”, Nature **363**, 56 (1993).

[103] A. V. Gorshkov, M. Hermele, V. Gurarie, C. Xu, P. S. Julienne, J. Ye, P. Zoller, E. Demler, M. D. Lukin, and A. M. Rey, “Two-orbital s u(n) magnetism with ultracold alkaline-earth atoms”, Nature Physics **6**, 289 (2010).

[104] D. P. Arovas, E. Berg, S. A. Kivelson, and S. Raghu, “The hubbard model”, Annual Review of Condensed Matter Physics **13**, 239 (2022).

[105] M. Qin, C.-M. Chung, H. Shi, E. Vitali, C. Hubig, U. Schollwöck, S. R. White, and S. Zhang (Simons Collaboration on the Many-Electron Problem), “Absence of superconductivity in the pure two-dimensional hubbard model”, Phys. Rev. X **10**, 031016 (2020).

[106] Y.-F. Jiang, T. P. Devereaux, and H.-C. Jiang, “Ground-state phase diagram and superconductivity of the doped hubbard model on six-leg square cylinders”, Phys. Rev. B **109**, 085121 (2024).

[107] C. Gross and I. Bloch, “Quantum simulations with ultracold atoms in optical lattices”, Science **357**, 995 (2017), eprint: `https://www.science.org/doi/pdf/10.1126/science.aal3837`.

[108] G. Burkard, T. D. Ladd, A. Pan, J. M. Nichol, and J. R. Petta, “Semiconductor spin qubits”, Rev. Mod. Phys. **95**, 025003 (2023).

[109] C. S. Chiu, G. Ji, A. Mazurenko, D. Greif, and M. Greiner, “Quantum state engineering of a hubbard system with ultracold fermions”, Phys. Rev. Lett. **120**, 243201 (2018).

[110] M. Xu, L. H. Kendrick, A. Kale, Y. Gang, C. Feng, S. Zhang, A. W. Young, M. Lebrat, and M. Greiner, “A neutral-atom hubbard quantum simulator in the cryogenic regime”, Nature **642**, 909 (2025).

[111] J.-Y. P. Delannoy, M. J. P. Gingras, P. C. W. Holdsworth, and A.-M. S. Tremblay, “Low-energy theory of the $t - t^{'} - t^{''} - U$ hubbard model at half-filling: interaction strengths in cuprate superconductors and an effective spin-only description of La_2CuO_4”, Phys. Rev. B **79**, 235130 (2009).

[112] J. R. Schrieffer and P. A. Wolff, “Relation between the anderson and kondo hamiltonians”, Phys. Rev. **149**, 491 (1966).

[113] A. H. MacDonald, S. M. Girvin, and D. Yoshioka, “$\frac{t}{U}$ expansion for the hubbard model”, Phys. Rev. B **37**, 9753 (1988).

[114] A. Bohrdt, E. Demler, and F. Grusdt, “Dichotomy of heavy and light pairs of holes in the t-j model”, Nature Communications **14**, 8017 (2023).

[115] A. Bohrdt, E. Demler, and F. Grusdt, “Rotational resonances and regge-like trajectories in lightly doped antiferromagnets”, Phys. Rev. Lett. **127**, 197004 (2021).

[116] H. Feshbach, “A unified theory of nuclear reactions. ii”, Annals of Physics **19**, 287 (1962).

[117] U. Schollwöck, “The density-matrix renormalization group”, Rev. Mod. Phys. **77**, 259 (2005).

[118] U. Schollwöck, “The density-matrix renormalization group in the age of matrix product states”, Annals of Physics **326**, 96 (2011).

[119] U. Schollwöck, “The density-matrix renormalization group: a short introduction”, Philosophical Transactions of the Royal Society A: Mathematical, Physical and Engineering Sciences **369**, 2643 (2011), eprint: https://royalsocietypublishing.org/doi/pdf/10.1098/rsta.2010.0382.

[120] E. Stoudenmire and S. R. White, “Studying two-dimensional systems with the density matrix renormalization group”, Annual Review of Condensed Matter Physics **3**, 111 (2012).

[121] J. Haegeman, J. I. Cirac, T. J. Osborne, I. Pi žorn, H. Verschelde, and F. Verstraete, “Time-dependent variational principle for quantum lattices”, Phys. Rev. Lett. **107**, 070601 (2011).

[122] J. Haegeman, C. Lubich, I. Oseledets, B. Vandereycken, and F. Verstraete, “Unifying time evolution and optimization with matrix product states”, Phys. Rev. B **94**, 165116 (2016).

[123] S. Paeckel, T. Köhler, A. Swoboda, S. R. Manmana, U. Schollwöck, and C. Hubig, “Time-evolution methods for matrix-product states”, Annals of Physics **411**, 167998 (2019).

[124] Z. Wang and L. Pollet, “Renormalized classical spin liquid on the ruby lattice”, Phys. Rev. Lett. **134**, 086601 (2025).

[125] L. Homeier, H. Lange, E. Demler, A. Bohrdt, and F. Grusdt, “Feshbach hypothesis of high-tc superconductivity in cuprates”, Nature Communications **16**, 314 (2025).

[126] A. Bohrdt, D. Greif, E. Demler, M. Knap, and F. Grusdt, “Angle-resolved photoemission spectroscopy with quantum gas microscopes”, Phys. Rev. B **97**, 125117 (2018).